Optimized treatment parameters to account for interfractional variability in scanned ion beam therapy of lung cancer

Optimierte Bestrahlungsparameter zur Kompensation von interfraktioneller Variabilität während einer Lungentumor-Therapie mit gescannten Ionenstrahlen
Zur Erlangung des Grades eines Doktors der Naturwissenschaften (Dr. rer. nat.)
vom Fachbereich Physik genehmigte Dissertation von MSc Romain Brevet aus Saint Brieuc, Frankreich
1. Gutachten: Prof. Dr. Marco Durante
2. Gutachten: Prof. Dr. Christoph Bert
Tag der Einreichung: 16. Dezember 2014, Tag der Prüfung: 4. Februar 2015
Darmstadt
— D 17

TECHNISCHE
UNIVERSITÄT
DARMSTADT

Fachbereich Physik
Institut für Festkörperphysik

Optimized treatment parameters to account for interfractional variability in scanned ion beam therapy of lung cancer
Optimierte Bestrahlungsparameter zur Kompensation von interfraktioneller Variabilität während einer Lungentumor-Therapie mit gescannten Ionenstrahlen

Vom Fachbereich Physik genehmigte Dissertation von MSc Romain Brevet aus Saint Brieuc, Frankreich

1. Gutachten: Prof. Dr. Marco Durante
2. Gutachten: Prof. Dr. Christoph Bert

Tag der Einreichung: 16. Dezember 2014
Tag der Prüfung: 4. Februar 2015

Darmstadt — D 17

Abstract

Scanned ion beam therapy of lung tumors is severely limited in its clinical applicability by intrafractional organ motion, interference effects between beam and tumor motion (interplay) as well as interfractional anatomic changes. To compensate for dose deterioration by intrafractional motion, motion mitigation techniques, such as gating have been developed. The latter confines the irradiation to a predetermined breathing state, usually the stable end-exhale phase. However, optimization of the treatment parameters is needed to further improve target dose coverage and normal tissue sparing.

The aim of the study presented in this dissertation was to determine treatment planning parameters that permit to recover good target coverage and homogeneity during a full course of lung tumor treatments. For 9 lung tumor patients from MD Anderson Cancer Center (MDACC), a total of 70 weekly time-resolved computed tomography (4DCT) datasets were available, which depict the evolution of the patient anatomy over the several fractions of the treatment. Using the GSI in-house treatment planning system (TPS) TRiP4D, 4D simulations were performed on each weekly 4DCT for each patient using gating and optimization of a single treatment plan based on a planning CT acquired prior to treatment. It was found that using a large beam spot size, a short gating window (GW), additional margins and multiple fields permitted to obtain the best results, yielding an average target coverage (V_{95}) of 96.5%. Two motion mitigation techniques, one approximating the rescanning process (multiple irradiations of the target with a fraction of the planned dose) and one combining the latter and gating, were then compared to gating. Both did neither show an improvement in target dose coverage nor in normal tissue sparing. Finally, the total dose delivered to each patient in a simulation of a fractioned treatment was calculated and clinical requirements in terms of target coverage and normal tissue sparing were considered. The results showed that the total V_{95} obtained for the entire course of the treatment was similar to the one obtained for the planning CT, which shows that interfractional variability was successfully compensated. For 4 patients out of 9, $V_{95} > 95\%$ was thus obtained for both the planning CT and the total dose target coverage. For the rest of the cohort, a slight modification of the contours or dose reduction should permit to obtain a better clinical treatment plan that could be delivered over the course of the treatment.

In the presented study, intrafractional motion occuring during the treatment of lung tumors was efficiently mitigated using optimized treatment planning parameters and gating, while interfractional variability showed the largest impact on dose delivery. Nevertheless, this variability was efficiently mitigated, as shown by target dose coverage obtained at the end of the treatment which was very close to the one obtained for the planning CT.

Zusammenfassung

Bei der Bestrahlung bewegter Tumoren, wie Lungentumoren, mit gescannten Ionenstrahlen können intrafraktionelle Organbewegungen, Interferenzen zwischen Tumor- und Strahlbewegung (sogenanntes Interplay) sowie interfraktionelle anatomische Variabilität zu einer klinisch inakzeptablen Dosisverteilung führen. Beeinträchtigungen der Dosishomogenität im Zielvolumen durch intrafraktionelle Bewegung und Interplay können mit unterbrochener Bestrahlung (Gating) teilweise kompensiert werden, bei der der Tumor nur während des stabilsten Teils der Bewegung bestrahlt wird. Dennoch ist eine weitere Optimierung der Bestrahlungsparameter notwendig, um Dosisabdeckung zu verbessern sowie Normalgewebsbelastung zu verringern.

In dieser Arbeit wurden Bestrahlungsparameter quantifiziert, um gute Dosisabdeckung des Ziels für Lungentumor-Bestrahlungen zu erreichen. Für 9 Patienten des MD Anderson Cancer Center standen 70 4D-Computertomographien zur Verfügung, mit denen die Entwicklung der Anatomie über den Verlauf der Behandlung beurteilt werden konnte. Für jeden Patienten wurden mit dem 4D-Bestrahlungsplanungsprogramm TRiP4D der GSI 4D-Rechnungen mit Gating und einem einzigen, vor der Bestrahlung optimierten Bestrahlungsplan durchgeführt. Rechnungen, die mit einem breiten Strahlfokus, einem kurzen Gating-Fenster, zusätzlichen Sicherheitssäumen und mehreren Bestrahlungsfeldern ausgeführt wurden, erzielten die beste Abdeckung ($V_{95} = 96.5\%$). Weiterhin wurde Gating mit zwei Techniken verglichen: die erste Technik stützt sich auf Rescanning (mehrere Bestrahlungen des Ziels mit einem Bruchteil der Dosis) und die zweite auf eine Rescanning/Gating Kombination. Mit diesen beiden Techniken konnten keine besseren Ergebnisse in Bezug auf Dosisabdeckung oder Normalgewebsbelastung erreicht worden. Schließlich wurde in einer Simulation eines klinischen Behandlungsschemas die Gesamtdosis für jeden Patient bestimmt und klinische Grenzwerte für Dosis und Normalgewebsbelastung einbezogen. Für alle Patienten waren die Dosisabdeckung des Planungs-CTs und der ganzen Behandlung ähnlich; interfraktionelle Variabilität wurde also kompensiert. Für 4 Patienten wurde ein $V_{95} > 95\%$ für das Planungs-CT und die totale Behandlung erreicht. Für die anderen Patienten könnten eine Änderung der Kontouren oder eine Reduzierung der Dosis einen besseren Bestrahlungsplan erzeugen, der während der ganzen Behandlung benutzt werden könnte.

In dieser Arbeit konnten intrafraktionelle Bewegungseffekte bei der Bestrahlung von Lungentumoren durch optimierte Bestrahlungsparameter und Gating weitgehend kompensiert werden, während interfraktionelle Variationen als die größere Quelle für Dosisunsicherheiten identifiziert wurden. Ähnliche Dosisabdeckungen für das statische Planungs-CT und die gesamte dynamische Behandlung haben dennoch gezeigt, dass diese effizient kompensiert werden konnten.

Publications related to this work

Scientific reports

R. Brevet, C. Graeff, C. Bert and M. Durante (2012). Confirmation of the tumour motion extraction method. *GSI Scientific Report 2012*, 471.

R. Brevet, D. Richter, C. Graeff, M. Durante and C. Bert (2013). Studying inter- and intrafraction motion mitigation with sequential 4DCTs of NSCLC patients. *GSI Scientific Report 2013*, 239.

Conference contributions

R. Brevet, P. Steidl, M. Durante and C. Bert (2012). Correlation score-based tumor tracking from MV-fluoroscopy using EPID without fiducial markers. *PTCOG 51*. Poster presentation.

R. Brevet, D. Richter, C. Graeff, M. Durante and C. Bert (2013). Impact of anatomic changes and treatment parameters on simulated dose to lung tumors in a patient cohort with sequential 4D-CTs. *European Journal of Cancer, 49 (Suppl. 2)*:S240. Poster presentation.

R. Brevet, D. Richter, C. Graeff, M. Durante and C. Bert (2014). Studying inter- and intrafraction motion mitigation with sequential 4DCTs of lung tumor patients. *Radiotherapy and Oncology, Vol 110 (Suppl. 1)*. Oral presentation.

R. Brevet, D. Richter, C. Graeff, M. Durante and C. Bert (2014). Combining multiple fields and ITV-PTV margins for motion mitigation using NSCLC sequential 4DCTs. *PTCOG 53*. Poster presentation.

Contents

List of Abbreviations

2D	two-dimensional
2FITV	two fields/ITV
2FPTV	two fields/PTV
3D	three-dimensional
3D0	static simulation using the planning CT
3DCT	three-dimensional computed tomography
3FITV	three fields/ITV
3FPTV	three fields/PTV
4D	four-dimensional
4D0	4D simulation using the planning CT
4DCT	time-resolved computed tomography
4DN	4D simulation using the N^{th} weekly CT
4DTPS	4D treatment planning system
AITV	appropriate ITV
AP	anteroposterior
BSR	breath-sampling rescanning
CBCT	cone-beam computed tomography
CN	conformity number
CT	computed tomography
CTV	clinical target volume
DNA	deoxyribonucleic acid
DVH	dose volume histogram
FWHM	full width at half maximum
GSI	GSI Helmholtz Center for Heavy Ion Research
GTV	gross tumor volume
GW	gating window
HIT	Heidelberg Ion-Beam Therapy Center
HU	Hounsfield unit
ICRU	International Commission on Radiation Units and Measurements
IES	iso-energy slice
IMRT	intensity-modulated radiation therapy
ITV	internal target volume
kV	kilovoltage
LEM	local effect model
LET	linear energy transfer
LFSG	large focus/short GW
LQ	linear-quadratic
LQ-L	linear-quadractic linear
LR	left-right
MDACC	MD Anderson Cancer Center
MGH	Massachusetts General Hospital
MLC	multi-leaf collimator

MLQ	modified linear-quadratic
MV	megavoltage
MXD	maximal dose point
NIRS	National Institute of Radiological Sciences
NSCLC	non-small cell lung cancer
OAR	organ at risk
PCR	phase-control rescanning
PMMA	polymethyl methacrylate
PRGT	perfect regating
PRSC	perfect rescanning
PSI	Paul Scherrer Institut
PTV	planning target volume
RBE	relative biological effectiveness
RiFi	ripple-filter
RTOG	Radiation Therapy Oncology Group
SFITV	single field/ITV
SFLG	small focus/long GW
SFPTV	single field/PTV
SFUD	single field uniform dose
SI	superior-inferior
SITV	single ITV
SOBP	spread-out Bragg peak
TPS	treatment planning system
TRiP4D	TRiP4D
TRiP98	TReatment Planning for Particles
USA	United States of America
USC	universal survival curve
WEPL	water-equivalent path length

1 Introduction

1.1 Motivation

Cancer is defined as *"a group of diseases characterized by uncontrolled growth and spread of abnormal cells"* (ACS, 2011). In 2008, more than 12.5 million new cases occurred worldwide (see Figure 1.1). It is expected to reach more than 20 million in 2030 due to population growth and aging. Cancer is, behind heart diseases, the second most leading cause of death worldwide with about 7.5 million of deaths in 2004, representing 12.6% of the total number of deaths. In the developed countries it is the leading cause of death with more than 2 million deaths, representing more than 26% of the total number of deaths.

Different types of cancer do not have the same incidence and death rates. Figure 1.2 shows an estimated distribution of the different types of cancer worldwide in 2008 in terms of new cases and deaths. In men, lung and bronchus are the most affected organs with more than 1 million new cases and about 1 million already known cases leading to death. In women, breast cancer is the most frequently occurring disease with more than 1.3 million new cases. While new lung and bronchus cancer are only the fourth most frequently occurring type of cancer way behind breast cancer, it is the second most deadly cancer with more than four hundred thousand deaths each year, only a few thousand less than breast cancer.

However, the rate of death caused by cancer from the years before 1990 is currently slowing down in the USA (Siegel et al., 2014) and it is estimated that more than 1.3 million deaths have been averted in this country since the nineties. Nowadays, due to better prevention and more effective treatments, the probability to die from cancer has been reduced to around 20-25% in the developed countries (IAEA, 2008).

Worldwide, it is also estimated that 45% of all cancer patients can be cured. Among those 45%, 23% undergo radiotherapy alone or in combination with surgery or chemotherapy-immunotherapy (IAEA, 2008; PTCOG). Radiotherapy being involved in half of the cured patient's treatments shows that this is a commonly used and effective technique to successfully treat cancer.

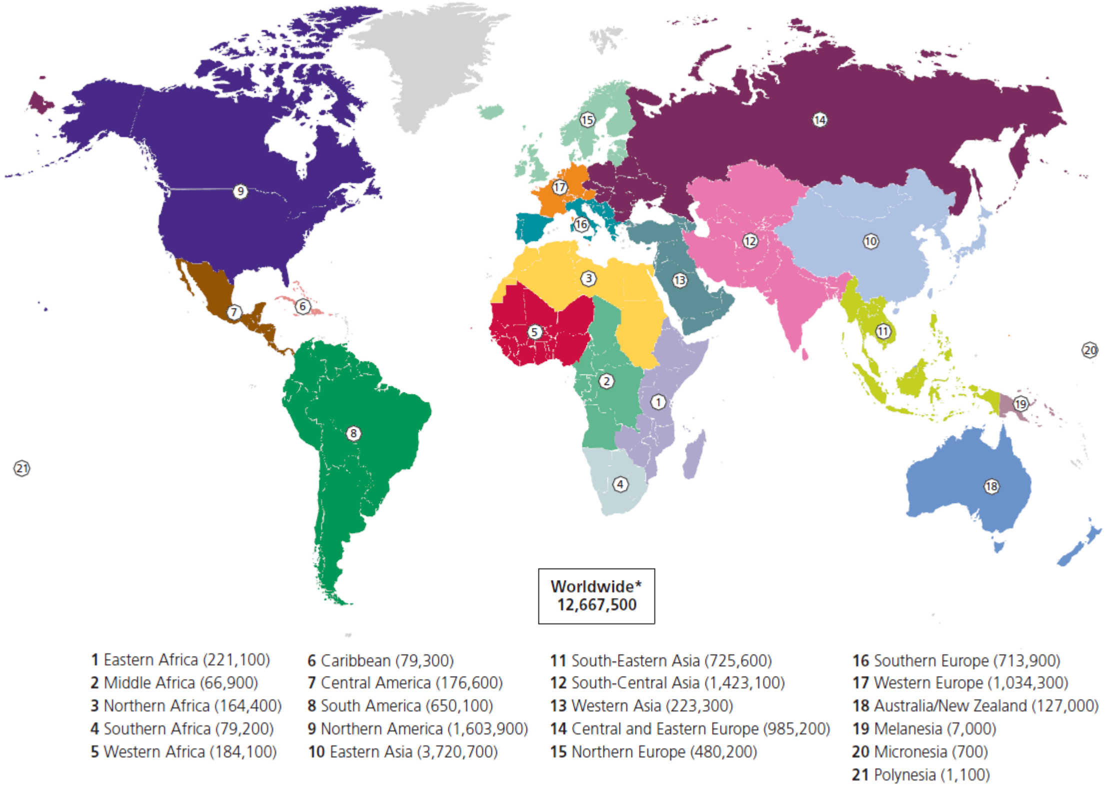

*Region estimates do not sum to the worldwide estimate due to calculation method.
Source: GLOBOCAN 2008.

Figure 1.1.: Estimated number of new cases of cancer worldwide. Figure from ACS (2011).

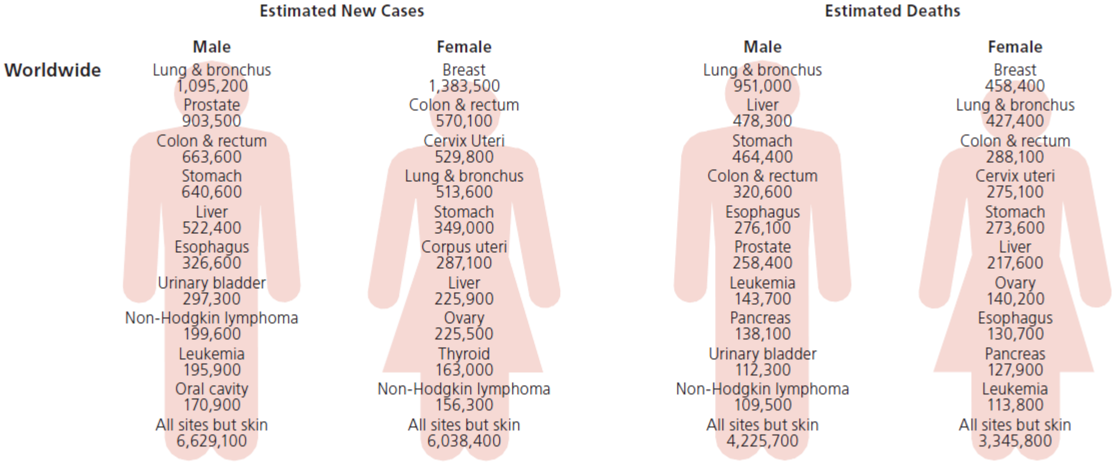

	Estimated New Cases		Estimated Deaths	
	Male	Female	Male	Female
Worldwide	Lung & bronchus 1,095,200	Breast 1,383,500	Lung & bronchus 951,000	Breast 458,400
	Prostate 903,500	Colon & rectum 570,100	Liver 478,300	Lung & bronchus 427,400
	Colon & rectum 663,600	Cervix Uteri 529,800	Stomach 464,400	Colon & rectum 288,100
	Stomach 640,600	Lung & bronchus 513,600	Colon & rectum 320,600	Cervix uteri 275,100
	Liver 522,400	Stomach 349,000	Esophagus 276,100	Stomach 273,600
	Esophagus 326,600	Corpus uteri 287,100	Prostate 258,400	Liver 217,600
	Urinary bladder 297,300	Liver 225,900	Leukemia 143,700	Ovary 140,200
	Non-Hodgkin lymphoma 199,600	Ovary 225,500	Pancreas 138,100	Esophagus 130,700
	Leukemia 195,900	Thyroid 163,000	Urinary bladder 112,300	Pancreas 127,900
	Oral cavity 170,900	Non-Hodgkin lymphoma 156,300	Non-Hodgkin lymphoma 109,500	Leukemia 113,800
	All sites but skin 6,629,100	All sites but skin 6,038,400	All sites but skin 4,225,700	All sites but skin 3,345,800

Figure 1.2.: Estimated new cancer cases and deaths worldwide in 2008. Figure from ACS (2011).

Now, clinical studies have shown that the physical and biological properties of ion therapy can allow obtaining better dose delivery conformity and tumor control rates as well as limited toxicity, for instance in the case of tumors located near critical structures which require precise dose delivery (Schulz-Ertner et al., 2007; Tsujii et al., 2004). Nowadays, further investigation is still carried out to obtain more clinical data (Durante and Loeffler, 2010). In particle therapy, pencil beam scanning (Haberer et al., 1993), which is likely to become the most used beam delivery technique in the future, has been developed but can currently only be used to its full potential for static tumors such as head and neck tumors. At the moment, treatment of moving targets, such as lung or liver tumors, with this beam delivery technique is limited by dose degradation caused by interference effects between the scanned beam and the tumor motion on a short scale of seconds to minutes, called interplay effects. On a longer time scale of hours to days, the treatment is affected by organ motion such as bowel movement or tumor shrinkage, which can cause changes in motion patterns and baselines (Britton et al., 2007; Sonke et al., 2008). Mitigation techniques have been developed in order to limit the effects of organ motion on dose delivery. Some, for instance, allow better compensation for the interplay effects previously mentioned while others are not applicable yet, due to computational or imaging constraints.

Treatment of lung tumors using carbon ion therapy has already been studied in clinical studies (Miyamoto et al., 2003, 2007). These studies showed promising results in terms of local tumor control and survival, especially for older patients with complications and small sized tumors. Also, a common practice in radiotherapy is to compute one treatment plan for the entire course of the treatment or for a couple of weeks before it might be adapted. Following this practice, the simulation studies presented in this dissertation aimed at obtaining satisfactory results in terms of target dose coverage and sparing of normal tissue, using optimized treatment planning parameters previously isolated.

1.2 Purpose of this work

As previously described, this study aimed at testing the impact of treatment planning parameters on dose delivery to the tumor and the organs at risk (OARs) over the entire course of a treatment. Obtained dose distributions were evaluated using dose coverage (ICRU, 2007) and normal tissue constraints (Grimm et al., 2011). Three main studies were carried out, all using a single treatment plan optimized prior to treatment for each patient and applying it in successive weekly dose calculations:

1. Firstly, using gating as motion mitigation method, the effect on dose delivery of four treatment planning parameters was investigated, so that they could be optimized to obtain conformal dose coverage of the tumor. Their effect on irradiation of surrounding organs was also studied.
2. Secondly, using the parameters yielding the best results in the first part, results obtained using gating and two other motion mitigation techniques, called perfect rescanning (PRSC) and perfect regating (PRGT), were compared in order to see if target dose coverage, as well as normal tissue sparing, could be further improved.

3. Finally, the use of a possible replanning factor based on inter-weekly beam range changes as well as robust field angles were investigated. Using the results of these two studies, the optimized parameters found in the first part and the best technique found in the second part, the simulation of clinical patient treatments was performed. This study aimed at investigating the efficiency of the optimized parameters in a single-plan-based scanned carbon ion beam treatment, by applying clinically used fractionation schemes and organ dose limits and by analyzing the obtained total target dose coverage and OAR exposure.

2 Research background & fundamentals

2.1 Particle therapy

This chapter introduces the important aspects of particle therapy, such as its biological and physical implications. It also depicts its evolution, starting with its historical background and finishing with its use in the treatment of moving tumors using techniques available nowadays.

2.1.1 Historical background

In January 1896, barely one month after Wilhelm Conrad Röntgen announced his discovery of the X-rays and demonstrated one of its properties by producing the first radiograph, the first medical use of this “new kind of ray” was reported. It had helped locating a piece of a knife in the backbone of a drunken sailor, who was paralyzed until the fragment was removed. Shortly after, the Austrian surgeon Leopold Freund presented the first therapy trial, he had been irradiating a hairy mole on the forearm of a patient, which had disappeared (Hall and Garcia, 2011; Kraft, 2000). Then, Antoine-Henri Becquerel described a skin erythema and its ulceration after leaving a radium container in his pocket and Pierre Curie noticed the same effect while repeating the experiment (Hall and Garcia, 2011). This was the starting point of the study of ionizing radiations on living things.

For a long time, radiation therapy development remained empirical. But it still followed two main tendencies: increasing the biological effectiveness of the radiation and achieving more conformal dose delivery to the target (Kraft, 2000). That is why, replacing X-ray tubes used at the beginning, gamma ray based treatments were developed to reduce the dose to the tissue in front of the target, followed by ions to increase the biological effectiveness.

The first time ions were proposed to be used as treatments for medical problems was in 1946 by Wilson (1946). His idea originated from the increasing energy of the new accelerators to be built, resulting in higher range in tissue allowing thus reaching deeper seated regions. He emphasized quite well the main qualities of such particles and the advantage they represent in comparison with photons. This will be described later in this chapter.

However, although cancer treatment can benefit a lot from this technique, many uncertainties are still present which have to be dealt with like relative biological effectiveness (RBE), which is nowadays determined using different methods from one continent to another (IAEA, 2008), for different tissue or cell types (Kase et al., 2008), intrafractional motion of moving tumors (Shirato et al., 2004; Bert and Durante, 2011) and its mitigation (Rietzel and Bert, 2010; Bert and Durante, 2011), interfractional anatomy changes or patient misalignments (Bert and Durante, 2011), interplay effects (Bert et al., 2008), effects of inhomogeneities on the Bragg peak (Sawakuchi et al., 2008), risks of secondary cancer (Kraft and Kraft, 2009) or organ at risk (OAR) dose limit values used nowadays, which have been presented for instance by Grimm et al. (2011) and Benedict et al. (2010) but which may not be "the maximal attainable safe dose" and are "mostly unvalidated". Jäkel et al. (2008) also published an interesting point of view regarding the future of heavy ion therapy and the issues to be faced, in which he concluded that heavy ion therapy still has to prove its safety and efficiency regarding some of the uncertainties described above as well as its cost effectiveness compared to photon radiotherapy.

Despite the uncertainties listed above, proton and heavy ion therapy treatments have been proven to be successful with many advantages such as better local control rates (Tsujii et al., 2007; Tsujii and Kamada, 2012). Also, the number of hadron therapy centers has not stopped increasing since the first facility in Berkeley in 1954. Nowadays, about 50 centers are in operation and more than 30 are under construction or at the planning stage (PTCOG). Besides, since 1954, more than one hundred thousand patients have been treated with protons and, since 1994 in Japan, 1997 in Germany and more recently in China and in Italy, more than ten thousand with carbons ions (Jermann, 2014). Previously mentioned advantages and specificities of particle therapy will be presented in the next sections.

2.1.2 Physical properties

The base of proton and heavy ion therapy is its favorable depth-dose profile which is naturally adapted to the situation (Chu et al., 1993; Kraft, 2007; Schardt et al., 2010). Figure 2.1 shows the advantage of charged particles. The right graph of 2.1 shows the absorbed dose in a certain depth of water for photons and ions (depth-dose-distribution). While photons have their maximum a little below the surface (green and black curves in the right graph of figure 2.1), ions (red curves) show a sharp peak at a certain depth determined by their energy (Bragg peak). This makes particle irradiation very interesting in the case of tumor treatment because deep-seated tumors can be treated with high precision while sparing normal tissue.

Absorbed dose is the mean energy dE deposited by ionizing radiation in mass element m. The unit is the Gray [Gy].

$$D = \frac{dE}{dm}; \quad [D] = 1\text{Gy} = 1\frac{\text{J}}{\text{kg}} \tag{2.1}$$

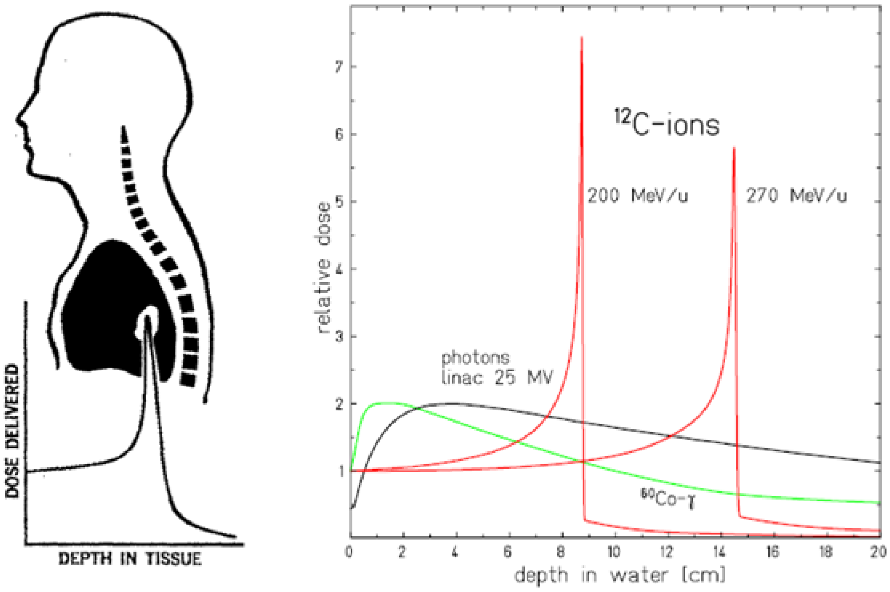

Figure 2.1.: Schematic illustration of the Bragg curve (left, from Chu et al. (1993)) and comparison of different depth-dose profiles (right, from Schardt et al. (2010)): the Bragg peak is a characteristic of protons and heavier ions and can be shifted by changing the kinetic energy of the particles.

It can be calculated using equation 2.2 where F is the fluence, ρ the mass density and dE/dx the energy loss of the particles per unit path length.

$$D\,[\mathrm{Gy}] = 1.6 \times 10^{-9} \times \frac{dE}{dx}\left[\frac{\mathrm{keV}}{\mu\mathrm{m}}\right] \times F\left[\mathrm{cm}^{-2}\right] \times \frac{1}{\rho}\left[\frac{\mathrm{cm}^3}{\mathrm{g}}\right] \tag{2.2}$$

The energy-loss rate dE/dx is then obtained by the Bethe-Bloch formula 2.3 which describes the slowing-down process of the particles (Bethe, 1930; Bloch, 1933b,a; Fano, 1963).

$$\frac{dE}{dx} = \frac{4\pi e^4 Z_t Z_p^2}{m_e c^2 \beta^2}\left[ln\frac{2m_e c^2\beta^2}{\langle I\rangle} - ln\left(1-\beta^2\right) - \beta^2 - \frac{C}{Z_t} - \frac{\delta}{2}\right] \tag{2.3}$$

Here Z_p and Z_t are the nuclear charges of the projectile and target, m_e and e are the mass and charge of the electron, $\beta = v/c$ (v being the velocity of the particle and c the speed of light), $\langle I\rangle$ is the mean ionization energy of the target. C/Z_t is the shell correction term which takes into account orbital velocities of the target electrons at low particle energies (Ziegler, 1999) and $\delta/2$ is the density-effect correction term valid for high energy particles (PDG, 2010).

Figure 2.2 shows that energy loss is mainly due to inelastic electronic scattering and that it increases with decreasing particle energy, due to the $1/\beta^2$ dependence, up to a maximum. While the projectile charge is equal to the atomic charge number Z_p at high velocities, recombination processes and ionization result in a decreasing mean charge state at lower velocities causing the inelastic electronic energy loss to drop again for lower particle energies. Thus Z_p has to be replaced by Z_{eff} using the following equation from Barkas (1963):

$$Z_{eff} = Z_p \left[1 - exp \left(-125 \beta Z_p^{-\frac{2}{3}} \right) \right] \tag{2.4}$$

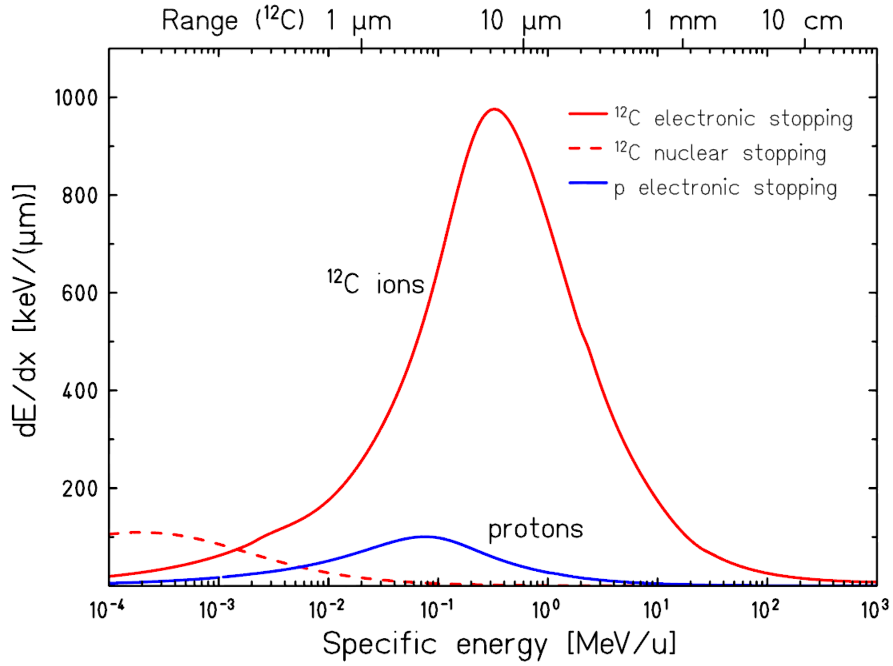

Figure 2.2.: Specific energy loss dE/dx of ^{12}C ions and protons in water from Schardt et al. (2010).

Figure 2.2 also shows that nuclear elastic reactions become the main contribution to energy loss when ions reach the low energies (less than 10 keV) at the end of the range. Moreover, for both protons and heavier ions, it is possible to shift the Bragg peak and to adjust its position by changing the kinetic energy of the incident particles (the two red curves on figure 2.1). However, three important differences between protons and heavier ions can be isolated, heavy ions exhibit:

- a narrower Bragg peak: range straggling is present with both protons and heavy ions in the limit of a large number of interactions. This is directly related to energy-loss straggling (Bohr, 1940; Ahlen, 1980) which follows a Gaussian distribution. The ratio of the straggling width σ_R and mean range R is given by equation 2.5:

$$\frac{\sigma_R}{R} = \frac{1}{\sqrt{M}} f \left(\frac{E}{Mc^2} \right) \tag{2.5}$$

where f is a slowly varying function related to the absorber and E and M are the particle energy and mass. In spite of this ratio being nearly constant, values for protons and heavier ions differ due to the $1/\sqrt{M}$ term, meaning it is much smaller for heavy ions than for protons. There is for instance a factor 3.5 between protons and ^{12}C ions (Schardt et al., 2010).

- a characteristic dose tail (see figure 2.3): this is due to nuclear fragmentation. This process plays a significant role in absorbed dose in the case of ions heavier than protons and consists for most of it in the peripheral collision of a projectile with the target nuclei (Kraft, 2000; Schardt et al., 2010). It can result in the complete disintegration of both elements or partial fragmentation and generally involves two steps: first nucleons are abraded in the contact zone and then the formed projectile emits nucleons or clusters to deexcite. Studies like Goldhaber and Heckman (1978), Hüfner (1985) and Lynch (1987) have permitted to isolate some effects of fragmentation:
    1. primary beam particles are lost and new lower-Z fragments are created, this effect increases with penetration depth,
    2. fragments are moving with roughly the same velocity as the primary particles, have longer ranges and cause the dose tail after the Bragg peak visible on Figure 2.3,
    3. angular distributions of fragments are larger than the one of the primary ions, but still mainly forward directed.

- a much smaller lateral beam spread at high depth (see figure 2.4): for low energy protons, scattering occuring in the nozzle mainly determines the width of the beam while for more energetic ones, scattering occuring in the water absorber dominates. This is mainly due to Coulomb scattering of the projectiles (Kraft, 2000) which was described theoretically by (Molière, 1948) and confirmed experimentally by Gottschalk et al. (1993) by measuring proton scattering. Carbon ions do not show such a large effect and a much smaller spread can be observed. For instance protons having a range $R = 15.6$ cm will show a angular spread which is 3 times larger than for ^{12}C ions at the same range (Schardt et al., 2010). Hence, two effects have to be considered during treatment:
    1. scattering before entering the patient caused by materials such as beam monitors or beam shaping devices. This is usually predominant at low energies and mostly for protons and can have significant effects on a scanned pencil beam,
    2. scattering in the patient body which dominates at higher energies. Once again ^{12}C ions are less affected by this effect but it is large enough that it needs to be incorporated into patient treatment planning.

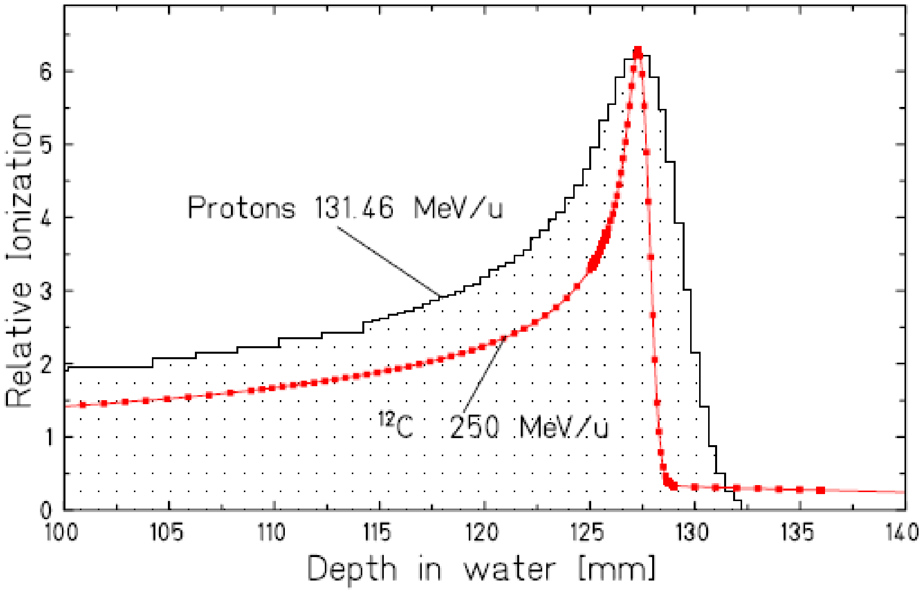

Figure 2.3.: Bragg peaks of protons and ^{12}C ions having the same range in water from Schardt et al. (2010): the tail of the Bragg peak for ions is clearly visible. Besides, the peak of ions is narrower than the one of protons.

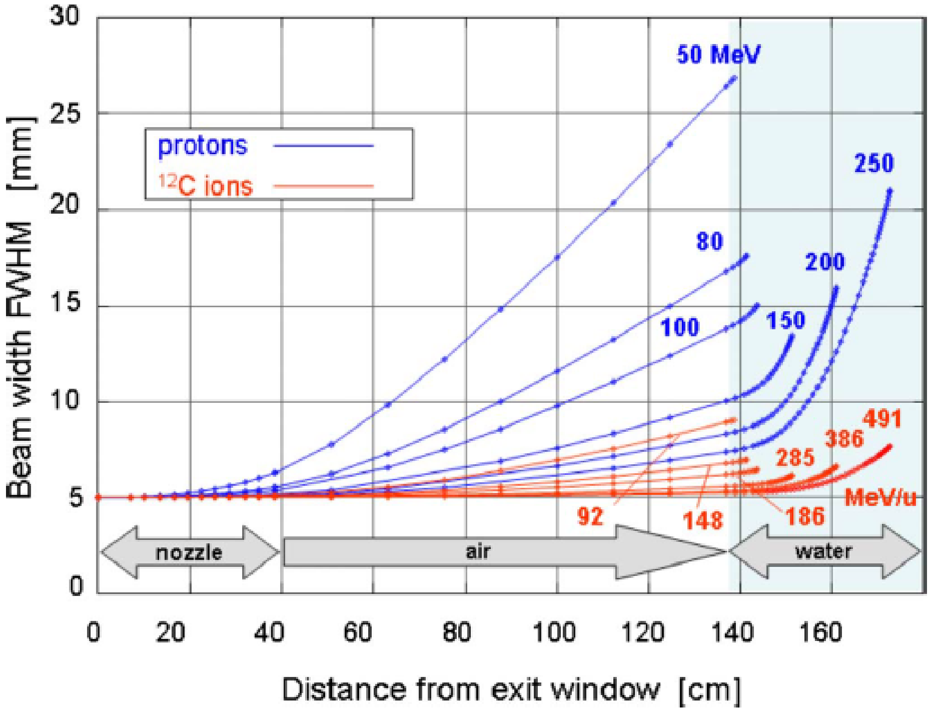

Figure 2.4.: Beam spread for ^{12}C ions and protons from Schardt et al. (2010): at high depth, the beam spread of the protons is much more important.

2.1.3 Biological properties

In addition to the many specificities described in the previous part, heavy ions and protons possess a larger biological effectiveness in comparison to particles showing a low linear energy transfer (LET) such as X-ray photons. Equation 2.3 shows the quadratic dependence of LET (through stopping power) on the projectile charge, which leads to high values in the case of heavier ions. It means more DNA damage on the ion tracks, especially at the end of the range, and the heavier the ion the more important the damage as displayed on Figure 2.5.

Besides, low energetic ions present in the region of the tumor being more likely to ionize compared to high velocity ones in the entrance channel, the biological effect is thus larger in the target than in the preceding tissue. Also, as displayed on figure 2.5, using ^{12}C ions permit to produce many more electrons compared to protons, which causes more DNA damage and thus again a larger biological effect. That is why the concept of relative biological effectiveness (RBE) has been developed. It can be applied between two different kinds of radiation (here a reference type of radiation compared to ions, the reference being in general X-rays, γ-rays or neutrons) and is defined as follows: it is the ratio of the dose of a reference radiation over the dose of ion irradiation necessary to obtain the same biological effect (isoeffect) (Schardt et al., 2010) (equation 2.6).

$$RBE_{iso} = \frac{D_{ref}}{D_{ion}} \tag{2.6}$$

Even though equation 2.6 looks simple, the RBE varies a lot depending on the dose (Figure 2.6) (Weyrather et al., 1999; Furusawa et al., 2000), the particle type and the energy (Belli et al., 1998; Scholz, 2003), the biological effect level (Figure 2.6) and the considered tissue (Weyrather et al., 1999). All these dependences were confirmed by in vivo animal studies such as Leith et al. (1982), Zacharias et al. (1997) and Ando et al. (1998). The concept of RBE is important because it can establish a link between ions and photons.

This link permits to see that ions have a larger biological effect than photons. Figure 2.5 shows the ionization processes responsible for radial dose distribution for protons and ^{12}C ions and which comprise two main successive steps:

1. first, electrons are emitted after the interaction of the incident ion with an atom or a molecule following inelastic coulomb interactions,

2. then, those electrons are scattered multiple times due to elastic interactions with the surrounding tissue or transfer their energy to the medium by the means of ionization or excitation.

Besides, in Monte Carlo simulations, analytical models and experimental studies a symmetric radial dose distribution following a $1/r^2$ dependence (r being the increasing distance) has been found (Chatterjee and Schaefer, 1976; Katz and Cucinotta, 1999; Paretzke, 1986; Krämer, 1995; Varma et al., 1977). Those ionizations and their distribution show that, compared to photons and for the same average macroscopic dose, ions cause more dense and complex damage at the microscopic level (Scholz, 2003), leading to a much higher probability of cell killing and making radiation damage of ions more efficient than that of photons (Nikjoo et al., 1999).

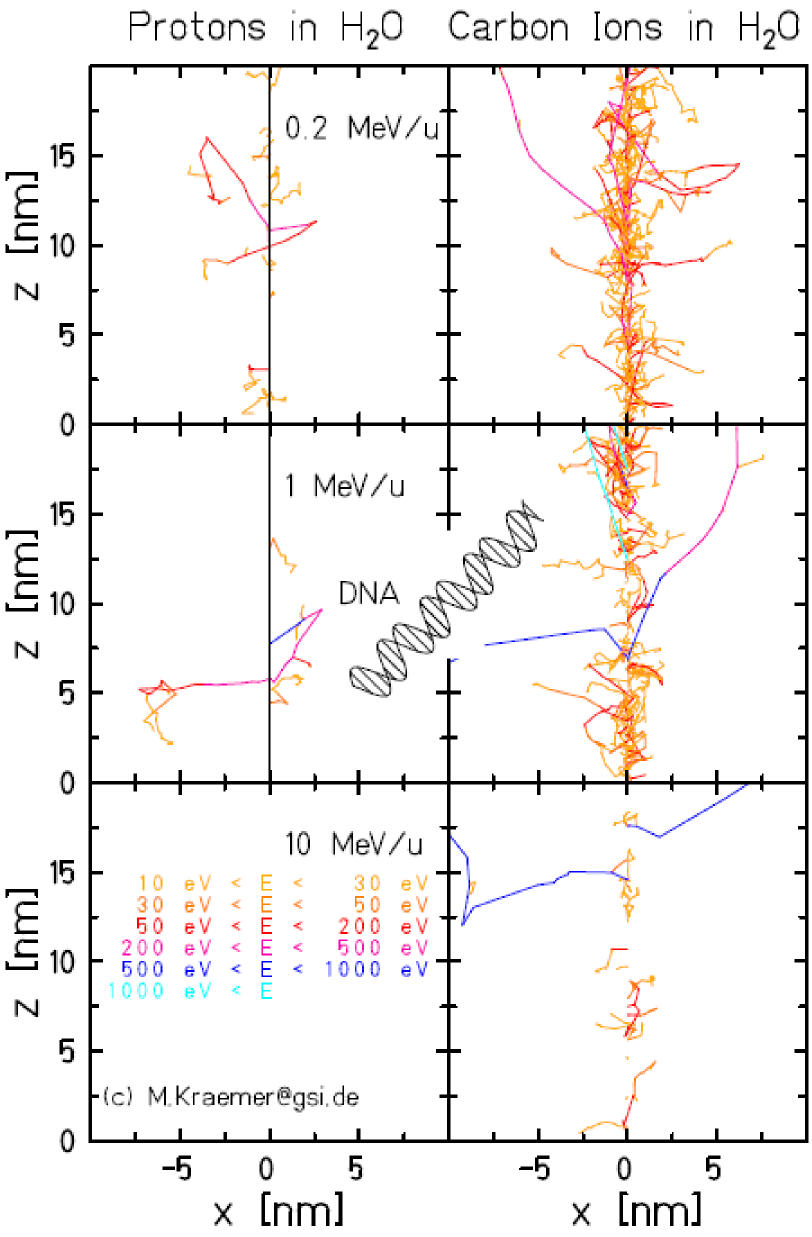

Figure 2.5.: Monte Carlo simulation of paths of emitted electrons with different energies created by protons and ^{12}C ions at 0.2, 1 and 10 MeV/u in water. Size comparison with a DNA molecule is displayed. Figure courtesy of M. Krämer.

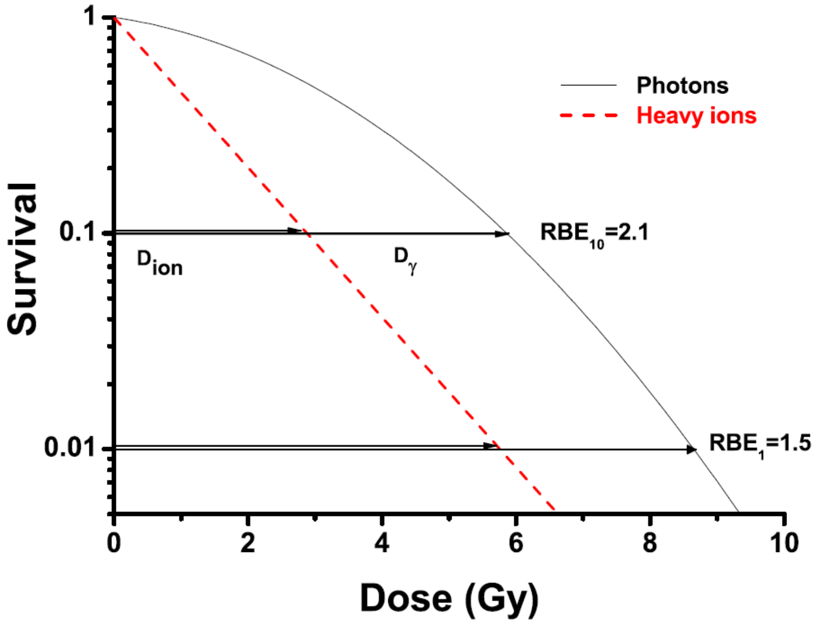

Figure 2.6.: Example of a cell survival curve and its use to determine RBE at 10% and 1% survival levels. Figure from Schardt et al. (2010).

Cell survival curves are a good method to calculate the RBE for a given cell line. Those curves generally follow the linear-quadratic (LQ) model (Hall and Garcia, 2011) given by equation 2.7:

$$S(D) = exp\left(-\alpha D - \beta D^2\right) \tag{2.7}$$

where S is the cell survival, D the absorbed dose and α and β parameters obtained experimentally. The shoulder of the cell survival curve (Figure 2.6) is determined by the ratio α/β which is often used in radiotherapy (Fowler, 2003). However other models exist, using the LQ model on one part of the curve and adding correction terms on the remaining part, such as the linear-quadractic linear (LQ-L) model (Astrahan, 2008; Scholz et al., 1997), the modified linear-quadratic (MLQ) model (Guerrero and Li, 2004) or the universal survival curve (USC) model (Park et al., 2008).

Besides, while a single value of RBE of 1.1 (Paganetti et al., 2002) is generally used for protons, there are several ways of calculating the RBE for heavier ions (Schardt et al., 2010; IAEA, 2008). In Japan, a passive shaping beam system has been designed (Kanai et al., 1997; Kagawa et al., 2002) and is used for treatment. Based on experience from neutron therapy, it was demonstrated by in vivo cell and mouse-skin reaction experiments that neutrons and ^{12}C ions show the same RBE for a LET of 80 keV/μm. By finding the neutron-equivalent position in a 6 cm ^{12}C (290 MeV/u) spread-out Bragg peak (SOBP) corresponding to a clinical RBE of 3, it was then possible to obtain the RBE in the middle of the SOBP, which was 2.38 (Kanai et al., 1999).

In general, values between 2.1 and 2.8 were found.

It works quite differently in GSI because, due to the beam delivery system called raster scanning (Haberer et al., 1993), the RBE needs to be calculated for each position in the treatment field to calculate the effect of the photon-equivalent dose. This is performed using the local effect model (LEM) (Scholz and Kraft, 1994, 1996). Using tables containing α values for ions and for many energies, (Scholz et al., 1997) developed a method to quickly calculate the associated β value. Using these values as inputs for the LQ-L model (Krämer et al., 2000; Krämer and Scholz, 2000), it is then possible to compute the RBE for any desired biological effect if the photon data is available. Depending on a lot of parameters, as described previously, RBE values can vary a lot.

2.1.4 Beam delivery techniques

Shortly mentioned above, there are several ways to deliver the beam to the tumor region with, as main requirements, accuracy and homogeneity. The two major strategies are referred to as passive and active beam delivery (Chu et al., 1993; Schardt et al., 2010).

2.1.4.1 Passive beam delivery

In the case of passive systems (like the fully passive system of figure 2.7), several elements are used to shape the beam delivered by the accelerator so that areas within the contours of the tumors are treated.

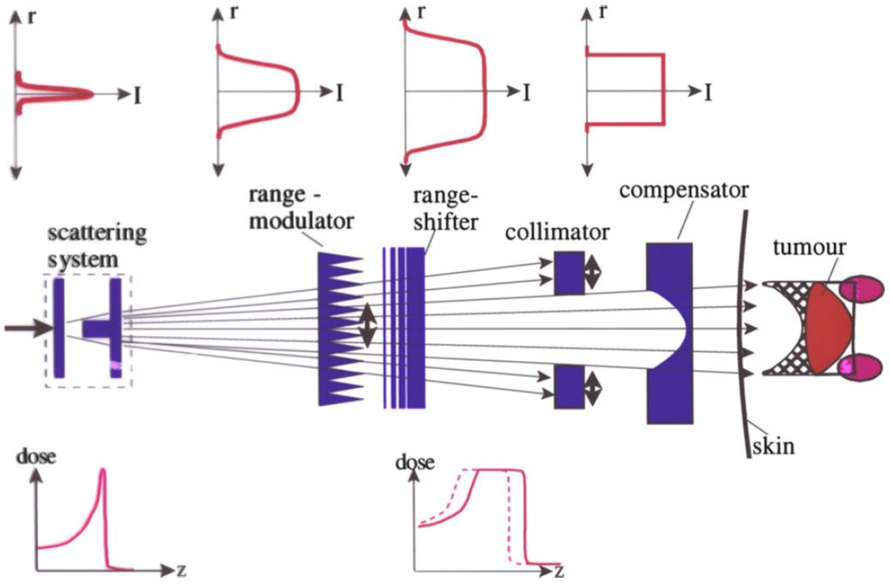

Figure 2.7.: Passive beam delivery system, from Schardt et al. (2010).

First the beam is broadened using a scattering device, then the range-modulator spreads out the monoenergetic Bragg peak so that the range of tumors in depth which can be treated is adjustable, next the range-shifter allows to adapt the position of the Bragg peak. Finally the collimator, which can be a multi-leaf collimator (MLC), cuts out the field area (the contour of the tumor) and the compensator (Figure 2.8) is used to adapt the distal depth according to the tumor shape and the tissue composition (Figure 2.8). Those two last elements are patient specific and must always both (when the collimator is not a MLC) be precisely fabricated. Work on design of many of these elements was done at the Harvard Cyclotron Laboratory (Koehler et al., 1975, 1977; Gottschalk and Wagner, 1989).

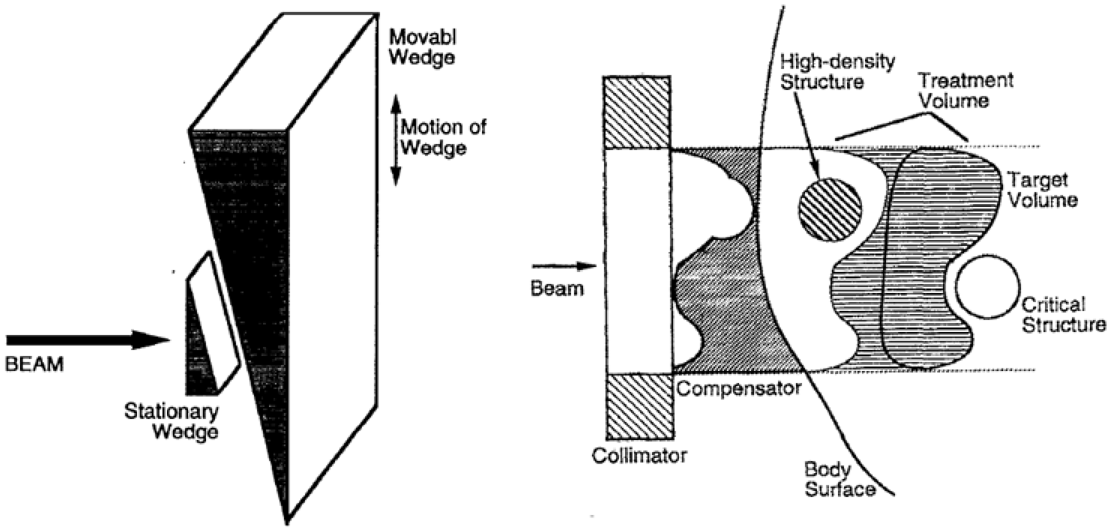

Figure 2.8.: Double wedge system used as a range shifter (left) and collimator-compensator systems (right) used to shape the beam. Figure from Chu et al. (1993).

The principle of the range shifter (like the double wedge system on figure 2.8) is to increase or decrease the depth of the material (for instance PMMA) so that the Bragg peak can be shifted. The energy loss is indeed linked to the depth of material (equation 2.3) so that the thicker the range shifter, the larger the shift. It can either be used with a single SOBP which covers the whole length of the tumor, but it has obvious limitations like dose delivery in the tissue surrounding the tumor (see figure 2.9.a), or be dynamically used (associated with a dynamic collimator) for the stacked irradiation technique which uses several smaller SOBPs to cover the tumor length (see figure 2.9.b), thus reducing the dose in the tissue the vicinity of the tumor (Chu et al., 1993; Schardt et al., 2010). However, cases presented in figure 2.8 and 2.9 are simple shaped tumors, and facing complex shaped ones could yield negative effects. More dose could for instance be delivered in the normal tissue for case (a) of figure 2.9 or, as it is not possible to vary dose level within one layer in case (b) of figure 2.9, dose inhomogeneities could appear in some areas of the tumor due to the irradiation of previous layers (like for a “H” shaped tumor).

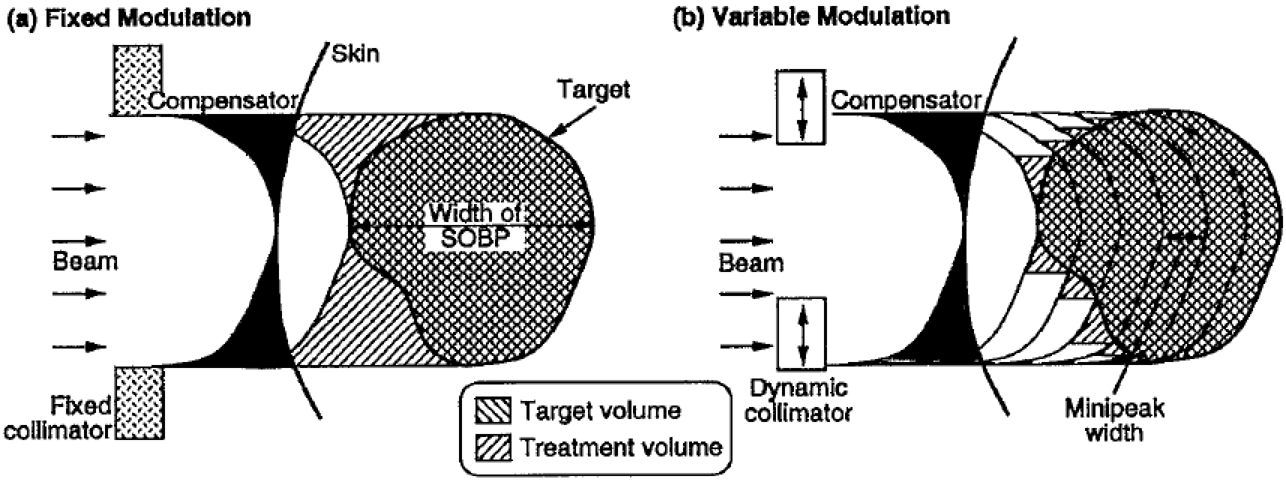

Figure 2.9.: Fixed configuration of the range shifter and the collimator (a), dynamic configuration of the range shifter and the collimator (b). Figure from Chu et al. (1993).

2.1.4.2 Active beam delivery

Scanning techniques permit to reduce those drawbacks. As well as for passive beam delivery techniques, several different methods exist. In the case of the raster scanning technique, the volume is first divided in voxels.

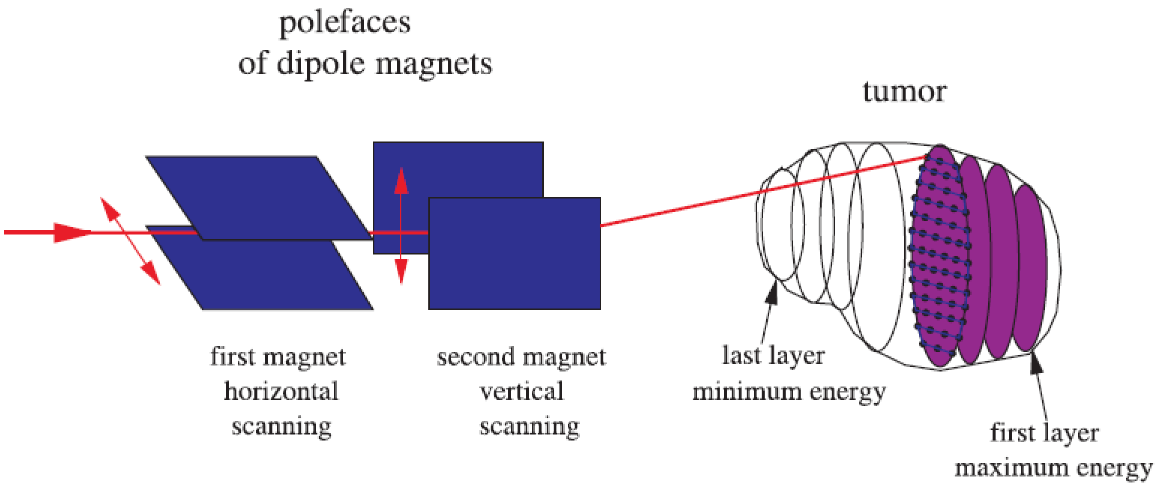

Figure 2.10.: GSI raster scanning system. Figure from Kraft (2007).

Then, for each position of the beam in the tumor (called raster point), a certain particle number is calculated and each one of these points contribute to several voxels of the target.

Finally a “pencil-like” beam is directed to each raster point as long as the particle number is not reached. Lateral scanning is done using fast magnets to irradiate the volume of the tumor. The adaptation of the position of the Bragg peak can be done by changing the beam energy either by using the accelerator or by using a range shifter like for the passive beam delivery stacked irradiation technique. Spot scanning, whose difference compared to raster scanning is that the beam is switched off between two raster points and which was first developed in Japan (Kanai et al., 1983) but then mostly used in PSI in Switzerland (Pedroni et al., 1995) is the other main technique used nowadays.

Figure 2.10 shows how raster scanning was implemented at GSI (Haberer et al., 1993) and then used at HIT in Heidelberg. Many advantages of scanning techniques can be pointed out, such as no patient specific hardware (like collimator or compensator used in the passive beam delivery techniques), a dose which can be varied from one voxel to another, allowing to compensate for the irradiation of the previous voxels, and a drastically reduced amount of material in the path of the beam upstream to the patient (no beam shaping needed), reducing particle loss and production of secondary particles like neutrons.

However it does require high precision and robustness of the accelerator and the control and safety systems in order to obtain stable and reproducible the beam positions. Today the trend is to replace passive beam delivery systems with active ones in the existing centers or to always use active techniques for new centers in construction.

Moreover, with the development of new gantries capable of rotating the beam direction around the patient like at HIT, it is possible to combine the precision of scanning techniques with the ability to deliver dose from any direction, resulting into a system which is able to target the tumor with high accuracy.

2.2 Tumor motion and its mitigation

Physical and biological properties of hadron therapy have been introduced in the previous sections. They showed that the precision of this technique allows conformal irradiation of a tumor by delivering high dose to a desired volume while sparing the normal tissue in the vicinity, due to the sharp dose fall-off obtained with protons or heavy ions. Now, the conformity mentioned above can be severely deteriorated when the tumor is located in areas of the body being subject to motion, such as the lungs during respiration or any other organ drifting between two fractions of the treatment. Indeed, due to very high range and tissue density sensitivity, treating moving tumors with ion therapy can lead to high dose deposition in the surrounding tissue. That may result in toxicity and late effects such as necrosis (Cox et al., 1995). Thus, it is mandatory to understand the origin and impact of the different types of organ motion and anatomy changes and how they can be compensated. This section will introduce these three aspects.

2.2.1 Organ motion and anatomy changes

(Langen and Jones, 2001) use three categories to classify the different types of motion or changes which can occur during a treatment:

Patient motion can appear between two fractions or during the treatment as well as during imaging. Immobilization techniques and devices have been developed to suppress or diminish this type of motion, which are nowadays clinically used.

Interfractional motion happens between two fractions of the treatment and can be seen on successive 4DCTs. It generally consists of organ shifts, tissue drifts and tumor shrinkage. Interfractional anatomic changes were described by (McClelland et al., 2011) who observed baseline shifts of several points in the lung or by Mori et al. (2009) who observed lung density changes and lung tumor shrinkage.

Intrafractional motion happens during beam delivery. It is mainly caused by breathing and heartbeat and shows different amplitudes from one patient to the other depending on the location of the tumor. Shirato et al. (2004) stated that respiratory organ motion is indeed the largest intrafractional motion which can be observed. Several studies have quantified this motion and observed that its main component is in general along the superior-inferior (SI) direction (Seppenwoolde et al., 2002; Britton et al., 2007; Liu et al., 2007). The anteroposterior (AP) and left-right (LR) components generally have smaller amplitude.

In this work, patient motion and interfractional motion are grouped together under the name of interfractional changes or interfractional variability and both intrafractional motion and interfractional changes are addressed. They can indeed cause undesired and large negative effects on dose delivery.

2.2.2 Consequences of tumor motion

In the case of scanned ion beam therapy, the three types of organ motion described above cannot only be considered as simple geometrical motions. Geometrically, it can be compared to photon beam therapy because, due to motion, the tumor goes out of the field repeatedly so that no conformal dose delivery can be obtained (Bortfeld et al., 2004). But using scanned ion beam therapy adds radiological effects which are larger than for conventional photon beam therapy. Both interfractional changes and intrafractional motion can result in a negative impact on dose delivery with under- and overdose in the target as well as in the OAR.

2.2.2.1 Radiological path length

Interfractional changes and intrafractional motion can both affect the radiological path length. Intrafractional motion is responsible for tumor motion during the treatment, as described in the previous subsection. Figure 2.11 displays the effects of respiratory organ motion along the radiological depth. Due to anatomic changes between the inhale and exhale phases, the latter is severely affected by changes in tissue density on the path of the beam (Bert and Durante, 2011). The same principle applies for interfractional changes, for which even larger anatomical differences can be observed compared to intrafractional motion (Nøttrup et al., 2007). Organ shifts or tissue drifts, as well as patient misalignment, sometimes lead to large geometrical changes, causing huge changes in radiological depth due to, for instance, higher tissue density possibly coming from the presence of bony material instead of muscle in the path of the beam. (Lomax, 2008b) also studied interfield motion (which can occur between two dose deliveries relative to two fields in a multiple fields treatment) and reported severe underdose in the tumor as a consequence of a simple 5 mm shift in the dose distribution. Moreover, both interfractional changes and intrafractional motion can be encountered at the same time and their effects are then added.

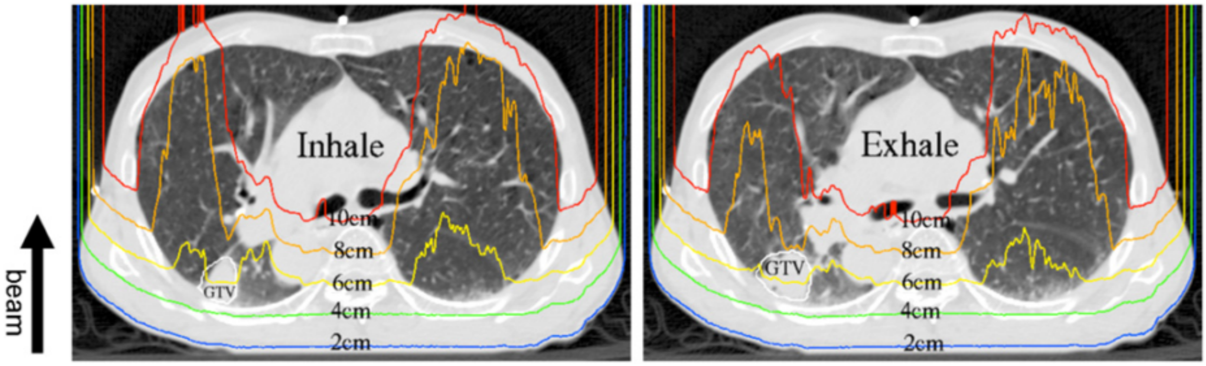

Figure 2.11.: Amplitude of the radiological pathlength changes from the inhale phase to the exhale phase. A moving tumor does not only imply geometrical changes but also radiological pathlength changes due to differences in tissue density. Figure from Bert and Durante (2011).

2.2.2.2 Interplay effects

In the case of scanned ion beam therapy, another effect has to be taken into account due to a double dynamic system composed of a moving tumor and a moving scanned pencil beam. Interferences of scanned beams and intrafractional organ motion, called interplay effects, can lead to severe inhomogeneity and largely deteriorated dose delivery (Lambert et al., 2005; Groezinger et al., 2006; Bert et al., 2008), as illustrated on figure 2.12, and can thus not be neglected. They strongly depend on the amplitude of the tumor motion, the relative direction of beam motion and target motion (Phillips et al., 1992) and multiple other factors. It has been demonstrated that irradiating the target multiple times (rescanning, see next section) permits to reduce these effects. Regarding the scanning direction, using beam scanning planes perpendicular to the tumor motion direction yields worse results compared to parallel scanning (see figure 2.12). Also, using additional margins has been proven to be ineffective regarding those interference effects (Phillips et al., 1992; Lambert et al., 2005; Groezinger et al., 2006; Bert et al., 2008).

Thus, in order to be able to efficiently treat tumors affected by the different types of motion and their consequences on dose delivery, different strategies had to be developed, which will be described in the next section.

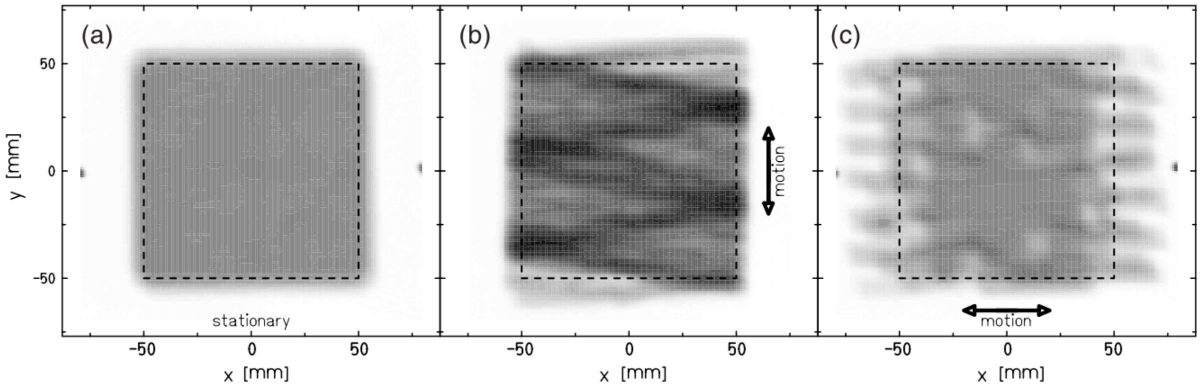

Figure 2.12.: Illustration of the impact of interplay effects on radiographic films. The scanning direction is horizontal. (a) represents the static case and (b) and (c) represents the dose delivery to radiographic films using a vertical and an horizontal target motion, respectively. Figure from Bert et al. (2008).

2.2.3 Tumor motion mitigation

2.2.3.1 Margins

A first solution to reduce the effects of intrafractional motion or interfractional variability is to use different types of margins to extend the irradiated region. To do so, different additional volumetric layers exist. Figure 2.13 illustrates them according to their definition in ICRU (1993, 1999), which are given here:

Gross tumor volume GTV: *"The GTV is the gross palpable or visible/demonstrable extent and location of malignant growth."*

Clinical target volume CTV: *"The CTV is a tissue volume that contains a demonstrable GTV and/or subclinical microscopic malignant disease, which has to be eliminated. This volume thus has to be treated adequately in order to achieve the aim of therapy, cure or palliation."*

Internal target volume ITV: *"This is the margin that must be added to the CTV to compensate for expected physiological movements and variations in size, shape, and position of the CTV during therapy."*

Planning target volume PTV: *"The PTV is a geometrical concept, and it is defined to select an appropriate beam size and beam arrangements, taking into consideration the net effect of all the possible geometrical variations, in order to ensure that the prescribed dose is actually absorbed in the CTV."*

Organ at risk OAR: *"Organs at risk are normal tissues whose radiation sensitivity may significantly influence treatment planning and/or prescribed dose."*

However, extending the irradiated volume results in more dose delivered to the normal tissue. This can become a serious problem when the motion of the target is large. To avoid that, some special beam delivery techniques exist which are presented below.

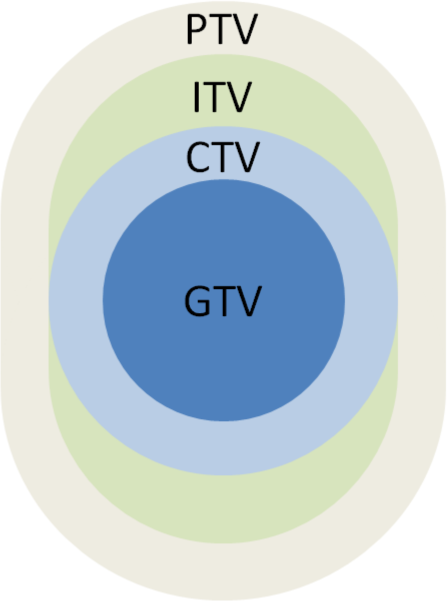

Figure 2.13.: The initial target and successive additional volumetric layers. The visible part of the tumor is contained in the GTV, the CTV takes possibly non-visible tumor spread into account, the ITV is composed of several motion state-specific CTVs and the PTV adds another volumetric extension.

2.2.3.2 Gating

Gating permits to mitigate intrafractional motion by only irradiating the target during a portion of a motion signal. The latter can either be obtained directly using fluoroscopic imaging, which yields the motion of the tumor itself (Shirato et al., 2000; Berbeco et al., 2004), or indirectly using external surrogates such as the ANZAI AZ-773V system (ANZAI MEDICAL CO., LTD) or laser triangulation systems (Minohara et al., 2000), which yield a signal correlated to the tumor motion. Thus, the tumor is only irradiated when the motion signal enters a previously chosen interval, called gating window (GW), and, in the case of a synchrotron, when the accelerator is ready to deliver the beam. As a consequence, a significantly smaller residual tumor motion has to be dealt with (see figure 2.14).

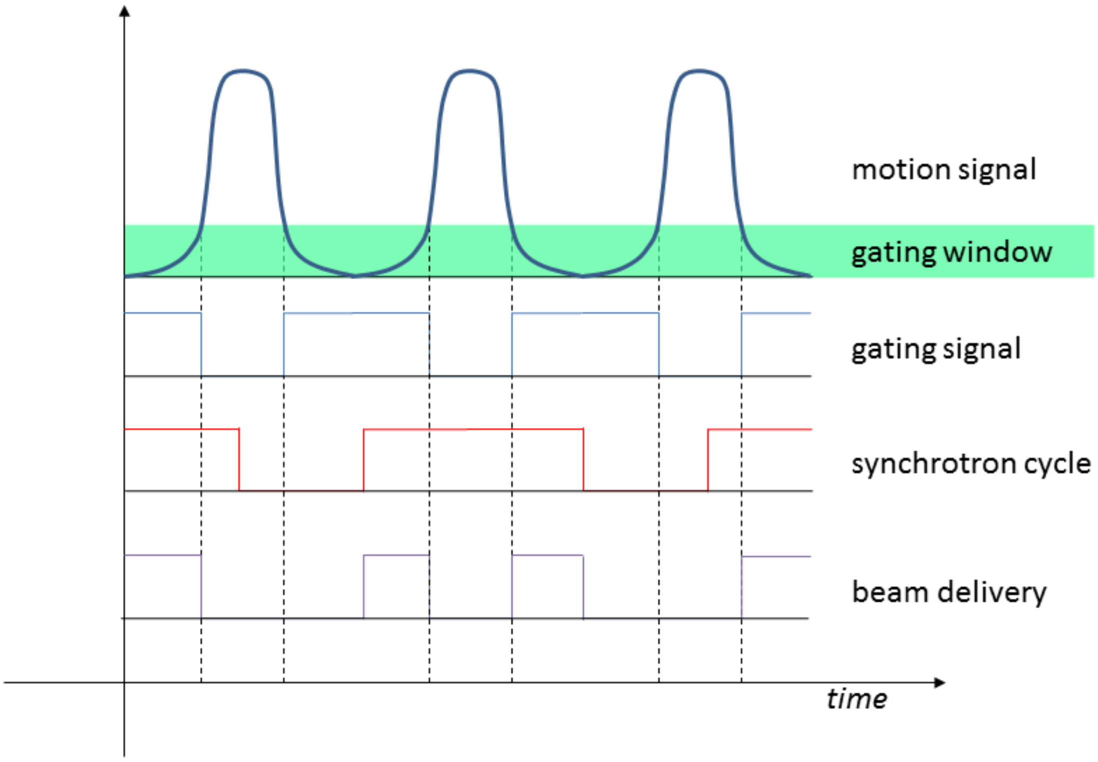

Figure 2.14.: Principle of the gating technique. The beam can be delivered when the gating signal is triggered, meaning when the motion signal enters the gating window (GW), but only if the pulsed beam of the synchrotron is available. This permits to obtain a significantly smaller residual motion, whose amplitude depends on the choice of the GW.

This technique has been developed about 25 years ago (Ohara et al., 1989) and is used nowadays in many centers in the world (Minohara et al., 2000; Iwata et al., 2010; Lu et al., 2007), mostly for tumor sites affected by respiratory motion such as the lungs (Iwata et al., 2010; Miyamoto et al., 2003; Nihei et al., 2006) or the liver (Chiba et al., 2005). As shown on figure

2.14, the end-exhale phase of the motion signal is often chosen as GW, because it is the phase for which this signal is the most stable (Balter et al., 1998; Ritchie et al., 1994).

Other studies using conventional radiotherapy have tested the feasibility of replacing the motion signal by the actual motion of the tumor obtained using megavoltage (MV) imaging, allowing then to measure if the tumor motion is inside or outside the GW (Berbeco et al., 2005b,a; Cui et al., 2007b,a, 2008; Tai et al., 2010). The advantage is that no additional dose is delivered to the patient, but MV-fluoroscopy offers very bad contrast compared to kilovoltage (kV) fluoroscopy, making the extraction of the tumor trajectory complex.

Now, one of the big disadvantages of gating is the increased duration of the treatment delivery, due to the fact that the target is only irradiated during part of the breathing cycle and, the shorter the GW, the longer the treatment delivery. Also, because of interplay effects due to residual tumor motion within the gating window, gating has not been used in centers using scanned ion beams and may require some more investigation in order to obtain conformal dose delivery (Bert et al., 2009).

2.2.3.3 Rescanning

Phillips et al. (1992) showed that irradiating the target multiple times with a proportionally reduced dose results in improved dose delivery. It is thus the principle of rescanning, which consists in irradiating the PTV multiple times. Similarly to gating, it permits to mitigate the effects of intrafractional tumor motion and obtain a homogeneous dose in the CTV. However, even though only a fraction of the dose is delivered in each rescan, the entire PTV is each time irradiated, which means surrounding tissue is also irradiated. Rescanning also allows mitigation of interplay effects by averaging them over several rescans. Specific characteristics can be found in Rietzel and Bert (2010). Zenklusen et al. (2010) also presents different rescanning configurations which could potentially be used in the future with the new gantry at PSI. The two most studied rescanning methods are slice-by-slice and volumetric rescanning (Bert and Durante, 2011). The first one aims at delivering the prescribed number of rescans to each slice successively while the second one delivers the rescans to the entire volume n times. Some other hybrid configurations exist, combing rescanning with gating, which will be described below. Finally, the number of fields, which is itself a kind of rescanning as the target is irradiated multiple times from different directions, has also been proven to improve dose homogeneity (Knopf et al., 2011).

It has been mentioned above that gating is sensitive to residual motion interplay effects. To limit their impact, some studies have been carried out, which combine gating and rescanning. Two methods, phase-control rescanning (PCR) (Furukawa et al., 2007, 2010) combined with gating at NIRS and breath-sampling rescanning (BSR) (Seco et al., 2009) at PSI, were developed. The original PCR technique did not include gating, but combining gating and rescanning permits indeed to cumulate capabilities of intrafractional motion mitigation of the two techniques while rescanning allows compensating for interplay effects.

2.2.3.4 Tracking

Tracking is a technique that allows potentially the best dose conformity. It was first proposed by Keall et al. (2001) for IMRT. It was shown in the study of Brown et al. (2007) that only 3 to 5 mm geometric margins around the GTV are needed and consitute the tracked irradiated volume (called PTV in their study). However, it requires precise motion monitoring and very fast computations in order to adapt the beam delivery laterally and, in the case of ion beam therapy and due radiological pathlength changes, in depth. Tracking is already used clinically in the Cyberknife Synchrony system (Accuray Inc., Sunnyvale, CA, USA) which uses a linear accelerator mounted to a robotic arm capable of compensating for intrafractional tumor motion (Brown et al., 2007; Kilby et al., 2010).

Tracking for a scanned ion beam system has been developed and implemented at GSI with initial studies performed by Groezinger et al. (2004, 2008). Lateral compensation was done using the raster scanning system and range compensation was performed using linear motor-driven double-wedge system (Weber et al., 2000). It has been implemented in the GSI treatment planning system (TPS) (Bert et al., 2007, 2010; Saito et al., 2009) and showed precision in terms of technical aspects as well as dosimetry. However, its clinical use is nowadays limited by the fact it is no online technique, meaning the 4D tracking treatment plan is generated using 4DCT imaging done before the treatment itself, meaning interfractional changes could occur in the meantime.

Some other techniques are being developed. Fassi et al. (2014) described a method relying on 4DCT imaging as well, but using an external surface surrogate to deform the 4DCT in order to adapt to the anatomy of the concerned treatment fraction and to generate a new breathing motion model.

This part showed the different types of motion which can appear during the treatment of tumors located in anatomic sites affected by organ motion. The consequences of those different motions as well as the methods used to mitigate them were then described. Some of them are already implemented in 4D treatment planning systems (4DTPSs) and used clinically. The next section will expose how moving tumors can be treated using a 4DTPS and what treatment schemes and organ dose limits are available.

2.3 Treatment of moving tumors

Because some tumors can be affected by organ motion, it was necessary to develop 4DTPSs capable of yielding treatment plans taking this motion into account. It required 4D anatomic information in order to calculate 4D-dose delivery and to implement the motion mitigation methods described above. The whole process aims at obtaining conformal dose delivery during each fraction of the treatment and limited irradiation of the surrounding tissue.

2.3.1 Time resolved computed tomography

Using anatomical data from the patient is mandatory to generate radio- or hadrontherapy treatment plans. X-rays have been used for medical imaging since the very end of the 19th century with the first radiograph. Since that time, machines and methods using X-rays have evolved a lot. Computed tomography CT is today the most commonly used method to obtain patient anatomical information in order to perform both radio- and hadrontherapy. It consists in one or two X-ray tubes rotating very fast around the patient. A detector ring (or more than one ring) detects the irradiation transmitted through the patient. The x-rays are attenuated by Compton or photoelectric effects when going through the patient (Kraft, 2000). One (or more, depending on the number of rings) axial slice of the patient is then reconstructed. The patient is moved for the acquisition of all needed slices and, thus, the 3D volume.

The obtained 3D dataset is composed of voxels whose values (CT numbers) are called Hounsfield units HU which represent the attenuation coefficients relative to water. While the lower values (-1000) represent air or vacuum, the higher values (2000) are reached for bony structures and 0 is used for water. Those units are obtained using the following equation:

$$HU(\vec{x}) = 1000 \times \frac{\mu(\vec{x}) - \mu_W}{\mu_W} \tag{2.8}$$

where $\mu(\vec{x})$ and μ_W are the X-ray absorption coefficients in tissue at location $\vec{x}$ and in water, respectively (Schardt et al., 2010). However, in order to properly calculate dose deposition during the treatment using CT, range values for each voxel have to be known. Water-equivalent path length WEPL values give the range of particles such as protons or ^{12}C ions in water and are linked to CT numbers. The first approximation of the relationship between CT numbers and WEPL values for ^{12}C ions was given by Minohara et al. (1993). One of the most recent calibrations is displayed on figure 2.15.

The basic CT technique has also been modified to be faster such as cone-beam computed tomography (CBCT) (Sonke et al., 2005) or used in temporal CT series, called time-resolved computed tomography (4DCT), to depict different phases of the motion of moving tumors. 4DCT is the most important 4-dimensional volumetric imaging technique, because 4D-treatment planning used for the treatment of moving tumors relies on CT data for dose calculations. It has been developed about 10 years ago (Ford et al., 2003; Keall, 2004; Rietzel et al., 2005) and permits, using techniques such as deformable registration, to map an anatomic point from one motion phase to any another. Several deformable registration algorithms exist such as those presented by Brock et al. (2006) and Rietzel and Chen (2006). Brock (2010) published a large comparison of the different algorithms used in several institution and concluded that the accuracy of deformable registration is generally similar to the voxel size. Combined to 4DCT, this tool is very useful for 4D-treatment planning, which is explained in the next section.

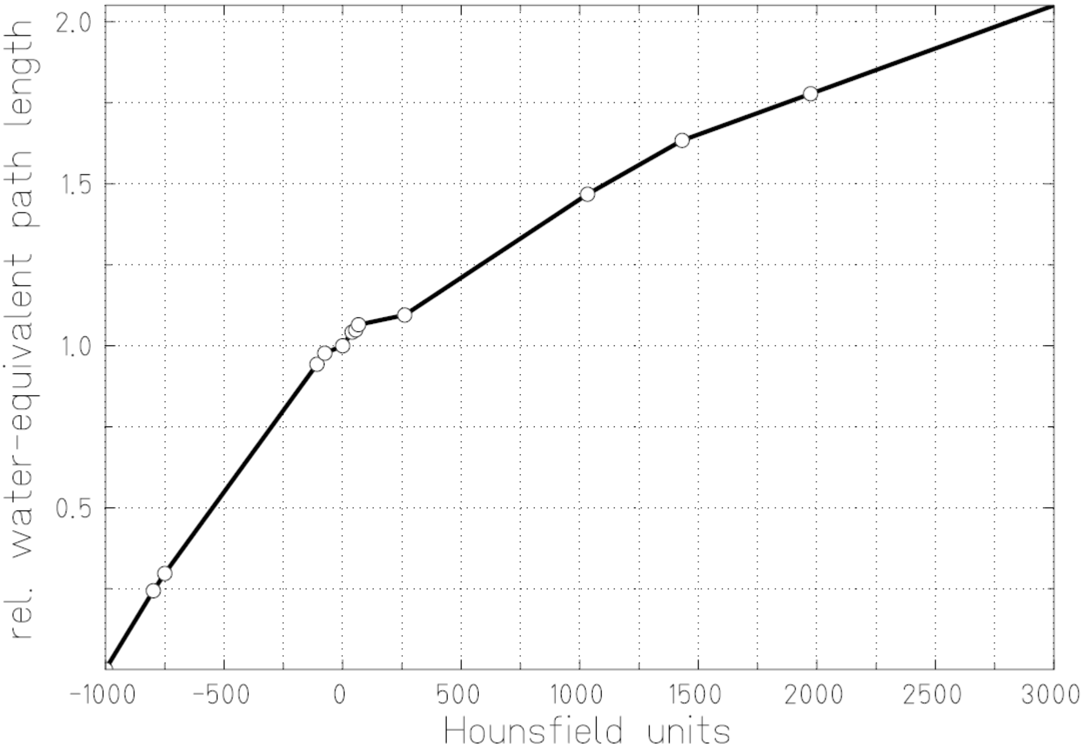

Figure 2.15.: Relationship between CT numbers in Hounsfield units HU and water-equivalent path length (WEPL) values for ^{12}C ions. Figure from Rietzel et al. (2007).

2.3.2 4D treatment planning

At GSI, an in-house 4DTPS is available, TRiP4D (Richter, 2012), based on TRiP98 (Krämer et al., 2000) and modified to be capable of generating 4D treatment plans for moving tumors. The different steps necessary to obtain a 4D treatment plan and the 4D dose delivery are described below.

First, it is necessary to have 4D data, which is provided by 4DCT. In addition, the tumor and the organs have to be contoured on at least one motion phase. Then, using the deformation maps obtained from deformable image registration, it is possible to propagate those contours to all motion states composing the 4DCT. Then, the target has to be defined. In the case of moving tumors, the target is usually composed of several tumor motion states, forming the previously described ITV. The concept of ITV has however been improved from its simple geometrical design to a volume taking WEPLs into account, as shown by Graeff et al. (2012) and Knopf et al. (2013).

Because no 4D-optimization process has been developed for particle therapy yet, a static treatment plan is first optimized on the ITV and is then used to generate a 4D-treatment plan. The latter is obtained from the static treatment plan by using the temporally correlated information from a motion surrogate signal and the time structure of the beam delivery, the beam delivery sequence and sorting all raster points with respect to the motion phases they were delivered in Richter (2012). Treatment plan and beam delivery can in principle incorporate any motion mitigation method which has been described in the previous section. Accelerator specifications and parameters included in the beam delivery sequence are mandatory to correcly reproduce the double dynamic nature of the system composed of the scanned beam and the moving tumor and thus to model interplay effects. Depending on the chosen motion mitigation technique, the dose corresponding to each raster point of the static treatment plan is distributed differently among the motion states of the 4D treatment plan. For instance, in the case of gating, the dose of each static raster point is distributed among the states composing the gating window.

Finally, the 4D biological or physical dose delivery can be simulated. 4D dose calculation has also originally been implemented in the GSI TPS by Gemmel et al. (2011) and accumulates the dose for each voxel over all motion states by using the same deformation maps used for contour propagation. This permits to accumulate the dose delivered in each motion state in one dose distribution matching the anatomy of one motion phase (called reference motion state). This reference motion state and the obtained dose distribution can then be overlaid to determine the quality of the 4D dose delivery.

2.3.3 Treatment schemes and constraints

Treatment plan have to be carefully generated regarding the organ at risks (OARs) in the vicinity of the tumor. Due to organ motion and the physical characteristics of ions, treatment of moving tumors can cause large dose delivery errors with high dose delivered to the surrounding tissue. The previously described motion mitigation techniques permit to reduce these errors more or less, depending on which technique is chosen. For instance, gating theoretically allows less OAR irradiation than rescanning, due to a smaller irradiated volume. Now, to improve dose delivery in the target, some treatment planning parameters have been investigated, which can allow obtaining better conformity, such as the beam focus width (Bert et al., 2009; Steidl, 2011; Richter, 2012) or the number of rescans and the number of fields (Knopf et al., 2011). Satisfactory dose delivery, which is generally obtained for target coverage (V_{95}) within a 95%/107% of the planned dose interval as recommended in ICRU (2007), was obtained in those studies using optimized parameters. But, if the latters permit to obtain better target dose coverage, they may result in more OAR irradiation and, because the previously mentioned studies focused on the target, no analysis was done concerning the dose delivered in critical structures outside of it.

In clinical studies and depending on the institute, different OAR constraints have indeed been set and used for IMRT treatments. Grimm et al. (2011) published a large overview in which dose/volume limits as well as maximal point doses are listed. As described by Benedict et al. (2010), those limits are however mostly unvalidated and based on clinical experience, but they still give an indication of how much dose is tolerated for each organ.

Also depending on the institute, beam delivery and motion mitigation techniques, as well as treatment schemes, vary. While Miyamoto et al. (2003, 2007) presented 9 and 18 fractions-based treatments using gating and passive beam delivery with different investigated doses per fraction for each fractionation scheme, some protocols including both chemotherapy and proton therapy can be found on PTCOG. So, nowadays, both OAR constraints and treatment schemes are institute-specific.

2.4 Summary

This chapter presented an overview of ion beam therapy. Physical and biological advantages of the technique have been pointed out, showing the benefits of using ions compared to photons. It has also been shown that different beam delivery techniques were developed and used, even though active beam delivery tends to become the most used beam deliver technique in the future in particle therapy. Also, potential problems occurring in the case of moving tumors have been discussed, as well as the different methods to mitigate them. Finally, the creation of a 4D-treatment plan using the GSI 4DTPS has been described. It has also be shown that treatment characteristics are institute-specific, depending on which beam delivery system and motion mitigation techniques are available as well as different clinician experience.

Now, one aspect of treatment is used in each institute, which is to generate a single treatment plan for the entire course of the treatment or, at least, for several fractions before it might be adapted. Using one treatment plan as well, this study aimed at investigating which parameters could be optimized to obtain both satisfactory dose delivery in the tumor and OAR sparing (chapter 3) and which mitigation technique can realistically be used (chapter 4). Two brief studies were also performed to determine if a replanning factor and field angles robust to inter-fractional variability can be isolated (chapter 5). Using the obtained results, a final treatment planning study was carried out to investigate the total dose delivered to the tumor and the OAR over the entire course of the treatment (chapter 5).

3 Treatment parameters optimization to compensate for interfractional anatomy variability and intrafractional tumor motion

3.1 Introduction

Treating moving targets such as non-small cell lung cancer (NSCLC) tumors using photon radiation therapy has been investigated (Korreman, 2012) and is being clinically used nowadays combined to real time tracking (Brown et al., 2007; Kilby et al., 2010). However, using heavy ion scanned beam therapy has shown many advantages compared to conventional radiotherapy (Amaldi and Kraft, 2005; Tsujii et al., 2008) by reducing the number of fields which have to be used as well as the dose delivered to the organs at risk (OARs) in the vicinity of the tumor. It also demands high precision and accuracy when applied to moving tumors because of the possible dose delivery error induced by range shifts themselves due to both intrafractional motion and interfractional anatomic changes and patient misalignments (Mori et al., 2008; Bert and Durante, 2011).

This is why several motion mitigation techniques such as gating, rescanning or tracking have been developed and are still under development (Knopf et al., 2010). Gating (Ohara et al., 1989; Minohara et al., 2000) is a technique which consists in turning the beam on when the moving tumor reaches a precise motion state, in general at the end of exhalation while the tumor is the most stable. It has shown great potential and has thus been successfully used in Japan combined to passive ion beam delivery (Tsujii et al., 2004; Iwata et al., 2010; Tsujii and Kamada, 2012). Active scanned beam delivery introduces interplay effects (Bert et al., 2008) and even though tumor motion mitigation techniques are used, these effects can lead to non-conformal dose delivery. In order to address specifically this problem, 4D treatment planning systems (4DTPSs) have been implemented (Bert and Rietzel, 2007; Richter et al., 2013) and permit to simulate treatment of moving targets using gating while also taking interplay effects into account.

Nonetheless, treatment parameters still have to be optimized to maximize motion mitigation obtained using gating. Several studies have been performed to determine the influence of different parameters on the dose delivery: Bert et al. (2009) proposed to increase pencil beam overlap to mitigate interplay effects as well as Steidl (2011) and Richter (2012) whose studies displayed the effects of different lateral grid spacing, iso-energy slice distance, focus size and Bragg peak width. In a combination gating and rescanning, Furukawa et al. (2007) proposed a method called phase-controlled rescanning, aiming at compensating further the residual tumor motion within the gating window. Rescanning was used as mitigation technique by Knopf et al. (2011) and the impact of the entry channel was also investigated through different field scenarios. Target definition including tumor motion, size and position (ICRU, 1999) as well as range adapted margins were discussed (Koto et al., 2004; Engelsman et al., 2006; Bert and Rietzel, 2007; Knopf et al., 2013) and implemented (Graeff et al., 2012).

However, those studies concentrated on intrafractional motion compensation, meaning that the possible anatomic variability between the time of the treatment planning CT and treatment or also between fractions was not taken into account. Simulations were in general restricted to a single 4DCT taken for treatment planning.

The purpose of this study was to investigate which parameters could be isolated and optimized in order to compensate correctly for both intrafractional tumor motion and interfractional anatomic changes and/or patient misalignments. To this end, in a cohort of patients with a time series of 4DCTs and for different combinations of treatment and/or beam parameters, one gating plan was optimized using the first weekly 4DCT of each patient and was forward calculated on the successive 4DCTs of the weeks following treatment planning. Results were then compared to determine the best configuration.

3.2 Materials and methods

3.2.1 Patient cohort

Data from 9 NSCLC lung tumor patients from MD Anderson Cancer Center (MDACC) (Britton et al., 2007) were used to perform this study, reaching a total of 70 weekly 4DCTs datasets. Each 4DCT was composed of 10 3DCTs representing 10 different tumor motion phases over the breathing cycle. End-exhale, referred to as state n°5, was set as the reference state.

Number of weeks, motion amplitude, angles for single field and multiple fields calculations, clinical target volume (CTV) volumes with and without additional margins are listed in table 3.1. Number of weekly 4DCTs per patient varies between 6 and 10, those were used as fraction numbers. Most of the patients have an average tumor motion below 5 mm and only one patient shows a tumor motion above 20 mm (Patient 9).

3.2.2 Treatment planning

3.2.2.1 Image Registration

Rigid registration of reference phases of each subsequent CT was performed to mimic patient setup and alignment. A short study has also been done to investigate if rigid registration was more precise using only bony anatomy rather than soft tissue. Comparison of the two methods has demonstrated that bony anatomy based rigid registration lead to a significant improvement in only one case over the 15 weeks of 2 patients studied (see appendix A). It was thus decided to use only soft tissue rigid registration to align CTs. Then non-rigid registration was used between each 4DCT motion phase using Plastimatch (Shackleford et al., 2010).

Table 3.1.: Description of the 9 NSCLC Patients from MDACC (see figure 3.1 for field angles illustration): patient number, number of weeks available, mean motion amplitude and range, field angle for single field calculations (SFUD), field angles for multiple fields calculations (SFUD1, 2 & 3), volume of the CTV (CTV) and volumes of the extended target: 3mm isotropic (I3), 3mm+3% range (R3) and combination of both (I3+R3).

			Angles [degree]				Volumes [cc]			
Pat.	Weeks	Motion [mm]	SFUD	SFUD1	SFUD2	SFUD3	CTV	I3	R3	I3+R3
1	8	3.4	240	180	225	270	236	322	406	518
2	6	8.6	0	0	315	270	574	718	891	1057
3	9	10.1	0	270	315	0	161	213	335	409
4	8	3.3	225	180	225	270	676	819	925	1089
5	10	4.1	0	0	315	270	372	472	648	791
6	8	1.8	0	0	315	270	705	828	935	1072
7	7	1.6	180	180	225	270	124	172	253	322
8	8	4	180	180	225	270	45	65	102	133
9	6	23.5	180	180	225	270	125	164	203	250

For each patient, contours were provided by physicians of MDACC for the first weekly 4DCT, including the gross tumor volume (GTV), the clinical target volume (CTV) and the planning target volume (PTV) for the tumor, and the OARs esophagus, heart and spinal cord. For patients 1 to 8 PTVs were generated for conventional radiotherapy treatment, but for patient 9 it had to be created using TRiP by adding 3 mm isotropic margins to the CTV. Those PTV contours were only used in the later automatic definition of lung contours. Files containing vector fields (between the first week and the following ones) obtained using deformable registration were then used to propagate the previously mentioned contours from the reference phase of the first weekly CT to the reference phases of the following ones (Richter et al., 2013). Finally, vector field files yielded by deformable registration applied on the 10 states of each weekly 4DCT permitted to propagate the contours from the reference state to the 9 other motion states. Concerning the lungs, a contour extraction algorithm based first on Hounsfield units related thresholding was implemented and used to obtain separately the left and right lungs contours for the reference phase of each 4DCT (see appendix B for details).

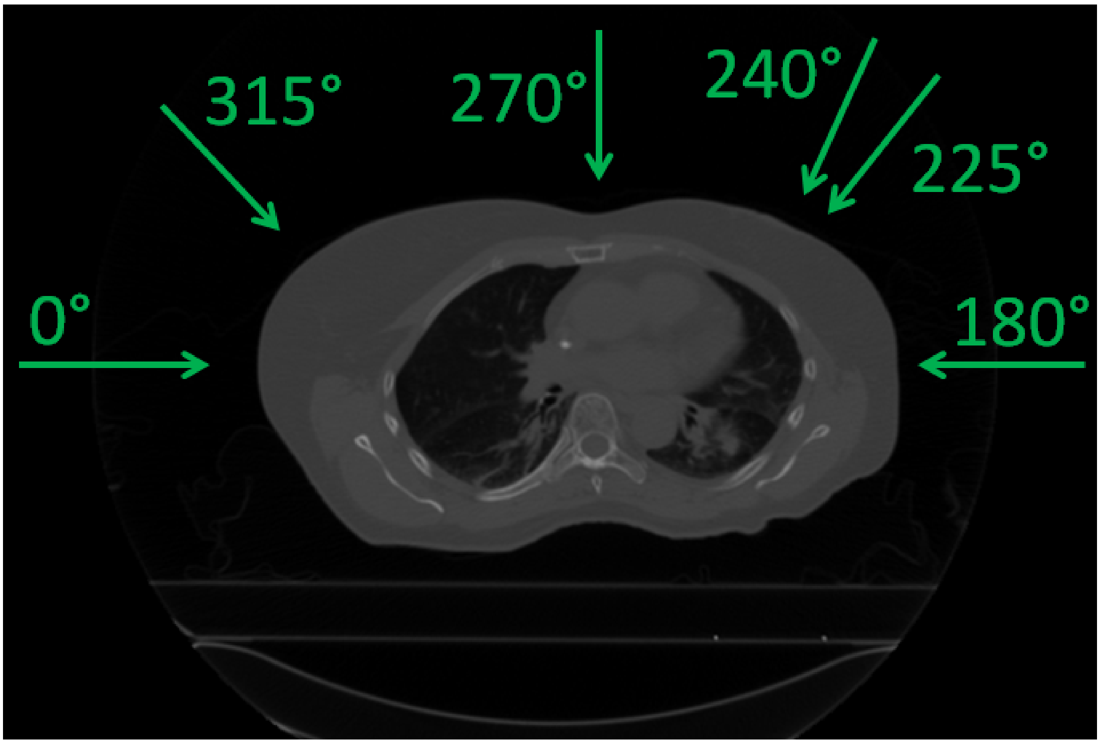

Figure 3.1.: Field angles used (see Table 3.1)

3.2.2.2 Optimization and 4D calculations

In this chapter, the technique used to mitigate motion was gating. All gating plans were simulated using the GSI treatment planning system TRiP4D (Richter et al., 2013), based on TRiP98 and modified to allow 4D-dose calculations.

For each patient, plans were initially optimized to the ITV of the first week's CT using one unique planned dose of 8.1 Gy(RBE). Motion related geometrical and range changes were considered according to Graeff et al. (2012). The generated raster scanning plan was then used for all 4D calculations of the first week itself and the followings ones as well, meaning that only one plan was used per patient and that there was no replanning before simulating the weeks following the first optimized week. In each case, the ITV was built using a combination of five CTVs (Graeff et al., 2012) from five different motion phases representing 25% of the amplitude (see figure 3.2). The motion surrogate was defined according to Lujan et al. (1999), i.e. a sine square, as displayed on figure 3.3, with a unique period of 3.6 seconds. Only one starting phase (0 degree) was studied because, due to gating, beam delivery for different starting phases is quickly synchronized after the first few spills of the synchrotron accelerator, thus calculations yield very similar results for different starting phases.

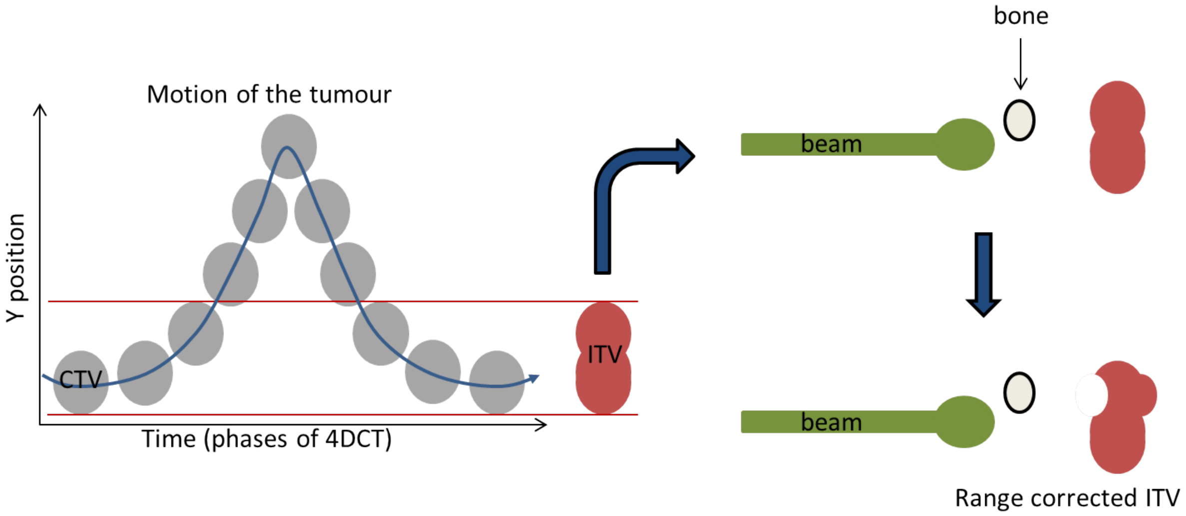

Figure 3.2.: Creation of a range-corrected internal target volume (ITV), first (in the case of this study) combination of five motion phases associated geometrically composes the geometric ITV which is then corrected for density changes (like bones or air of the lung) in the path of the beam. This correction leads to the final range-corrected ITV.

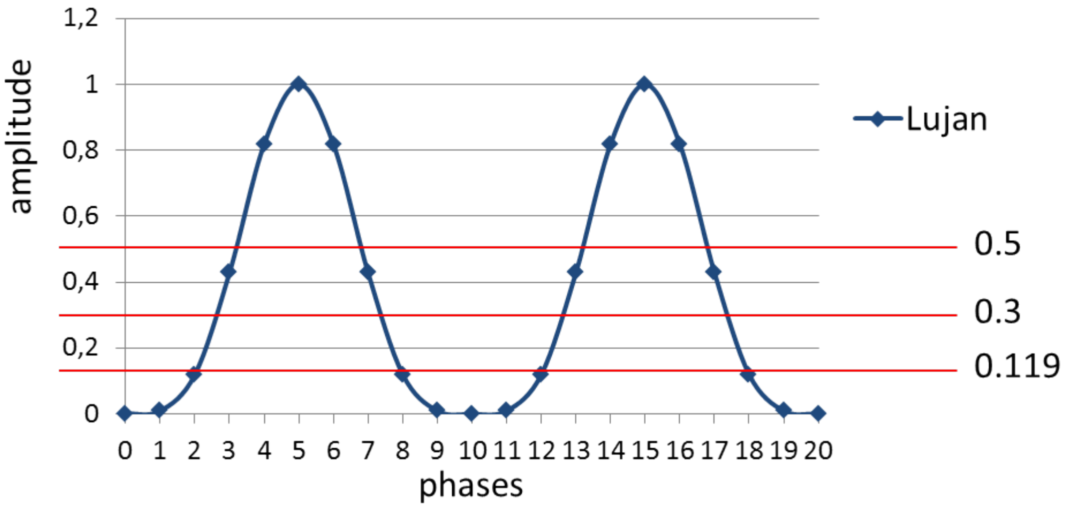

Figure 3.3.: Motion surrogate and gating windows (see appendix C).

As other fixed treatment parameters, the distance between each raster position was set to 2 mm on each iso-energy slice (IES) and the distance between two IESs was set to 3 mm water-equivalent using a ripple-filter (RiFi) of 3 mm (Weber and Kraft, 1999). The contour extension value (see appendix D), which defines the part of the lateral dose fall of which is taken into account in the simulations, was set to 0.35.

3.2.2.3 Investigated parameters

The impact of different treatment plan parameters on the dose delivery was investigated using the field angles listed in table 3.1. First, using one single field (see column “SFUD” of table 3.1 and figure 3.1) and ITV margins only, variations in focus size and length of the gating window (GW) were performed. Three GWs: 11.9%, 30% and 50% of the amplitude (see figure 3.3) and three beam foci: 6mm, 10mm and 15mm (FWHM) were chosen as varying parameters. Two configurations in particular were compared:

- **LFSG:** large focus (15mm) and short GW (11.9%),
- **SFLG:** small focus (6mm) and long GW (50%).

As a second part, using the same single field angles, additional margins added in the optimized plans were also investigated as another solution to recover good target coverage. Three different cases were studied: 3mm isotropic margins (geometrical, referred to as I3), 3mm+3% range margins (water equivalent, referred to as R3) and combination of both (referred to as I3+R3, see figure 3.4). Resulting dose deliveries were compared to the results obtained using ITV only. Combinations of GWs and foci (same 3 foci and 3 GWs than in the previous paragraph) were again investigated in each case to observe the impact of additional margins on the range.

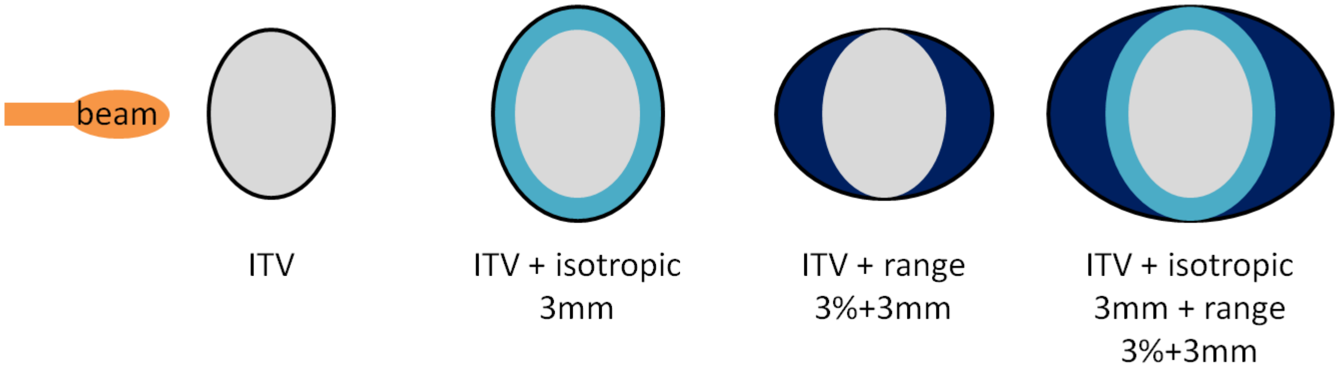

Figure 3.4.: Different margins cases used in the second part of the study. From the left to the right, configurations displayed are referred to as ITV, I3, R3 and I3+R3.

Finally, still using the 9 possible GW/focus combinations, the number of fields was varied from 1 to 3 (see table 3.1 for field angle values, columns “SFUD1” to “SFUD3” and figure 3.1) using only ITV margins first and then using the additional PTV margins which had been determined to yield the best results in the second section of this chapter, resulting in the following cases:

- **SFITV:** single field to ITV only,
- **SFPTV:** single field to the isotropic/range margins (same as I3+R3),
- **2FITV:** ITV only but with 2 fields,
- **2FPTV:** same margins as SFPTV but with 2 fields,
- **3FITV:** ITV only but with 3 fields,
- **3FPTV:** same margins as SFPTV but with 3 fields.

3.2.3 Data analysis

In each case, the dose distribution of each week was obtained by accumulating the dose delivered to each motion state on the reference phase of the 4DCTs using state-to-state non-rigid vector fields. And to estimate the impact of each previously described parameter and configuration on the dose delivery, four different indexes were used for the tumor itself:

- **Target coverage, V_{95}:** volume of the target to which 95% of the planned dose is delivered, representing the quality of target dose coverage, unit is percentage of volume,
- **Overdose, V_{107}:** volume of the target to which 107% of the planned dose is delivered, representing the volume affected by overdose in the tumor, unit is also percentage of volume,
- **Homogeneity, $D_5 - D_{95}$:** the lower, the better (D_5 and D_{95} being the dose delivered to 5% and 95% of the target in the dose volume histogram (DVH), respectively),
- **Conformity number (CN) (van't Riet et al., 1997):** allowing a quantification of the high dose regions inside and outside the tumor (the higher, the better) and defined by:

$$CN = \frac{V_{95\%,\mathrm{CTV}}}{V_{\mathrm{CTV}}} \times \frac{V_{95\%}}{V_{\mathrm{CTV}}} \tag{3.1}$$

  where $V_{95\%,\mathrm{CTV}}$ is the V_{95} value defined above, V_{CTV} the volume of the CTV and $V_{95\%}$ the total volume which receives at least 95% of the dose.

The combination of those four indices permits to determinate precisely the quality of the dose delivery in the tumor but two additional indexes were needed to specifically estimate the impact of the different parameters and configurations on the dose delivered to the OARs:

- **20% volume dose, V_{20}:** allowing knowing the volume which receives 20% of the dose, unit is percentage of volume,

- **Maximal point dose (MXD):** maximal voxel dose received in the tumor, unit is Gy(RBE).

The main focus of this study is the impact of treatment plan parameters on dose delivery. All dose calculations were computed for the weekly simulations but not for the cumulated total treatment regime. Therefore, OAR limit dose values from the literature were not taken into account in this chapter, but are used only a general indicator of plan quality. In chapter 5 the total dose delivery over the entire course of the treatment is computed and also clinical dose limits are considered. This chapter aims at determining clearly the effect of the investigated parameters on the decreased quality of the dose delivery due to both interfractional anatomy changes and intrafractional tumor motion.

In each case, a Wilcoxon signed-rank test (W) was performed using a level of significance of 0.05 to estimate the difference between two sets of datapoints. In the case of samples containing more than 10 values, the p-value (p) was computed using the obtained z-score (z).

3.3 Results

All simulations were performed on the weekly 4DCTs with a planned dose of 8.1 Gy(RBE). In all following figures the average value (marker), the median value (horizontal bar in the box), the 25th and 75th percentile and the total range of all values are given. In some cases, different types of simulations were studied and referred to as:

- **3D0 simulations:** planned, static dose simulations using the first weekly CT (week 0 in reference phase),
- **4D0 simulations:** 4D dose simulations using the first weekly 4DCT (week 0) and the same plan than 3D0 simulations, which contains the effects of intrafractional motion only,
- **4DN simulations:** 4D dose simulations using all following weekly 4DCTs (weeks 1 to 5-9) and the same plan than 3D0 simulations, which contains the effects of both intrafractional motion and interfractional patient anatomic changes.

3.3.1 Beam focus and gating window

First the impact of the focus size and the length of the GW was investigated. Figure 3.5 shows V_{95}, V_{107}, homogeneity ($D_5 - D_{95}$) and conformity number (CN) for different GW/focus combinations, for all patients.

3D simulations show conformal results no matter which combination is used, even though slightly better results were obtained using the largest focus ($W > W_{critical}$). High average V_{95} of about 99%, average CN between 0.64 and 0.72, average homogeneities of about 5% and V_{107} almost equal to 0% are obtained in each case.

Looking at the 4D0 results permits to see the effect of intrafractional tumor motion on the target coverage: V_{95} ranges increase drastically while V_{95} average values decrease, overdose (V_{107}) goes from almost 0% to more than 14% for some cases and homogeneity is also degraded. Besides, an influence of focus and GW on V_{95}, V_{107} and homogeneity can already be pointed out ($W > W_{critical}$): using a large focus and a short GW (configuration LFSG) increases the average V_{95} up to 99.3%, compared to the 86.8% obtained with the smallest focus and the longest GW (configuration SFLG) and V_{107} and homogeneity go back to 0% and around 5%, respectively. CN, however, shows no significant ($W < W_{critical}$) change between the two configurations but decreases slightly compared to static calculations.

4DN results of the following weeks permit to investigate the effect of intrafractional motion as well but also interfractional changes. The latter, coupled to the first one, degrades V_{95}, homogeneity and CN compared to the 4D0 simulations. And, as well as for the latter, an impact of focus and GW on V_{95}, V_{107}, homogeneity and CN is present. Again, using configuration LFSG permits to obtain higher V_{95} ($p < 0.05$), illustrated by an average of 90.9% compared to 77.7% obtained with configuration SFLG, lower V_{107} ($p < 0.05$) with an average falling down to 0% and better homogeneity ($p < 0.05$), its mean value being reduced to 10.7% compared to 24.5%. Although figure 3.5 shows similar ranges and average values for CN, using configuration LFSG permits to improve the results slightly but with enough significance ($p < 0.05$).

Figure 3.6 shows the impact of configurations LFSG and SFLG, respectively the best and worst combinations previously found in terms of tumor dose delivery quality, on the dose delivered to five organs at risk: the esophagus, the heart, the spinal cord, the ipsilateral lung and the contralateral lung. Bars are quite large for all organs for V_{20} as well as for MXD except for the MXD in the ipsilateral lung: this is due to the fact tumors were not located at the same place for all patients and that different field angles were used. However, the ipsilateral lung was always irradiated by definition, which is why the MXD values are in the same order of magnitude. Looking at each combination separately, 3D0 and 4D0 yield approximately the same results in terms of average values and ranges. 4DN calculations show similar average values but with V_{20} and MXD maximal values which are often higher, such as the spinal cord for which V_{20} and MXD maximal values reach 30% and 9.7 Gy(RBE), respectively, compared to the 3.7 to 7.9% and the 4.6 to 6.9 Gy(RBE) obtained for static and 4D0 calculations, or the heart for which V_{20} maximal values reach about 13.3% to 22% compared to the 5 to 12.8% obtained for static and 4D0 calculations.

Now, looking at the differences between the best (LFSG) and the worst (SFLG) combinations permits to isolate some effects caused by these two configurations. In the case of 4DN simulations, for which both interfractional anatomic changes and intrafractional motion are present, V_{20} values are only slightly increasing, but with enough significance ($p < 0.05$), when the best configuration (LFSG) is used compared to the results obtained with the worst one (SFLG). In the case of the spinal cord, MXD also increases slightly ($p < 0.05$) for configuration A but aver-

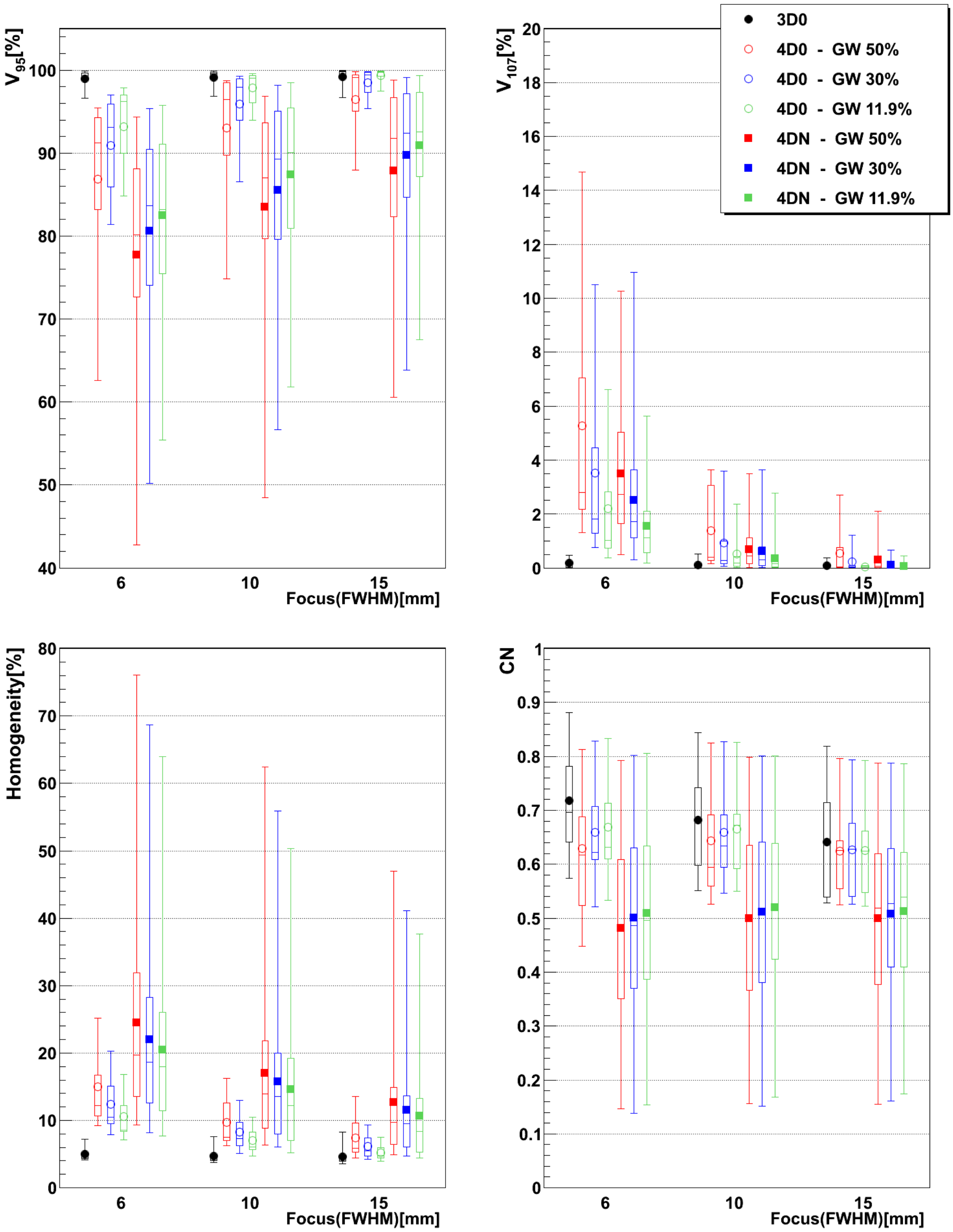

Figure 3.5.: Impact of the focus and the GW on V_{95}, V_{107}, homogeneity and CN. Each 3D0 and 4D0 bar is composed of 9 points and each 4DN bar of 61 points (homogeneity bars for 4DN calculations are in fact composed of 59 points due to two weeks for which more than 5% of the volume of the tumor was not irradiated, making it impossible to calculate the D95 value, and thus the homogeneity).

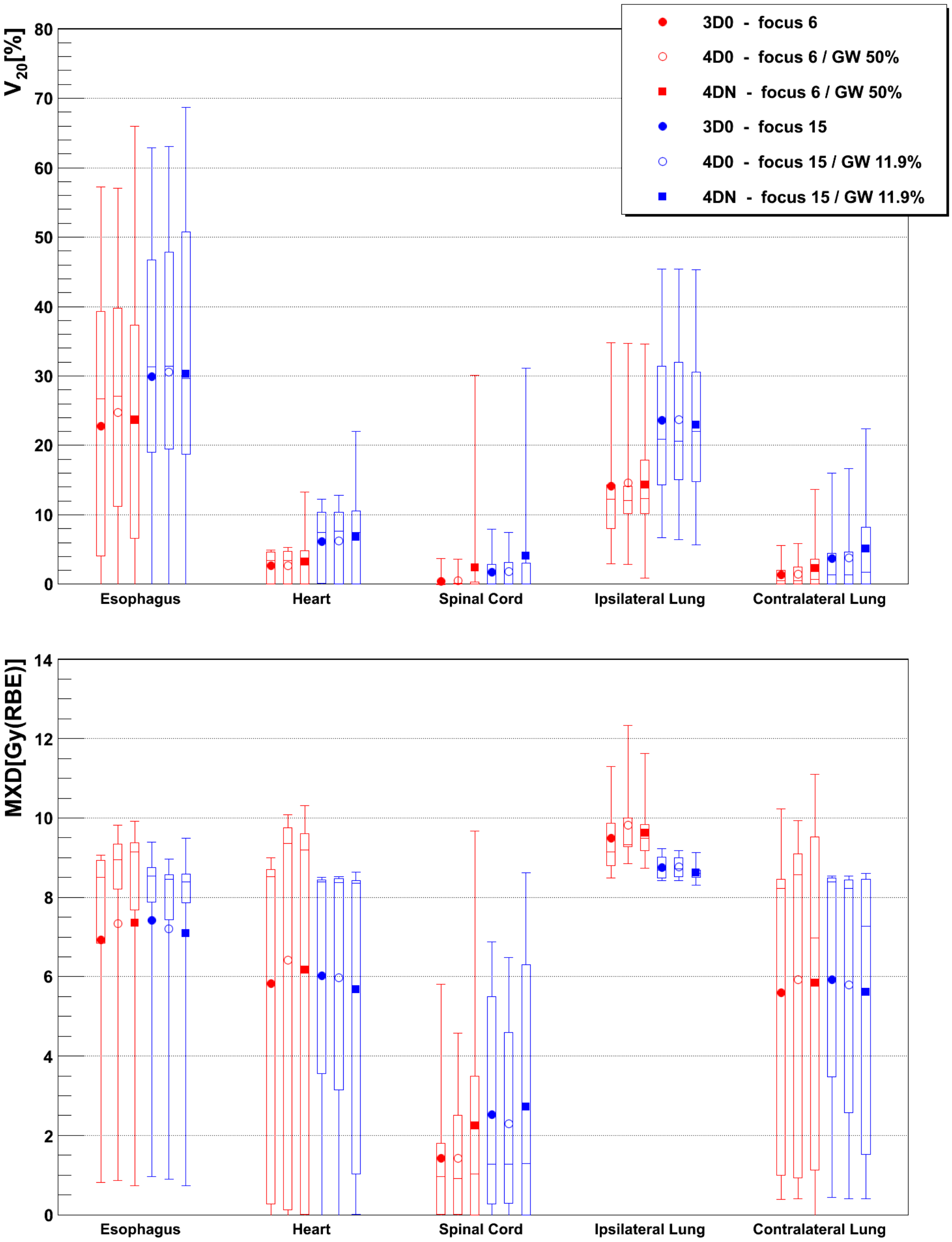

Figure 3.6.: Impact of the best and worst focus/GW on the dose delivered to the OARs. Results for five organs at risk are displayed: the esophagus, the heart, the spinal cord and the ipsilateral and contralateral lungs. Each 3D0 and 4D0 bar is composed of 9 points and each 4DN bar of 61 points.

age values remains similar at about 2.5 Gy(RBE). For the other organs, MXD decreases slightly ($p < 0.05$) when the best combination is used and average values are again very similar at around 7 Gy(RBE) for the esophagus, 6 Gy(RBE) for the heart and the contralateral lung and 9 Gy(RBE) for the ipsilateral lung.

Dose distributions of simulations done using the two combinations of the smallest focus and the longest GW and the largest focus and the shortest GW are displayed for the 7th weekly CT of patient 3 on figures 3.11.a-c and 3.11.d-f, respectively.

3.3.2 Margins

After the focus and the GW, different types of additional margins were investigated and compared to the ITV only as presented in the previous section. Figure 3.7 shows the impact on V_{95}, V_{107}, homogeneity and CN for ITV only (ITV), ITV + 3mm isotropic margins (I3), ITV + 3%+3mm range margins (R3) and a combination of both margins (I3+R3), respectively.

3D0 simulations yield similar results in terms of average V_{95} at around 99%, V_{107} at 0% and homogeneity at 5%. ITV (ITV) and additional isotropic margins (I3) also show similar CN with mean values of about 0.68, but the minimal value is lower in the second case (0.53 compared to 0.45). Using range margins (R3) and the isotropic/range margins combination (I3+R3) reduces CN ($p < 0.05$), illustrated by average values falling down to 0.51 and 0.53, respectively.

4D0 results show similar V_{107} and homogeneity distributions in each case, very slightly diminishing (less than 1% and about 1.5%, respectively, $p < 0.05$) when additional margins are added. V_{95} gradually increases when additional margins are used ($p < 0.05$), the I3+R3 case yielding the best results with an average value of 96.6% even though there no significant difference with the R3 case ($z < z_{critical}$, mean value of 96.3% for the R3 case). The R3 and I3+R3 cases allow obtaining better V_{95} than the I3 case ($p < 0.05$, mean value of 95.9% for the I3 case), the latter yielding itself better V_{95} than the ITV case ($p < 0.05$, mean value of 94.7%). CN is degraded when additional margins are used ($p < 0.05$), illustrated by mean values going from 0.64 in the ITV case to 0.53, to 0.5 and to 0.42 for I3, R3 and I3+R3, respectively.

Finally, results obtained from 4DN simulations follow the same behavior than 4D0 results but have larger distributions (except for V_{107}). V_{95} increases with additional margins ($p < 0.05$), the best target coverage being obtained with the I3+R3 case. Also range margins yield better results than isotropic margins ($p < 0.05$) in terms of V_{95}, homogeneity and V_{107}. The latter, as well as for 4D0 results, decreases very slightly but with enough significance ($p < 0.05$). Homogeneity is also better when additional margins are used ($p < 0.05$), with average values going from 16.6% in the ITV case to 11.8% in the I3 case, to 10.3% in the R3 case and down to 8.9% in the combined isotropic/range margins case. CN follows the same trend than for 3D0 and 4D0 simulations ($p < 0.05$), with decreasing mean values of 0.5 in the ITV case, 0.46 when isotropic margins are used, 0.45 for range margins and 0.39 for the combination of both.

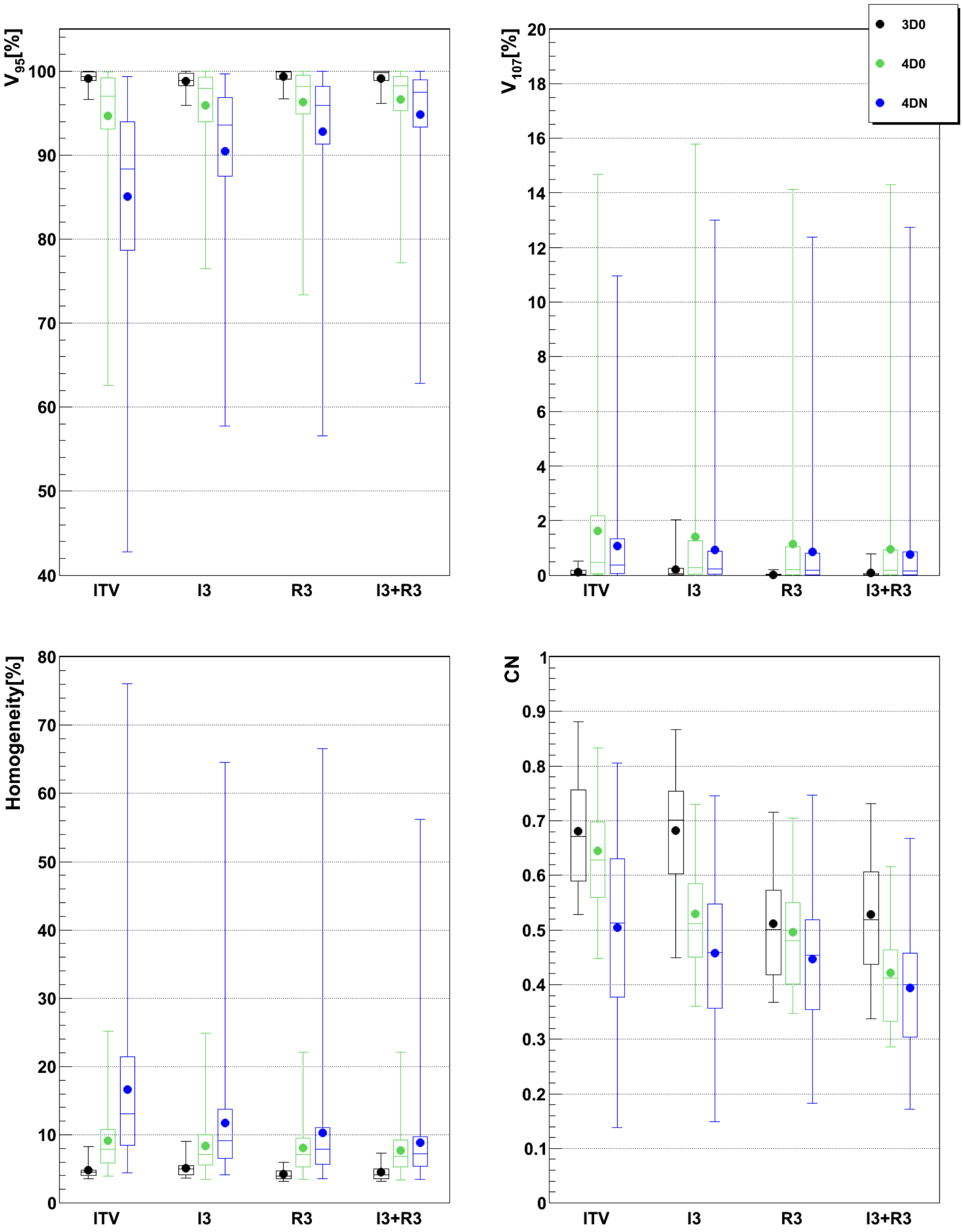

Figure 3.7.: Impact of additional margins on V_{95}, V_{107}, homogeneity and CN: ITV (ITV margins only), I3 (3mm isotropic margins), R3 (3mm+3% range margins) and i3+R3 (3mm isotropic + 3mm+3% range margins). Each 3D0 bar is composed of results obtained using all 9 patients and 3 foci, representing 27 points, and each 4D0 and 4DN bar are composed of results obtained using all 9 patients, 3 foci and 3 GWs, representing 81 and 549 points, respectively (homogeneity 4DN bars are in fact composed of only 531 points due to the same reason described in the legend of figure 3.5).

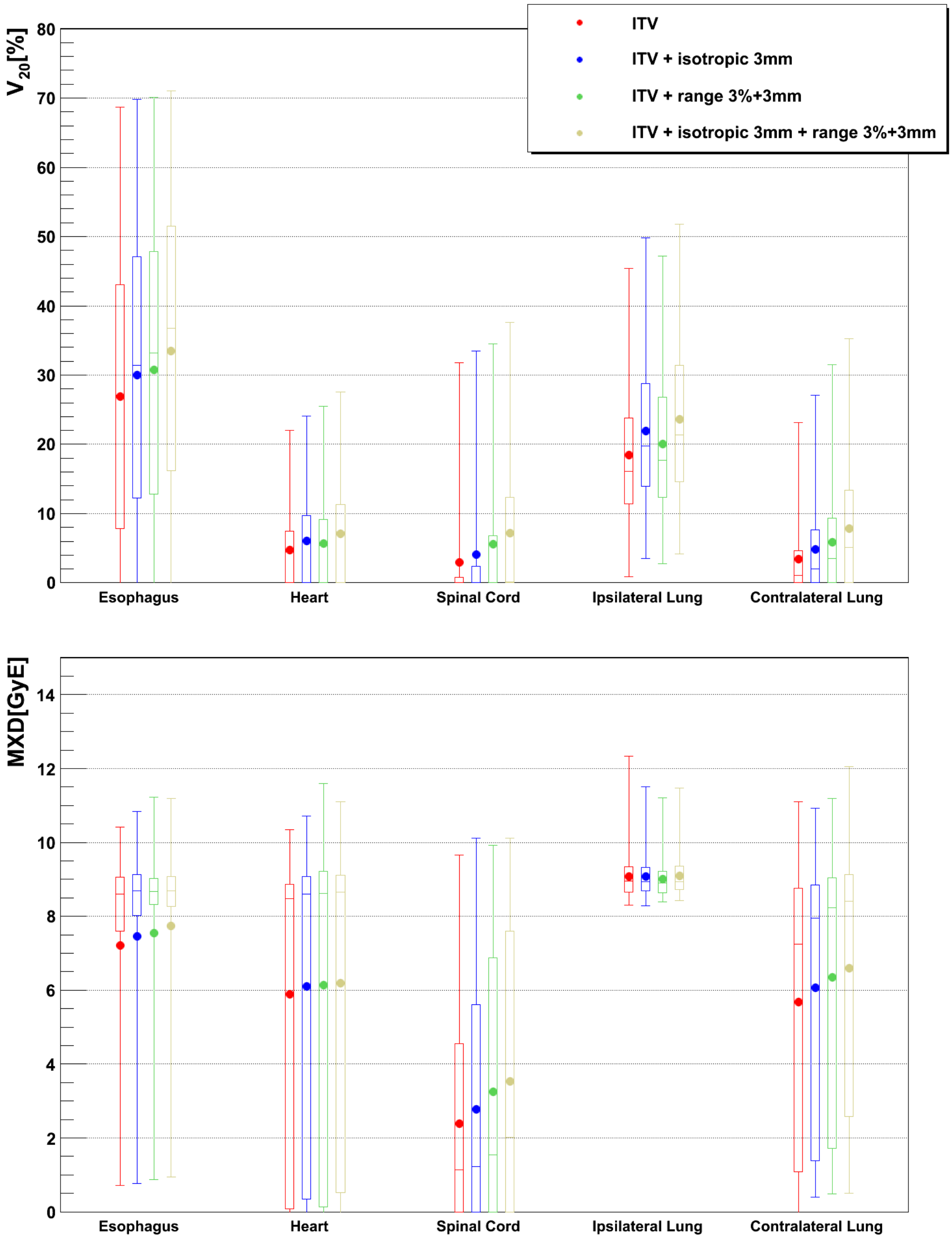

Figure 3.8.: Impact of additional margins on the dose delivered to the organs at risk. Results are displayed for five organs at risk: the esophagus, the heart, the spinal cord and the ipsilateral and contralateral lungs. Each bar is composed of results obtained from all 4D calculations (4D0 and 4DN put together) of all weeks of all patients using 3 foci and 3 GWs, representing 630 points per bar.

Figure 3.8 shows the impact the different margins on the dose delivered to the OARs. Looking at V_{20} first, using additional margins increases gradually the irradiated volume ($p < 0.05$), with mean values going from 26.8% (ITV) to 33.4% (I3+R3), from 2.9% (ITV) to 7.2% (I3+R3) and from 3.5% (ITV) to 7.9% (I3+R3) in the case of the esophagus, the spinal cord and the contralateral lung, respectively. For the heart and the ipsilateral lung, V_{20} values obtained using range margins are slightly lower than those obtained using isotropic margins ($p < 0.05$). However, for those two OARs, the lowest values are still obtained using ITV margins only ($p < 0.05$) with average values of 4.8% and 18.4% and the highest ones using the isotropic/range margins combination ($p < 0.05$) with average values of 7.1% and 23.6%.

Now, looking at the maximal point dose, values are very similar in all margins cases for each OAR with slight increases or decreases only. However, those are significant enough ($p < 0.05$) to be pointed out. In the cases of the esophagus, the heart, the spinal cord and the contralateral lung, MXD increases as additional margins are used. I3+R3 simulations yield the highest values, followed by R3 simulations which are themselves higher than the I3 simulations. Concerning the ipsilateral lung, R3 simulations yield lower MXD values than ITV, I3 and I3+R3 simulations, for which results cannot be significantly differentiated ($z < z_{critical}$). Moreover, for each margins case most of the MXD values remain between 8.5 and 10 Gy(RBE).

Dose distributions (using again the 1st and the 7th weekly CTs of patient 3) using the largest focus and the shortest GW combined to ITV margins (ITV), ITV and additional 3mm isotropic margins (I3), ITV and additional 3mm+3% range margins (R3) and ITV and additional 3mm isotropic and 3mm+3% range margins (I3+R3) are displayed on figures 3.11.d-f, 3.11.g-i, 3.11.j-l and 3.11.m-o, respectively.

3.3.3 Number of fields

After margins, increasing the number of fields was carried out to investigate the effect on dose delivery. Figure 3.9 shows the impact of the number of fields combined or not with margins.

3D0 simulations yield very similar results in all cases for V_{95} and homogeneity, even though the best results are obtained using the 3FPTV combination ($p < 0.05$). V_{107} seems to increase when more fields are used ($p < 0.05$), illustrated by mean values going from about 0% to 3.7% and 2.2% in the ITV and the PTV cases, respectively. CN increases gradually with the number of fields ($p < 0.05$) with an exception in the SFPTV case which shows higher values than 2FPTV and 3FPTV cases ($p < 0.05$). Also, values obtained using PTV margins are lower ($p < 0.05$), following the trend of the mean values: 0.68, 0.72, 0.73 and 0.53, 0.47, 0.49 for the SFITV, 2FITV, 3FITV and SFPTV, 2FPTV, 3FPTV, respectively.

In the case of the 4D0 calculations, V_{95} increases slightly using more fields ($p < 0.05$), as shown by higher mean values of 97.6% and 97.4% in the 2FITV and 3FITV cases, respectively, compared to 94.7% in the SFITV case. Using PTV margins make those values increase further

($p < 0.05$) by 1.5% to 2%. V_{107} and CN values follow the same trend than for 3D0 calculations ($p < 0.05$), the first ones going from 1.6% to 4.1% in the ITV cases and from 0.9% to 2.4% in the PTV cases and the second ones from 0.64 to 0.71 in the ITV cases and from 0.42 to 0.48 in the PTV cases. Homogeneity values are similar in all cases but some significant trends ($p < 0.05$) can be pointed out: 2FITV simulations yield better values than the two other ITV cases, 2FPTV and 3FPTV simulations yield better values than SFPTV cases and each PTV simulation permits to obtain better results than the corresponding ITV simulation.

About 4DN results and looking first at the results obtained using only ITV margins, increasing the number of fields makes the mean V_{95} increase ($p < 0.05$), with mean values going from 85.1% with one field to 88.1% with 2 fields and to 87.3% with 3 fields. Using PTV margins makes V_{95} further increase ($p < 0.05$), reaching a mean value of 96.9% in the 3FPTV case. ITV margins' V_{107} mean values are similar to the ones obtained using PTV margins results although values increase slightly as more fields and margins are used ($p < 0.05$). Increasing the number of fields also permits to make homogeneity decrease and CN increase ($p < 0.05$). Adding PTV margins makes V_{107} values and CN values diminish further ($p < 0.05$) down to 37.4% and 0.48, respectively, for 3FPTV, the lowest CN mean value being reached for SFPTV at 0.39.

Figure 3.10 displays V_{20} and the maximal point dose using the same 6 fields/margins combinations. Looking at ITV simulations first, it is possible to observe different behaviors for the OARs. In the esophagus, using more fields makes V_{20} increase slightly ($p < 0.05$) with 2FTIV simulations yielding higher V_{20} than 3FITV simulations while MXD is reduced ($p < 0.05$), 2FITV and 3FITV yielding similar results ($z < z_{critical}$) lower than SFITV simulations. For the heart, 2FITV and 3FITV simulations yield lower and higher V_{20} than SFITV simulations, respectively ($p < 0.05$), while MXD increases gradually with the number of fields ($p < 0.05$). V_{20} in the spinal cord is higher when two fields are used compared to one and three fields calculations ($p < 0.05$) while MXD is lower in the case of 3FITV simulations ($p < 0.05$), the two other ones yielding similar results ($z < z_{critical}$). In the ipsilateral lung, using more fields also increases gradually V_{20} ($p < 0.05$) as well as MXD which is higher in the 3FITV case ($p < 0.05$). Finally, the 3FITV configuration allows lower V_{20} and MXD in the contralateral lung ($p < 0.05$).

Now, adding PTV margins has the same significant ($p < 0.05$) impact for each OAR on V_{20} as well as on MXD. For each OAR, both of them increase slightly compared to the corresponding ITV simulations.

Example dose distributions using week 6 of patient 3 from single field ITV simulations (SFITV) and single field, 2 fields and 3 fields PTV simulations (SFPTV, 2FPTV and 3FPTV) can be observed on figures 3.11.d-f and 3.12.a-f, respectively.

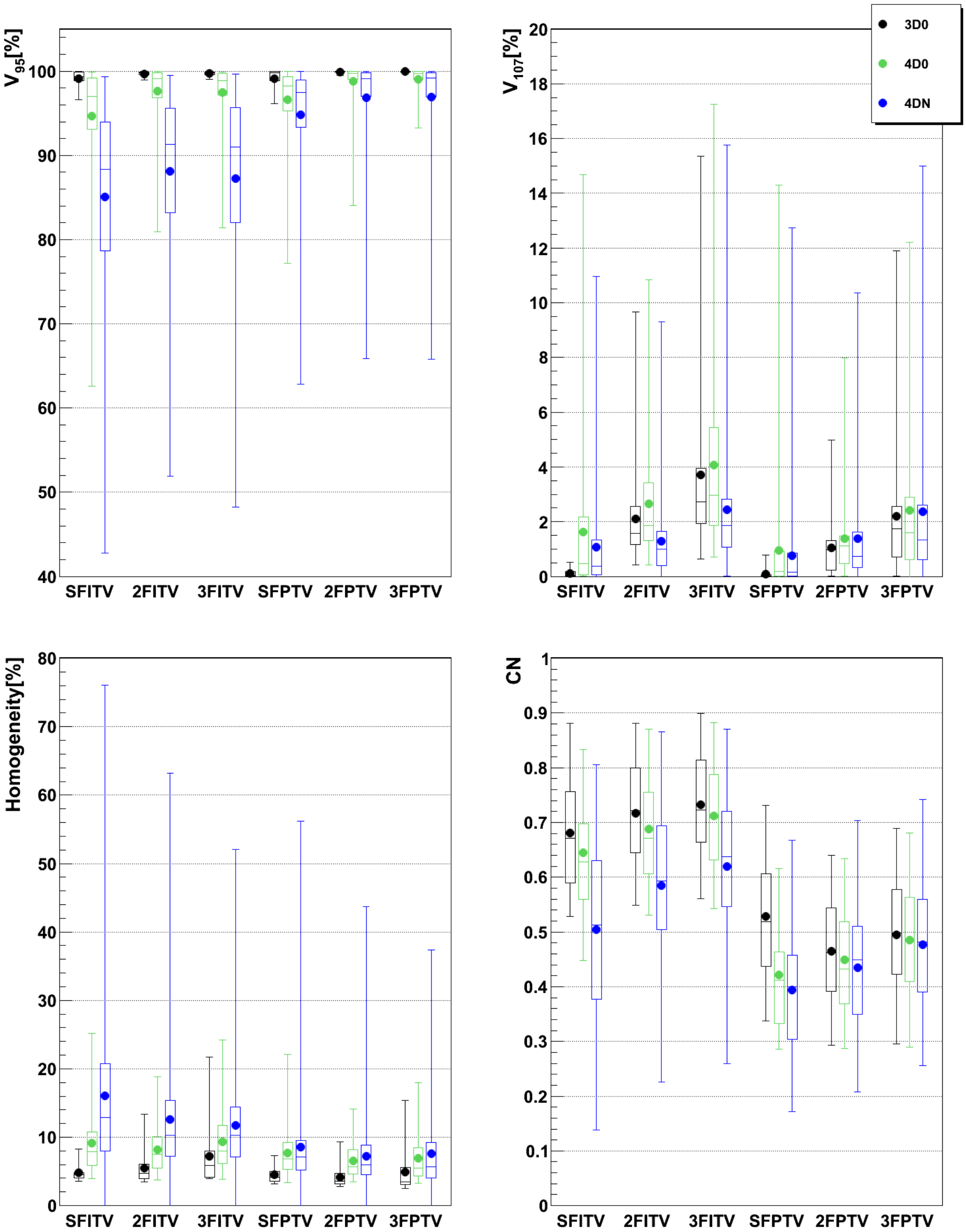

Figure 3.9.: Impact of different numbers of fields on V_{95}, V_{107}, homogeneity and CN: 1, 2 and 3 fields with ITV (ITV margins only) and PTV (3mm isotropic + 3mm+3% range margins). Each 3D0 bar is composed of results obtained using all 9 patients and 3 foci, representing 27 points, and each 4D0 and 4DN bar are composed of results obtained using all 9 patients, 3 foci and 3 GWs, representing 81 and 549 points, respectively (homogeneity 4DN bars are in fact composed of only 531 points due to the same reason described in the legend of figure 3.5).

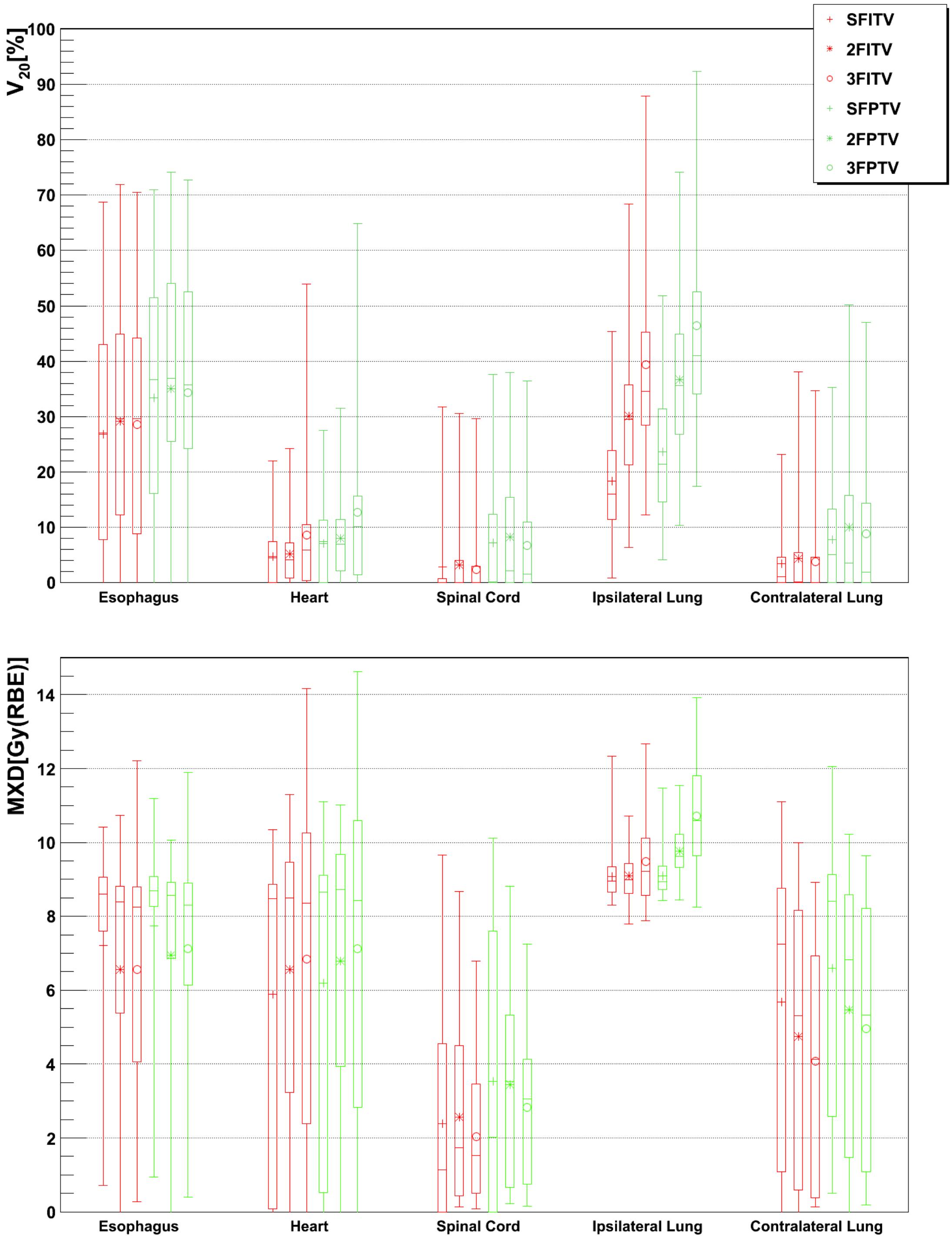

Figure 3.10.: Impact of different numbers of fields on the dose delivered to the organs at risk. Results are displayed for five organs at risk: the esophagus, the heart, the spinal cord and the ipsilateral and contralateral lungs. Each bar is composed of results obtained from all 4D calculations (4D0 and 4DN put together) of all weeks of all patients using 3 foci and 3 GWs, representing 630 points per bar.

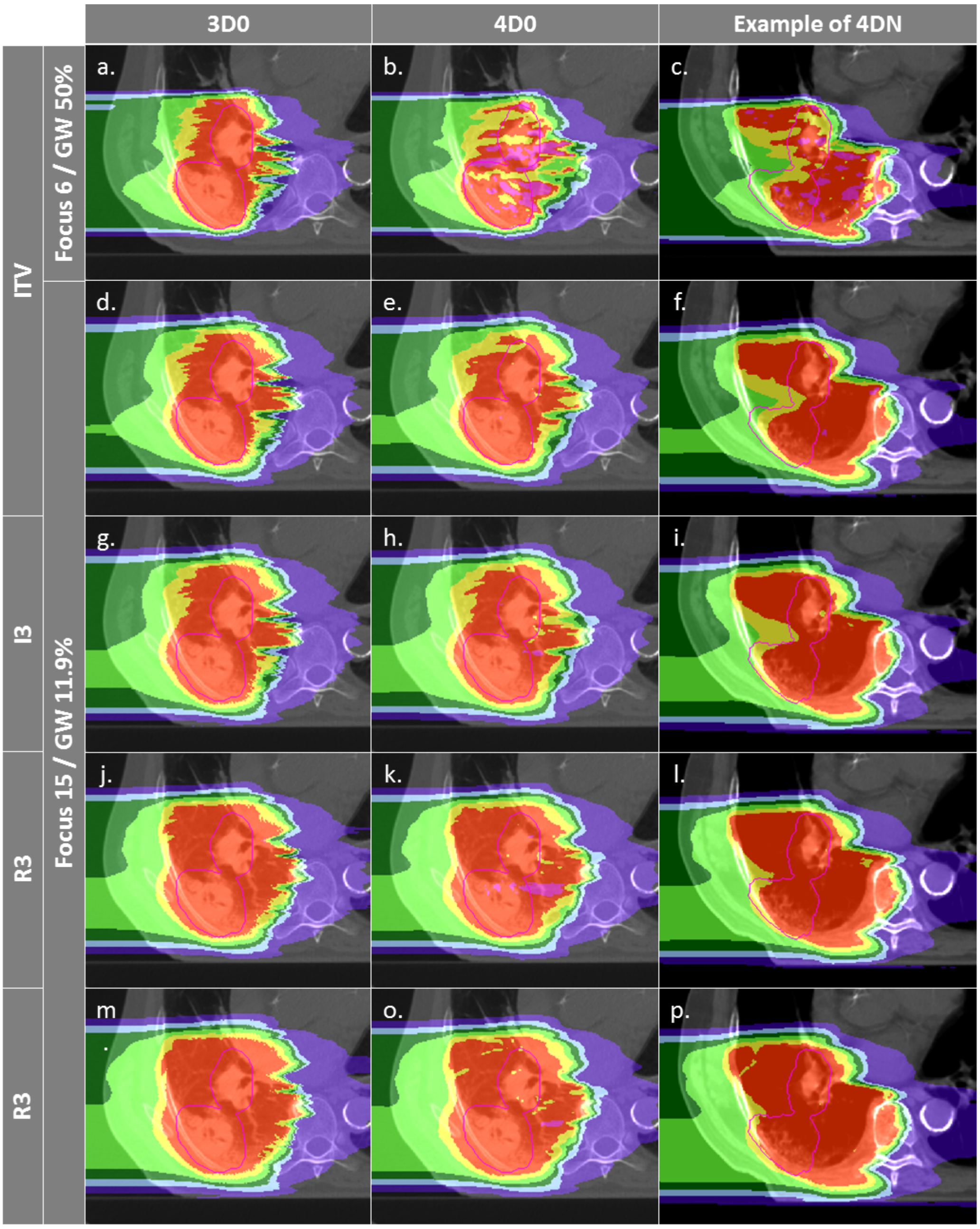

Figure 3.11.: Dose distributions of patient 3 using different weekly CTs and configurations for single field calculations. Pink contours represent the CTV. First column displays 3D0 simulations, second column 4D0 simulations and the third one 4DN simulations using week 6. Cases a-c and d-f are obtained using the SFLG and the LFSG configurations, respectively, with ITV margins only. Examples g-i, j-l and m-p are obtained using the LFSG configuration in combination to 3mm isotropic margins, 3mm+3% range margins and the combination of both previous margins, respectively. An evolution of target coverage, homogeneity, overdose and OAR dose delivery is clearly visible. Compared to 3D cases, 4D simulations show the effects of intrafractional motion and interplay for the simulations done using week 0 and the effects of interfractional changes in addition for cases simulated using week 6. Using a larger focus and a shorter GW in combination to isotropic and range margins permits to obtain better target coverage and homogeneity, no significant overdose but OARs are more irradiated.

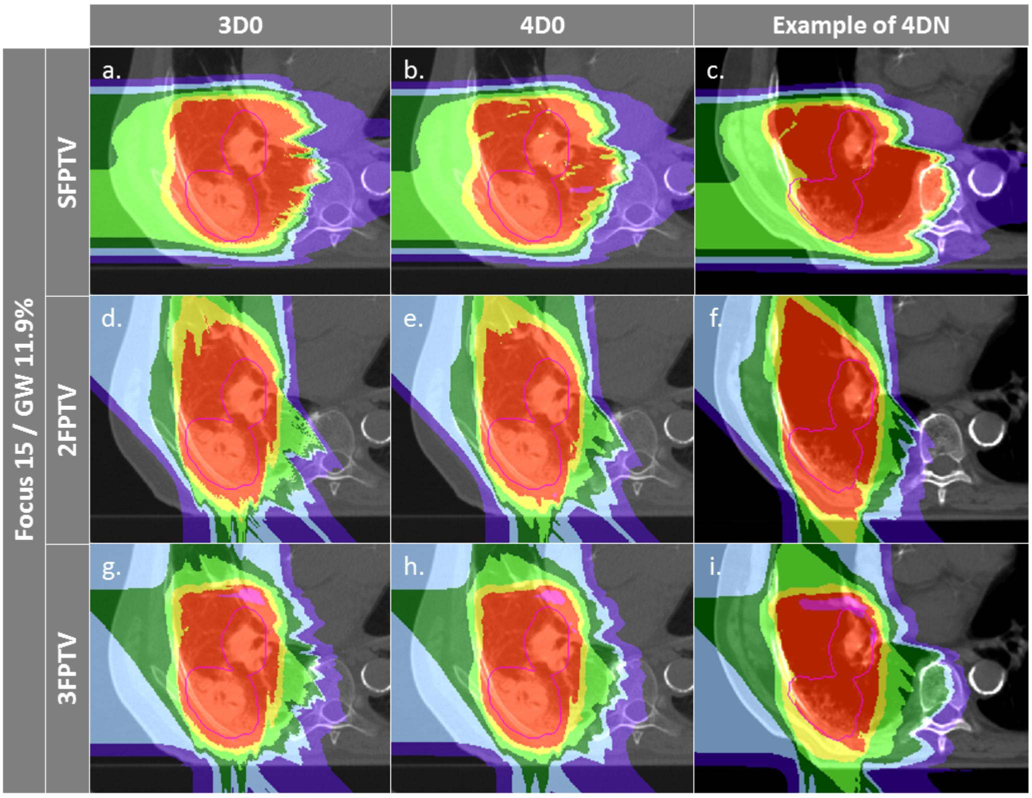

Figure 3.12.: Dose distributions of patient 3 using different weekly CTs and configurations for different numbers of field. Pink contours represent the CTV. First column displays 3D0 simulations, second column 4D0 simulations and the third one 4DN simulations using week 6. Cases a-c, d-f and g-i are obtained using the LFSG configuration combined to isotropic and range margins and one, two and three fields, respectively. An evolution of target coverage, homogeneity, overdose and OAR dose delivery is here again clearly visible. Compared to 3D cases, 4D simulations show the effects of intrafractional motion and interplay for the simulations done using week 0 and the effects of interfractional changes in addition for cases simulated using week 6. These effects are quite well mitigated here. Using a larger focus and a shorter GW in combination to isotropic and range margins and more fields shows further target coverage and homogeneity improvement, a little overdose near the tumor (due to a low contour extension value) and better sparing of OARs.

3.3.4 Tumor motion and size dependence

Results concerning the impact of some parameters on the dose delivery have been presented in the three previous sections but no distinction was done between patients. Some additional results will be presented here which depict the influence that the size and the motion magnitude of the tumor can have on the quality of the treatment and how two different parameter combinations can mitigate it.

First, the influence of the motion magnitude on V_{95} and homogeneity is displayed on the left and middle graphs of figure 3.13. The results here are that, looking at the red configuration, small motion patients have mean V_{95} 20% higher and homogeneity 18% better than large motion patients and that, looking at the green configuration, this influence is reduced to 3% and 2% for V_{95} and homogeneity, respectively.

Dependence of CN to the size is shown on the right graph. Patients with smaller tumor show mean CN 25% and 16% lower than bigger ones using the red and green configurations, respectively. The green configuration mitigates thus in average less the influence of the size on CN.

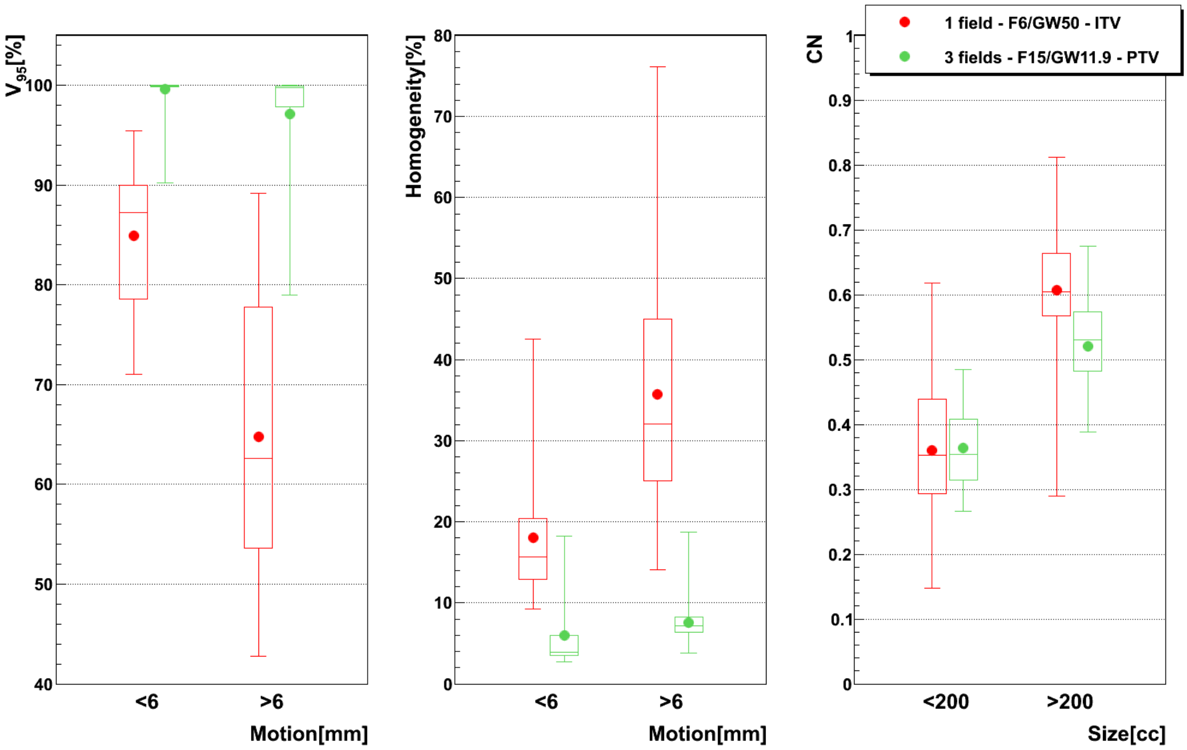

Figure 3.13.: Influence of motion magnitude on V_{95} and homogeneity and tumor on CN, using two different treatment configurations. The red configuration represents simulations done using 1 field, a focus of 6 mm, a 50% GW and ITV margins only and the green configuration 3 fields, a focus of 15 mm, a 11.9% GW and PTV margins (3mm isotropic + 3mm+3% range margins). For the left and middle graphs, bars representing tumors whose motion is lower than 6 mm are composed of 21 and 20 points for V_{95} and homogeneity (3 patients, 21 weeks), respectively, while bars representing tumors whose motion is larger than 6 mm are composed of 49 and 48 points for V_{95} and homogeneity (6 patients, 49 weeks), respectively (one less point/week for homogeneity because of the same reason described in the previous figures). In the case of the right graph, small tumor ($< 200cc$) bars are composed of 30 points (4 patients, 30 weeks) and big tumor ($> 200cc$) bars are composed of 40 points (5 patients, 40 weeks). See table 3.1 for more details about patients.

3.4 Discussion

In this study, a time series of 4DCTs of lung cancer patients was investigated for inter- and intrafractional effects of motion, anatomic changes and setup errors. Most studies of particle therapy for moving targets focus on 4DCTs at a single time point, assuming nearly perfect treatment conditions. In this respect, the findings of this study offer highly important, previously unstudied information for a more clinically realistic scenario.

3.4.1 Beam focus and gating window

Results show that the larger the focus and the shorter the GW, the better are V_{95}, V_{107} and homogeneity, meaning intrafractional motion mitigation is more effective using a large focus and a short GW, as illustrated by figure 3.11. Only the volume of the target (see table 3.1 and figure 3.13) seems to have a direct impact on CN: CN values yielded from simulations done with bigger targets (patients 1, 2, 4, 5 and 6) are higher than with smaller ones (patients 3, 7, 8 and 9); that can be observed on figure 3.13 (and especially for the presented cases with ITV margins only). Thus GW and focus do not show a significant influence on CN, which does not have a particular behavior regarding those parameters and is more patient specific: the range of the distributions for each week of each patient is not very large, except for patient 9 (see appendix E.1). That means that, although V_{95} increases using a large focus and a short GW, the total volume to which 95% of the planned dose is delivered increases as well, meaning that OARs in the vicinity of the tumor are irradiated. Nonetheless, the increase seems to be moderate since CN is not heavily influenced.

In both studies by Steidl (2011) and Richter (2012), a larger focus permits to obtain better results in terms of homogeneity and target coverage, which is in agreement with what has been observed here. However, while a decreasing CN is obtained with increasing focus size in the study by Steidl (2011), this behavior is not present in the study by Richter (2012) and here. This can be explained by the fact Steidl (2011) used a different CN which integrates the dose values obtained in all the voxels of the CTV and thus ignores the high interplay-dependency of V_{95}, the latter being itself the main component of the here used CN. Richter (2012) shows that CN is decreasing with larger foci only for static cases (a behavior which can be also observed for static cases on figure 3.5), while it is more patient specific for cases with motion and tends to converge on values obtained with static cases. The same behavior is observed here: weekly detailed figures of each patient from appendix E.1 show that CN is really patient and week specific, meaning that no real typical impact of focus or GW can be highlighted. As a global result, CN is slightly higher for larger focus, but when studied separately for each patient and each week, CN values do not show any systematic behavior.

The fact that the focus size has a much more significant influence on the results compared to gating window can also be noticed. This is obtained due to the size of the largest focus (15 mm) which is larger than the tumor motion for patients 1 to 8 or similar to the tumor motion for patient 9 (see table 3.1). Hence it is much easier to cover the moving tumor with this large focus.

Concerning the dose delivered to the OARs, it is in general not so different when the worst (longest GW/smallest focus) and the best (shortest GW/largest focus) configurations are compared (figure 3.6) in terms of V_{20} and MXD. OAR irradiation is also related to the patient anatomy, the location of the tumor and the chosen field angle. Even though a slight increase of the V_{20} values can be observed, results obtained using a larger focus are quite similar to those obtained using the smallest one. Now, although V_{20} increases in the case of the ipsilateral lung (which would have been expected considering the use of a larger focus and the fact the tumor is located in this lung), this represents an increase of a volume in which only 20% of the planned dose is delivered, meaning that, even though this low dose region is slightly larger around the tumor, high dose regions do not follow this evolution (as shown by a stable CN).

But comparing V_{20} and MXD obtained from the 3D0 and 4D0 simulations to those obtained from 4DN simulations permits to see that another factor deteriorates the precision of the beam delivery: interfractional anatomic changes. Indeed, in some cases and due to those changes, results are unsatisfactory compared to all the other values of the other weeks of the same patient. Those cases also show typically lower V_{95}, lower CN and lower homogeneity and deteriorated dose distributions (see figures 3.11.c and 3.11.f). This can be observed on figure 3.5 with the minimal V_{95} values obtained from the 4DN simulations, which are really below those obtained from 3D0 and 4D0 simulations, as well as on figure 3.6 on which V_{20} maximal values for the esophagus, the heart, the spinal cord and the contralateral lung increase when simulations with motion are done using weeks following the planning week. Dose distributions of those weeks and overlaid CTs (concerned week and optimized week) from each patient clearly show different types of motion such as organ shifts, tissue drifts and patient misalignment. Overlaying weekly CTs permits to notice that, sometimes, the shape of the entry channel of the patient is completely different from one week to the other, resulting in density changes which lead to range errors which themselves are responsible for a deteriorated dose delivery quality in the target and an increased irradiation of the OARs. Registration can also be a problem but it is very rare (see appendix A).

Dose distributions displayed on figure 3.11 can summarize what has been said before: interfractional changes (very large in the case of the patient displayed on figure 3.11.c and 3.11.f but also linked to the choice of the entry channel) between the displayed and the planning week cause an enormous range difference, leading to large dose delivery errors. However, V_{95} and homogeneity are clearly better using a large focus and a short GW (figures 3.11.d-f) as well as V_{107} (less pink areas on figures 3.11.d-f compared to figures 3.11.a-c, meaning less overdose). Besides, in this extreme case, OARs receive more dose because of interfractional changes again (figures 3.11.c and 3.11.f), but those are generally not so important, which means irradiation of OARs remains similar, as shown by the average values of figure 3.6.

3.4.2 Margins

Nonetheless, to recover for the interfractional changes, the study then consisted in using additional ITV-PTV margins. In his Study, Shirato et al. (2004) concluded in 2004 that a reduction of the margins cannot be recommended to reduce intrafractional motion. Knopf et al. (2013) and Albertini et al. (2011), using different sorts of margins, confirmed that margins permit indeed to compensate efficiently for tumor motion. Figure 3.7 shows improving results when the irradiated volume is extended. Sorted by increasing order isotropic, range and the isotropic/range combination margins yield better results, for both 4D0 and 4DN simulations (3D0 remaining similar except for CN): V_{95}, homogeneity and CN are quite sensitive to additional ITV-PTV margins. V_{95} and homogeneity improve indeed significantly in terms of distribution range and mean value. And even though the effects of interfractional changes can still be observed for 4DN simulations (low minimal V_{95} and high maximal homogeneity values), using a combination of additional isotropic and range margins permits to increase the minimal V_{95} value of those by 20%, as well as also improving the homogeneity by 20% compared to the cases for which only ITV margins are used. That means logically that combining those two margins to extend the irradiated region permits to cover the possible anatomic changes from one fraction to another better.

CN, however, reduces due to more dose delivered in the vicinity of the target volume. This can be observed in figure 3.11.d-o: V_{95}, V_{107} and homogeneity are improved but the irradiated volume outside the tumor clearly increases gradually as more additional margins are used. OARs in the vicinity are indeed being more irradiated, as shown by the increasing V_{20} values of figure 3.8 However the maximal point dose remains similar or is only slightly higher, which is quite logical considering isotropic margins only add 3 mm to the target and range margins mostly affect the treated lung, whose MXD was already quite high.

V_{107} is apparently not very sensitive to margins. Figure 3.7 shows that distribution ranges and mean values remain in the same order of magnitude and if there is a change, it is patient specific and cannot be observed as a systematic behavior (see patient specific weekly graphs in appendix E.1). Considering margins are only an extension of the volume, this result is fairly expected, considering the good V_{107} already obtained in the previous part by just using a large focus on tumors, whose size varies from about 50 cc to more than 700 cc.

Figures 3.11.d-f and 3.11.m-o show how margins can allow dose recovery in the tumor for a patient with severe intra- and interfractional motion. In this case, combination of range and isotropic margins permits to reach a mean V_{95} value 20% higher compared to the use of ITV margins only. Homogeneity is also largely improved by 15% by using combined isotropic/range margins. Thus, to the conclusions of Knopf et al. (2013) and Albertini et al. (2011), stating that intrafractional motion can be mitigated by the use margins, can be added the fact that margins also allow to compensate efficiently for dose delivery deterioration caused by interfractional changes. However, it is also clearly visible that OARs such as the spinal cord and of course the ipsilateral lung are more irradiated. But, again, OAR irradiation is patient, tumor location and field specific (as shown by very large V_{20} distributions in the case of the esophagus for instance), meaning choosing an appropriate entry channel is very likely to reduce the dose delivered to the spinal cord in the example of figure 3.11.

To conclude this part about margins, the combination of isotropic and range margins showed the best results in terms of target coverage and homogeneity, allowing further recovery of deteriorated dose delivery mainly due to interfractional anatomic changes. However, because of the extended volume but also depending on the tumor location, more dose was delivered in the OARs near the tumor.

3.4.3 Number of fields

As a possible solution to reduce the dose in the OARs and further improve dose delivery in the target, using more fields with or without ITV-PTV margins was investigated. First, using more fields only combined to ITV margins permits indeed to increase V_{95} and to obtain better homogeneity and CN. The fact V_{95} is lower when three fields are used compared to cases using only two fields can be easily explained: there is nowadays no automatic optimized method to choose field angles due to patient specific anatomies, so they were chosen such as one field is set in the left-right (LR) direction directly headed to the tumor, one 45° further in the direction of the anteroposterior (AP) axis and one in the AP direction going from the chest to the back. However, using this technique can unfortunately result in a third field going through shifted tissue (because of interfractional changes), leading then to range errors. This is why, for the final study of this thesis, the range changes from one week to another were studied to try to isolate directions which could be less affected by interfractional changes. Despite this result, even though target coverage may be deteriorated due to a questionable entry channel and the effect of interfractional changes being clearly visible on figure 3.9 with a very large difference in average value as well as in distribution between 4D0 and 4DN calculations, homogeneity and CN, which are apparently less influenced by field directions, are still further improved. This shows that choosing field directions carefully to avoid regions affected by interfractional changes would result in good target coverage, good homogeneity and good CN. This is in agreement with Knopf et al. (2011), who showed that better homogeneity can indeed be obtained using multiple fields, the difference between her study and this one being that the motion mitigation technique used in her study was rescanning.

V_{107} is increasing here, but it is due to the use of 0.35 as the contour extension value in

TRiP4D (see appendix D). A value of 1.1, as recommended by Weber (1996), will be used in the next chapter and yields much better V_{107} results close to 0% for three field calculations. Due to the high number of computations and the likely minor impact on the final conclusions, simulations were not repeated with a higher contour extension value.

Using additional margins like previously presented, meaning the combination of isotropic and range margins, permits to improve further results. V_{95} average values for 4DN simulations tend to converge to the values obtained for 4D0 simulations, showing that interfractional changes are almost completely mitigated. Low minimal values are still present but are higher than in the ITV cases. The same behavior can be observed for homogeneity whose mean values for 4D0 and 4DN simulations are almost identical. In this case maximal homogeneity values obtained using ITV-PTV margins are also reduced compared to the corresponding ITV case. CN is however drastically reduced due to the extended irradiated volume which is now partly composed of normal tissue from the surrounding OARs. Nonetheless, as for V_{95} and homogeneity, 4DN and 4D0 calculations yield similar results, meaning again that interfractional changes are correctly compensated.

Extending the irradiated volume causes indeed an increase in V_{20} values but which is not so important. It is never higher than 10%, meaning enlarging target contours do not cause a major change in the irradiation of OARs. However, if the SFITV and the 3FPTV cases are compared, the increase becomes quite large in the case of the ipsilateral lung, which is quite normal considering both extended volume and more fields used, resulting logically in more dose in the ipsilateral lung. But, again, V_{20} does not specifically represent high dose regions and looking at dose distributions displayed on figures 3.12.a-f permits to see the great advantage of using three fields combined with additional margins. It allows obtaining a conformal dose distribution, with a target which is completely and homogeneously covered, and reduced high dose regions outside the tumor. Once again field directions can be chosen differently to avoid or decrease further the irradiated volume of lung visible on figures 3.12.g-i. Moreover overdose due to the use of three fields and also visible on figure 3.12.i (the pink area besides the tumor) is disappearing when the optimal contour extension value is used in TRiP4D.

To conclude this last part, looking at figure 3.13 shows that the best combination (3 fields, large focus, short GW and PTV margins) is able to mitigate efficiently the tumor motion and size dependences of V_{95} and homogeneity and CN, respectively, as well as provide conformal fraction treatment, represented by the obtained high V_{95}, good homogeneity and acceptable CN. V_{107}, if a correct contour extension is chosen, is also close to 0. However, comparison with other mitigation techniques is a topic of interest which will be developed in the next chapter to investigate further possible improvement of the tumor treatment and reduction of the irradiation in the OARs.

4 Comparing motion mitigation techniques using optimized parameters

4.1 Introduction

In the previous chapter, using a combination of three fields and a range-based ITV with PTV margins composed of 3mm (geometrical) isotropic margins and 3mm+3% (water equivalent) range margins, a large focus (15 mm, FWHM) and a short gating window (GW, 11.9% of the amplitude) yielded the best results in terms of dose coverage and homogeneity. The best conformity number (CN) values were obtained using 3 fields combined to ITV margins alone and deteriorated when adding PTV margins. Now, even though gating has shown good conformity, whether it was performed clinically combined to passive beam delivery (Tsujii et al., 2004; Iwata et al., 2010; Tsujii and Kamada, 2012) or simulated with active beam scanning like in the previous chapter, further investigation was a necessary step to determine if this technique was the best suited to mitigate intrafractional motion and interfractional anatomic changes using only one plan optimized with the first weekly 4DCT.

Thus, it was decided to do a comparison of the results yielded using gating with other techniques such as rescanning only or a combination of rescanning and gating, referred to as re-gating. Rescanning has indeed shown interesting results for protons: varying the number of rescans as well as some other treatment parameters such as field directions was done by Knopf et al. (2011), resulting in a more significant effect of this mitigation technique when less fields were used and in a satisfactory homogeneity obtained after only a few rescans. It was however stated that large motion amplitude tumors may require rescanning to be combined with another mitigation technique such as gating or breath-hold. The rescanning method used in this paper, referred to as perfect rescanning (PRSC), was different compared to the normal rescanning process because its principle was to deliver homogeneously one tenth of the dose to each one of the 10 motion states of the 4DCT. Thus it only allowed studying the effects of tumor motion without interplay effects by delivering a fraction of the dose to each motion state.

Furukawa et al. (2007, 2010) also proposed a method combining rescanning and gating, called phase controlled rescanning, whose principle is to deliver rescans inside the gating window. This method was tested experimentally and showed encouraging results with an obtained 4D dose delivery quite similar to the one obtained in the static case, proving that this method could be used efficiently to compensate for tumor motion (Mori et al., 2013a,b). The so called perfect regating (PRGT) technique used here borrowed the same idea of combining gating and rescanning, meaning that the previously described PRSC method was modified so that one third of the planned dose was delivered homogeneously to 3 of the 10 motion states. Interplay effects were thus again ignored.

In this chapter, gating simulations, which were performed again (see appendix D), were compared to results obtained using perfect rescanning and perfect regating. The aim was to determine if a further increase in target dose conformity and better organ at risk (OAR) sparing were achievable. The three motion mitigation techniques were used in combination with the optimized parameters found in the previous chapter.

4.2 Materials and methods

4.2.1 Patient cohort

In this chapter, 6 patients from the 9 described in chapter 3 were used to compare motion mitigation techniques: patients 1, 2, 3, 7, 8 and 9. As preliminary simulations with the remaining patients 4, 5 and 6 showed good results (see appendix E.1 for the detailed patient results obtained in 3), no matter which configuration was used, they were excluded to allow for a larger set of simulation parameters in the given time frame. Thus it was decided to focus on the patients showing large motion and/or small size tumors, meaning that, for the 6 chosen patients, a total of 44 weekly 4DCTs were used. Number of weeks for each patient, alignment and registration methods and fields are the same as presented in the previous chapter.

4.2.2 Treatment parameters

In this chapter, comparison of gating, rescanning and regating was done using optimized parameters isolated in the previous chapter, as described above in the introduction. Thus, only one gating window (GW, 11.9% of the amplitude) was used for gating and three fields (see chapter 3) combined to PTV margins (3FPTV case of chapter 3) were used for each motion mitigation case. However, 3 different foci (6, 10 and 15 mm, FWHM) were used again. As in the previous chapter, the distance between each raster position was set to 2 mm on each isoenergy slice (IES) and the distance between two IESs was set to 3 mm water-equivalent using a ripple-filter (RiFi) of 3 mm (Weber and Kraft, 1999).

4.2.3 Gating

All gating plans were simulated using the GSI 4D treatment planning system (4DTPS) TRiP4D (Richter, 2012), based on TRiP98 and modified to allow 4D-dose calculations. The gating process used in this chapter is also the same as in the previous one. To obtain each 4D beam delivery sequence, a motion surrogate, the optimized static treatment plan and the accelerator specifications (synchrotron of HIT in this case) are necessary. The motion surrogate and the optimized plan are used to distribute the dose delivery among the selected motion states corresponding to the GW and accelerator specifications add the interplay effects by simulating the dynamic behavior of the accelerator, such as the scanning speed. Thus, 4D gating simulations contain the two dynamic systems necessary to simulate interplay effects: the moving tumor and the 4D gating plan delivered using a realistic accelerator behavior (Richter, 2012). In this chapter, 4D simulations were performed using a contour extension of 1.1 instead of 0.35, as recommended by Weber (1996) (see appendix D). But, except for this value, the motion surrogate (sine square with a unique period 3.6 seconds) and the ITV definition (range corrected ITV composed of 5 motion state CTVs representing 25% of the amplitude) were the same as in the previous chapter. For each patient, plans were initially optimized to this ITV computed with the first week's CT, using one unique planned dose of 8.1 Gy(RBE).

4.2.4 Perfect rescanning (PRSC)

All rescanning plans were also simulated using TRiP4D (Richter, 2012). However, the simulation process is different compared to gating: first the optimized plan was generated using an ITV which was composed of all ten motion states of the 4DCT, then the main principle of the rescanning process used here is to deliver homogeneously and identically one tenth of the planned dose (see figure 4.1) to each one of the ten motion states of the 4DCT. So, here, no motion surrogate is used and the dose of each raster point of the static treatment plan is divided by 10 and distributed identically on all 4DCT states. Thus, because there is no double dynamic system as for gating, interplay effects are not taken into account.

4.2.5 Perfect regating (PRGT)

Regating plans were simulated using TRiP4D (Richter, 2012). Even though the optimized plans were those that were computed for gating, because the ITV is identical, the technique is again different compared to gating and more similar to the rescanning process described above. Indeed the difference with PRSC is here that one third of the planned dose is delivered homogeneously to only 3 motion states which compose the GW (see figure 4.1). Those 3 motion states correspond to the GW that was used for gating. Therefore, again, interplay effects are ignored because of the absence of a double dynamic system.

Rescanning

State	0	1	2	3	4	5	6	7	8	9
Fraction of the dose	1/10	1/10	1/10	1/10	1/10	1/10	1/10	1/10	1/10	1/10

Regating

State	0	1	2	3	4	5	6	7	8	9
Fraction of the dose	0	0	0	0	1/3	1/3	1/3	0	0	0

Figure 4.1.: Diagrams of the perfect rescanning (PRSC) and perfect regating (PRGT) techniques dose delivery. Motion state n°5, set as the reference state, represents the end-exhale state. In the case of PRSC, one tenth of the dose is delivered to each motion state of the target and in the case of PRGT, one third of the dose is delivered to each one of the three motion states composing the GW. Interplay is not taken into account for both techniques.

4.2.6 Data analysis

For each mitigation technique, the dose distribution of each week was obtained by accumulating the dose delivered to each motion state on the reference phase of the 4DCT using state-to-state non-rigid vector fields. Comparison of the obtained accumulated dose between the three mitigation techniques was then done by investigating differences in target coverage (V_{95}), overdose (V_{107}), homogeneity and conformity number (CN) for the tumor and V_{20} and maximal dose point (MXD) for the surrounding organs at risk.

For each comparison, a Wilcoxon signed-rank test (W) was performed using a level of significance of 0.05 to estimate the difference between two samples. In the case of samples containing more than 10 values, the p-value (p) was computed using the obtained z-score (z).

4.3 Results

All results were simulated on the weekly 4DCTs with a planned dose of 8.1 Gy(RBE). In all following figures the average value (marker), the median value (horizontal bar in the box), the 25th and 75th percentile and the total range of all values are given. More details about the planned, static dose on the first week (3D0), the 4D dose on the first week (4D0) and the 4D dose on all following weeks (4DN) can be found in the previous chapter.

4.3.1 Gating and PRSC

Results obtained using gating and PRSC in terms of target coverage (V_{95}), overdose (V_{107}), homogeneity and CN can be observed on figure 4.2.

3D0 simulations yield very similar results ($z < z_{critical}$) in terms of V_{95} with an average value higher than 99.9% for both cases. Overdose is also similar ($z < z_{critical}$), even though the maximal value is a bit higher in the case of gating. It is the same for homogeneity, whose average values are similar in both cases ($z < z_{critical}$), but whose maximal values are different with a higher one for gating at 7.3% and a lower one for PRSC at 4.2%. Only CN shows a significant difference ($p < 0.05$), illustrated by an average value 14% higher in the case of PRSC at 0.49 compared to 0.43 obtained with gating as well as higher minimal and maximal values (0.42 compared to 0.38 and 0.64 compared to 0.56, respectively).

4D0 simulations show that rescanning permits to obtain better values in terms of target coverage ($p < 0.05$). V_{95} values are indeed almost identical to values obtained for 3D0 in the case of PRSC, as shown by an average value higher than 99.9% (minimum: 99.8%), while the mean V_{95} decreases to 99.4% (minimum: 97.0%) in the case of gating. Homogeneity and CN are better ($p < 0.05$) in the case of PRSC, illustrated by average values of 2.4% and 0.52, respectively, compared to 4.4% and 0.44 obtained in the case of gating. On the contrary, overdose is slightly better in the case of gating ($W < W_{critical}$).

Finally, 4DN simulations show the largest differences. V_{95} appears to be better in the case of gating compared to PRSC ($p < 0.05$), illustrated by mean values of 97.0% and 96.2%, respectively. V_{107} is almost identical in both cases ($z < z_{critical}$) and close to 0. And again, homogeneity and CN are better in the case of PRSC ($p < 0.05$), as shown by mean values of 4.3% and 0.49, respectively, compared to 5.2% and 0.43 obtained with gating. On figure 4.4, the dose volume histogram (DVH) of the CTV is displayed for patient 2 and for the two techniques. It shows that results are indeed very close and, depending on the week, slightly better for one technique or for the other one. The patient-specific weekly results can also be seen in appendix E.2 and show that gating generally yields better V_{95} and homogeneity and PRSC better CN.

Figure 4.3 shows results obtained using gating and PRSC regarding the dose delivered to the OARs. Even though those results are close to each other, some trends can be isolated. Concerning the esophagus, V_{20} is similar using both mitigation techniques ($z < z_{critical}$). For all the other organs at risk, V_{20}, even though the distributions look very similar in both cases, significant trends can be pointed out ($p < 0.05$): in the case of the heart, the ipsilateral lung and the contralateral lung, PRSC yields better results while in the case of the spinal cord, gating permits to obtain lower V_{20} values.

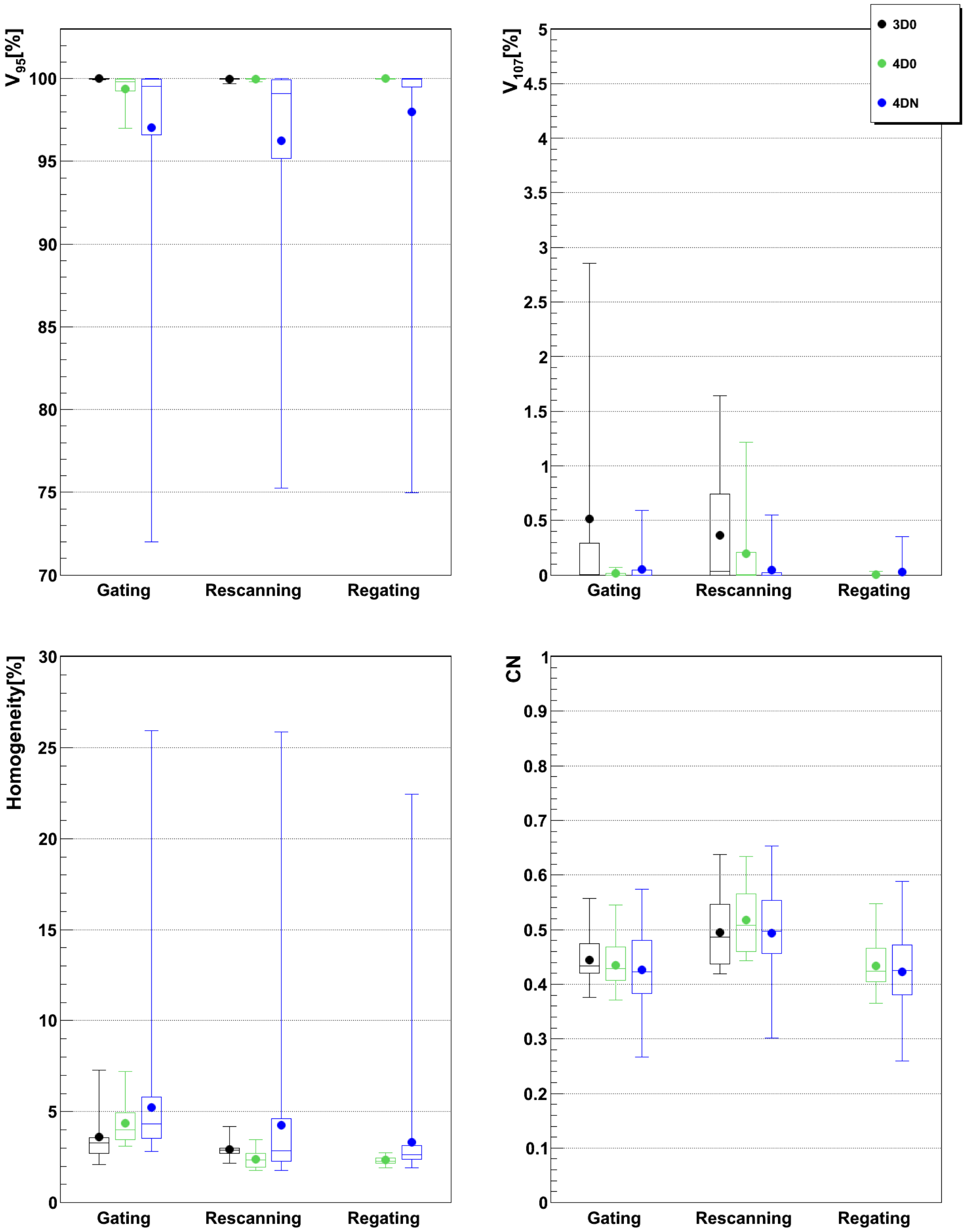

Figure 4.2.: Comparison of V_{95}, homogeneity, V_{107} and CN obtained using gating, PRSC and PRGT. Each 3D0 bar is composed of 18 datapoints, representing static simulations done with 3 foci using week 0 of each patient (3D0 simulations were not performed in the case of regating). 4D0 bars are also composed of 18 datapoints, representing 4D simulations done with 3 foci and one GW in the case of gating using week 0 of patient. 4DN bars are composed of 114 datapoints, representing 4D simulations done with 3 foci and one GW in the case of gating using week 1 to 5-8 of each patient (see previous chapter for specifications concerning 3D0, 4D0 and 4DN).

Concerning the maximal point dose, values are also similar from one mitigation technique to the other but, except for the spinal cord ($z < z_{critical}$), all the other organs show again a significant behavior ($p < 0.05$) when the two mitigation techniques are compared. Thus, using PRSC permits to obtain slightly lower MXD for the esophagus, the heart and the ipsi- and contralateral lungs.

Figure 4.4 shows that different trends can be observed depending on the chosen dose interval. For instance, in the case of the ipsilateral lung, gating and PRSC yields similar results on a dose interval going from 0 to 30% while gating permits to obtain better results above 30% of the dose. In the case of the spinal cord, the global trend described above for V_{20} is respected with better values obtained on the entire dose distribution in the case of gating.

Figure 4.6.a-c and 4.6.d-f show static and 4D dose distributions obtained using the 1st and the 7th weekly CTs of patient 3 and gating and rescanning as motion mitigation techniques, respectively.

4.3.2 Gating and PRGT

Figure 4.2 also shows results obtained for gating and PRGT. 3D0 simulations were only performed for gating because the same optimized plan was used for both motion mitigation techniques. The results in terms of V_{95}, V_{107}, homogeneity and CN are already described in the previous section. PRGT yields better results for 4D0 simulations in terms of V_{95} and homogeneity ($p < 0.05$), with 100% and 2.3% as average values, respectively, compared to 99.4% and 4.4% obtained for gating. Compared to 3D0 simulations done for gating, PRGT 4D0 simulations yield almost the same results with almost perfect V_{95}, very low V_{107} and lower homogeneity (see figure 4.2). Comparing overdose and CN, better results are obtained using PRGT for the first one ($W > W_{critical}$) and gating for the second one ($p < 0.05$).

4DN simulations, no matter whether gating or regating is used, show drastically decreased minimal values and lower average values concerning V_{95} compared to 3D0 and 4D0 simulations. Respectively, for gating and PRGT, minimal values drop to 72.0% and 75.0% and average values, which were higher than 99% for 3D0 and 4D0 simulations, are reduced to 97.0% and 98.0%. Homogeneity follows the same behavior and is degraded, meaning slightly higher mean values and much higher maximal values, while CN shows larger ranges (see figure 4.2). Now, comparing the results of the two motion mitigation techniques, they both yield similar results and trends can be observed as PRGT yields better V_{95}, V_{107} and homogeneity ($p < 0.05$) while gating permits to obtain better CN ($p < 0.05$). Better V_{95} in the case of PRGT can indeed be observed in the case displayed on figure 4.4 and in appendix E.2, where detailed weekly results are available.

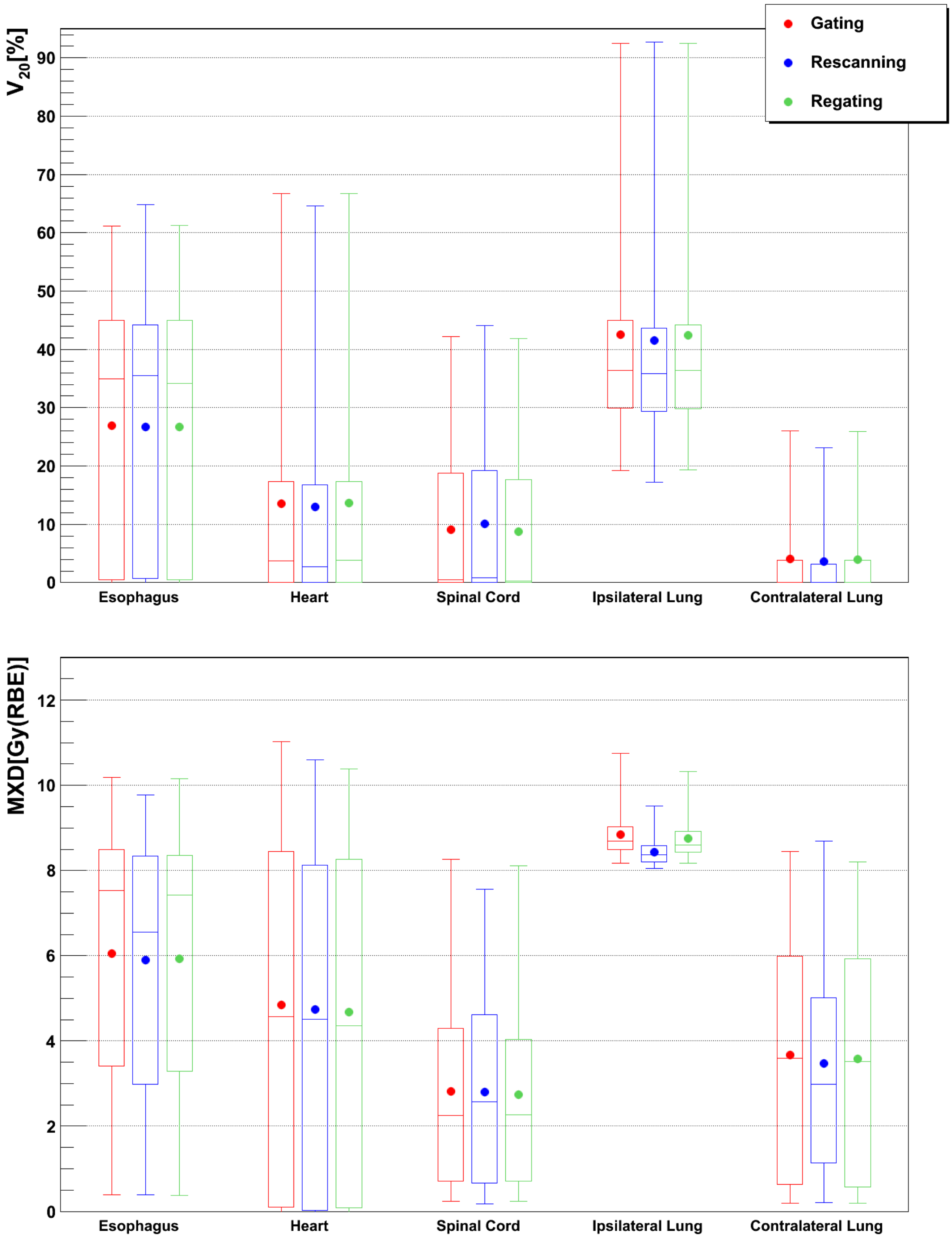

Figure 4.3.: Comparison of V_{20} and the maximal point dose obtained using gating, PRSC and PRGT. Each bar is composed of 132 datapoints obtained from all 4D calculations (4D0 and 4DN, all weeks of all patients) performed using 3 foci (and one GW in the case of gating).

Figure 4.3 also shows results obtained using gating and PRGT concerning the dose delivered to the organs at risk. Like in the previous section where V_{20} and MXD were similar for gating and PRSC, V_{20} and MXD results are here again similar but showing significant trends ($p < 0.05$) when the two techniques are compared. Thus, for each OAR, PRGT permits to obtain lower V_{20}. MXD values also show very little differences but, as well as for V_{20}, PRGT yields lower MXD values in the case of each OAR ($p < 0.05$).

Figure 4.4 shows that, for patient 2 and for both displayed OARs, dose distributions are indeed very similar and, depending on the dose percentage in the DVH, slightly better results can be obtained using one technique or the other.

Figure 4.6.a-c and 4.6.g-h show static (only for gating) and 4D dose distributions obtained using the 1st and the 7th weekly CTs of patient 3 and gating and PRGT as motion mitigation techniques, respectively.

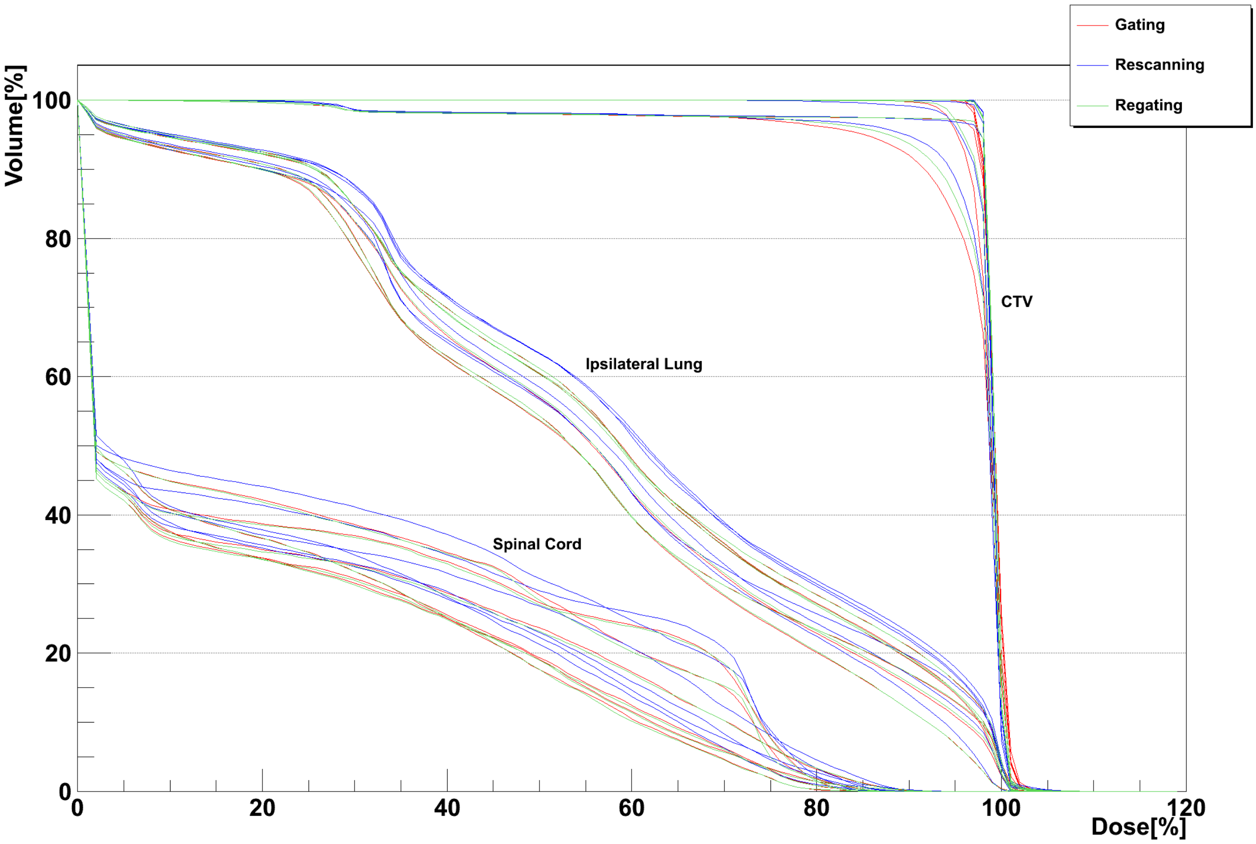

Figure 4.4.: Dose volume histogram (DVH) showing the difference in dose delivery to the CTV, the ipsilateral lung and the spinal cord for gating (red), PRSC (blue) and PRGT (green) using patient 2 weekly 4DCTs. Results for the 6 weekly 4DCTs and for each mitigation technique are displayed using a configuration composed of a focus width of 15 mm (FWHM) and a GW of 11.9%. The two weekly CTV DVHs which show a decrease at about 30% of the dose are the consequence of large interfractional anatomic changes displayed on figure 4.5.

4.3.3 PRSC and PRGT

The last possible comparison using figures 4.2 and 4.3 can be done between the PRSC and regating methods.

Looking at 4D0 simulations, the two mitigation techniques yield again similar results and the only significant differences can be observed for overdose and CN. Indeed PRGT permits to obtain lower V_{107} ($p < 0.05$) but both techniques yield very close values lower than 1.5%. Then PRSC yields higher CN ($p < 0.05$), as illustrated by mean values reaching 0.52 in the case of PRSC and only 0.43 in the case of PRGT.

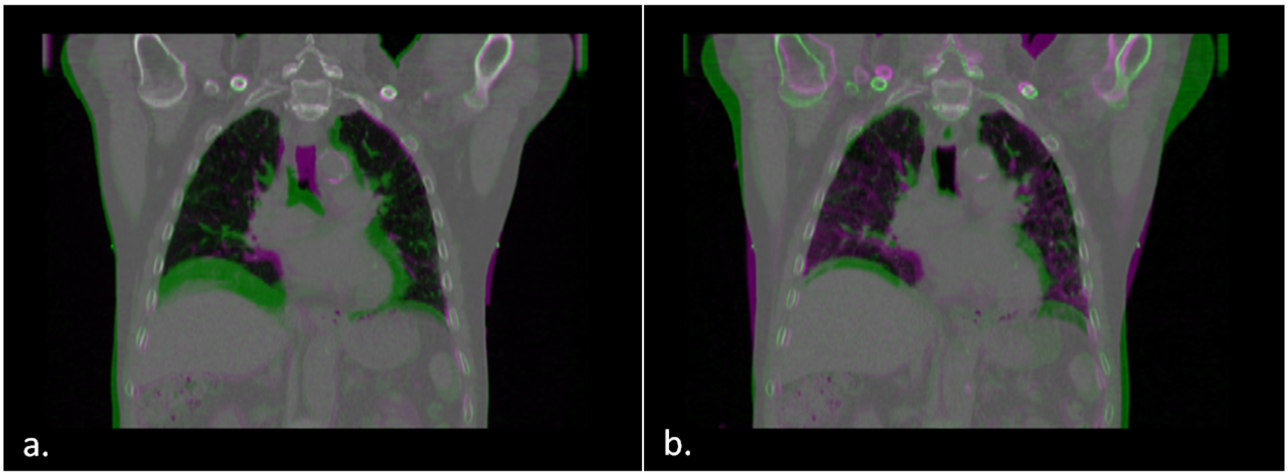

Figure 4.5.: Overlaid 4DCTs of patient 2: case *a* represents weeks 0 and 4 and case *b* weeks 0 and 5. Large interfractional anatomic changes can be seen which lead to the decrease in target coverage visible on figure 4.4.

In the case of 4DN simulations, similar trends are observed compared to 4D0 calculations, which were already described in the previous subsections and comparing the two mitigation techniques, using PRGT allows obtaining better results ($p < 0.05$) in terms of target coverage, overdose and homogeneity. This can be observed on figure 4.2 with average V_{95} and homogeneity values of 98.0% and 3.3% for PRGT compared to 96.2% and 4.3% for PRSC. V_{107} values are in each case lower than 1%. And the best CN is yielded by PRSC ($p < 0.05$). Once again, depending on the week, figure 4.6 shows that different trends concerning the dose delivered to the CTV can be observed, but looking at weekly results in appendix E.2 permits to see that PRGT yields the best V_{95} and homogeneity while PRSC permits to obtain better CN.

Figure 4.3 permits to see that the dose delivered to the OARs is again very similar using one technique or the other but for some organs, a trend can be isolated when comparing the PRSC and regating methods. Then using PRSC yields lower V_{20} values ($p < 0.05$) in the cases of the heart and the ipsi- and contralateral lungs. On the contrary, using PRGT permits to obtain lower V_{20} ($p < 0.05$) in the spinal cord. Both techniques yields similar results in the case of the esophagus ($z < z_{critical}$).

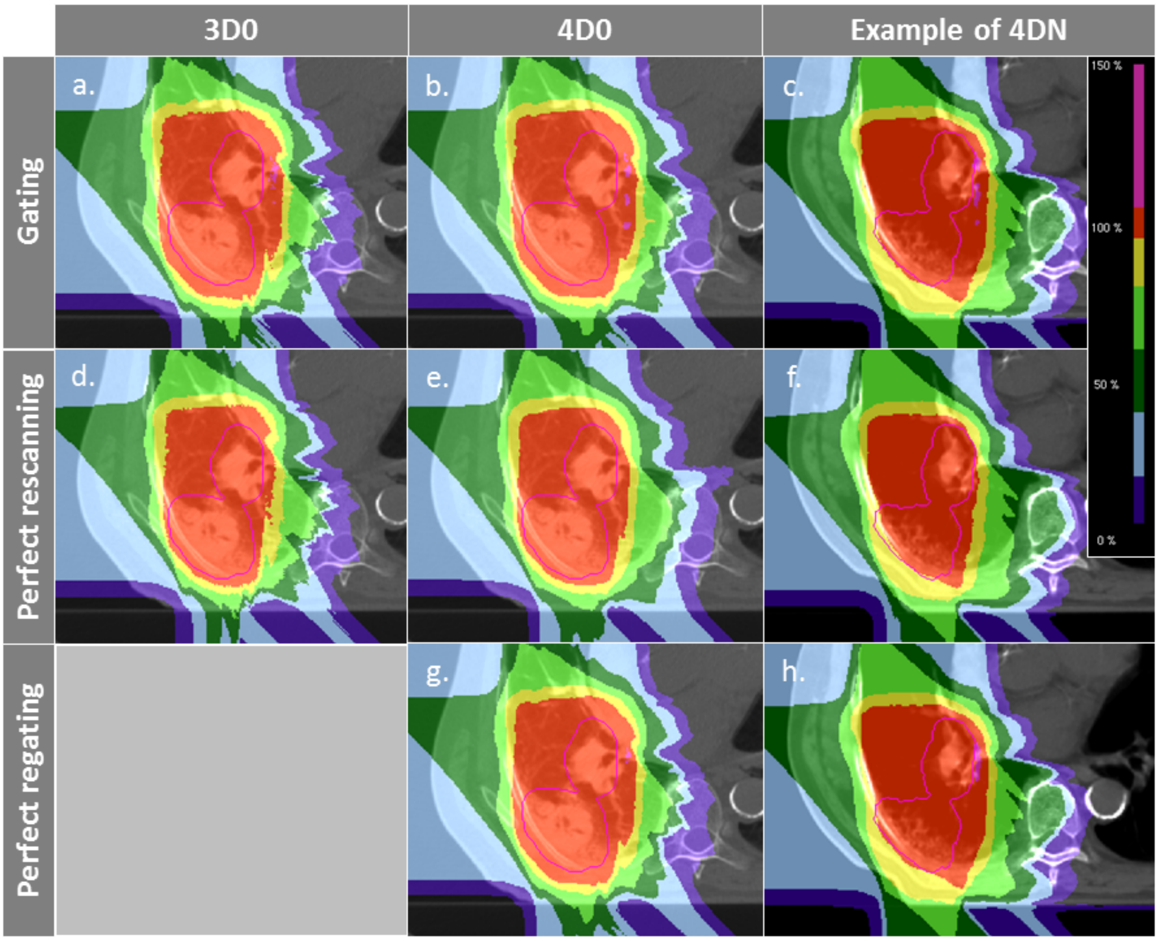

Figure 4.6.: Dose distributions obtained using different motion mitigation techniques. First line is composed of gating simulations, second line of rescanning simulation and third line of regating simulations. First column represents examples of 3D0 simulations, second column 4D0 simulations and third column 4DN simulations. 3D0 and 4D0 simulations were done using week 0 of patient 3 and 4DN week 6 of patient 3. Because the optimized plan was the same for gating and regating, the static simulation (3D0) was not repeated for regating. All displayed dose distributions used 15 mm as beam focus (FWHM).

Now, looking at the maximal point dose, using PRSC yields lower MXD values ($p < 0.05$) in the case of the heart and the ipsi- and contralateral lungs. The difference between the values obtained the two techniques in the cases of the esophagus and the spinal is not significant ($z < z_{critical}$). Figure 4.4 shows that PRGT results are very close to the ones obtained using gating. Thus the comparison of PRGT with PRSC is the same as the one explained in the gating/PRSC comparison, showing slightly better results for one technique or the other depending on which dose interval is observed.

Figure 4.6.d-f and 4.6.g-h show static (for PRSC) and 4D dose distributions obtained using the 1st and the 7th weekly CTs of patient 3 and PRSC and PRGT as motion mitigation techniques, respectively.

4.4 Discussion

In this chapter, relevant patient-4DCT datasets showing large tumor motion and/or small tumor size, representing 6 of the 9 patients in the series of 4DCTs, were used to investigate which motion mitigation technique among gating, perfect rescanning (PRSC) and perfect regating (PRGT) yielded the best results. While gating permits to study the effects of intrafractional motion and interplay on the dose delivery, PRSC and PRGT do not take into account interplay effects. Weekly treatment simulations were performed using optimized parameters found in the previous chapter, such as the width of the focus or PTV margins.

Looking at results obtained using gating, PRSC and PRGT, it is possible to estimate the effect of both interfractional changes and intrafractional motion on the quality of the tumor treatment given by each motion mitigation technique. Even though it is only partially feasible in the case of the PRSC and regating methods, due to the fact that interplay effects are not taken into account and the tumor motion is only simulated using the ten states of each 4DCT and three states for PRSC and PRGT, respectively, it permitted to do a first comparison.

Results show that, globally, the three motion mitigation techniques were able to compensate identically for tumor motion and anatomic changes from one fraction to the next one. Although significant trends could be observed, the amplitude of the differences between results obtained using different techniques was never large, as illustrated by their distributions on figure 4.2 and the DVHs on figure 4.4. Only the conformity number showed a significant and large difference, PRSC yielding higher values than gating and PRGT. This can be due to the fact that treatment plans used for gating and PRGT were optimized on an ITV composed of 5 motion states and that the 4D dose delivery was then performed using only a 11.9% GW (corresponding to 3 motion states). This can lead to dose delivery outside the target because the planned volume was too large. V_{95} and homogeneity, except for 4D0 simulations, behaved the exact same way for the three mitigation techniques. Even though gating plans were only optimized on ITVs composed of 5 motion states, static simulations yielded excellent results for all three methods with almost perfect V_{95} and good homogeneity for most of the cases (figure 4.2). Looking at the results obtained for 4D0 simulations using PRSC and PRGT, it is clearly visible that interplay effects were not taken into account when they are compared to the results obtained using gating. Despite the fact that V_{95} and homogeneity average values are quite satisfactory in all cases, it is possible to see the effects of intrafractional motion combined to interplay by looking at the minimal V_{95} value and the maximal homogeneity value obtained using gating, which were degraded compared to the corresponding extrema obtained using PRSC and PRGT (figure 4.2).

Now, 4DN simulations show that interfractional changes can have a huge impact on target coverage and homogeneity, potentially higher than intrafractional tumor motion and interplay. Discussing the choice of a rescanning method, Seco et al. (2009) stated that interplay effects are mainly responsible for non-systematic errors in dose distribution. However, looking at 4DN simulations on figure 4.2, although interplay effects are not taken into account in the cases of the PRSC and regating methods, the V_{95} minimal values and the homogeneity maximal values are drastically reduced and increased, respectively, like for gating, compared to 4D0 simulations. The impact on CN is also noticeable for all three techniques, 4DN simulations yielding larger distributions showing roughly the same maximal value but a lower minimal value than for 3D0 and 4D0 simulations. Sonke et al. (2008) also pointed out that, while intrafractional motion was quite stable from one fraction to another, large interfractional variability could be sometimes observed. Indeed, looking at the weekly and patient specific results in appendix E.2, weekly cases can be observed, which show lower V_{95} and CN, and higher homogeneity and which correspond to weekly CTs for which interfractional anatomic changes, such as organ drifts or tissue shifts, are present. Those weekly cases were already observed in the previous chapter using gating whose results are also displayed on figure 4.2. The latter shows that V_{95}, CN and homogeneity are affected the same way by interfractional changes, no matter whether PRSC and PRGT is used as alternative technique. Then, comparing the changes between the three motion mitigation techniques, the largest difference can be observed for CN whose values, as described and explained above in the case of 4D0 simulations, are again higher in the case of PRSC. Moreover, as 4DN simulations show V_{95} average values of 97% and 98% for gating and PRGT, respectively, and as intrafractional motion was already compensated efficiently using the parameters found in chapter 3, it can be assumed that interplay effects are the cause of the 1% difference. Therefore, using rescanning, which is particularly effective to compensate for these interplay effects (Rietzel and Bert, 2010), would not result in a significant improvement.

Concerning the irradiation of the OARs, the three mitigation techniques showed again similar results no matter whether one looks at the V_{20} or at the maximal point dose (figure 4.3). Some trends were identified but the amplitude of the differences between results was not large (figure 4.4). Thus, despite the fact that high dose regions may be a bit larger in the case of gating and PRGT, as previously shown by a lower CN, intermediate dose regions are roughly identical as well as maximal values. Because interplay effects are not taken into account in the rescanning and the regating processes used in this study, the similarity between the results obtained using gating, PRSC and PRGT shows that interplay does not impact severely the dose delivered to the OARs, at least when optimized treatment plan parameters are used.

Comparing gating, PRSC and PRGT showed that the three techniques globally yielded similar results, in terms of target coverage and organ irradiation, as shown by figure 4.6 on which no significant difference between the three techniques for static and 4D dose distributions can be observed. Even though some patient specific behaviors can be observed (figure 4.4 and appendix E.2), the differences are never large. Moreover, 4DN dose distributions displayed on figure 4.6 also permit to estimate the importance of interfractional anatomic changes by looking at the shape of the high-dose regions compared to the ones displayed on 4D0 dose distributions. This leads to think interfractional changes actually have a more important negative impact on treatment delivery than intrafractional tumor motion and interplay when a unique treatment plan is generated using the first weekly 4DCT.

To conclude this chapter, it has been shown that PRSC and PRGT do not allow a relevant improvement in the results compared to gating, no matter whether one looks at the dose delivered to the tumor or to the surrounding tissue. Moreover, it seemed that interplay had a much less significant impact on dose delivery than interfractional anatomic changes, which could be due to the fact that the intrafractional tumor motion amplitude is smaller than 5 mm for 6 patients out of 9. Thus, gating remains a better solution to mitigate motion using only one optimized plan over the whole course of the treatment.

Now, Hui et al. (2008) performed similar weekly simulations using a single treatment plan with protons and recommended to use adaptive replanning for cases showing large interfractional anatomic changes. A replanning factor based on the amplitude of interfractional variability could permit to decide, for each new fraction, whether a new treatment plan is needed or not. Also, using gating, it only remained to determine if some field angles could be found, for which interfractional range differences would be minimized, and if a replanning factor could be isolated, with which it would be possible to know, for each treatment fraction, if a new optimized plan was necessary. Then it was possible to simulate a clinical treatment for the 9 patients which were available. Therefore, the next and last chapter will focus on the search of optimized field angles and of a replanning factor, followed by this clinical treatment simulation relying on treatment schemes described by Miyamoto et al. (2003, 2007) and adapted for the number of available weekly CTs for each patient using the biological effective dose equation.

5 Simulation of a clinical optimized treatment scheme

5.1 Introduction

The two previous chapters permitted to isolate optimized parameters and to determine that gating allowed obtaining the best results compared to rescanning and regating processes for which interplay was not taken into account. The last chapter also showed that interfractional changes, such as patient misalignments or organ drifts, were responsible for major dose delivery deterioration, potentially more significant than negative effects caused by intrafractional motion or interplay. Besides, as described above, the two previous chapters aimed at studying the influence of treatment planning parameters or mitigation techniques on dose delivery, but only on a weekly basis with no clinical consideration.

Thus, knowing which parameters permit to compensate best for intrafractional motion as well as interfractional changes and which motion mitigation technique can realistically be used, it was decided to simulate a clinical study using the conclusions of the two previous chapters. Using a fractionation scheme corresponding to the number of weekly 4DCTs available for each one of them, patients of the cohort underwent a patient-specific treatment simulation. The final goal was to observe, at the end of the treatment, the total dose delivered to the tumor as well as to the organs at risk and the surrounding tissue.

To perform such a study, clinical information is needed, such as potential optimal field angles, treatment schemes and fractionation or organ dose limits. Some studies give details about different clinical treatment protocols performed for instance at NIRS or at Massachusetts General Hospital (MGH) (PTCOG; Miyamoto et al., 2003, 2007). Information about fractionation schemes, motion mitigation techniques, beam delivery systems or follow-up visits is detailed. However, information about patient setup such as gantry or couch angles is not available. Optimal patient setup is important, because it can allow better critical structures sparing in the patient's body and still obtain good treatment delivery. This is part of uncertainties and starting conditions while generating a treatment plan. Those have been studied (Lomax, 2008a,b; Albertini et al., 2010, 2011) and while effects of interfractional changes were addressed by Lomax (2008b), the possibility of using field angles more robust to interfractional variability was not suggested. Thus, it was decided to see if it was possible to isolate preferential field angles or directions, which would be less affected by interfractional variability while avoiding critical structures and which would then be used in the final clinical simulations. Interfractional changes, potentially responsible for large dose delivery errors, have also directly been studied (McClelland et al., 2011; Hui et al., 2008; Sonke et al., 2008) and it was shown that it can result in large differences causing themselves a negative impact on dose delivery. Using only one treatment plan for the entire course of treatment results indeed in severely deteriorated dose delivery for some fractions, as shown in chapter 3. The idea of a replanning factor was thus here investigated so that, just by comparing information about the planning week and the following ones, it could be decided to recalculate a new treatment plan if changes were too important. Such a factor could then also be used in the clinical simulations.

During a treatment, toxicity in the organs at risk (OARs), well described by Cox et al. (1995), should be avoided. To prevent reactions due to overdose in the OAR, dose limits were set for conventional radiotherapy treatments (Grimm et al., 2011; RTOG, 2014). But Grimm et al. (2011), by quoting a lot a different references, shows that very different values are used from one study to the other and, even though those values are accepted and are set by professional clinicians, Benedict et al. (2010) stated that they are mostly unvalidated. Nevertheless, some of those OAR dose limits, all coming from RTOG (2014), were used in this study to set organ constraints in the treatment plan optimization process.

Therefore, in this chapter, before the clinical simulation was performed, two brief studies aiming at isolating first a replanning factor and second optimal field directions were carried out. Then, using optimized parameters found in chapter 3 and gating, each patient 4DCT dataset was used to investigate the total dose distribution at the end of a fractionation personalized treatment.

5.2 Materials and methods

5.2.1 Patient cohort

The same dataset of 9 NSCLC lung tumor patients from MDACC (The University of Texas MD Anderson Cancer Center) (Britton et al., 2007) was used as in the last chapter (see chapter 3 for more details). Number of weeks, motion amplitude, angles for multiple fields calculations, planned doses per fraction and in total are listed in table 5.1.

5.2.2 Influence of the weekly range difference on target coverage

Chapter 3 permitted to find treatment planning optimized parameters in order to obtain satisfactory target coverage and chapter 4 confirmed gating was the best mitigation technique compared to the perfect rescanning and regating processes.

Table 5.1.: Description of the 9 NSCLC Patients from MDACC (see figure 5.1 for field angles illustration): patient number, number of weeks available, average motion amplitude, field angles for multiple fields calculations (SFUD1, 2 and 3), planned dose per fraction and in total. Dose fractionation schemes are detailed in the next section.

			Angles [degree]			Dose [Gy(RBE)]	
Patient	Weeks	Motion [mm]	SFUD1	SFUD2	SFUD3	per fraction	Total
1	8	3.4	130	180	250	8.6	68.8
2	6	8.6	0	40	310	10.3	61.8
3	9	10.1	90	280	320	8	72
4	8	3.3	180	225	270	8.6	68.8
5	10	4.1	0	50	270	7.4	74
6	8	1.8	0	50	300	8.6	68.8
7	7	1.6	140	180	270	9.3	65.1
8	8	4	90	180	270	8.6	68.8
9	6	23.5	90	140	230	10.3	61.8

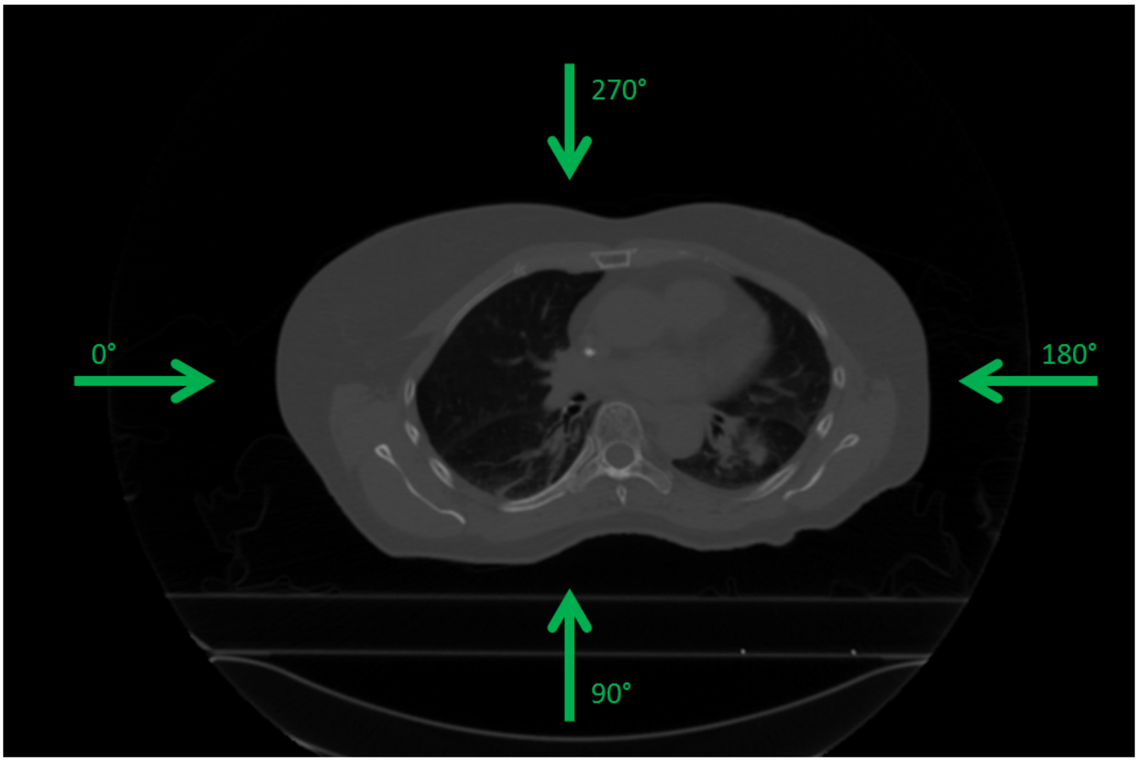

Figure 5.1.: Directions of the four main field angles. Values listed in table 5.1 can be visualized using those four main directions.

However, even when optimized parameters were used, some weekly cases showed deteriorated dose delivery due to interfractional changes resulting in range differences between the first week and the next ones. Thus, before carrying out the new simulations using appropriate treatment schemes, a brief study was performed in order to determine if, just by knowing the range difference between the planning week and the following fractions, it could be possible to predict the resulting target coverage. The latter being then known, it could be possible to decide if replanning would be necessary or not for the concerned fraction.

To isolate such a replanning factor, the target coverage difference between week 0 and week N single field calculations using ITV margins only (SFITV configuration in chapter 3) was computed. It was compared to the difference of the corresponding weekly water-equivalent tumor median ranges in the field direction (see field angles in table 5.1). Those ranges were indeed computed for each of the ten 4DCT motion states by calculating, for each voxel of the clinical target volume (CTV) located on the path the beam, its water-equivalent range and then finding the median value. The 3 foci and 3 GW used in chapter 3 were used and the range difference was computed for each of the 10 motion states of each weekly 4DCT.

5.2.3 Investigating field angles

Following the determination of a possible replanning factor using weekly water-equivalent tumor range differences, another brief study was performed in order to investigate if some field angles are less affected by interfractional changes.

For each of the 9 patients, the water-equivalent tumor median range difference between the planning week and the following ones was computed for 18 different gantry angles 10° apart from each other. This allowed covering the patient lateral tumor side, meaning the side corresponding to the tumor location. This was done for the reference phase of each weekly 4DCT and displayed on polar graphs (see appendix E.3), representing a total of 70 weekly polar distributions. The average weekly range difference was computed for each patient and displayed in a new polar graph to compare patient-specific results. Those were then analyzed to determine if general field directions can be isolated, which show minimal range differences.

5.2.4 Clinical simulations

To investigate the validity of the optimized parameters found in chapter 3 combined to gating in a clinical treatment, new simulations were carried out. Those optimized parameters consisted in a large focus (15mm, FWHM), a short gating window (GW, 11.9% of the motion amplitude), 3mm isotropic (geometrical) and 3%+3mm range (water-equivalent) margins and 3 fields. The same principle of one treatment plan applied to the following fractions was used, but appropriate treatment schemes, such as the planned dose, field angles or organ constraints were this time taken into account.

5.2.4.1 Treatment schemes

Miyamoto et al. (2003, 2007) reported results of treatment of NSCLC tumors at NIRS using carbon ion therapy. A total dose of 72 Gy(RBE) was delivered over 3 weeks in 9 fractions of 8 Gy(RBE) each. This scheme was used as a basis to calculate patient dedicated schemes in this study. To do so, the equivalent effective dose in 2 Gy(RBE) fractions ($ED_{2\mathrm{Gy(RBE)}}$) was computed using the following equation (IAEA, 2008).

$$ED_{2\mathrm{Gy(RBE)}} = \frac{D_{\mathrm{xGy(RBE)}}\left(x + \frac{\alpha}{\beta}\right)}{\left(2 + \frac{\alpha}{\beta}\right)} \tag{5.1}$$

where x corresponds to the desired dose per fraction and $D_{\mathrm{xGy(RBE)}}$ to the total dose over the whole treatment. The ratio α/β was set to 6 Gy, in accordance with RBE studies done at GSI, themselves using results coming from clinical studies in Marburg and in Japan (Kanai et al., 2006), even though the latest studies (Elsaesser and Scholz, 2007; Kase et al., 2008) used a value closer to 5 Gy. In the case of the fractionation scheme described above (9 fractions of 8 Gy(RBE), total dose of 72 Gy(RBE)), an equivalent dose ($ED_{2\mathrm{Gy(RBE)}}$) of 126 Gy(RBE) was found. Now, knowing the number of fractions per patient for this study (column 2 of table 5.1) and using $D_{\mathrm{xGy(RBE)}} = nx$ in equation 5.1 (n being the number of fractions), it was possible to determine the appropriate dose per fraction x for each patient so that $ED_{2\mathrm{Gy(RBE)}}$ was equal to 126 Gy(RBE) simply by resolving the following second degree polynomial (obtained from equation 5.1):

$$nx^2 + n\frac{\alpha}{\beta}x - ED_{2\mathrm{Gy(RBE)}}\left(2 + \frac{\alpha}{\beta}\right) = 0 \tag{5.2}$$

Taking the positive solution of the polynomial in equation 5.2 permitted to obtain the values listed in the seventh column of table 5.1 for each patient and then to calculate the total doses listed in column 8 by just multiplying the weekly dose by the number of weeks.

5.2.4.2 Optimization and 4D calculations

As in the two previous chapters, treatment plans were generated using the first weekly 4DCT of each patient using TRiP4D (Richter et al., 2013). Plans were optimized on a WEPL-ITV (Graeff et al., 2012) composed of 5 motion states CTVs, representing 25% of the motion amplitude. Parameters found as optimal in chapter 3 were used, meaning a focus of 15 mm (FWHM), a gating window corresponding to 11.9% of the amplitude, three fields (see table 5.1 for field angles) and a combination of isotropic (3mm geometrical) and range (3mm+3% water equivalent) margins.

For all simulations, the motion surrogate was defined according to Lujan et al. (1999), i.e. a sine square with a unique period of 3.6 seconds and 0 degree as starting phase. As explained in chapter 3, only one starting phase was studied because, due to gating, beam delivery for different starting phases is quickly synchronized after the first few spills of the synchrotron accelerator, thus calculations yield very similar results for different starting phases. As other fixed treatment parameters, the lateral distance between raster positions was set to 2 mm on each iso-energy slice (IES) and the distance between two IESs was set to 3 mm water-equivalent using a ripple-filter (RiFi) of 3 mm (Weber and Kraft, 1999).

In the case of the esophagus and the heart, organ constraints were also added to limit the maximal dose delivered to the OARs to 40% of the planned dose. This percentage used for each patient permitted to obtain at least a maximal dose in the OARs below or slightly above the corresponding maximal dose limits listed in table 5.3. This was the result of a trade-off between conformal target dose delivery and OAR sparing. The weight for each organ was set so that both the tumor and the organ would have equal weight in the optimization process of the treatment plan computation.

5.2.4.3 Calculation of the total dose

Computation of the total dose to investigate the quality of the whole treatment was done by using vector fields obtained from the deformable registration between the first week (used to generate the treatment plan) and each following one. Each weekly dose distribution obtained after the 4D calculations was deformed to match the anatomy of the planning 4DCT. They were then added to obtain the total treatment dose distribution (Janssens et al., 2009).

5.2.5 Data analysis

The dose distribution of each week was obtained by accumulating the dose delivered to each motion state on the reference phase of the 4DCT using state-to-state non-rigid vector fields. Then, the total dose was accumulated as described in the previous section. As in chapters 3 and 4, target coverage (V_{95}), overdose (V_{107}), homogeneity and the conformity index (CN) were investigated to estimate the quality of the dose delivery for the static calculations using the planning CT (3D0), 4D calculations using the planning 4DCT (4D0) and the following weekly 4DCTs (4DN) and the total treatment calculations (total) obtained by adding all deformed weekly dose cubes.

Table 5.2.: Organ volume/dose limits for a 5*10Gy(RBE) treatment scheme from RTOG (2014) adapted for each fractionation scheme. Adaptation of the values was done with an α/β ratio of 3 for the heart, the spinal cord and the lungs and 10 for the esophagus, corresponding to late- and early-responding tissues, respectively (Hall and Garcia, 2011). In the case of the spinal cord and the lungs, two different OAR limits were available, written here as 1 and 2.

		Dose for each number of fractions [Gy(RBE)]					
Organ	Volume [cc]	5 (RTOG, 2014)	6	7	8	9	10
Esophagus	<5	27.5	28.8	29.9	30.8	31.6	32.2
Heart	<15	32	34.4	36.6	38.5	40.3	41.9
Spinal cord 1	<0.25	22.5	24.1	25.4	26.7	27.7	28.7
Spinal cord 2	<0.5	13.5	14.3	15.0	15.6	16.1	16.5
Lung 1 (right & left)	1500	12.5	13.2	13.8	14.3	14.8	15.2
Lung 2 (right & left)	1000	13.5	14.3	15.0	15.6	16.1	16.5

To assess the dose delivered to the organs at risk and to see if it did not exceed limits leading to toxicity, critical and maximal values from Grimm et al. (2011) and RTOG (2014) were used which are listed in tables 5.2 and 5.3. Those are RTOG values which are used for 5*10 Gy(RBE) treatments and which were adapted for each fractionation scheme using the same method explained above with equations 5.1 and 5.2. Two different α/β ratios were used for the spinal cord, the heart and the lung, which are late-responding organs (with slow cellular proliferation), and the esophagus, which is an early-responding organ (due to mucosa composed of rapidly dividing cells), meaning α/β ratios of 3 and 10, respectively, as explained by Hall and Garcia (2011).

Table 5.3.: Organ maximal point doses (MXDs) for a 5*10Gy(RBE) treatment scheme from RTOG (2014) adapted for each fractionation scheme. Adaptation of the values was done with an α/β ratio of 3 for the heart, the spinal cord and the lungs and 10 for the esophagus, corresponding to late- and early-responding tissues, respectively (Hall and Garcia, 2011).

	MXD for each number of fractions [Gy(RBE)]					
Organ	5 (RTOG, 2014)	6	7	8	9	10
Esophagus	105% of total planned dose (see table 5.1)					
Heart	105% of total planned dose (see table 5.1)					
Spinal cord	30	32.2	34.2	36.0	37.6	39.1

Also, for some of the OARs such as the spinal cord and the lungs, 2 different dose limits were available (see tables 5.2 and 5.3). For columns 2 and 4 to 8 of table 5.2, dose limit values (columns 4 to 8) were compared to the dose delivered in the corresponding volume (column 2) of each organ. In RTOG (2014), the maximal point dose (see table 5.3) in the cases of the esophagus and the heart were originally 105% of the dose prescribed to the PTV (IMRT) but it was here applied as 105% of the planned dose in the CTV.

All simulations were performed on the weekly 4DCTs with a patient-specific planned dose (see table 5.1). The first two brief studies aimed at finding a replanning factor and field angles which were robust with respect to interfractional changes. In the final study, the quality of the dose delivery to the tumor was investigated for 3D0, 4D0 and 4DN calculations as well as for the total dose distributions. Comparison of the dose delivered to the OARs with organ dose limits were performed using the total dose distributions only.

5.3 Results

All simulations were performed on the weekly 4DCTs with a patient-specific planned dose (see table 5.1). The first two brief studies aimed at finding a replanning factor and field angles which were robust with respect to interfractional changes. In the final study, the quality of the dose delivery to the tumor was investigated for 3D0, 4D0 and 4DN calculations as well as for the total dose distributions. Comparison of the dose delivered to the OARs with organ dose limits were performed using the total dose distributions only.

5.3.1 Influence of the weekly range differences on target coverage

Figure 5.2 shows results obtained by comparing V_{95} differences between week 0 and week N as a function of the water-equivalent tumor median range difference between both weeks. It is possible to differentiate two behaviors corresponding to two range difference regions marked by the two black ellipses. The first one, composed of points having range differences going from 0 to about 6 mm, shows V_{95} differences comprised between 0 and 10%. The second one, composed of points having range differences going from about 6 to 14 mm, shows V_{95} values lower than 10%.

Two noticeable outliers can be observed having range differences of about 14 mm but showing only V_{95} differences of 5% and 7%. They were obtained using patient 6, which has the biggest tumor among the patients cohort. This patient showed no V_{95} difference below 9%, whether the range difference was only 1 or 14 mm.

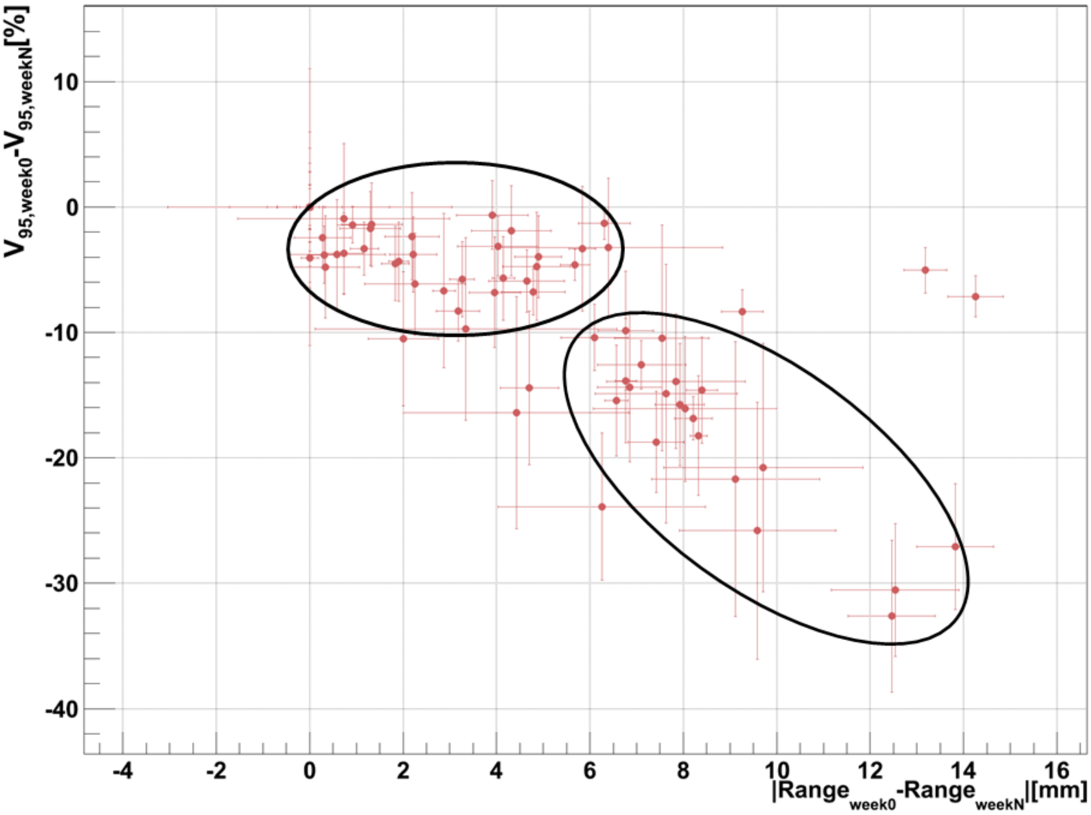

Figure 5.2.: Target coverage difference between the weeks 0 and N as a function of water-equivalent tumor median range difference (absolute value) between weeks 0 and N. Vertical bars show the standard deviation of the calculations using 3 foci and 3 GW, horizontal bars show the standard deviation of the water-equivalent tumor median range difference of each of the 10 motion states, the central point being the mean value for both of them. Two black ellipses indicate two noticeable behaviors whether the range difference is lower or larger than about 6 mm.

5.3.2 Investigation of robust field angles

Figure 5.3 permits to observe the average water-equivalent tumor median range differences between the planning week and the following ones (see patient-specific cases in appendix E.3. Differences were investigated for 18 field angles spread over 180°, covering all the field directions corresponding to the side of the patient (left or right) where the tumor is located.

Looking at each patient separately, it is possible to observe field angles for which ranges between week 0 and week N are similar or where the difference is lower than 3 mm. However, from one patient to the other, values for which the differences are low are not the same and, except the ventral side of the patient which shows in each case average interfractional differences lower than 5 mm, no particular direction can be isolated, which would be less sensitive to interfractional changes.

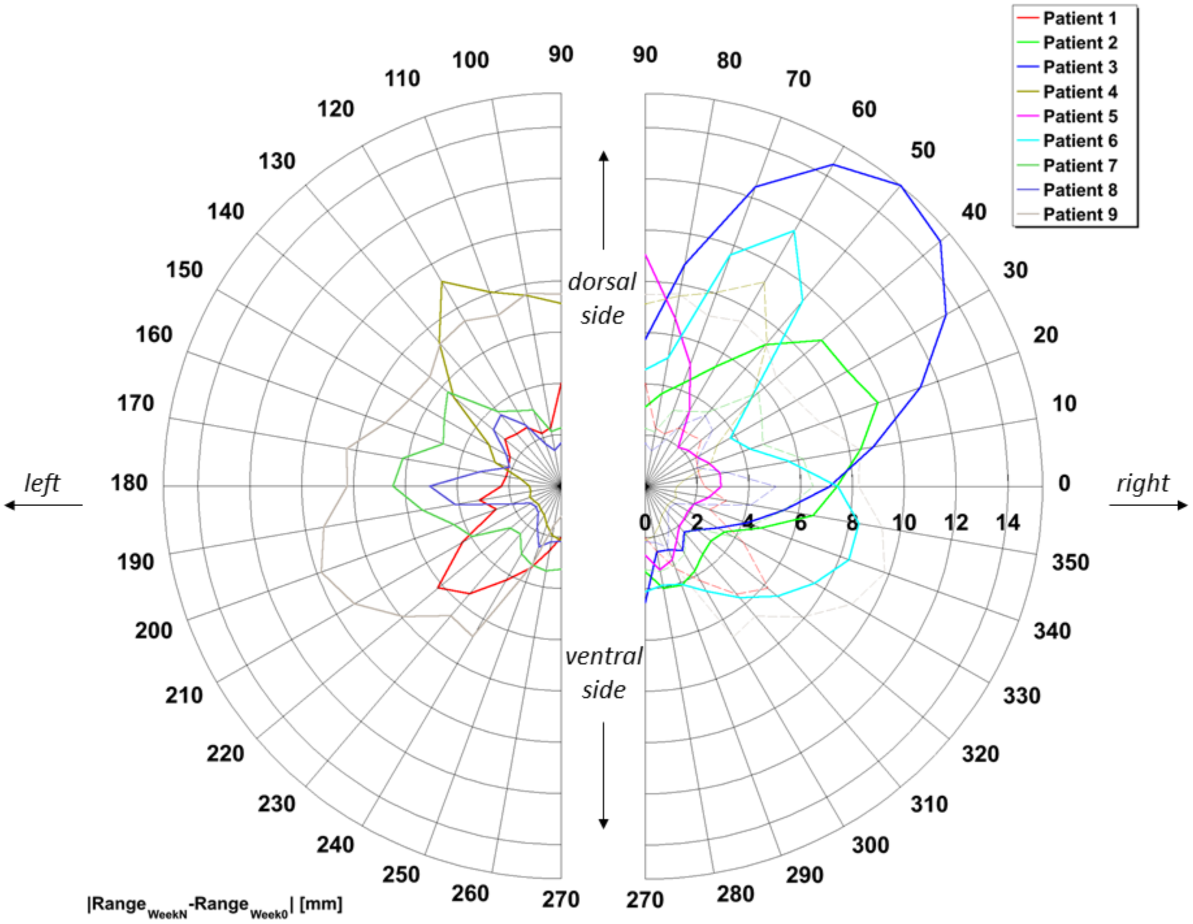

Figure 5.3.: Average water-equivalent tumor median range differences between weeks 0 and N for each patient and for 18 field angles covering 180° (10° apart from each other) of the side of the patient corresponding to the tumor location. Angle values are the same as angles displayed on figure 5.1: 90° corresponds here to the beam incidence from the dorsal side and 270° from the ventral side of the patient, curves obtained for tumors located on the left side were also mirrored and are displayed with dotted lines on the right side. See appendix E.3 for weekly details for each patient.

5.3.3 Simulation of a clinical study

Figure 5.4 shows the obtained V_{95}, V_{107}, homogeneity and CN for 3D0, 4D0 and 4DN calculations as well as for the total treatment dose cubes. Static simulations show average values of 95.8%, 1.5%, 8.7% and 0.59 in terms of target coverage, overdose, homogeneity and CN, respectively. Except for one patient, all V_{95} values are above 93% and all V_{107} values below 2.5%.

Looking at 4D0 calculations permits to see that results are similar to 3D0 calculations, as illustrated by similar average values: 95.7%, 1.6%, 8.8% and 0.58 in terms of V_{95}, V_{107}, homogeneity and CN, respectively. Extrema are also similar.

4DN calculations show some difference compared to the two previous ones. V_{95} and homogeneity are deteriorated, as shown by their mean values which drop to 93.4% and increase to 10.%, respectively. There is also deterioration of the minimum of the V_{95} distribution and the maximum of the homogeneity distribution which drops to less than 70% for 4DN calculations, compared to about 87% in the 3D0 and 4D0 cases, and increases to about 30% for 4DN calculations, compared to 19% in the 3D0 and 4D0 cases. Distribution of CN is larger than in the 3D0 and 4D0 cases and the average value is slightly lower at 0.56.

Finally, total dose distributions yield average V_{95} and homogeneity of 94.3% and 8.3%. Overdose is lower than in the other cases, as illustrated by a mean value of 0.7% and a maximal value also lower than in the other cases. CN shows a mean value of 0.52 and a distribution similar to the one obtained with 4DN simulations.

Now, looking at figure 5.6, it is possible to see if dose limits in each organ at risk were respected or not. Regarding dose/volume limits (see table 5.2 and middle values of figure 5.6), dose limits are respected for all patients only for the first limit of the lung (1500cc/12.5Gy(RBE) in RTOG (2014)). For most of the patients, dose limits concerning the spinal cord (1 and 2) and the second lung dose limit (1000cc/13.5Gy(RBE) in RTOG (2014)) are respected but, for two patients, the first spinal cord limit is exceeded by about 3 Gy(RBE) and 16 Gy(RBE) and the second spinal cord limit by about 11.5 Gy(RBE) and 24.5 Gy(RBE) and for another patient, the second lung dose limit is exceeded by about 5 Gy(RBE). In the case of the esophagus and for 5 patients, the dose delivered to the dose-limit corresponding volume is lower than the limit while, for 4 patients, the dose limit is exceeded, sometimes by more than 27 Gy(RBE). Results obtained for the heart show 3 patients for which the limit is exceeded, one showing more than 25 Gy(RBE) above the limit.

Concerning the maximal point dose, values on the right of figure 5.6 show the difference between the maximal values found in each OAR and the limits listed in table 5.3. As no maximal OAR dose limit was found in the case of the lung, it was not possible to do any calculations. In the cases of the esophagus and the heart, all values from the total dose distributions are below the maximal dose limits, except one value in each case which is very slightly higher (0.005 Gy(RBE) for the esophagus, 0.3 Gy(RBE) for the heart). Regarding the spinal cord, most of the maximal point dose values are also below the limit but, for 2 patients, the limit is exceeded by 1.5 Gy(RBE) and 11 Gy(RBE).

As an example of 3D0 (static simulations using the planning CT), 4D0 (4D simulations using the planning 4DCT) and 4DN (4D simulations using the following weekly 4DCTs) simulations and to show a resulting total treatment distribution, figure 5.5 shows dose distributions obtained with patient 2.

On figure 5.6, it can be observed that the minimal total dose requirement prescribed by ICRU (2007) ($V_{95,\mathrm{ICRU}} = 95\%$) is respected (green crosses) for cases showing a target coverage above 95% for 3D0 simulations already (static simulations done using the planning CT). All cases

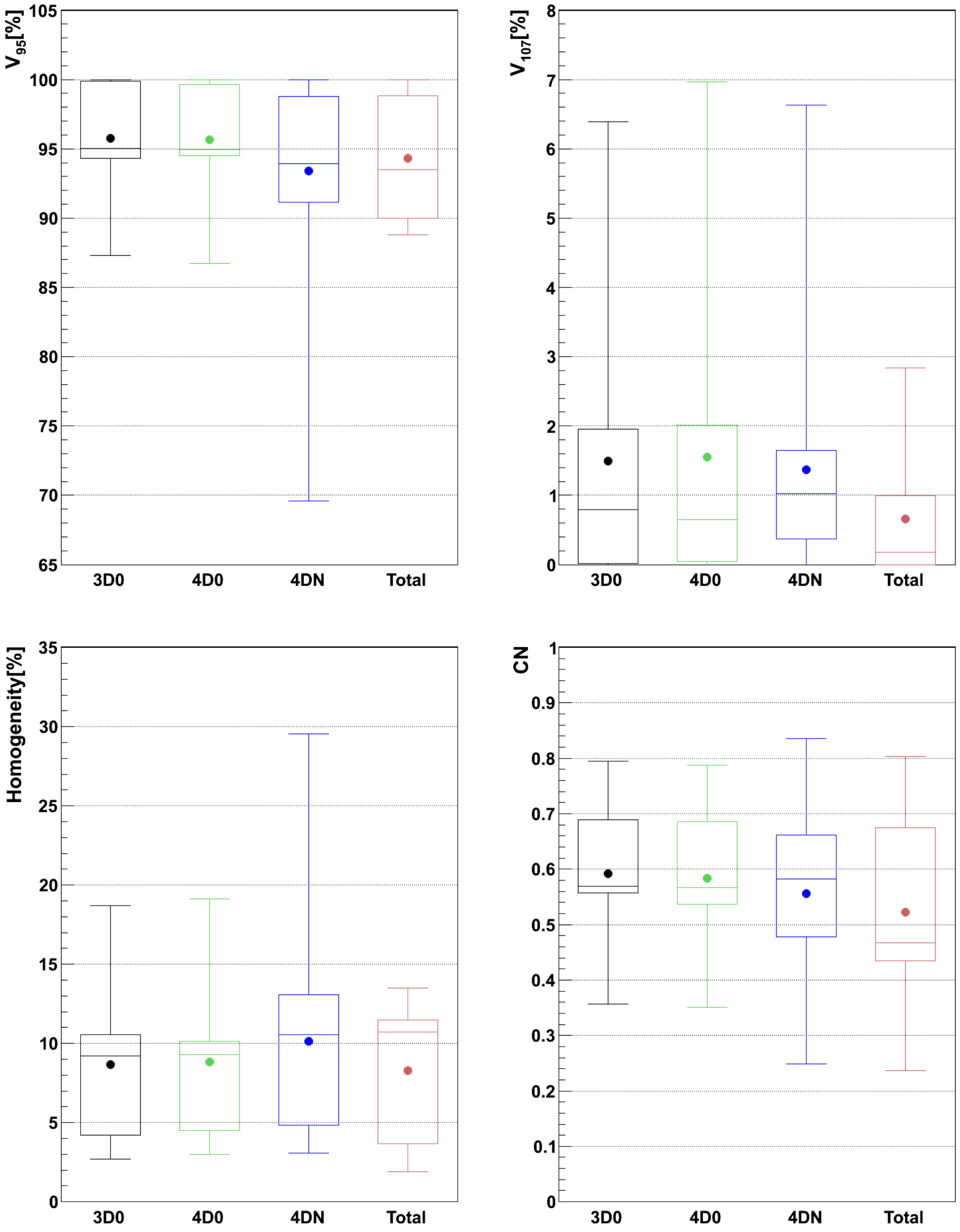

Figure 5.4.: Target coverage (V_{95}), overdose (V_{107}), homogeneity and conformity number (CN) obtained for 3D0, 4D0 and 4DN calculations as well as for the total treatment. The average value (marker), the median value (horizontal bar in the box), the 25th and 75th percentile and the total range of all values are given. 3D0, 4D0 and Total box and whisker plots are composed of 9 points and 4DN ones of 61 points.

which show a $V_{95,\mathrm{Total}}$ below the ICRU requirement (red crosses) also show a V_{95} around or below 95% for 3D0 simulations. Moreover, even though most of the OAR dose limits from RTOG (2014) are respected in the case of patients showing a $V_{95,\mathrm{Total}}$ above 95%, the dose delivered to the esophagus and the heart exceeds the limits for two and one of them, respectively, despite the organ constraints.

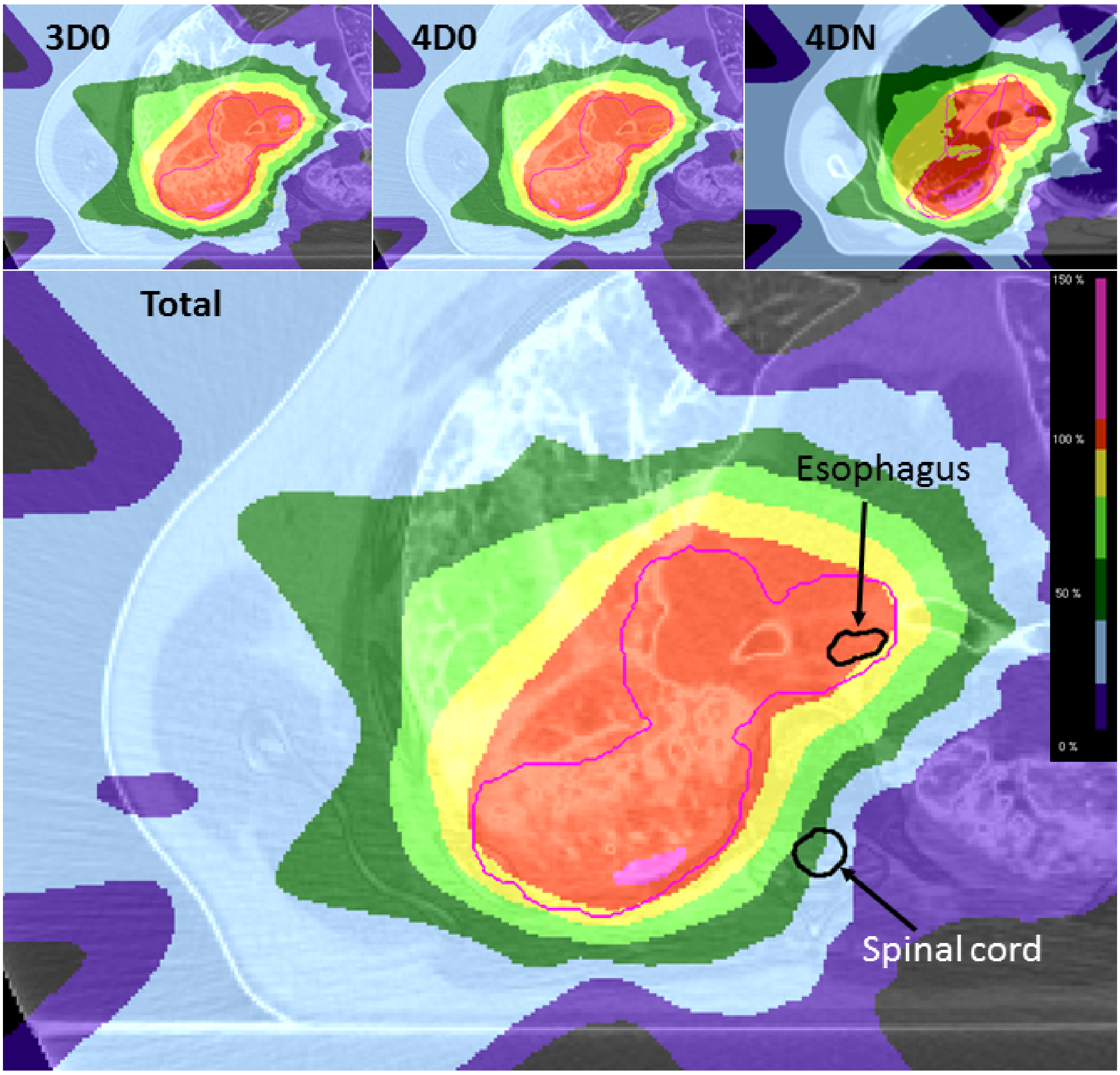

Figure 5.5.: Dose distributions obtained for patient 2. The 3D0 distribution was obtained with a static calculation using the first weekly 4DCT (week 0), the 4D0 and the 4DN distributions were obtained with 4D calculations using week 0 and week 4 of patient 2, respectively, and the "Total" distribution was obtained by adding all the weekly deformed dose distributions and represents the total dose delivered during the treatment. The pink contour is the CTV, the esophagus and the spinal cord are visible on the total dose distribution.

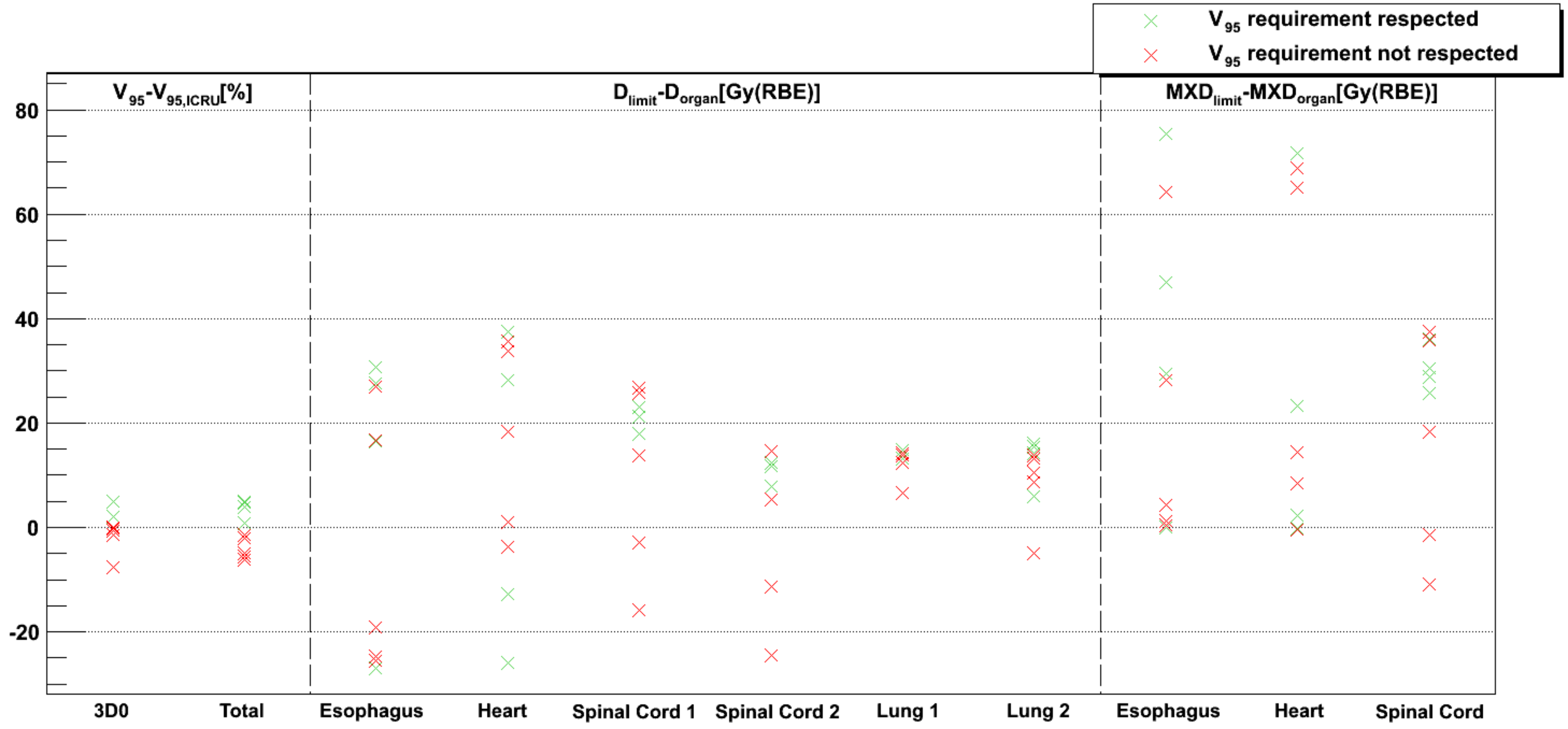

Figure 5.6.: 3D0 and "Total" V_{95} results of the 9 patients subtracted to the ICRU requirement ($V_{95,\text{ICRU}} = 95\%$) and differences between the dose/volume values and the corresponding dose limits from (RTOG, 2014) (see tables 5.2 and 5.3). Green crosses represents patients for which $V_{95,\text{Total}} > 95\%$ and red crosses patients for which $V_{95,\text{Total}} < 95\%$. Postive values indicate that requirements (for both V_{95} and OAR dose limits) are respected and negative values indicate underdose in the tumor ($V_{95} < 95\%$) and overdose in the OARs.

5.4 Discussion

5.4.1 Influence of the range differences on target coverage

Target coverage differences between weeks 0 and N showed two different behaviors corresponding to range difference values lower or higher than about 6 mm, as shown on figure 5.2. So it means that, just by analyzing a new weekly 4DCT, it would be possible to calculate the median range of the tumor, then compute the difference with the range of the tumor on the planning CT and have an estimation of the resulting target coverage. Obtaining less than 6 mm as range difference would mean that the target coverage is not likely to be reduced by more than 10%, while, by obtaining a value higher than 6 mm, one may risk to obtain severely deteriorated target coverage. Then, it could be decided to set a 6 mm range difference threshold as a replanning factor, so that if the range difference would be larger than 6mm, one would not risk to obtain a target coverage approximately 10% lower than the one obtained on the first week.

However, this would only be optimal for single field calculations for a very low amount of fractions. Indeed, by using more fields, if one field had more than a 6 mm range difference, it would be balanced by the two other ones and it would actually affect only one third of the planned dose, which would then be 10% lower than expected. Thus the total dose delivered per fraction would actually be only one 30th lower. Also if several fractions are used for the treatment, this already small negative effect would be counterbalanced again by the fractionation principle.

Therefore, the idea of a replanning factor based on interfractional range changes is not optimal when a multiple fields plan is used in a treatment composed of several fractions. This is why it was decided not to use one in this study.

5.4.2 Investigation of robust field angles

Results showed that, apart from the ventral side of the patient, no particular field angle could be isolated, which is more robust to interfractional changes than others for all patients. Consequently, that field angles have to be chosen specifically for each patient.

Now, even though each patient shows optimal angles (see appendix E.3) with almost no range differences between the planning week and the following ones, it would not have been realistic to choose field angles according to a graph showing range differences from week 0 to N. Indeed, the treatment plan is generated using the first 4DCT, so that, at that time, no information about the following weeks is available. Moreover, the optimal angles shown on the weekly graphs of appendix E.3 may not be the safest solutions regarding the organs at risk. Looking at the beam incidence for those angles, it crosses some critical structures such as the heart or, due to range uncertainties caused by intrafractional motion and interfractional changes, may be responsible for dose delivery to organs located in the vicinity of the tumor.

Also, using more fields can logically permit to divide the dose delivery by only delivering a fraction of the planned dose for each chosen field direction but the choice of field angles has to be done carefully, or the following negative effect might be observed: it is indeed possible that one field angle yielding good results for one week may be responsible for huge dose delivery errors for a following fraction if the patient's anatomy changes or if there is any misplacement. Thus, using more fields permits to distribute the dose over a number of entrance channels but at the same time increases the volume in the vicinity of the tumor which might be affected by dose delivery errors due to range changes. This could be the cause of unexpected OAR irradiation leading to toxicity.

Therefore, field angles listed in table 5.1 were chosen based on the first weekly 4DCT also used to generate the treatment plan so that, for each direction, the beam would avoid organs at risk (or minimize the volume of organs) directly on its path or distal of the tumor in the same direction. For each patient, the three field directions were also set so that their overlap was minimal in order to avoid high dose in the surrounding tissue and organs.

5.4.3 Simulation of a clinical study

Results obtained in this chapter for the 3D0, 4D0 and 4DN regarding the dose delivery to the tumor were deteriorated compared to those obtained in the previous chapter using gating even though the same optimized parameters were used. This can be explained easily by the fact that organ constraints were here taken into account which aimed at limiting the dose delivered to the critical structures, in this case the esophagus and the heart. Because most of the tumors were located at a reasonable distance from the spinal cord or because it was easy to choose field directions which would avoid it, no constraints were used regarding this OAR. Figure 5.6 shows that, except for two patients, the spinal cord did indeed not need any particular attention. Dose distributions obtained for one of this patient are displayed on figure 5.5. Looking at the position of the spinal cord and the esophagus relative to the total dose distribution, one can observe that they are located within the CTV. This was not the only case showing such kind of configuration, for which the CTV was contoured ignoring the nearby OARs. This was the case for the esophagus for almost half of the patients and this is very well illustrated on figure 5.6, on which it can be observed that, for a non-negligible percentage of patients (5 out of 9), a very high dose exceeding the dose limit is delivered to this organ which is known to be particularly sensitive to irradiation. This was due to the fact that the esophagus, or at least a part of it, was actually located inside the CTV. Also, using 40% of the planned dose as maximal allowed dose in the esophagus and the heart permitted, for each patient, to have a trade-off between target and OAR dose delivery. A higher value would have deteriorated the tumor dose coverage and lower value would have allowed more dose in the critical structures. However, as displayed on figure 5.6, it can be observed that OAR constraints used for the esophagus and the heart were not effective for two of the cases showing a $V_{95,\text{Total}}$ above 95% (two green crosses below 0 in the case of the heart and the green cross below 0 in the case of the esophagus), which means the optimization process could not spare the OARs efficiently. For the case showing overdose in the esophagus, it is due to the fact the esophagus is located deep inside the CTV, which leads to the unefficiency of the 40% dose constraint and, for the two cases showing overdose in the heart, the latter is not entirely surrounded by the tumor but still by a non-negligible part of it, which causes median dose (30-40 Gy(RBE)) delivery in a large volume of the organ.

Now, regarding the OAR dose limits themselves, the chosen RTOG dose limits are normally used for a 5*10 Gy(RBE) treatment, which corresponds to a $ED_{2\text{Gy(RBE)}}$ of 100 Gy(RBE) (using equation 5.1) and which is lower than the 126 Gy(RBE) obtained from the chosen treatment scheme from Miyamoto et al. (2003, 2007). It means that the chosen organ dose limits might be slightly too low. However, adapting the treatment scheme used by Miyamoto et al. (2003, 2007) for a 5 fractions treatment (using equation 5.2), a dose of 11.5 Gy(RBE) is obtained for each fraction, which is only 1.5 Gy(RBE) above the RTOG treatment example. Thus, that and the fact Benedict et al. (2010) stated that dose limits are "mostly unvalidated" and that "while most are based on toxicity observation and theory, there is a measure of educational guessing involved as well", the chosen organ dose limits can be considered legitimate even though slightly overestimated in the sense that they are too strict. In the case of the heart and the esophagus, although some maximal point doses obtained using the OAR constraint (40% of the planned dose) were slightly higher than the maximal dose allowed by RTOG (2014), it can be once again counterbalanced by the fact that those should be used for a 5*10 Gy(RBE)-based treatment compared to the 9*8 Gy(RBE)-based treatment used in this study showing a higher $ED_{2\text{Gy(RBE)}}$. Now, some of the organ dose results obtained in this study exceed limits by more than 20 Gy(RBE), and having slightly higher dose limits (corresponding to the 9*8Gy(RBE)-based treatment scheme chosen in this study) would not change the situation in those cases. But, looking at OAR dose limits coming from other studies than RTOG (2014) in Grimm et al. (2011), it could be observed that some of them were higher than the ones chosen here: up to 52.5 Gy(RBE) for both the esophagus and the heart compared to the 27.5 Gy(RBE) and 32 Gy(RBE) from RTOG (2014), respectively. Assuming α/β ratios are similar, most of the cases exceeding the dose limits from RTOG (2014) would then respect these higher ones.

With respect to target dose coverage, it can be noticed that, indeed, static simulations yield deteriorated results compared to the ones obtained in the previous chapter. The reason has been explained above and, even by trying different field combinations, results did not improve or improved only slightly. As explained above, to avoid to deliver more dose to the OARs (by allowing stricter dose constraints, meaning that more dose could have been delivered to the OARs), it was decided to keep the dose constraints as they were initially set (40% of the planned dose) because the resulting target coverage (V_{95}) was not lower than 90% for most of the cases.

Then, looking at 4DN calculations on figure 5.4 and 5.5, it is again obvious that interfractional changes play a large role in fractionated treatments when they are compared to 4D0 results. Baseline shift using 4D-CBCT, as proposed by Sonke et al. (2008), might allow compensating for interfractional geometric organ shifts or tissue drifts as their study also showed that the tumor trajectory was stable from one fraction to another, but not for the possible induced range changes or for tumor shrinkage resulting in more dose in the surrounding normal tissue. Hui et al. (2008) recommended using replanning to obtain satisfactory weekly dose delivery in the case of large interfractional anatomic changes. In this chapter, although a few V_{95} values are below 70%, most of the results were only slightly deteriorated compared to the 4D simulations done using the planning 4DCT (4D0 simulations). So the conclusion of chapter 3, concerning the capability of optimized parameters to compensate efficiently for both intrafractional motion and interfractional changes, applies here as well, despite the fact static results were deteriorated. Moreover, looking at the total dose delivery, the effects of fractionation can be observed: it permitted to counterbalance weeks for which dose delivery was unsatisfactory so that, finally, only a few patients showed V_{95} lower than 90% and, in general, the “Total” dose delivery was only slightly deteriorated compared to the results obtained from the static calculations. In ICRU (2007), a possibility of dose constraints is to obtain V_{95} within a “-5% and +7% of the planned dose” interval. This was obtained for 4 out of the 9 available patients (see detailed results for patients 1, 3, 8 and 9 in appendix E.3) and, as displayed on figure 5.6, it can be noticed that those patients are the same patients who showed a V_{95} above 95% for the 3D0 calculations. Therefore, using gating and the optimized parameters found in chapter 3 permits to ensure a conformal “Total” target dose coverage if the 3D0 one is itself above 95%. Nevertheless, three other patients showed a V_{95} between 90 and 95% and the two last ones a V_{95} slightly below 90% (5 red crosses on figure 5.6) and, when looking at the 3D0 results on figure 5.6, it can be observed that those patients show also results below or around 95%. Thus, while dividing the dose delivery into several fractions appeared to be another way of compensating efficiently for interfractional changes, final dose delivery of some patients did not fulfill ICRU (2007) dose criterions. More importantly, the result of the static simulations using the planning CT already permits to have an idea whether the total target dose delivery is going to be conformal or not.

Nevertheless, figure 5.5 illustrates quite well how difficult it is to plan knowing only the anatomy on the planning week and using this treatment plan for all the following fractions. For different rescanning configurations and for unique simulations (no successive weekly calculations), Knopf et al. (2011) tested several field combinations but there was no particular advantage of one compared to the others. In this study, only patient 8 could be considered as a perfect case with a small tumor showing an average motion of 4 mm and located at a large distance from any critical structure so that the three fields could be chosen orthogonal to each other (see table 5.1), allowing thus reducing high dose regions in the ipsilateral lung while still not affecting any OAR. For this patient, final total target coverage of about 100% was obtained.

For all other patients, even though field directions were chosen carefully using the planning 4DCT to minimize the dose in the surrounding tissue and organs, the tumor was so close to at least one of them that nothing, apart from using organ dose constraints, could be done to avoid to cross the mentioned critical structure. Moreover, some patients, for which satisfactory OAR irradiation was obtained on the first week, showed large interfractional changes from one week to the other, leading to more dose delivered to the OARs than initially expected during the following fractions.

To conclude this section, even though weekly dose delivery to the tumor was decreased due to the proximity of OARs, using optimized parameters combined to the gating motion mitigation technique permitted to obtain satisfactory target coverage, overdose and homogeneity for 4 patients according to some of the ICRU (2007) constraints, the 5 other ones showing results slightly below those constraints. It was also observed that patients showing satisfactory dose target coverage for static simulations are likely to show conformal total treatement dose delivery as well. For most of the OARs, dose limits were respected but, in some cases, they were exceeded mostly due to the fact the concerned OAR was located inside the CTV, close to it or in the direction of one of the fields impacted by range changes caused by interfractional changes.

6 Discussion

In this dissertation, the GSI in-house treatment planning system (TPS) was used and, for each patient, all weekly simulations were done using a single treatment plan based on the planning CT and generated for the whole treatment. The first goal of this study was to optimize treatment planning parameters to obtain satisfactory target dose coverage for successive weekly fractions, using gating as motion mitigation technique. Then, results obtained using gating and two other motion mitigation techniques were compared to determine if target dose conformity could be further improved. Finally, the simulation of a clinical study using treatment schemes and OAR dose limits from clinical reports was performed and dose delivery to the target and the organs at risk OARs was investigated. Several effects had to be compensated, such as intrafractional motion (Seppenwoolde et al., 2002; Mori et al., 2007; Shirato et al., 2004), interfractional variability (Sonke et al., 2008; Mori et al., 2009; Britton et al., 2007) and interplay effects (Bert et al., 2008). Intrafractional motion and interplay effects have already been widely studied in the case of particle therapy (Bert and Durante, 2011), but interfractional variability and its effect on dose delivery have not been estimated extensively for the entire course of a treatment using particle therapy because available complete 4DCT datasets covering several weeks of treatment are rare. In photon therapy, interfractional changes do not have the same impact as in particle therapy, because photons are much less sensitive to changes in the radiological path length. However, because of tumor shrinkage during the treatment, it might still be necessary to re-optimize treatment plans to spare normal tissue (Britton et al., 2007). Some studies for photon radiotherapy have shown that interfractional variations can be up to 10 times larger than tumor intrafractional motion (Nøttrup et al., 2007) and that some of the used motion mitigation techniques, such as abdominal compression, can actually increase interfractional changes (Mampuya et al., 2013). All this shows that interfractional variability, combined with intrafractional motion in the case of lung tumors and motion-induced interplay, is a serious issue. This study shows that, for unproblematic cases, it can be compensated using optimized parameters and patient-specific entry channels.

Bert et al. (2009), Richter (2012) and Steidl (2011) investigated the impact of the beam focus and the raster point spacing on the delivered dose for irradiation of moving tumors in treatment planning studies and in experiments. Bert et al. (2009) concluded that increasing the overlap between the pencil beams, obtained either by increasing the beam focus or by decreasing the raster point spacing, permitted to obtain improved dose homogeneity. Richter (2012) and Steidl (2011) both confirmed that the use of a large focus could to some extent compensate for deterioration of target coverage and homogeneity caused by intrafractional motion and interplay effects. The same impact of the focus on dose delivery was observed here. But while those previous studies concentrated on intrafractional motion and single field treatments only, this work also has investigated the impact of interfractional variability applying an optimized treatment plan to a number of of 4DCT datasets each corresponding to one treatment fraction. While a larger focus can improve dose coverage in the presence of intrafractional motion and interplay effects, no additional benefit has been found with respect to mitigation of interfractional changes. The reason for this is that the observed interfractional motion was mainly governed by large geometric and range changes leading to under dose in the tumor and dose deposition in normal tissues. Mitigation of interfractional changes could be more efficiently achieved by using ITV-PTV margins which compensate for organ shifts or tissue drifts and range changes by extending the irradiated volume. So, not only do the margins, combined to a mitigation technique such as gating or rescanning, permit to compensate for intrafractional motion (Albertini et al., 2011; Knopf et al., 2013), but they can also drastically improve results for cases showing large interfractional changes. Obviously, the disadvantage is that more dose is delivered to the surrounding normal tissue. Now, in this work, it was also shown that multiple fields can be used to spread the delivered dose over several entry channels and avoid high dose areas around the tumor while leading to more conformal dose delivery to the tumor, in agreement with Knopf et al. (2011). But, despite the use of multiple treatment fields, using ITV-PTV margins can still lead to doses exceeding organ dose limits, as described in chapter 5 and further discussed later in this chapter.

Considering the influence of the gating window (GW), it could be observed that the GW had a larger influence on dose delivery using the single ITV (SITV) configuration described in appendix C, 4D simulations showing the largest V_{95} for the shortest GW and smallest V_{95} for the longest GW. Using the appropriate ITV (AITV) configuration (also described in C), the longest GW yielded better results and the shortest GW worse results, and it resulted in similar V_{95} for the 3 GWs (see appendix C). Deciding to use the SITV configuration yielded better results using the shortest GW, due to the fact that generating a treatment plan using 5 motion states and delivering the 4D gating plan on only 3 motion states already formed an additional margin. This had the same impact as ITV-PTV margins, which compensates more efficiently for interfractional motion but also leads to a larger irradiated volume of normal tissue, as previously explained. However, in spite of the larger impact of the GW for the SITV configuration, the GW still showed a smaller influence on dose delivery than the width of the focus. This demonstrates again that using a large focus is one of the key elements to obtain better target coverage and better homogeneity.

Then, although gating yielded satisfactory results in terms of target coverage and homogeneity, a comparison with rescanning and regating processes ignoring interplay effects referred to as perfect rescanning (PRSC) and perfect regating (PRGT) (both described in chapter 4), respectively, was performed. By again using only one treatment plan, results showed that the three techniques yielded similar results for the dose to the tumor and the OAR. The results obtained using techniques taking into account and ignoring interplay effects were similar, due the fact that the intrafractional tumor motion amplitude was smaller than 5 mm for 6 out of the 9 available patients. This lead to think that those effects, even though they can themselves be the source of dose conformity deterioration (Bert et al., 2008), have a minor impact on dose delivery compared to interfractional variability. The latter is indeed responsible for severe dose delivery errors, due to the high range sensibility of ions. And as shown by Nøttrup et al. (2007), its amplitude is also potentially much larger than the one of intrafractional motion.

Furukawa et al. (2007, 2010) at NIRS and Seco et al. (2009) at MGH have implemented techniques combining gating and rescanning called phase-control rescanning (PCR) and breath-sampling rescanning (BSR). Using BSR, Seco et al. (2009) showed that it is possible to obtain minimal dose delivery errors within a short treatment time. Since fractionation and multiple irradiations of the target permit to reduce interplay effects (Phillips et al., 1992) and since the principle of gating is to deliver treatment during the most stable phase of the tumor motion, combining these two techniques is potentially one of the most promising motion management solutions available nowadays to treat moving tumors using scanned ion beam therapy. Mori et al. (2013a,b) obtained similarly results using PCR. It is important to note that the studies using both PCR and BSR have taken into account the full temporal structure of the beam delivery, therefore modeling the interplay effect. However, in the study presented in this work, PRGT and rescanning both neglect the interplay effect and try to approximate the result of PCR and BSR by a priori distributing dose contributions equally over all motion states. However, in the presented study PRGT did not show an improvement compared to gating. The differences between this study and the study from Seco et al. (2009) can be explained by the fact that in this work interfractional changes and intrafractional motion were considered for most of the 4D simulations (simulations using weekly 4DCTs following the planning week), Seco et al. (2009) tested BSR using simulations considering intrafractional motion only. Furthermore they performed single field calculations with a 5 mm beam spot for a simple parallelepiped-shaped target, i.e. a very simplified geometry with no surrounding structures. While their results demonstrate the feasibility of the technique in a simplified setup, the robustness of this technique with respect to interfractional anatomy changes has not been demonstrated yet.

To perform the final study in the last chapter, OAR dose constraints were used, which were taken from RTOG (2014). Grimm et al. (2011) presented a large overview of the OAR dose constraints currently available in the literature and used in IMRT treatments. Depending on the source, these constraints are very variable and at least some of them are unvalidated, as described by Benedict et al. (2010). In general, higher constraints could be found for a larger number of fractions. The patient-specific fractionation schemes used in chapter 5 were derived from a treatment scheme described in Miyamoto et al. (2003, 2007) but no OAR constraints were associated with the protocols reported in these clinical reports and the dose delivered to the OARs was only investigated through early and late effects follow-ups. Even though Grimm et al. (2011) assembled a large amount of data from different studies, the data was available for IMRT treatments only using 6 or less fractions. Dose limits from RTOG (2014) were adapted to each fractionation scheme but there is still some uncertainty in the OAR constraints used in this work. The general tendencies observed here with respect to OAR exposure and dose conformity, however, can be expected to be independent of the precise OAR limits used.

As the previously discussed organ constraints were used in the framework of a simulated clinical study, using optimized parameters previously presented permitted to obtain satisfactory target coverage and OAR sparing (except two cases showing overdose in the heart and the esophagus) for four patients according to target dose constraints from ICRU (2007), while the five other cases showed some slight underdosage in the tumor and exceeded OAR dose limits. This emphasizes the difficulty of using only one treatment plan prior to the entire course of the treatment in the case of patients showing large intrafractional motion sometimes combined to interfractional changes and a tumor located in the vicinity of OARs. The aspect of replanning has been discussed in chapter 5. Hui et al. (2008) recommend using adaptive replanning for cases showing large interfractional anatomy changes. But in this study, due the use of several fields which permit to distribute the dose delivery over several directions and which therefore reduce the potential dose delivery errors, it was assumed that computing a new treatment plan would not result in a large improvement. It was indeed observed that interfractional variability did not impact all three field directions, but only one in general. Thus, using replanning would only improve the situation for the concerned field direction and for only one fraction, meaning a target coverage maximal improvement of one third of the weekly planned dose and, hence, only a small fraction of the total planned dose. Also, because of fractionation, one weekly unsatisfactory dose delivery can be counterbalanced by the other ones. So, unproblematic cases showing small motion, a tumor located distant from any critical structure or, on the contrary, an OAR located deep within the CTV (leading to the unefficiency of organ dose constraints) permitted to obtain good results with V_{95} above 95% (even 100% in one case). But, for some other patients with complex anatomy and tumor location, V_{95} below 90% and exceeded OAR dose limits could have either questioned the choice of treating the patient using scanned ion beam therapy or possibly lead to replanning to avoid too much overdose in the OARs during the treatment.

Field angle choices could obviously be improved on an individual basis by experienced physicians or by implementing an optimization algorithm which would aim at generating a treatment plan using fields minimizing the dose delivered to the OARs and maximizing the tumor dose delivery. Besides, the number of fields may also be optimzed: some cases in this study showed satisfactory target coverage (see chapter 3) and homogeneity using only two fields. Two optimized entrance channels might then be capable of yielding good treatment delivery while reducing the volume surrounding the tumor in which dose is delivered. Knopf et al. (2011)

tested several field configurations to irradiate liver tumors (the liver being located just below the lungs and the diaphragm) but no optimal direction was found. Here, only the ventral side of the patient showed average interfractional range changes below 5 mm for all patients. According to the influence of interfractional range changes on target coverage described in chapter 5, this would lead to an estimated maximal 10% decrease in V_{95} for single field calculations. But using several fields would reduce this value, as explained above, making the anteroposterior (AP) direction a potential good field choice. However, the anatomy of the patient and the tumor location also has to be taken into account, meaning that an OAR could actually be present on the path of the beam consequently invalidating the previous choice. Once again, this demonstrates the complexity of treatment planning, because a parameter set to optimize to a specific criterion might be the cause of deterioration of another criterion.

Finally, as briefly mentioned above, one of the advantages of BSR (Seco et al., 2009) is its capability to deliver conformal dose in a very short time of a few minutes. Treatment duration is indeed an element that should be considered in the search for an optimal dose delivery. For multiple reasons, patients cannot stay a long time on the couch and it is better to deliver the treatment as fast as possible. Indeed, even though the patient is partly immobilized, a short treatment time reduces the probability of anatomic changes or small patient motion occurring during beam delivery. One purpose of this study was to test the feasibility of using only one treatment plan for the entire course of the treatment instead of using a replanning strategy. Being able to avoid replanning will keep the global treatment time low. Even though GPU-based treatment planning has been investigated and permits to decrease plan optimization times by a factor of 20 to 40 for IMRT, as shown by Men et al. (2009), it is still far from being clinically used, because the GPU-based treatment plans need firstly to be compared with regular treatment plans for validation and also because it requires large hardware and software upgrades.

7 Conclusion

In this dissertation, using the GSI in-house 4D treatment planning system TRiP4D and a cohort of patient time-resolved computed tomography (4DCT) datasets for lung tumor patients, 4D gating simulations using scanned ion beam therapy have been performed.

In the first study (chapter 3), which aimed at finding optimized treatment planning parameters in order to compensate for dose delivery deterioration caused by intrafractional tumor motion, that is interplay effects and interfractional variability, it was found that the use of a large focus (15 mm, FWHM), a short gating window (11.9% of the motion amplitude), additional ITV-PTV margins (3mm isotropic + 3%+3mm range margins) and 3 fields yielded the best results in terms of target dose coverage (average $V_{95} = 96.9\%$). Using this configuration, intrafractional motion was efficiently compensated. However, due to the additional margins, more dose was delivered to the surrounding normal tissue.

In chapter 4, results obtained using perfect rescanning (PRSC) and perfect regating (PRGT) (both ignoring interplay) were compared to those obtained using gating but did not yield an improvement. Results in terms of target coverage were indeed very close: 97% for gating, 96.2% for PRSC and 98% for PRGT, meaning that interplay effects did not have a large impact on dose delivery and that these effects and intrafractional tumor motion were already efficiently compensated using gating. The remaining influence of interfractional organ motion on the delivered dose was similar for all three studied techniques. Thus, using gating, the final study aimed at estimating the potential influence of interfractional motion on the total dose delivered to the tumor and the organs at risk (OARs) during the treatment and at determining if it could be mitigated.

Two first brief studies in chapter 5 showed that a replanning factor would not yield an additional advantage due to the use of multiple fields which spread the dose over several entrance channels and that, apart from the ventral side of the patient, no robust field direction could be isolated. Finally, the simulation of a clinical treatment course using gating and the optimized parameters previously found in chapter 3 permitted to demonstrate that the total V_{95} obtained over the entire course of the treatment was similar to the one obtained for the planning CT, meaning that interfractional variability was efficiently compensated. Therefore, for 4 patients out of the 9 available, which showed a V_{95} above for the planning CT, it was possible to obtain $V_{95} > 95\%$ as well for the total target dose coverage. For the 5 other cases, modifying slightly the contours or reducing the planned dose should also lead to an acceptable clinical plan that could effectively be delivered over the course of the treatment in spite of interfractional changes.

A Comparison of different rigid registration methods for 4DCT alignment

A.1 Introduction

Using Plastimatch (Shackleford et al., 2010), soft tissue rigid registration is the method which was used in this study to align weekly 4DCTs so that the same coordinates could be used from one week or fraction to another. It showed successful results and permitted to yield aligned CTs in most of the cases. However, it seemed to partly fail for one weekly 4DCT, causing misalignments leading to non-conformal dose delivery. The idea was then to align CTs using only the bony anatomy and not the complete range of Hounsfield units present in the datacube, and to investigate the impact on the obtained results in terms of target coverage, overdosage, homogeneity and conformity number.

A.2 Materials and methods

A.2.1 Patient data

4DCT datasets from 2 NSCLC lung tumor patients from MDACC (Britton et al., 2007) were used to investigate the difference between soft tissue and bony anatomy registration. Patients 3 and 9 described in chapter 3, composed of 9 and 6 weekly 4DCTs and having an average tumor motion of 10.1 mm and 23.5 mm, respectively, were chosen among the available patients. Week 9 of patient 3 is the week for which soft tissue rigid registration failed to create vector fields able to align correctly the CTs.

A.2.2 Soft tissue rigid registration as CT alignment method

The method used to align weekly 4DCTs in this thesis is described in the blue steps on figure A.1. It is based on soft tissue rigid registration, meaning the whole CTs undergo rigid registration.

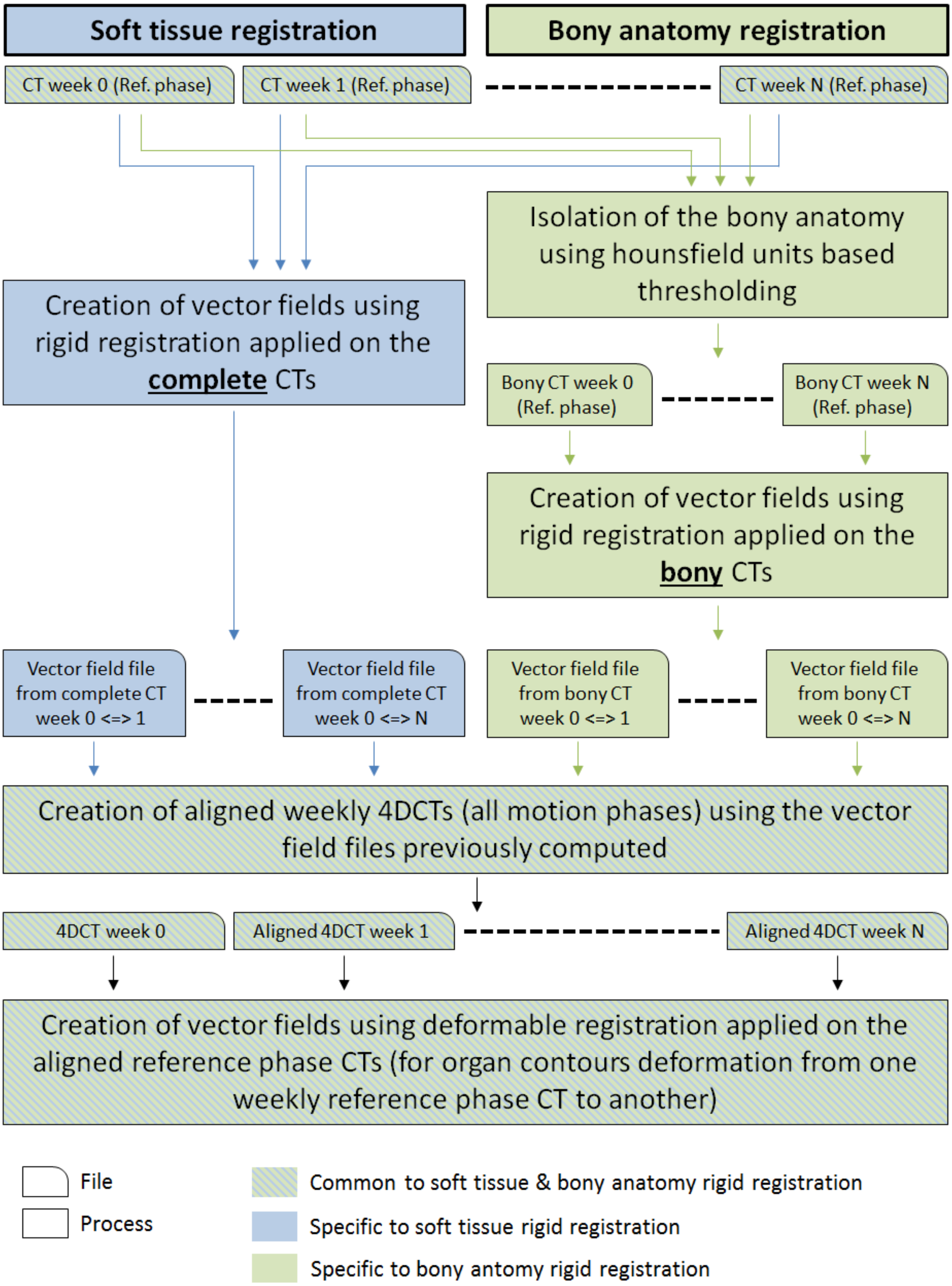

Figure A.1.: Description of the two different rigid registrations used to align weekly CTs. Blue steps are soft tissue rigid registration specific, green steps are bony anatomy rigid registration specific, striped steps are common to the two methods.

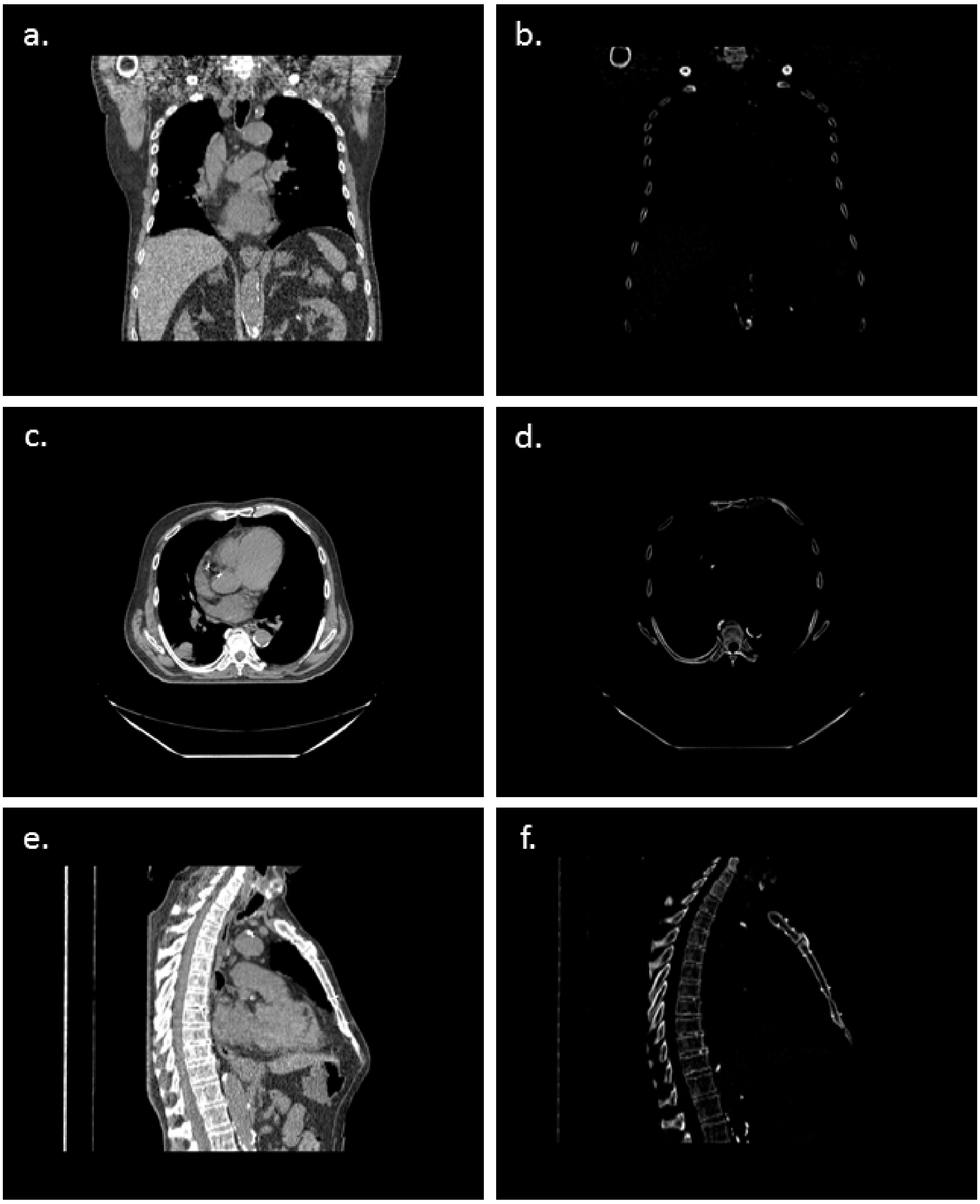

Figure A.2.: CTs before (images on the left) and after (images on the right) Hounsfield units based thresholding. Antero-posterior (AP) view is displayed on a and b, superior-inferior (SI) view is displayed on c and d and left-right (LR) view is displayed on e and f.

Reference phases of each weekly 4DCT are thus used to create vector fields between week 0 and the following weeks. Using those, all phases of each weekly 4DCT can be aligned rigidly to the corresponding ones of the first week. Afterwards, using the reference phase of the new aligned CTs, it is possible to perform non-rigid registration to obtain a new deformable vector field which is used to propagate the organ contour from one week to another. Deformable registration between reference phase and the 9 other phases of each 4DCT is then done to create the deformable vector fields necessary to the 4D treatment calculations.

A.2.3 Bony anatomy rigid registration as CT alignment method

Investigated as comparison here, rigid registration using only the bony anatomy is presented in the green steps of figure A.1. The principle is similar, except only the bony anatomy present in the CT is used instead of the whole datacube. It means that, before vector fields are created, low and high Hounsfield units' (HU) thresholds are used on each reference phase CT and only values between 100 and 1000 are selected. An example of a resulting CT can be seen on figure A.2. Only then, using this time the "bony" CT, vector fields are generated using rigid registration between reference phases of week 0 and the following weekly 4DCTs. Finally, the obtained vector fields are used to align all the phases of the complete 4DCTs (entire datacubes). The following (organ contour propagation and non-rigid vector fields between each 4DCT phase) is similar to the previous paragraph.

A.2.4 Data analysis

The dose distribution of each week was obtained by accumulating the dose delivered to each motion state on the reference phase of the 4DCT using state-to-state non-rigid vector fields. V_{95}, V_{107}, homogeneity and CN were analyzed to investigate the differences between the two types of registration. A Wilcoxon signed-rank test (W) was performed using a level of significance of 0.05 to estimate the difference between two sets of datapoints. As the samples contain more than 10 values, the p-value (p) was computed using the obtained z-score (z).

A.3 Results

V_{95}, V_{107}, homogeneity and CN are quite similar, no matter whether soft tissue or bony anatomy rigid registration was used. Some significant trends ($p < 0.05$) can be pointed out, such as better V_{95} and CN and higher V_{107} when bony anatomy registration is used, but the amplitude of the changes are small (see figure A.3). Apart from all the similar weeks, for weeks 4 and 9, homogeneity was not computable (D_{95} level was not reached) for simulations done using CTs aligned with bony anatomy rigid registration and soft tissue rigid registration, respectively.

Also, weeks 9 and 12 show a large difference between the two cases, with a mean V_{95} which is almost 17% higher in the case of bony anatomy registration for the first example and a mean homogeneity and a mean V_{95} which are 32% and 9% worse, respectively, also in the case of bony anatomy rigid registration for the second one.

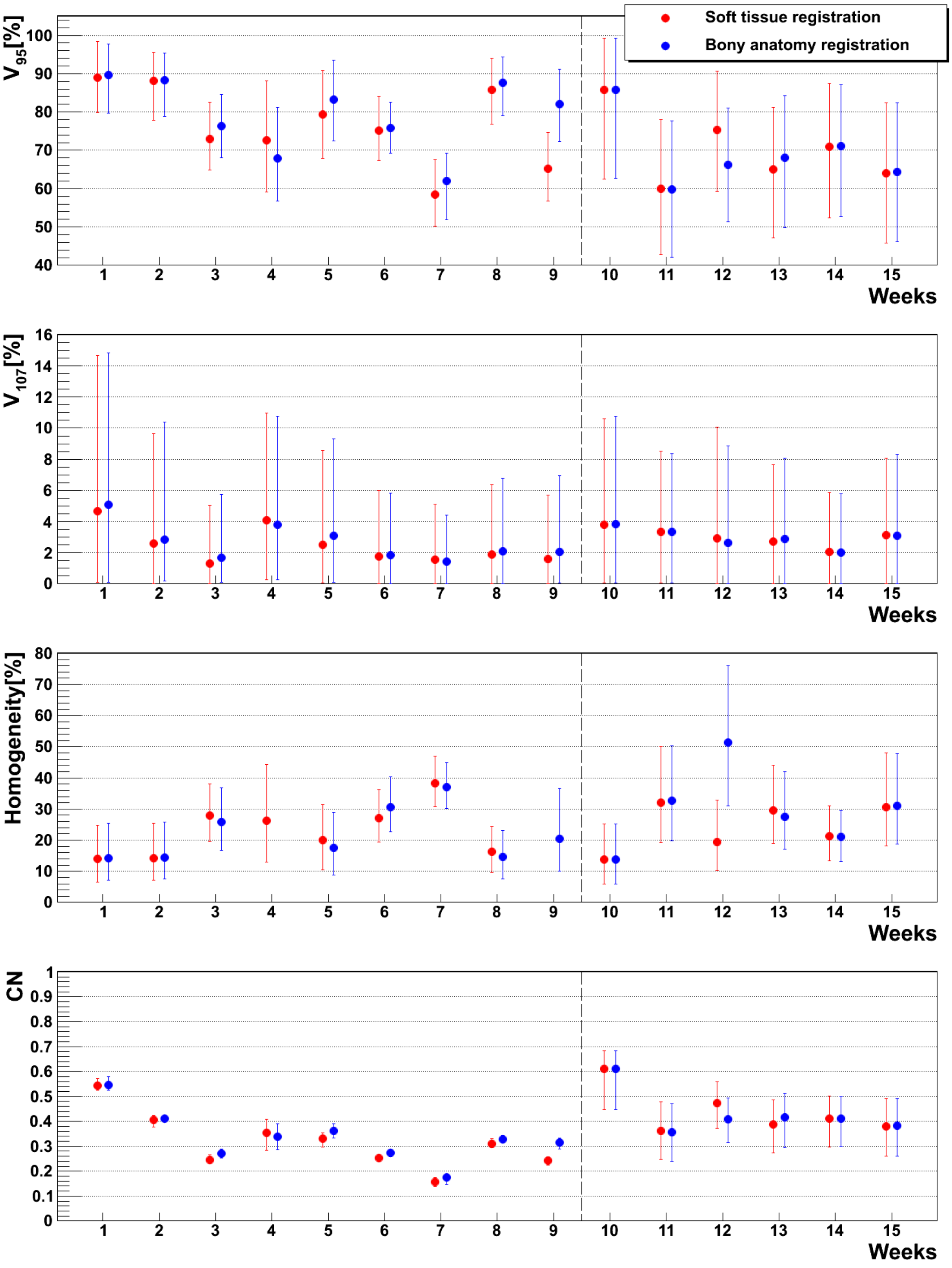

Figure A.3.: Results obtained using soft tissue (red) and bony anatomy (blue) rigid registration as weekly 4DCT alignment method. Each bar shows 4D simulations which were performed using the 9 combinations possible using 3 different beam foci (6, 10 and 15 mm, FWHM) and 3 different GWs (11.9, 30 and 50% of the motion amplitude) for each week of patients 3 (weeks 1 to 9) and 9 (weeks 10 to 15). Bars represent the distribution from minimum to maximum and the markers correspond to the mean values.

A.4 Discussion and conclusion

Using bony anatomy rigid registration to align weekly 4DCTs did not show large differences with results obtained using soft tissue rigid registration in general, as shown by the very low difference between V_{95}, V_{107}, homogeneity and CN. It did permit to improve significantly the results in terms of V_{95} for week 9 of patient 3, which was the week that soft tissue rigid registration had failed to align correctly. However, looking at the patient 3 and its third week, the opposite effect could be observed. It means bony anatomy rigid registration could maybe be performed in the case soft tissue rigid registration fails to align CTs, but there is yet no reason to replace it completely and use only the bony anatomy in the first place. This is why this comparison has been done with only two patients and why aligned 4DCTs obtained using soft tissue rigid registration have been used in this thesis.

B Lung contours extraction from 4DCT datasets

B.1 Introduction

Because the goal of this thesis is to obtain conformal dose delivery to lung moving tumors while respecting the organ at risk (OAR) dose limits, it was necessary to have the important OAR contours to observe their irradiation during treatment. However, although contours of the heart, the spinal cord or the esophagus were provided with the 4DCT datasets, lung contours were not. Thus, an algorithm had to be implemented in order to extract them from the reference phase of each 4DCT.

B.2 Materials and methods

B.2.1 Patient data

A total of 70 weekly 4DCTs from 9 NSCLC lung tumor patients from MDACC (Britton et al., 2007) were used in this thesis, as described in chapter 3. For each weekly 4DCT, although different tumor and organ contours such as the clinical target volume (CTV) or the heart, respectively, were provided by physicians, the lung contours had to be extracted to investigate the dose received in different treatment configurations.

B.2.2 Lung contour extraction algorithm

Even though the aim was to implement a common algorithm to be used with all 4DCTs, some patient-specific parameters had to be used. For one patient, one additional step had to be implemented as well. First step consisted in simple low and high Hounsfield units (HU) threshold combined to volumetric selection (step 1 on Figure B.1). Table B.1 shows patient-specific threshold values that were used as low and high thresholds.

Table B.1.: Thresholds used to isolate lung tissue [HU] in the first step and minimal volumes [voxels] used to identify lungs in the fifth step.

Patient	Lower threshold	Higher threshold	Minimal volume
1	-900	-650	30,000
2	-850	-400	30,000
3	-900	-600	50,000
4	-850	-400	30,000
5	-925	-500	500,000
6	-900	-500	100,000
7	-900	-500	100,000
8	-950	-700	100,000
9	-800	-450	100,000

However, even though lung tissue voxels were isolated, some parts of the couch as well as some other organ tissue whose values were comprised in the thresholding window were selected as well, meaning an additional step had to be performed. Volumetric selection was then implemented by using a 2D-Gaussian (equation B.1) on each CT-slice and selecting voxels comprised in the area where values were higher than 5.5.

$$2DG = 10 \times exp\left(-\frac{(x-x_0)^2}{2\sigma_x} - \frac{(y-y_0)^2}{2\sigma_y}\right) \tag{B.1}$$

where x_0 and y_0 are the coordinates of the center of the CT slice and $\sigma_x = x_0/2$ and $\sigma_y = y_0/2$. After those two first steps, the original CT cube was transformed into a binary cube containing lung tissue, but also other residual structures (limited due to the volumetric selection, see result of step 1 on figure B.1).

Combining dilating and eroding then permitted to remove the air cavities in the lung such as bronchioles and alveoli. The principle of dilating is, if a voxel binary value is equal to 0 (representing air), to set it to 1 if the distance to the nearest lung voxel is less than a given length (3 mm in this study). Eroding is the opposite: if a lung voxel is closer than a given length (3 mm again) to an air voxel, it is then set to 0. The dilating/eroding combination was done two times in a row (step 2 on figure B.1), followed by two other successive eroding steps (step 3 on figure B.1).

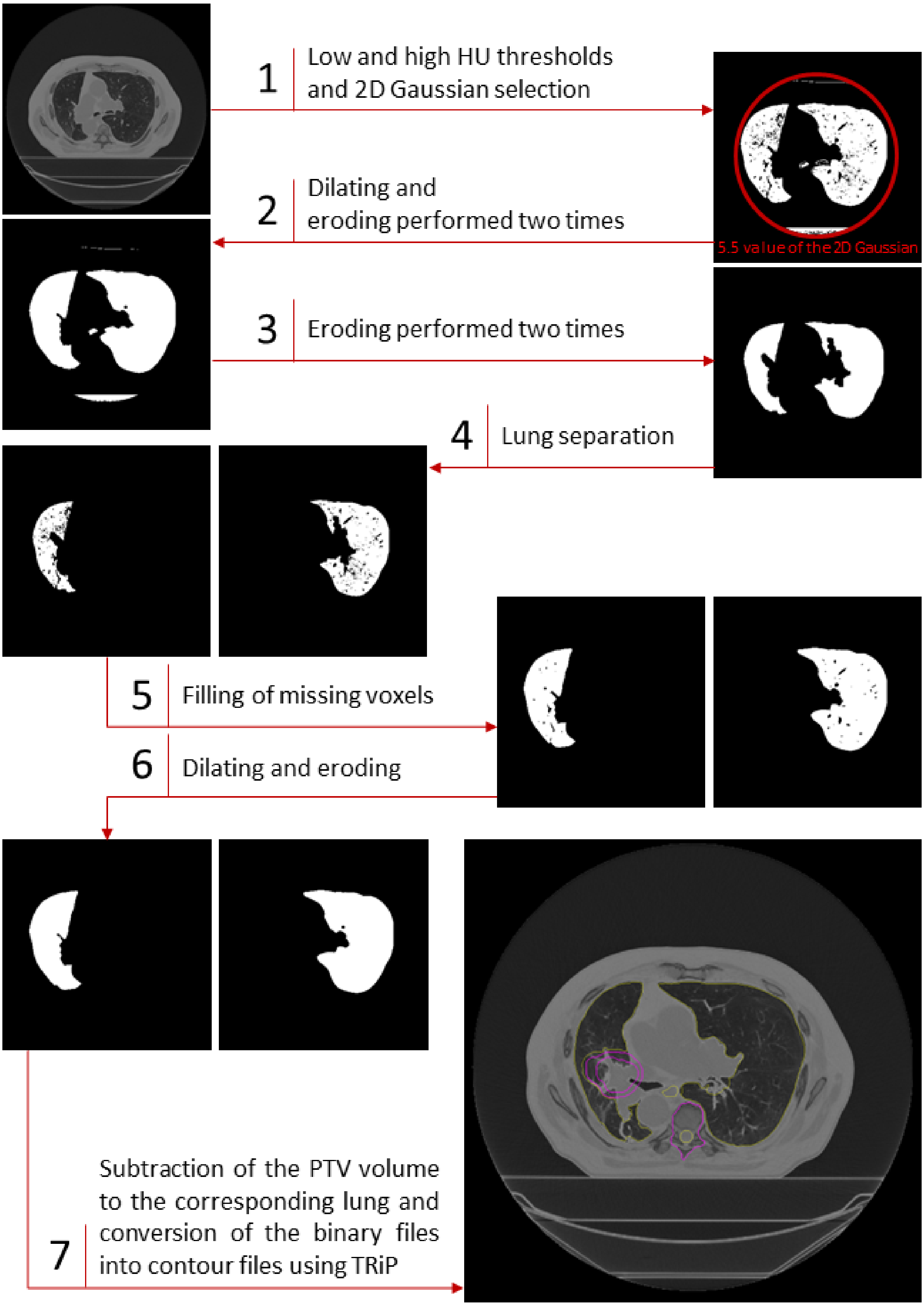

Figure B.1.: Description of the two different rigid registrations used to align weekly CTs. Blue steps are soft tissue rigid registration specific, green steps are bony anatomy rigid registration specific, striped steps are common to the two methods.

Those aimed at reducing the lung volumes enough (especially in the region located in the front of the chest where the two lungs almost touch each other) so that the two lungs can be separated in order to yield two different contours files containing the left and the right lung. It also permitted to remove the residual undesired structures such as the couch (see result of step 3 on figure B.1). That is why, for all patients but patient 3 (particular case described later in this section), lung separation and isolation was done automatically using those two eroding steps and size thresholds (see Table B.1 and step 4 on figure B.1) to ignore the undesired structures remaining in the binary cube, if the two eroding steps did not make them disappear, resulting in two binary files containing the left lung for one and the right lung for the other.

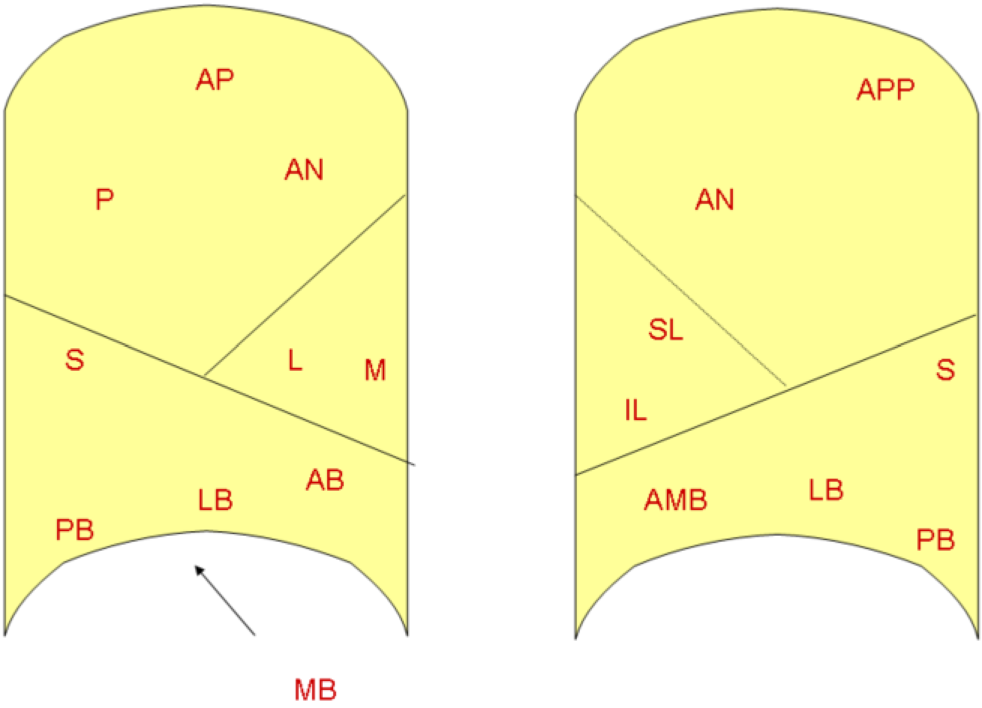

Figure B.2.: Diagram of the lungs representing the different lobes and segments, from Wikipedia. In the right lung (here on the left), the apical (AP), the posterior (P) and the anterior (AN) segments compose the superior lobe, the lateral (L) and the medial (M) segments the middle lobe and the superior (S), the medial-basal (MB), the anterior-basal (AB), the lateral-basal (LB) and the posterior-basal (PB) segments the inferior lobe. In the left lung (here on the right), the apico-posterior (APP) and the anterior (AN) segments compose the superior lobe, the inferior-lingular (IL) and superior-lingular (SL) segments the middle lobe and the superior (S), the anteromedial-basal (AMB), the lateral-basal (LB) and the posterior-basal (PB) segments the inferior lobe.

In each of the two obtained binary cubes, the next step consisted in filling missing voxels (step 5 on figure B.1). For each voxel whose value was 0 in the binary cubes, the same voxel in the original CT was analyzed and if its value was in the same HU window as for step 1 (or slightly different), the voxel was set to 1 in the binary cube. All voxels in the same CT slice in a 3 by 3 neighborhood underwent the same tests, and if one of those corresponded to the same conditions, its neighborhood was also checked and so on. This was iterated slice by slice until all voxels were analyzed. Due to the carina and its HU which were similar to the lungs, this was not done in 3 dimensions because it would have linked the two lungs back together through the structure of the carina. To remove the last "air" values in each lung ("0" values), dilating and eroding were performed one time each (step 6 on figure B.1). Finally, the planning target volume (PTV) was subtracted to the corresponding lung file and each one of the two lung binary files was transformed into contour files using TRiP (step 7 on figure B.1). The final result can be observed on figure B.1.

As previously mentioned, one additional step had to be implemented for patient 3 in order to separate the two lungs. Because, for this patient, the lungs were very close on the ventral side, the dilating/eroding steps (step 2 on figure B.1) linked the two lungs together so that the following step (eroding two times: step 3 on figure B.1), even when performed 3 times, did not manage to yield the two separated lungs. It means that the two lungs were linked and that they were present on both left lung and right lung binary files, even after the normally successful separation step (step 4 of figure B.1). Thus a new step was placed directly after step 1 of figure B.1 and consisted in finding the minimal value of the projection of a CT slice on the horizontal axis. The aim was to find the location where the lungs almost touch each other in the front of the chest so that the coordinates can be used later (before step 7 of figure B.1) to separate them.

B.3 Results & conclusion

For all patients, the obtained contours were conformal to the shape of the lungs when directly compared to the corresponding CTs. However, due the choice of filling missing voxels (step 5 on figure B.1) only in 2 dimensions, some extreme parts of the lungs such as the posterior-basal segment of the inferior lobes or the extreme top part of the apical segment of the superior lobes (see figure B.2) were ignored. But performing the same in 3 dimensions, which would yield the whole lungs without missing parts, linked them back together through the carina due to its similar HU values. That is why the following trade-off was chosen, aiming at keeping lungs separated (using only 2D filling of missing voxels) but missing at the end small parts of the lungs, representing a negligible volume compared to the total size of the organ. The additional step implemented specifically for patient 3 was also quite successful and managed to yield quite precisely the separation point of the two lungs, as displayed on figure B.3.

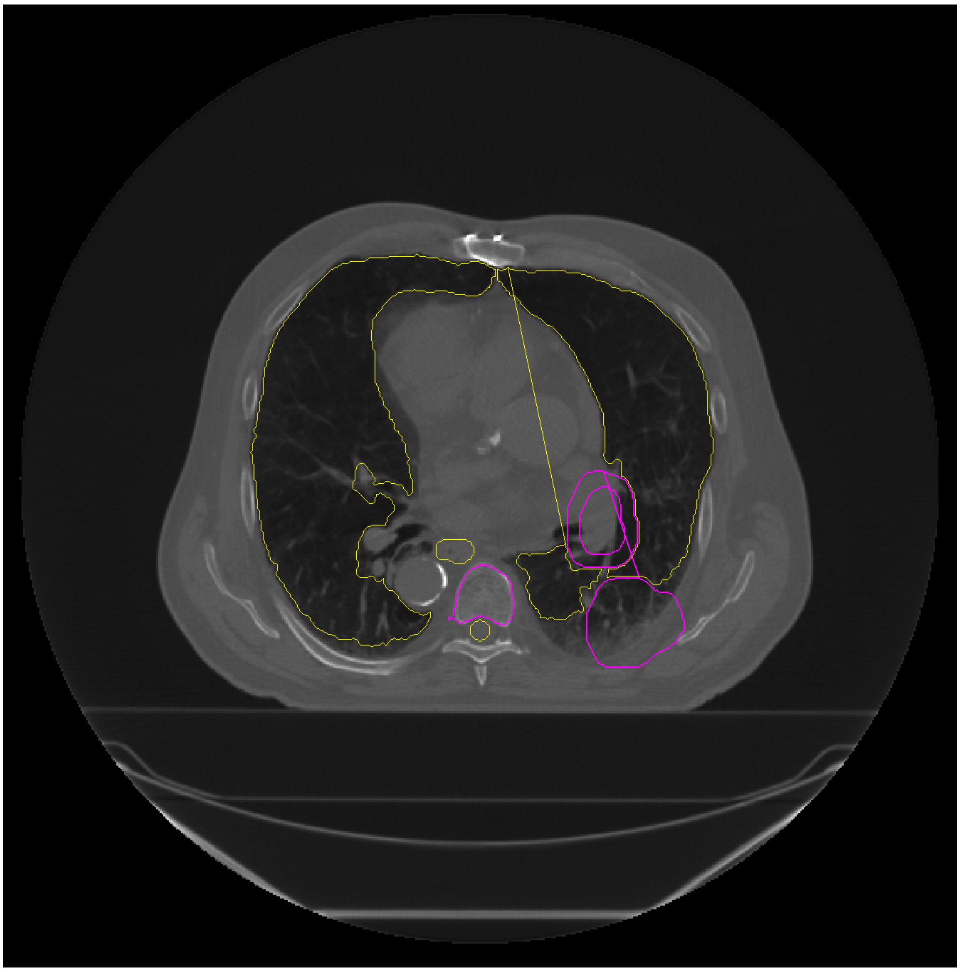

Figure B.3.: Example of lung contours (in yellow) obtained for patient 3.

C Feasibility of using a single ITV for different gating windows

C.1 Introduction

Using a 4D treatment planning system (4DTPS) from GSI, TRiP4D (Richter et al., 2013), and range adapted-ITV margins (Graeff et al., 2012) permits to investigate the effect of several parameters on weekly 4D treatment simulations. In this dissertation, gating (Ohara et al., 1989; Minohara et al., 2000) was one of the investigated motion mitigation methods. The aim of this brief study is to investigate whether using a single ITV or corresponding ITVs for three different gating windows leads to significant changes on dose distribution.

C.2 Materials and methods

C.2.1 Patient data

4DCT datasets from 2 NSCLC lung tumor patients from MDACC (Britton et al., 2007) were used to investigate the difference between dose distributions obtained a single ITV or GW-corresponding ITVs for different gating windows. Patients 8 and 9 from chapter 3, composed of 8 and 6 weekly 4DCTs and having an average tumor motion of 4 mm and 23.5 mm, respectively, were chosen among the available patients, representing a small motion and a large motion example.

C.2.2 Treatment planning

Treatment planning specifications were the same than the ones described in chapter 3 of this study except for the ITV. Figure C.1 represents the two options that were compared: appropriate ITV (AITV), represented by cases a, b and c for GW-corresponding ITVs, and single ITV (SITV), represented by case d for one single ITV combined to each GW. GW 30% simulations were identical for the two configurations because the ITV was the same (phases 3-7 in each case).

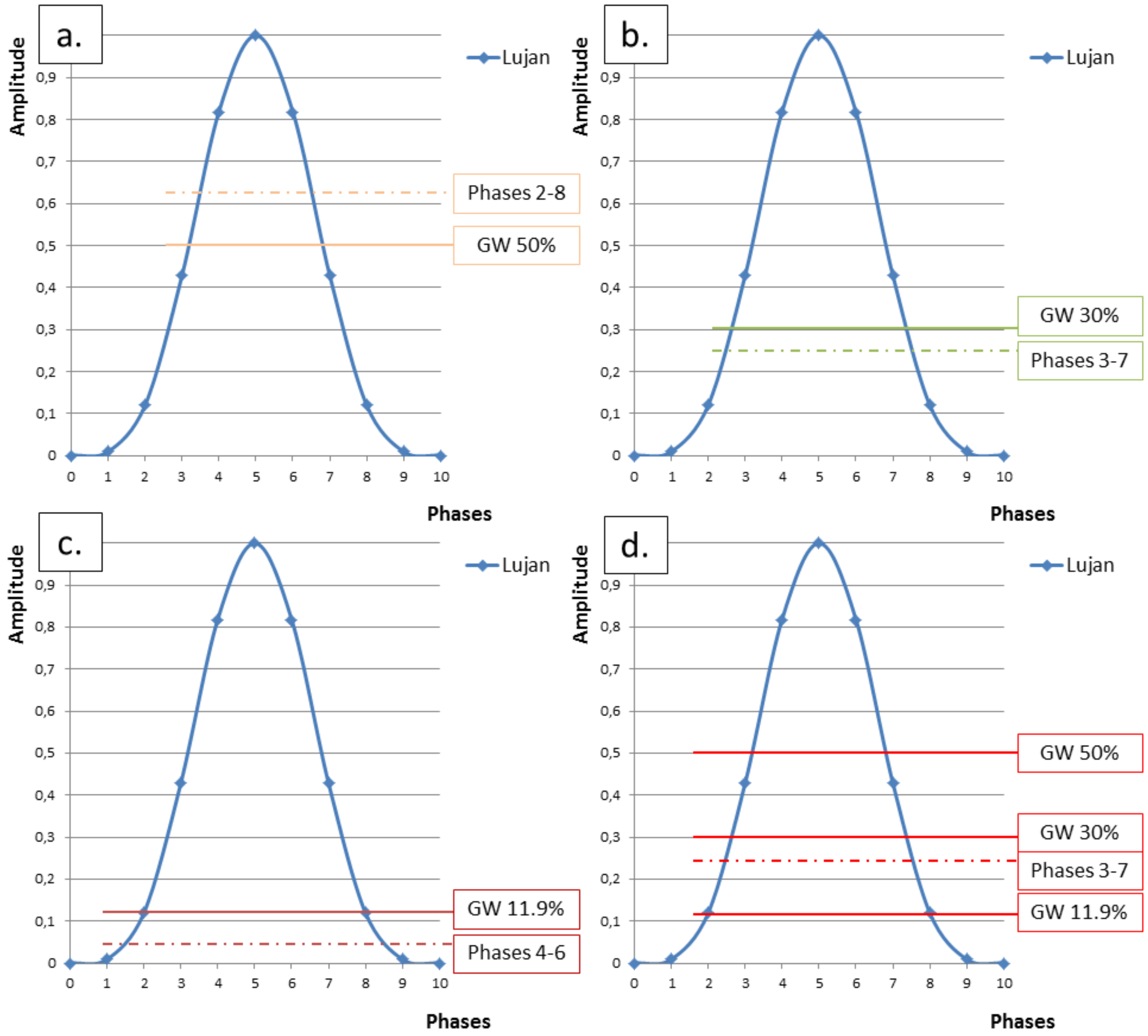

Figure C.1.: Different cases compared. Cases a, b and c were calculated using the corresponding ITV for each GW (AITV), case d shows the other possibility to perform all GW-specific simulations using only one ITV (SITV).

C.2.3 Data analysis

The dose distribution of each week was obtained by accumulating the dose delivered to each motion state on the reference phase of the 4DCT using state-to-state non-rigid vector fields. V_{95}, V_{107}, homogeneity and CN were used to compare the results. In each case, a Wilcoxon signed-rank test (W) was performed using a level of significance of 0.05 to estimate the difference between two sets of datapoints. In the case of samples containing more than 10 values, the p-value (p) was computed using the obtained z-score (z).

C.3 Results

In the case of the median GW (30%), no change was logically observed because the ITV is identical for the two cases.

Then, looking at each patient separately and beginning with patient 8 (small motion), it is possible to see that for most of the cases, using an appropriate ITV yields better V_{95} for the long GW with foci 6 and 15 and lower V_{95} for the short GW with foci 6 mm and 10 mm ($W > W_{critical}$). V_{107} is only significantly ($W > W_{critical}$) affected in the cases 10/11.9 and 15/50 of figure C.2 with lower values in the AITV case, even though the changes are slight. Homogeneity is also only slightly affected, because only cases 6/50 and 10/50 show better homogeneity ($W > W_{critical}$). Finally, using the AITV configuration, CN is lower with the largest focus and higher with the smallest focus ($W > W_{critical}$). Now, whether it is for V_{95}, V_{107}, homogeneity or CN, the differences between the two configurations are not large.

Patient 9 (large motion) shows more important differences but similar trends. Thus, using the AITV configuration permits to obtain better V_{95} with the longest GW but lower V_{95} with the shortest one, no matter which focus is used ($W > W_{critical}$). Regarding V_{107}, no particular trend can be isolated except for the cases 6/11.9 and 10/50 with lower and higher V_{107}, respectively, when the AITV configuration was used. Using the AITV configuration permits to improve homogeneity for the longest GW and all foci but deteriorates it in the case 15/11.9 of figure C.2 ($W > W_{critical}$). Finally CN is improved in the AITV case using the longest GW and foci 6 mm and 10 mm ($W > W_{critical}$).

Finally, looking at the significance of the difference between the two configurations and using both patients for the comparison, the same trends can be observed once more. V_{95} is better when the AITV configuration is used with the longest GW while it is lower when the AITV configuration is used with the shortest GW, no matter which focus is used ($p < 0.05$). V_{107} is only slightly but significantly better in the cases 6/11.9 and 10/11.9 for the AITV configuration ($p < 0.05$). Using the latter yields better homogeneity in the case of the longest GW but significantly lower homogeneity is only obtained with a focus of 6 mm in the case of the shortest GW ($p < 0.05$). Finally CN did not show any significant trend ($z > z_{critical}$ in each case).

Dose distributions of figure C.3 display comparisons between the two configurations for the two concerned GW (11.9 and 50%).

C.4 Discussion & conclusion

Looking at the comparison of the two configurations using both patients, it seemed that trends were more important for V_{95} for which, no matter which focus was used, better values were obtained in the case of the longest GW and lower values in the case of the shortest GW using the appropriate ITV. For V_{107}, homogeneity and CN, some trends could also be observed, but not applied to each focus.

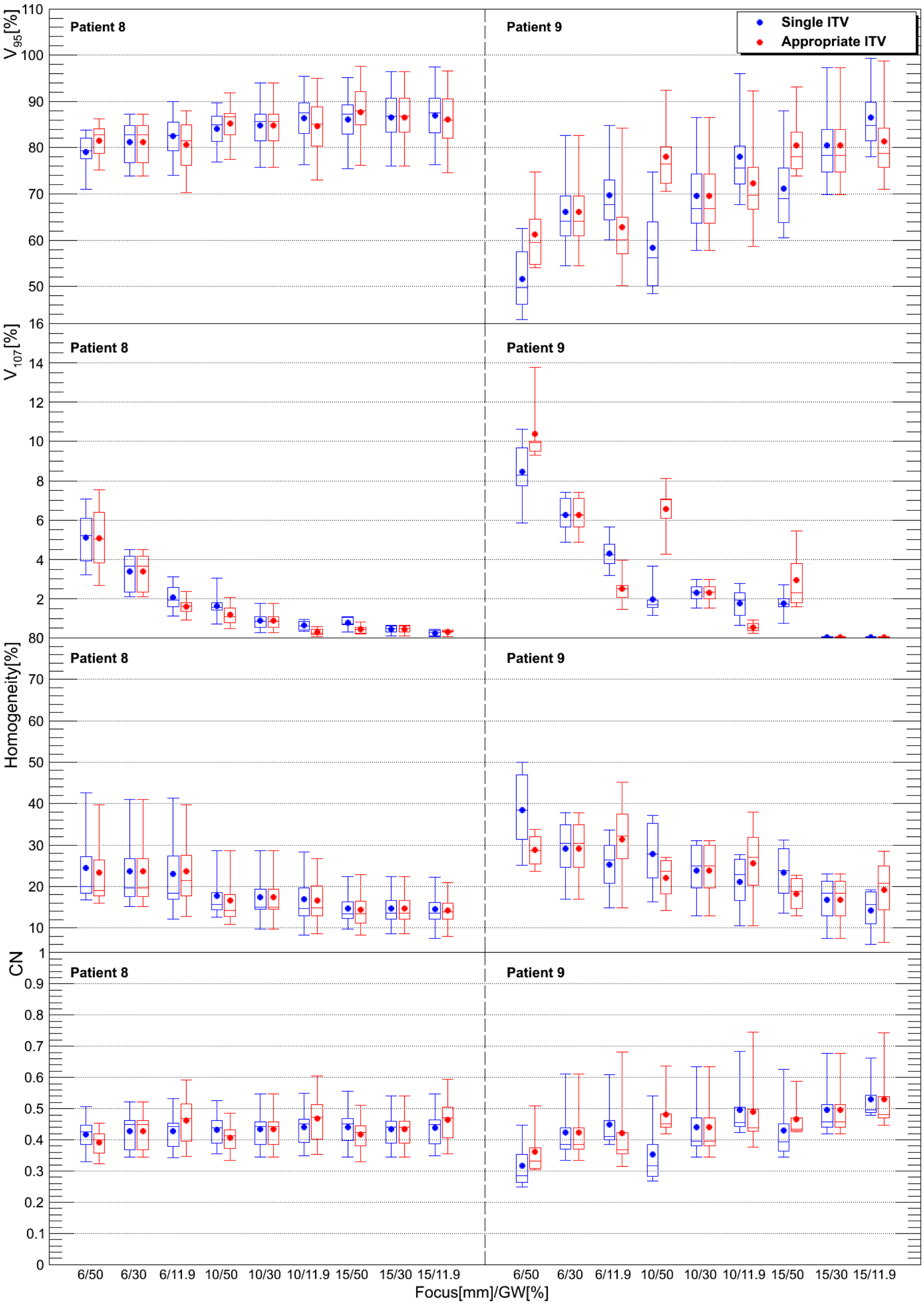

Figure C.2.: Comparison of results for patient 8 and 9 using one single ITV (SITV, blue) and GW-corresponding ITVs (AITV, red). Each bar is composed of 8 and 6 points for patients 8 and 9, respectively, and the comparison is displayed for each focus/GW combination.

Obtaining better target coverage for the long GW by using appropriate ITVs was expected since the treatment plan is applied to a too large volume in the SITV case, which means dose will not be delivered to the extreme phases (2 and 8 for this GW) of the 4DCT. And it is the opposite for the short GW, as if additional margins were already used to extend the target, thus improving motion compensation.

Moreover and quite logically, the larger the motion is, the more important the differences are. As most of the patients of this thesis show tumor motion lower than 20 mm, it can be expected that the impact on V_{95} of using the SITV configuration will be in between the two examples shown in this brief study. Also, as using an appropriate ITV has only a small impact on V_{107}, homogeneity and CN, and as it permits to obtain better results using a short GW, it was decided to use the SITV configuration in this thesis.

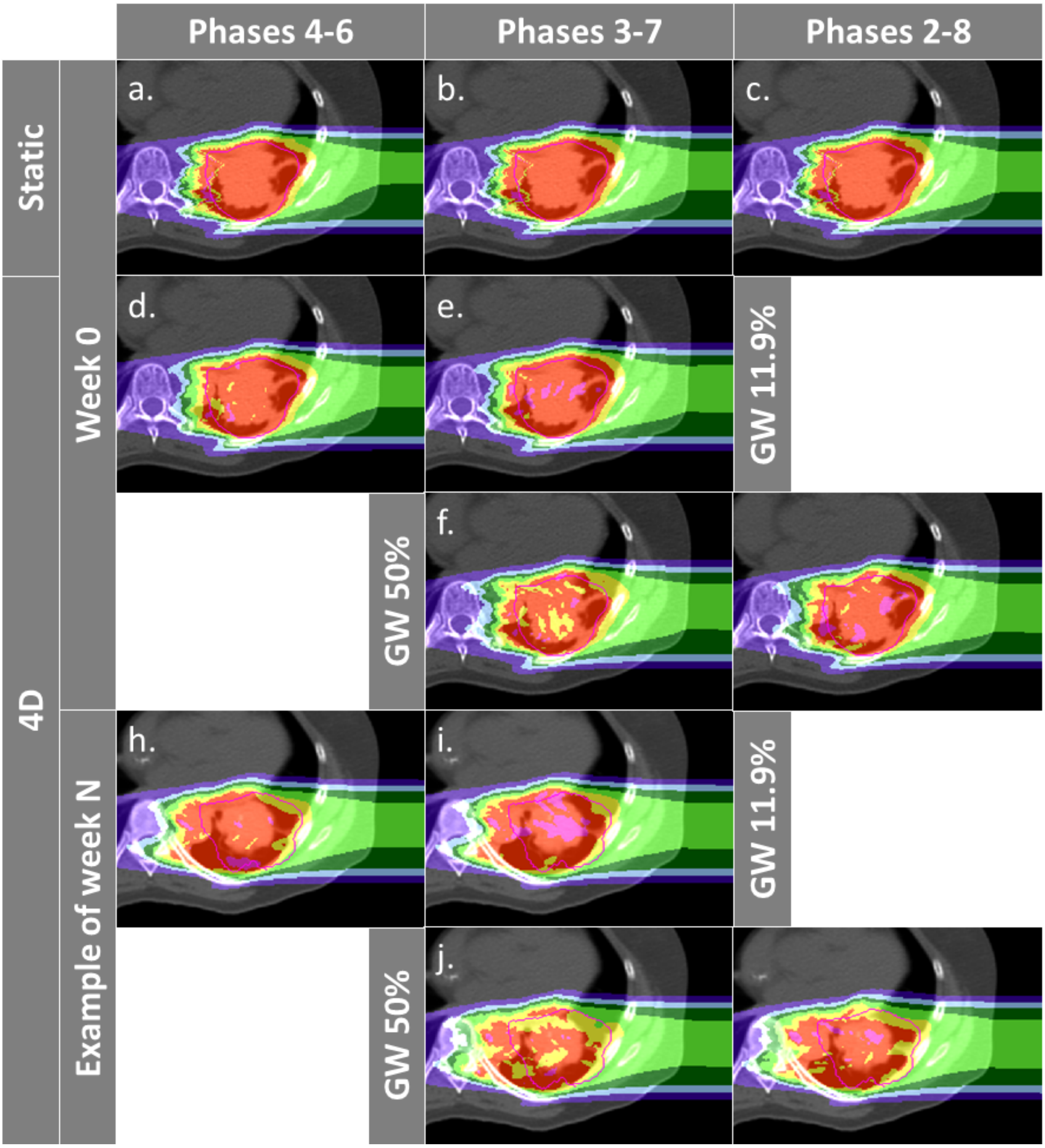

Figure C.3.: Comparison of dose distributions obtained using the AITV and SITV configurations. Columns 1 and 3 show AITV configurations for the GW 11.9% and 50%, respectively, while column two shows the SITV configuration.

D Impact of the TRiP contour extension value on overdose

D.1 Introduction

In chapter 3, gating simulations showed increased overdose when more fields were used. A modification of a TRiP-specific treatment planning parameter, known as “contour extension” and which will be described in this appendix, was thus performed to see if using a higher value, as recommended by Weber (1996) to run realistic simulations, would permit to obtain lower overdose.

D.2 Materials and methods

D.2.1 Patient data

Six patients from the 9 listed in chapter 3 were used to investigate the effect of the contour extension on overdose: patients 1, 2, 3, 7, 8 and 9, meaning that a total of 44 weekly 4DCTs were used. Number of weeks for each patient, alignment and registration methods and fields are the same as presented in chapter 3.

D.2.2 Simulations

All gating plans were simulated using the GSI 4D treatment planning system (4DTPS) TRiP4D (Richter et al., 2013), based on TRiP98 and modified to allow 4D dose calculations. The gating process used in this chapter is also the same as in chapter 3. One gating window (GW, 11.9% of the amplitude), 3 different foci (6, 10 and 15 mm, FWHM), 3 fields (see chapter 3) and PTV margins (3FPTV case of chapter 3) were used for each weekly 4DCT, representing 3 focus/GW combinations. The motion surrogate (sine square with a unique period 3.6 seconds) and the ITV definition (range corrected ITV composed of 5 motion state CTVs representing 25% of the amplitude) were the same as in chapter 3. For each patient, plans were initially optimized to this ITV computed with the first week’s CT, using one unique planned dose of 8.1 Gy(RBE). Also, the distance between each raster position was set to 2 mm on each iso-energy slice and the distance between two iso-energy slices was set to 3 mm water-equivalent.

D.2.3 Contour extension

The principle of the contour extension in TRiP is explained on figure D.1. A quick comparison was done to observe the impact of the contour extension value on overdose (V_{107}): gating simulations using the value used in chapter 3 (0.35) and the value recommended by Weber (1996) (1.1, to take into account an appropriate lateral dose fall off) were compared.

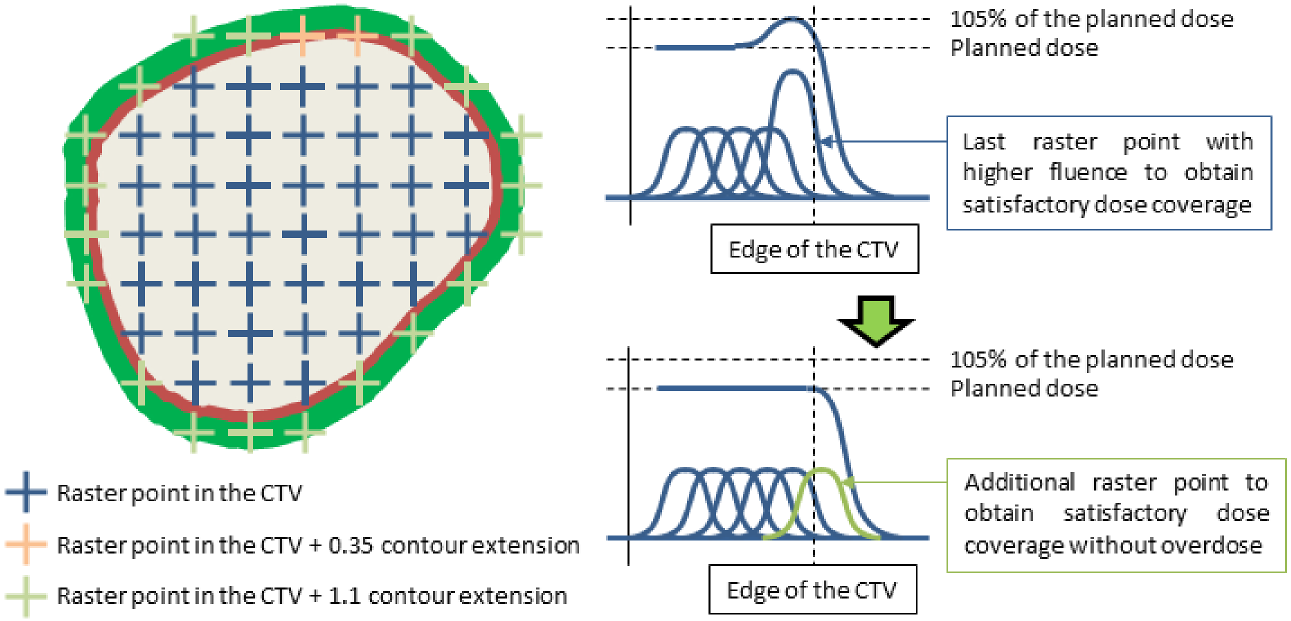

Figure D.1.: Principle of the contour extension in TRiP. Artificially extending the CTV permits to add additional raster points outside of the original CTV and to obtain satisfactory dose coverage for the entire CTV without overdose.

D.2.4 Data analysis

The dose distribution of each week was obtained by accumulating the dose delivered to each motion state on the reference phase of the 4DCT using state-to-state non-rigid vector fields. The impact of the contour extension value on V_{107} was investigated. A Wilcoxon signed-rank test (W) was performed using a level of significance of 0.05 to estimate the difference between two samples. Because samples contained more than 10 values, the p-value (p) was computed using the obtained z-score (z).

D.3 Results

All results were simulated on the weekly 4DCTs with a planned dose of 8.1 Gy(RBE). In all following figures the average value (marker), the median value (horizontal bar in the box), the

25th and 75th percentile and the total range of all values are given. Details about the planned, static dose on the first week (3D0), the 4D dose on the first week (4D0) and the 4D dose on all following weeks (4DN) are given in chapter 3.

Figure D.2 show the influence of the contour extension value used in TRiP on overdose for 4D 3FPTV simulations (4D0 and 4DN mixed together) using three foci and one gating window, representing 18-27 datapoints for each contour extension value and patient. Using a contour extension value of 0.35 as in chapter 3 yielded a mean overdose of 3%. Some patients were more affected than others, like patient 8 showing an average V_{107} of 8.5%, compared to patient 2 and its average V_{107} of 0.7%.

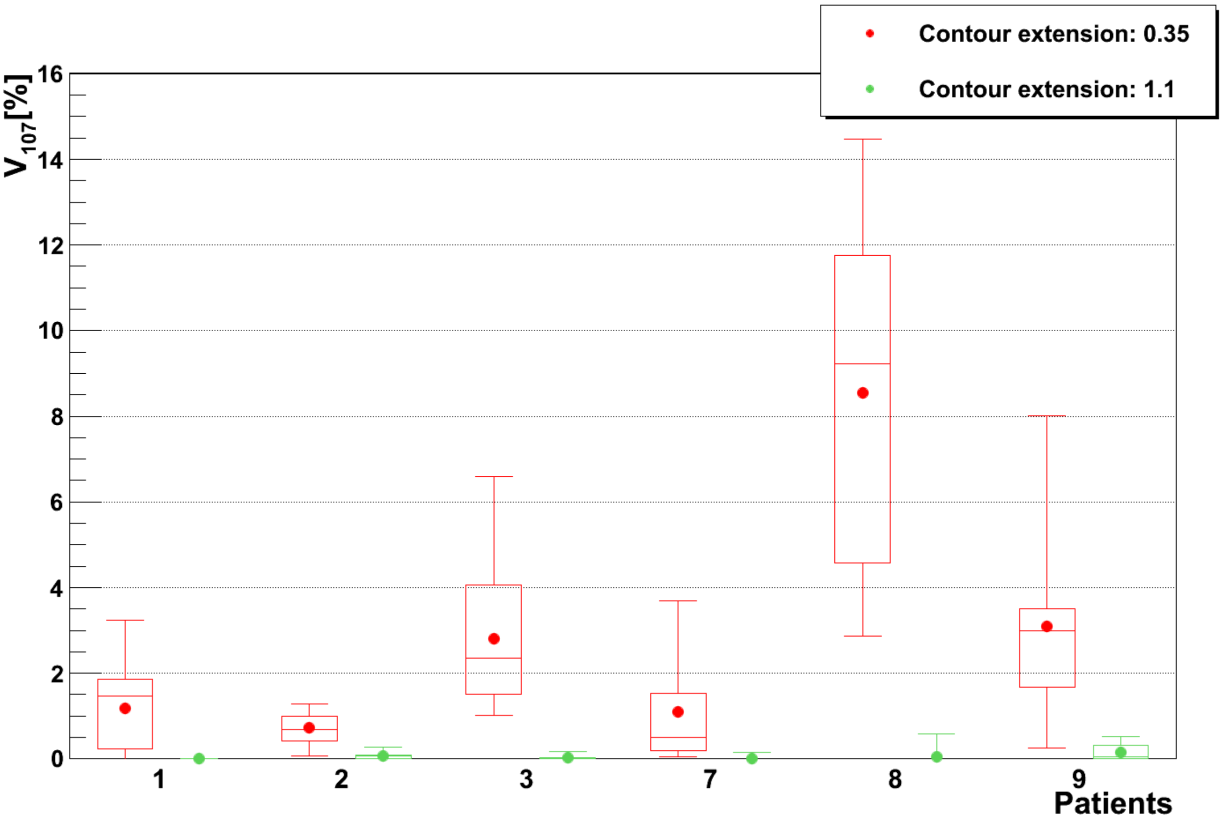

Figure D.2.: Impact of the contour extension value on V_{107}. Each bar represents 4DN simulations done using one GW (11.9% of the amplitude), three different foci, PTV margins and 3 fields, representing for each patients three times the number of available weeks (as described in chapter 3).

Using 1.1 as contour extension value permitted to reduce overdose in each case ($p < 0.05$) and to obtain a mean V_{107} lower than 0.1%. Patient 8, whose V_{107} was high, showed a large improvement, falling down to 0.2% and patients for which V_{107} was already low (1, 2 and 7) showed values almost equal to 0%.

Figure D.3 shows the difference on dose distributions between the two contour extension values with the example of week 6 of patient 3. Overdose (pink regions) present above the tumor on the top image (corresponding to the low contour extension value) disappears on the bottom image (corresponding to the appropriate contour extension value). Some overdose can still be observed on the right of the tumor but the global overdose region is drastically reduced.

D.4 Discussion & conclusion

Results showed that using an appropriate contour extension value permitted to improve significantly the results in terms of overdose. Using 0.35 as contour extension value (like in the previous chapter) was not satisfactory because, in order to obtain 100% of the planned at the edge of the CTV, the fluence of the last lateral raster point had to be increased and it resulted in overdose. Here, choosing 1.1 as a new value permitted to take into account raster points located outside the original CTV so that 100% of the planned dose could be delivered to the whole CTV without overdose. The other consequence was that the lateral dose fall-off might be slightly widened.

To conclude, the problem which appeared in chapter 3 when more fields were added, consisting in overdose inside and in the vicinity of the tumor and in an undesired tail in the dose volume histograms (DVHs), could be solved here. V_{107} values showed significant improvement (figure D.2) which was also visible on dose distributions (figure D.3). Thus, it has also been shown that using appropriate treatment settings, such as an appropriate TRiP contour extension value, is mandatory to obtain conformal dose delivery and, in this case, very low overdose.

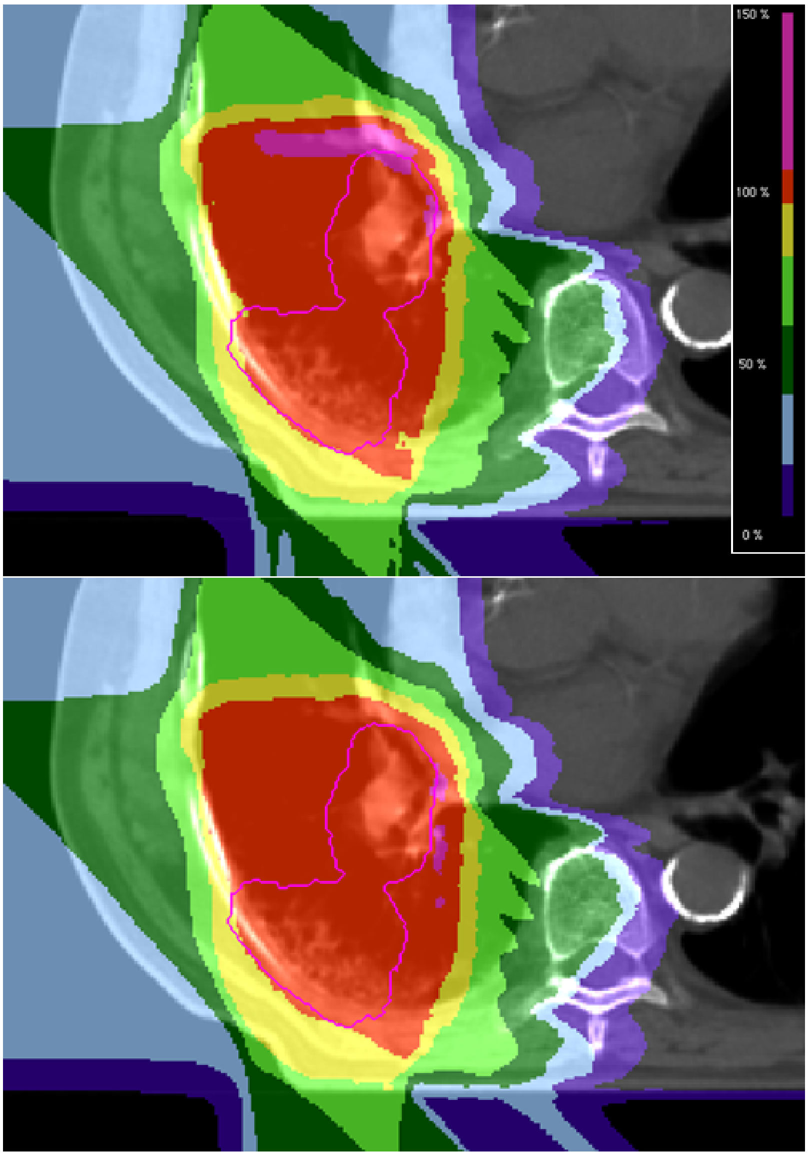

Figure D.3.: Dose distributions obtained using a low (0.35, top) and an appropriate (1.1, bottom) contour extension value. Overdose (pink regions) can be easily observed on the top image and drastically reduced when the correct contour extension value is used (bottom). The pink contour represents the CTV.

E Detailed patient and weekly graphs

This appendix contains detailed results of all patient weekly calculations done in this dissertation. Section E.1 corresponds to calculations presented in chapter 3, section E.2 to chapter 4 and section E.3 to chapter 5.

E.1 Optimization of treatment planning parameters

E.1.1 Focus and gating window (GW)

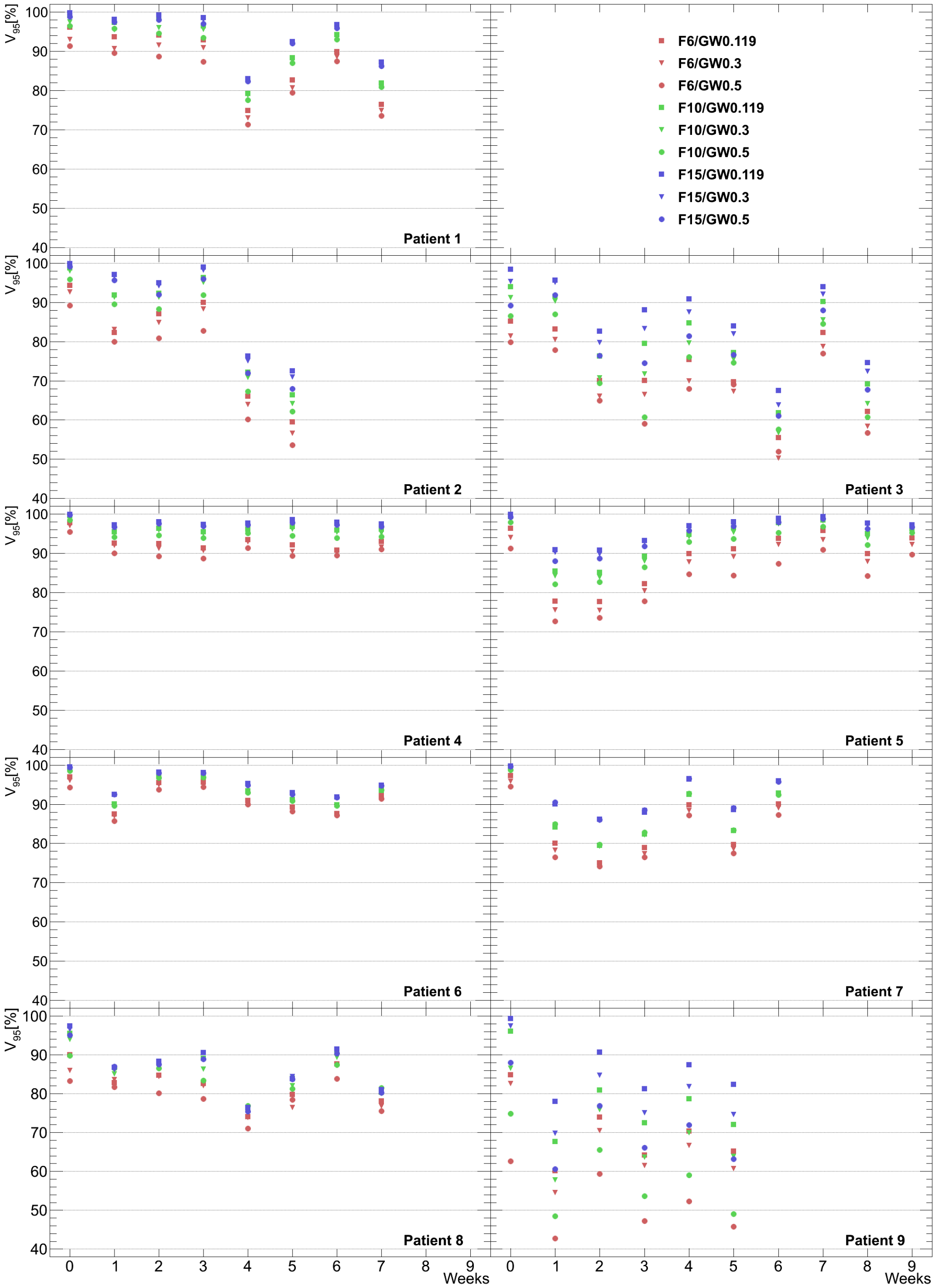

Figure E.1.: Detailed results of the impact of the gating window (GW) and the focus (F) on target coverage V_{95}.

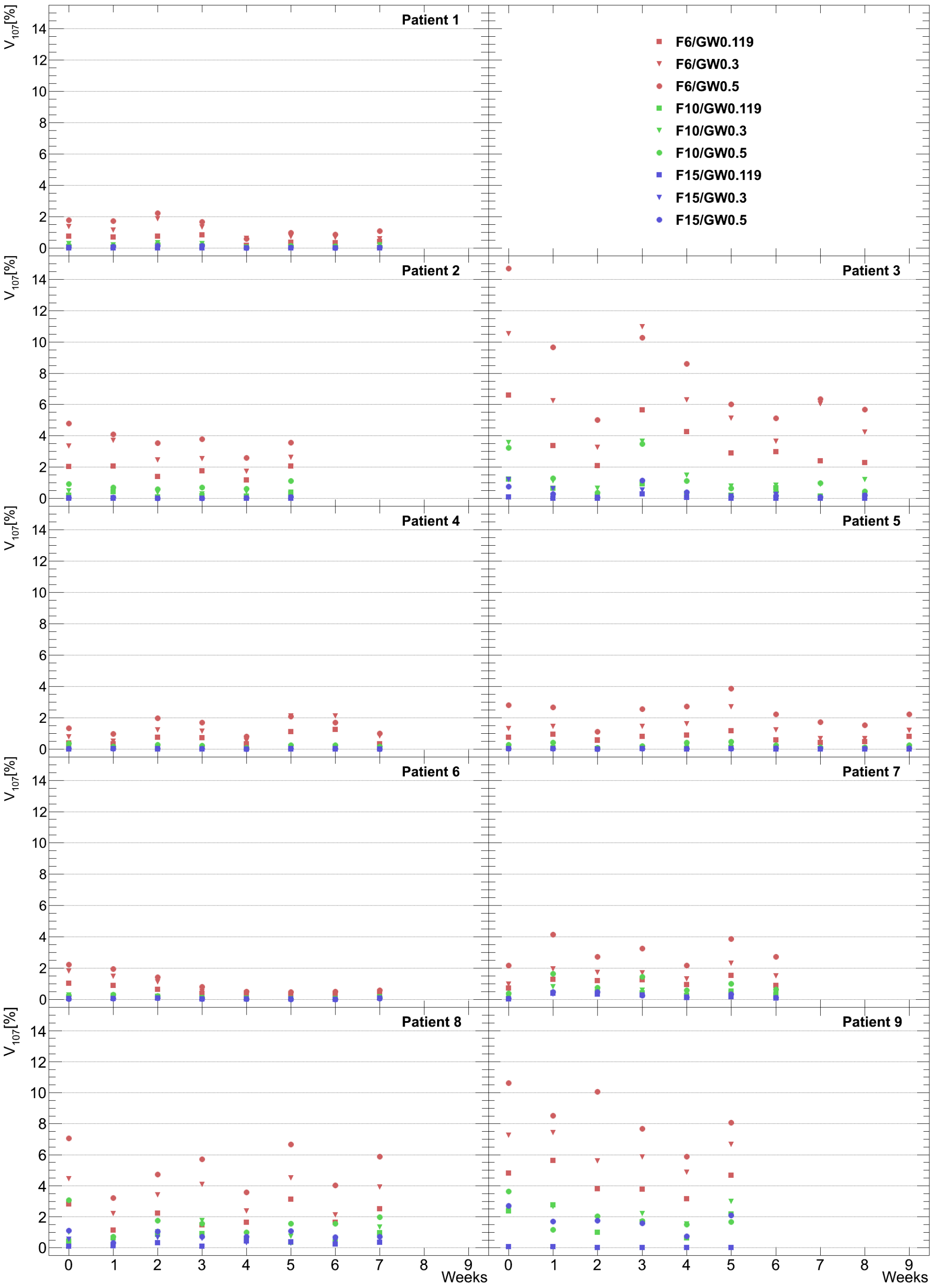

Figure E.2.: Detailed results of the impact of the gating window (GW) and the focus (F) on overdose V_{107}.

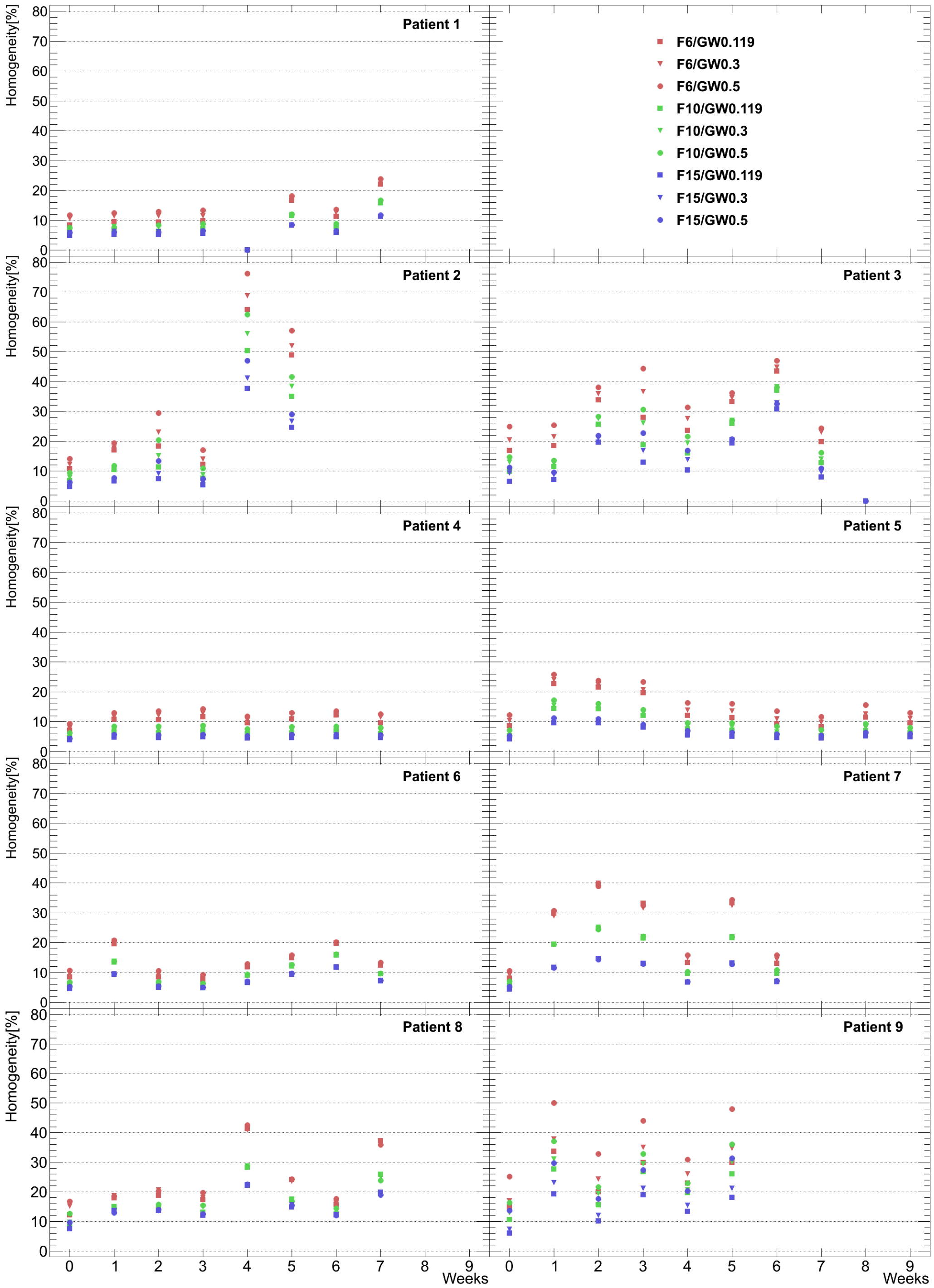

Figure E.3.: Detailed results of the impact of the gating window (GW) and the focus (F) on homogeneity.

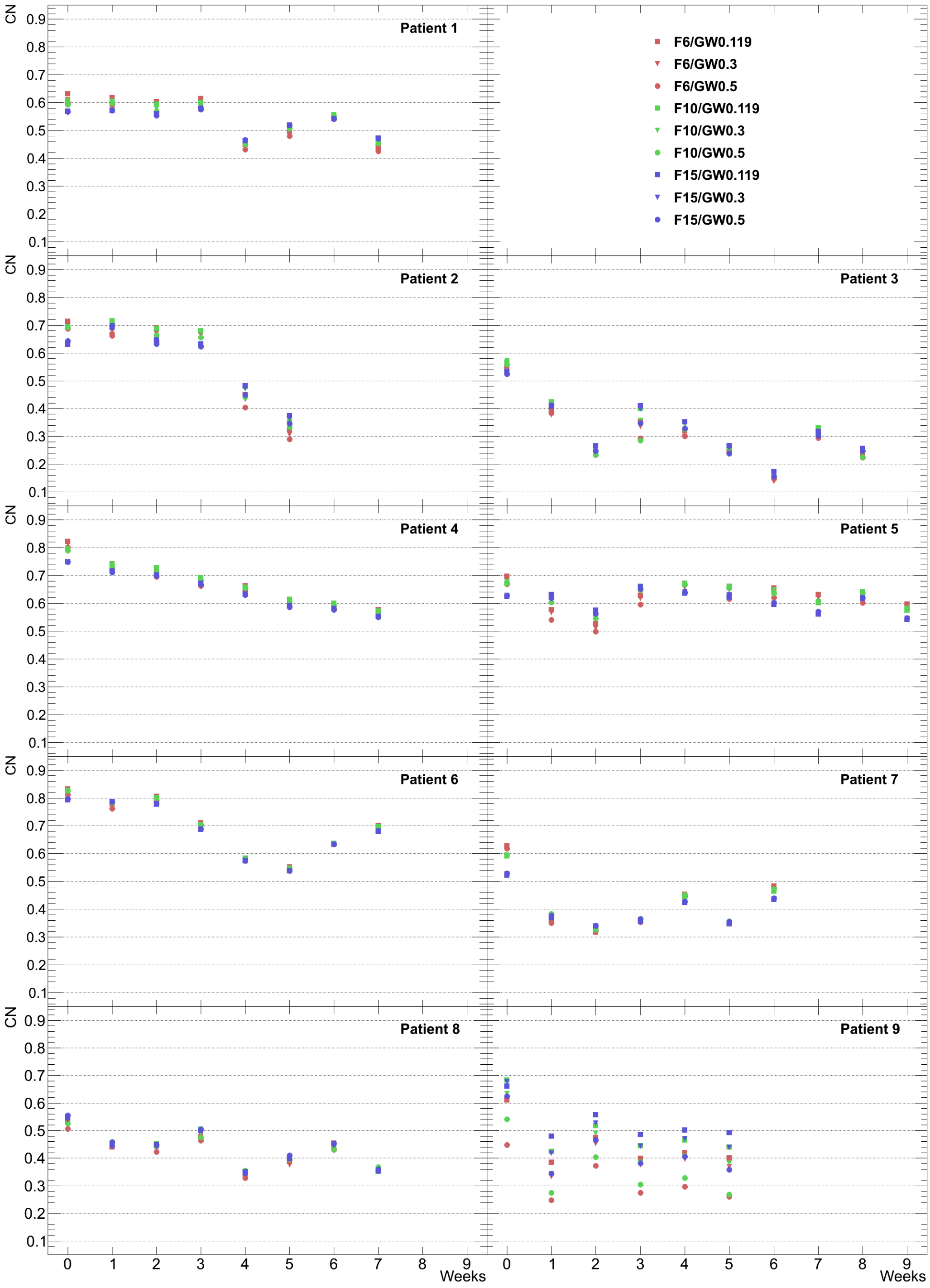

Figure E.4.: Detailed results of the impact of the gating window (GW) and the focus (F) on the conformity number (CN).

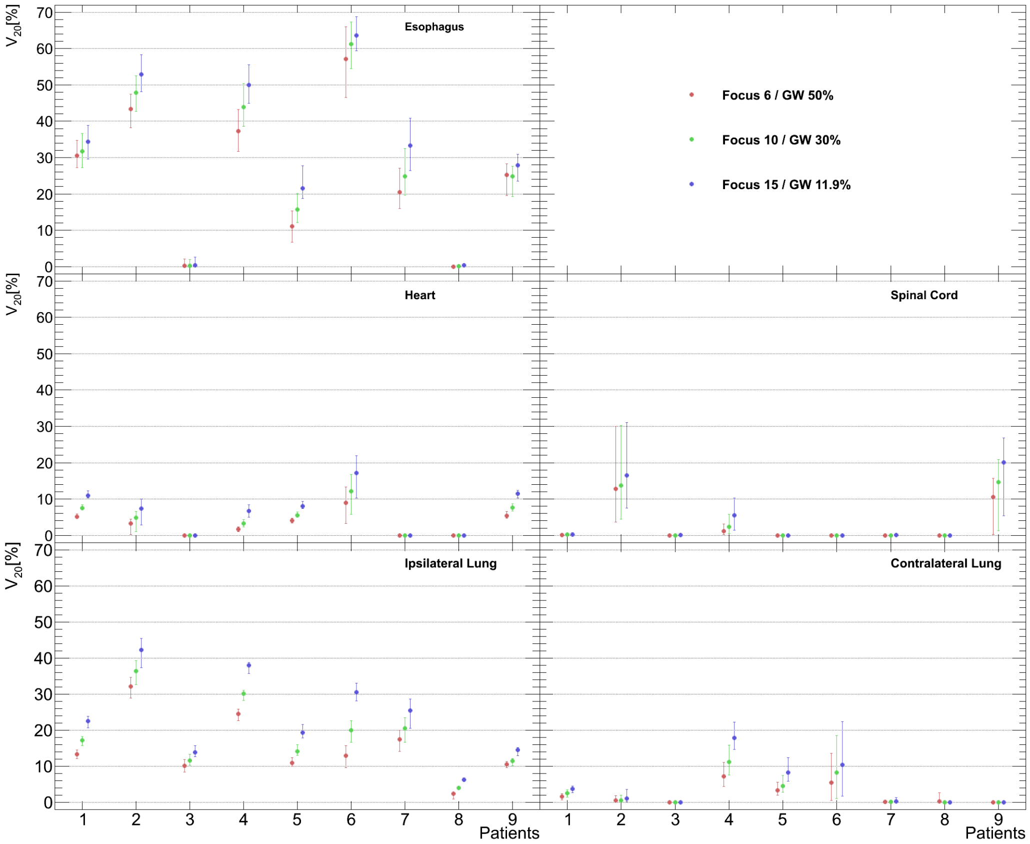

Figure E.5.: Detailed results of the impact of the gating window (GW) and the focus (F) on the 20% dose volume V_{20} in the organs at risk OAR.

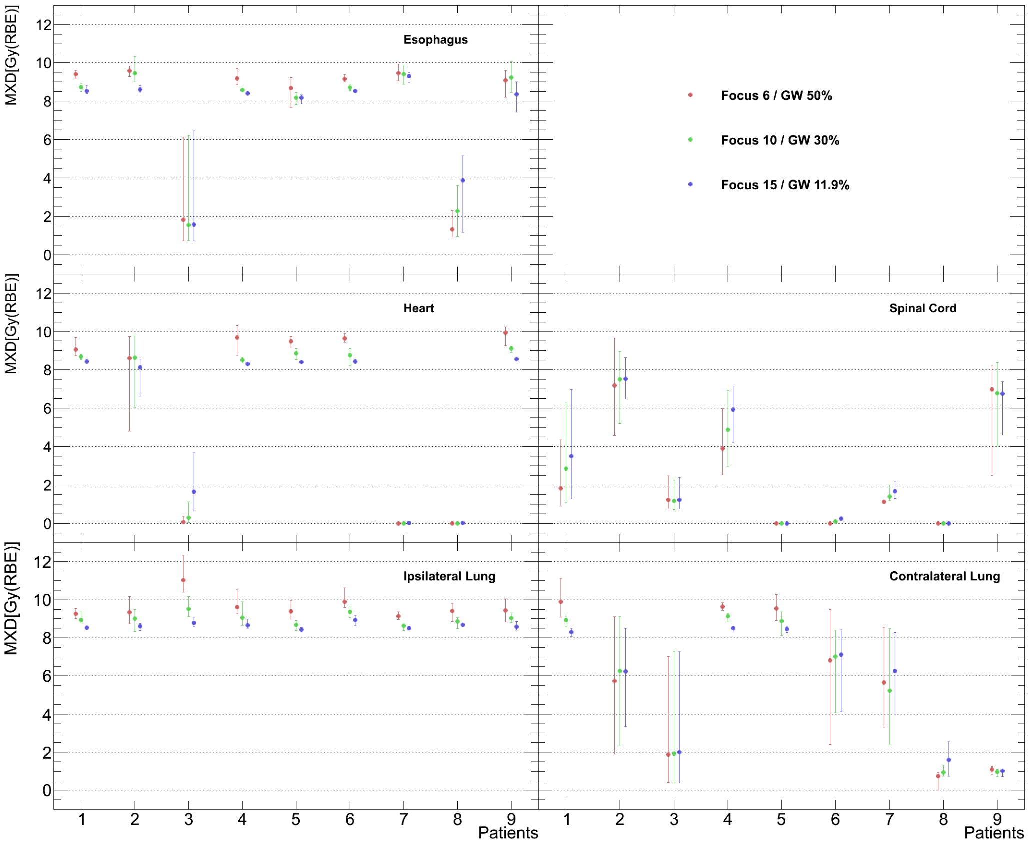

Figure E.6.: Detailed results of the impact of the gating window (GW) and the focus (F) on the maximal dose point (MXD) in the organs at risk OAR.

E.1.2 Margins

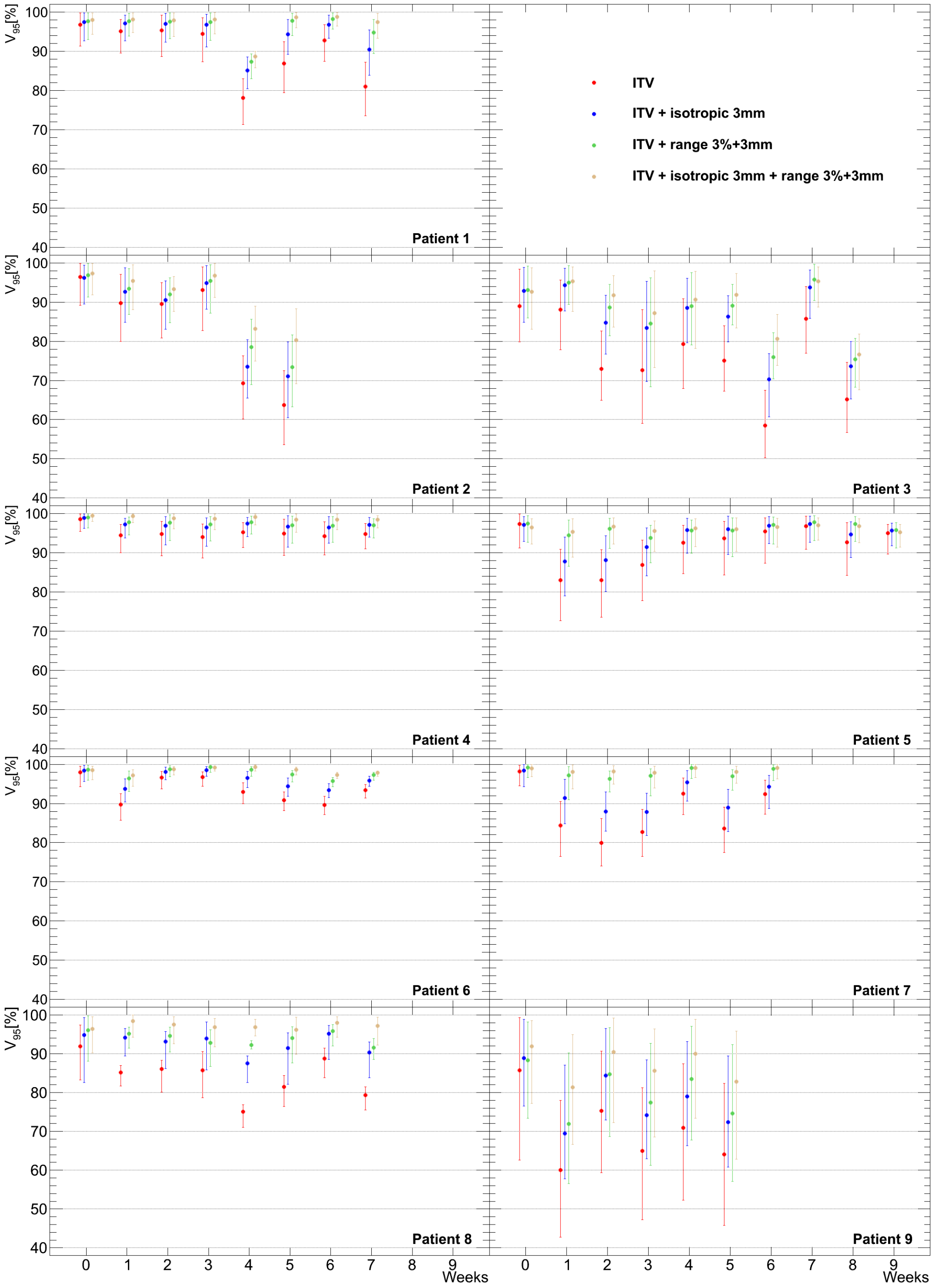

Figure E.7.: Detailed results of the impact of different margins on target coverage V_{95}.

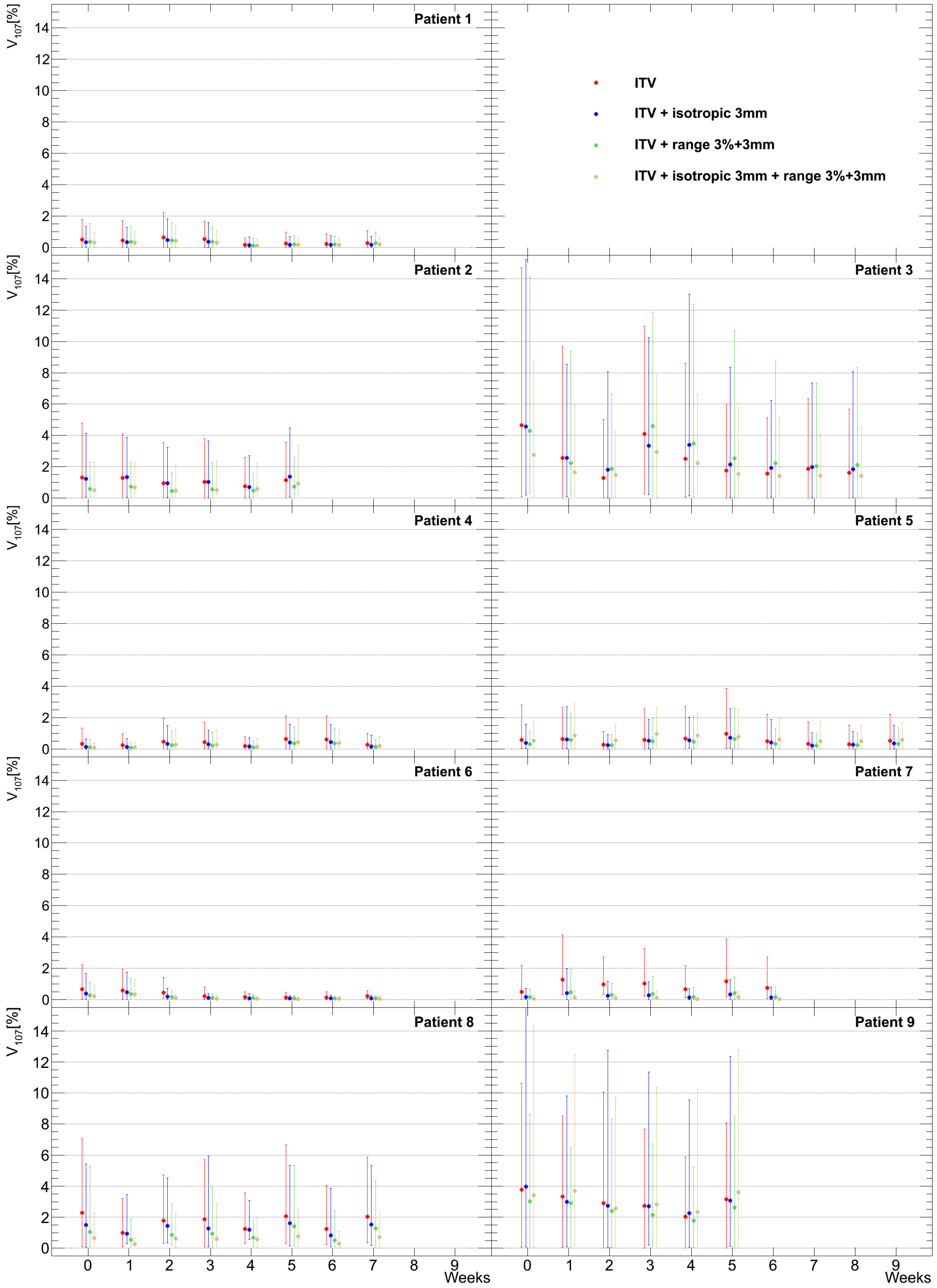

Figure E.8.: Detailed results of the impact of different margins on overdose V_{107}.

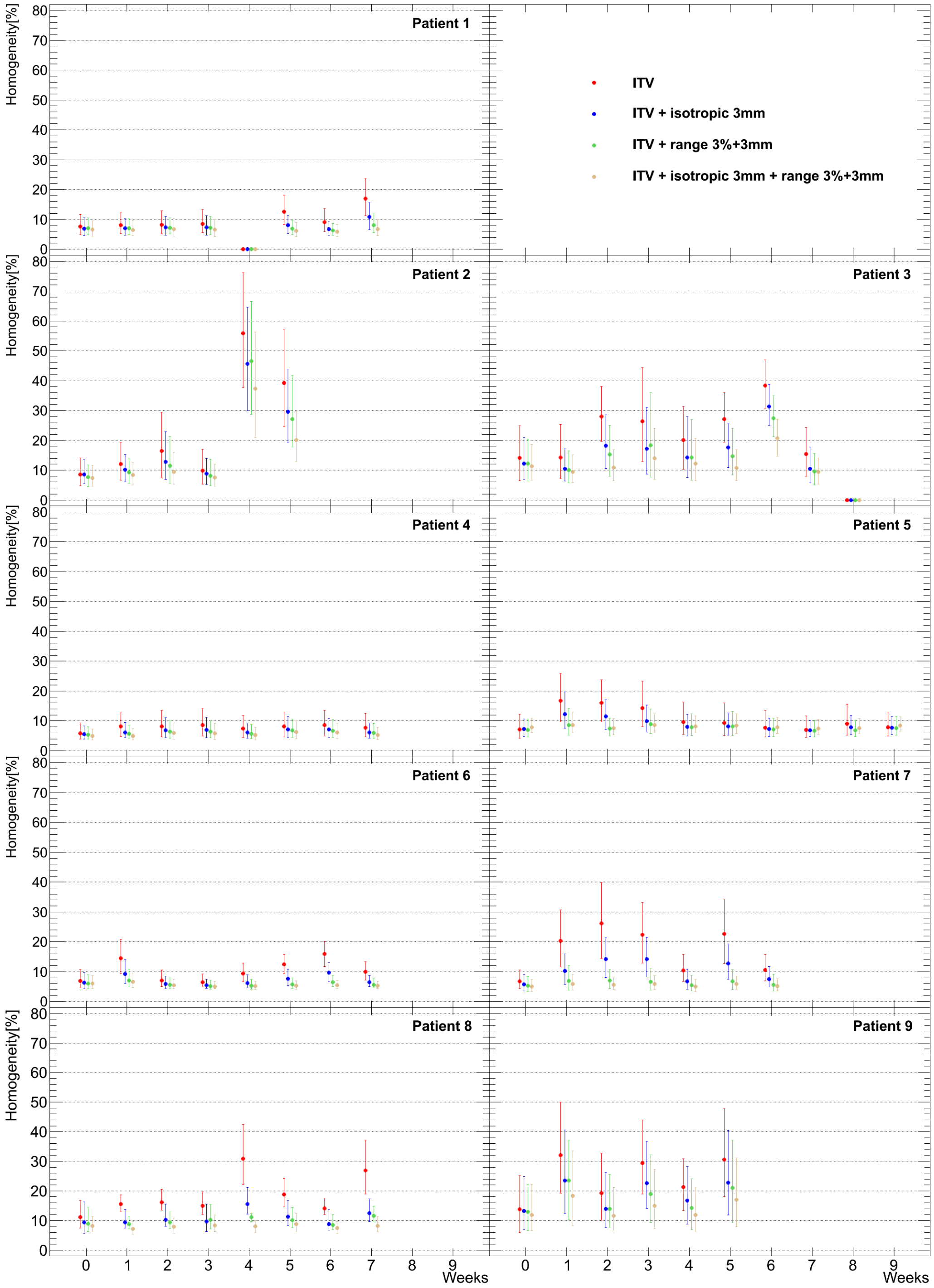

Figure E.9.: Detailed results of the impact of different margins on homogeneity.

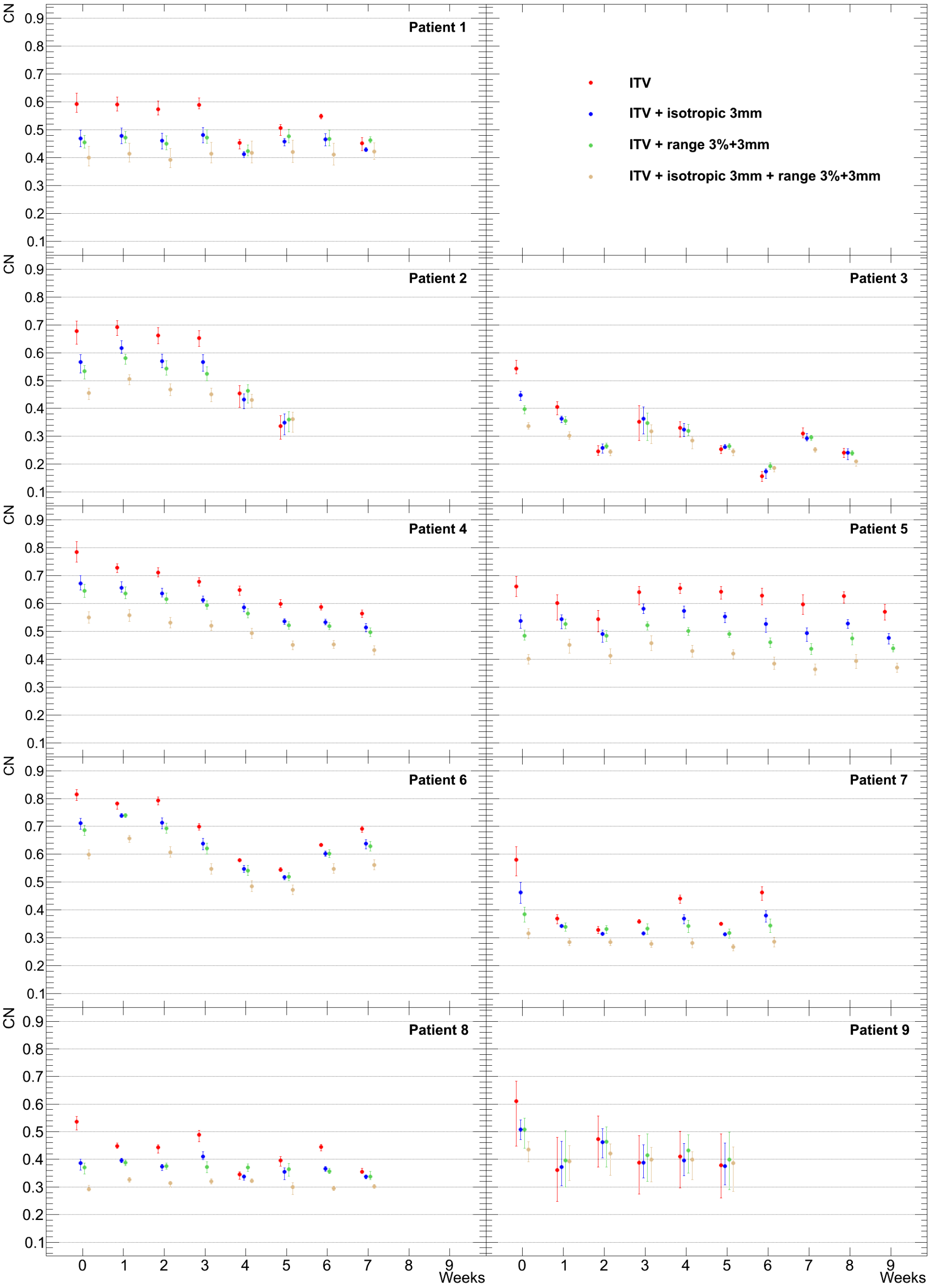

Figure E.10.: Detailed results of the impact of different margins on the conformity number (CN).

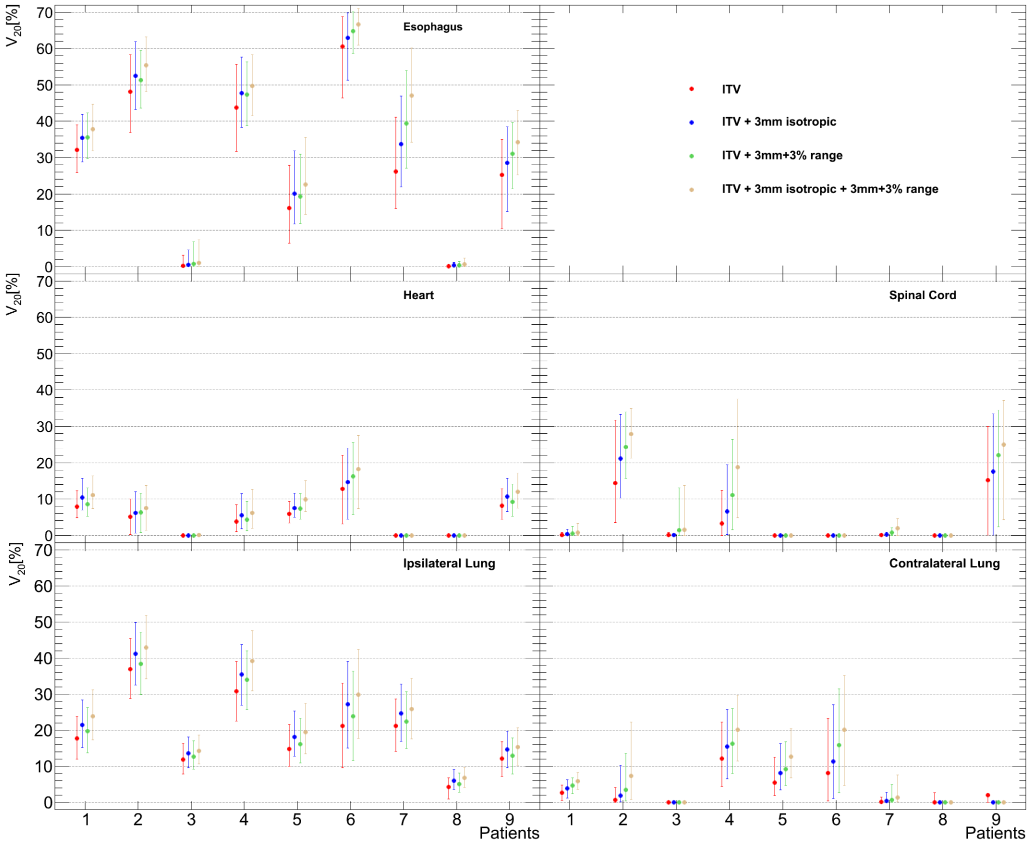

Figure E.11.: Detailed results of the impact of different margins on the 20% dose volume V_{20} in the organs at risk (OARs).

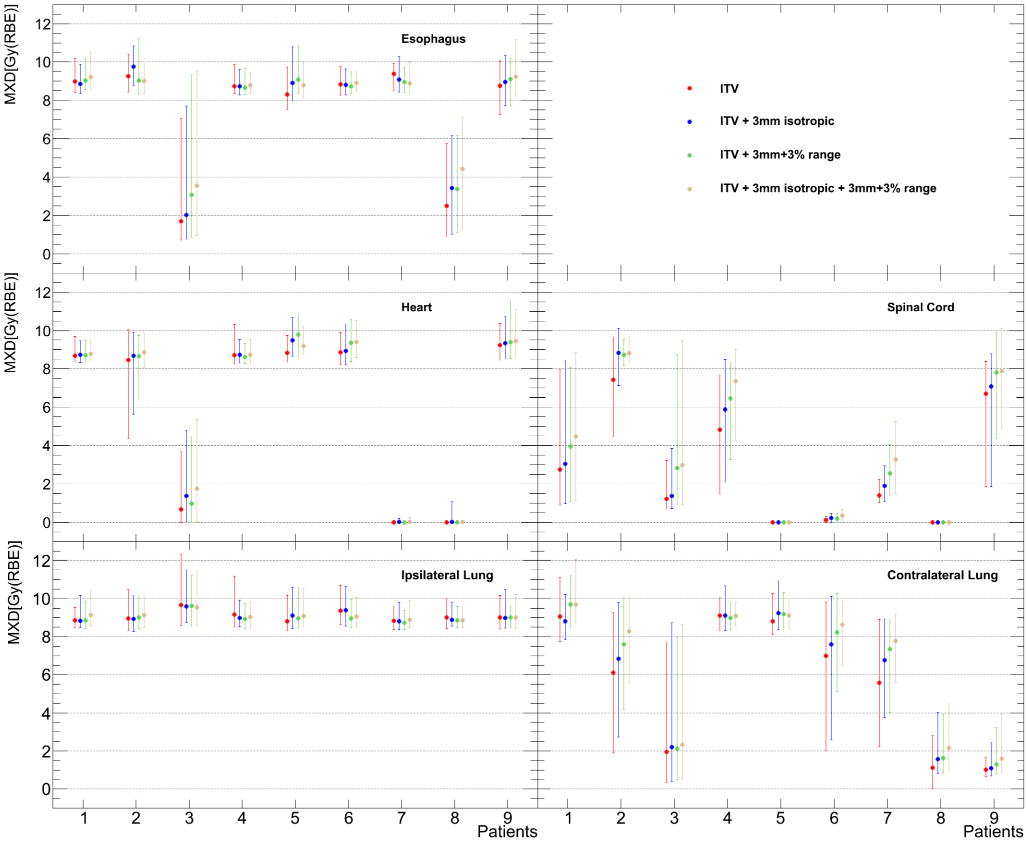

Figure E.12.: Detailed results of the impact of different margins on the maximal dose point (MXD) in the organs at risk (OARs).

E.1.3 Number of fields

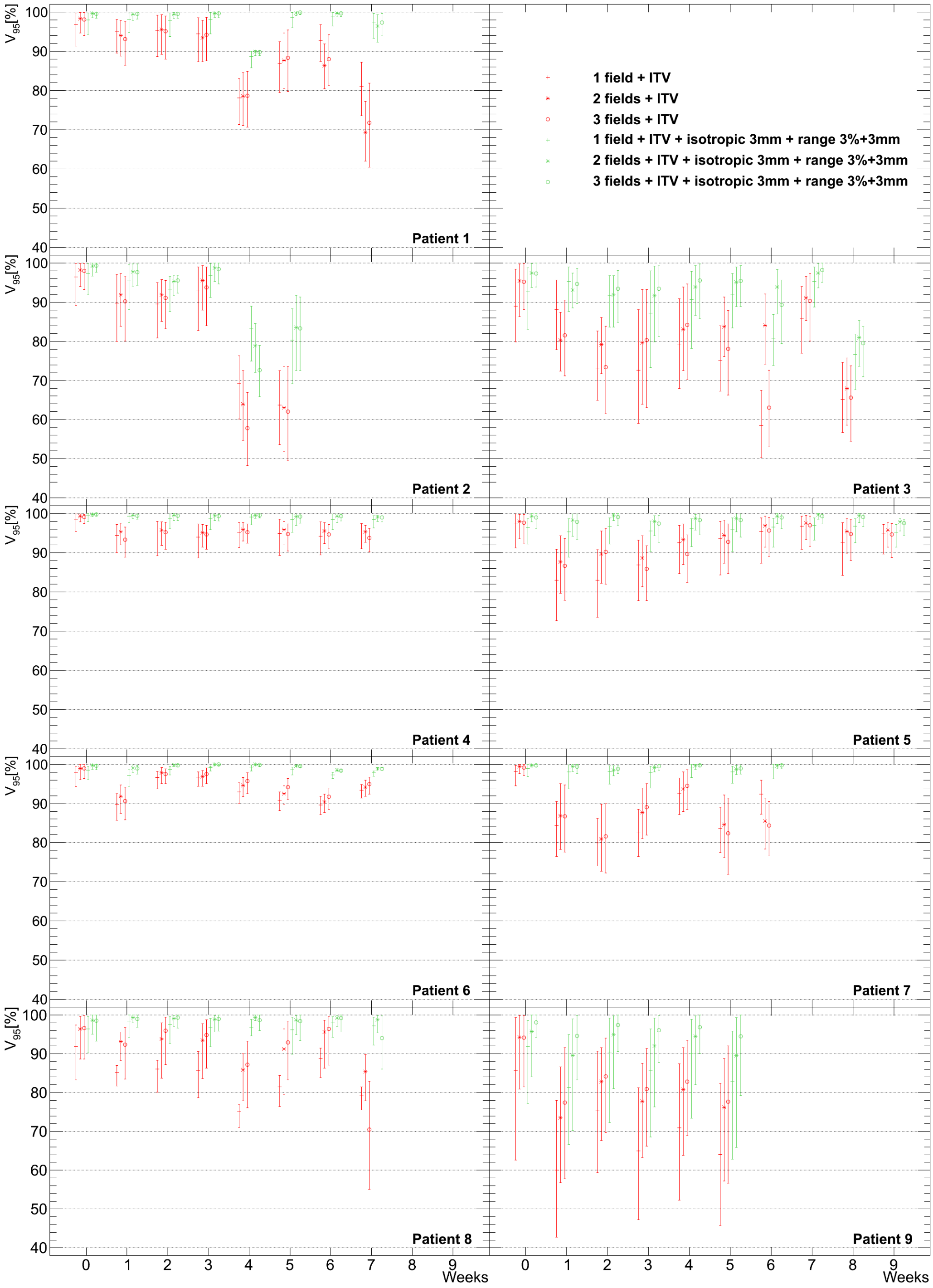

Figure E.13.: Detailed results of the impact of different numbers of fields and margins on target coverage V_{95}.

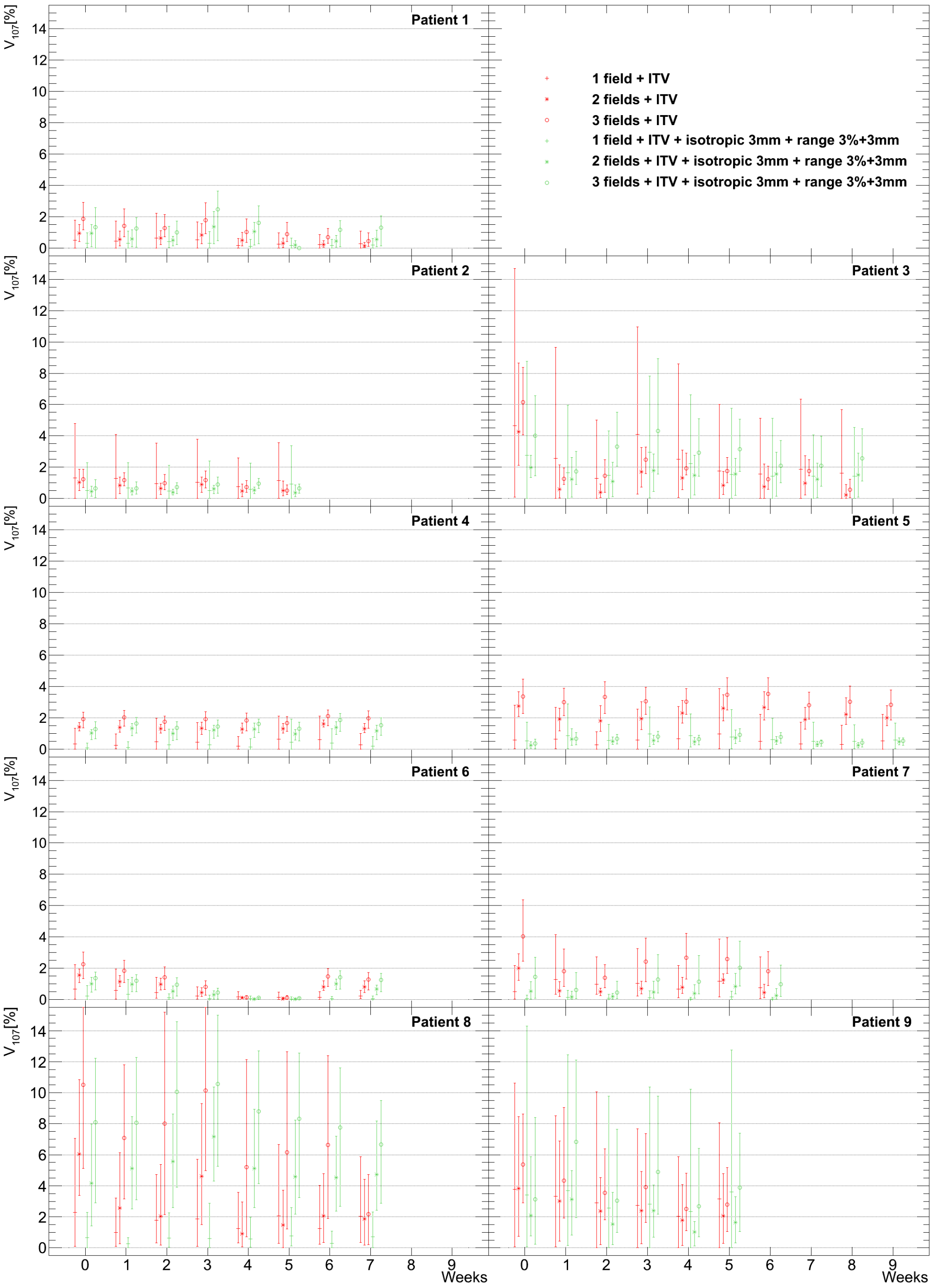

Figure E.14.: Detailed results of the impact of different numbers of fields and margins on overdose V_{107}.

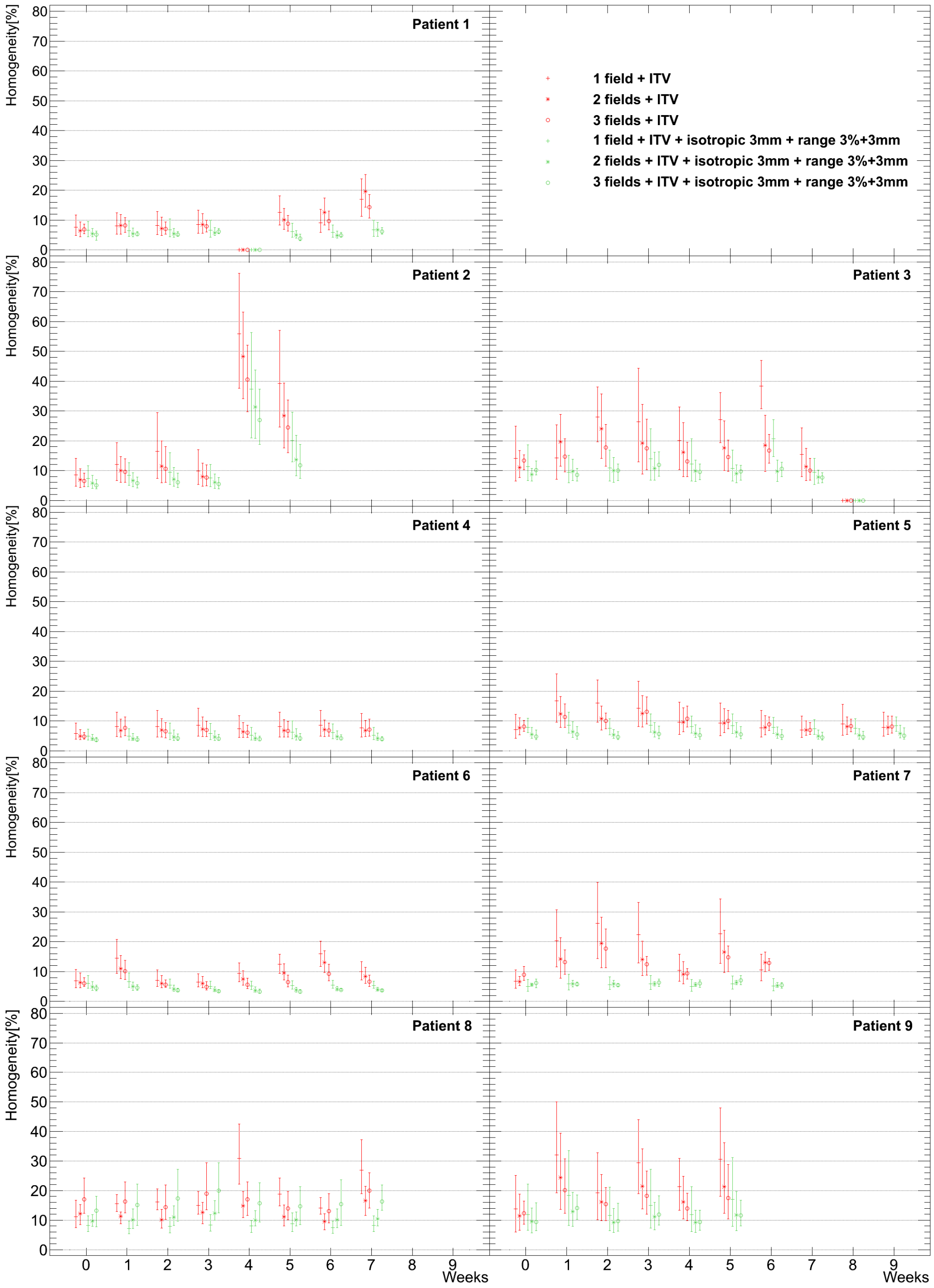

Figure E.15.: Detailed results of the impact of different numbers of fields and margins on homogeneity.

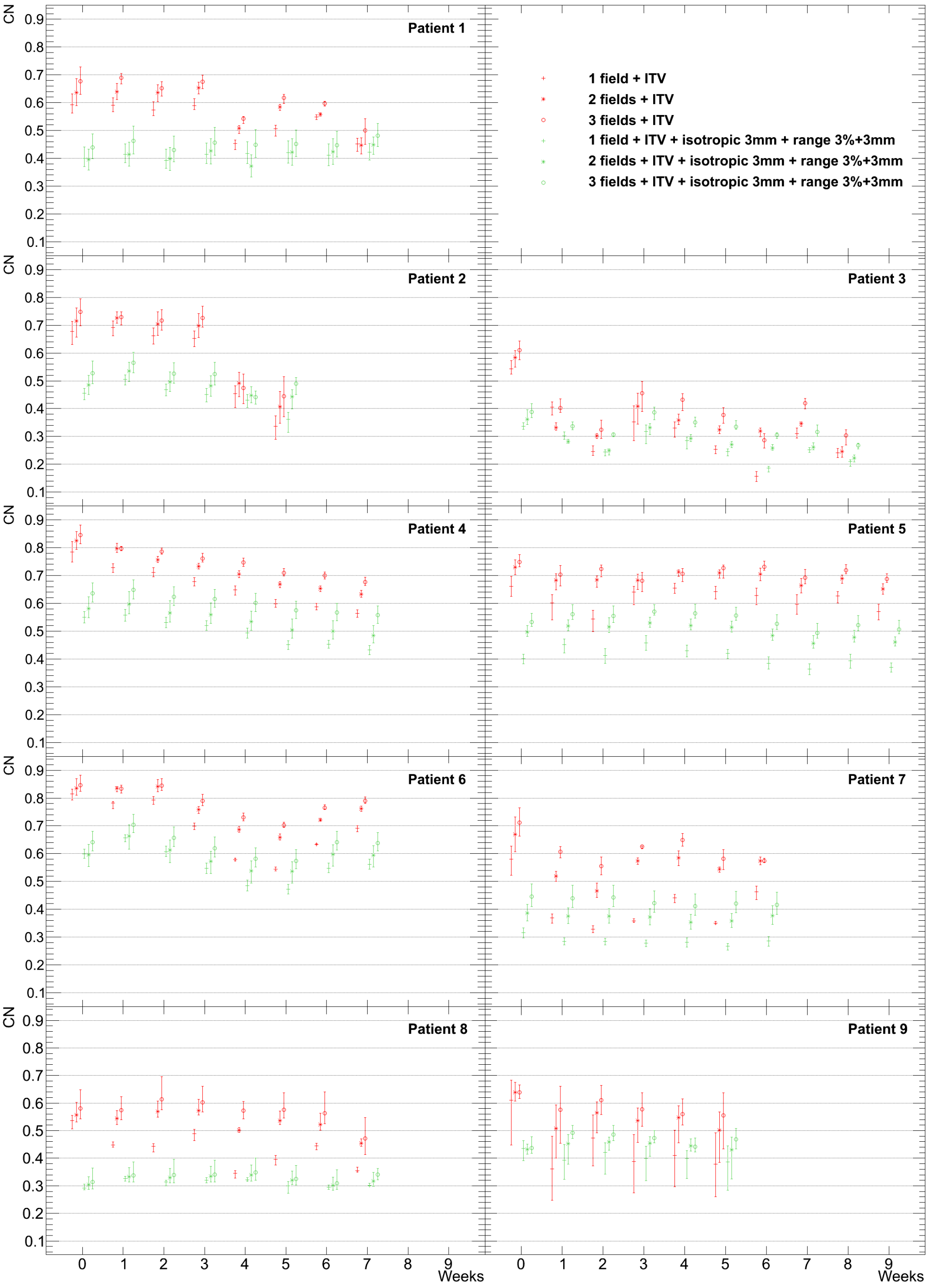

Figure E.16.: Detailed results of the impact of different numbers of fields and margins on the conformity number (CN).

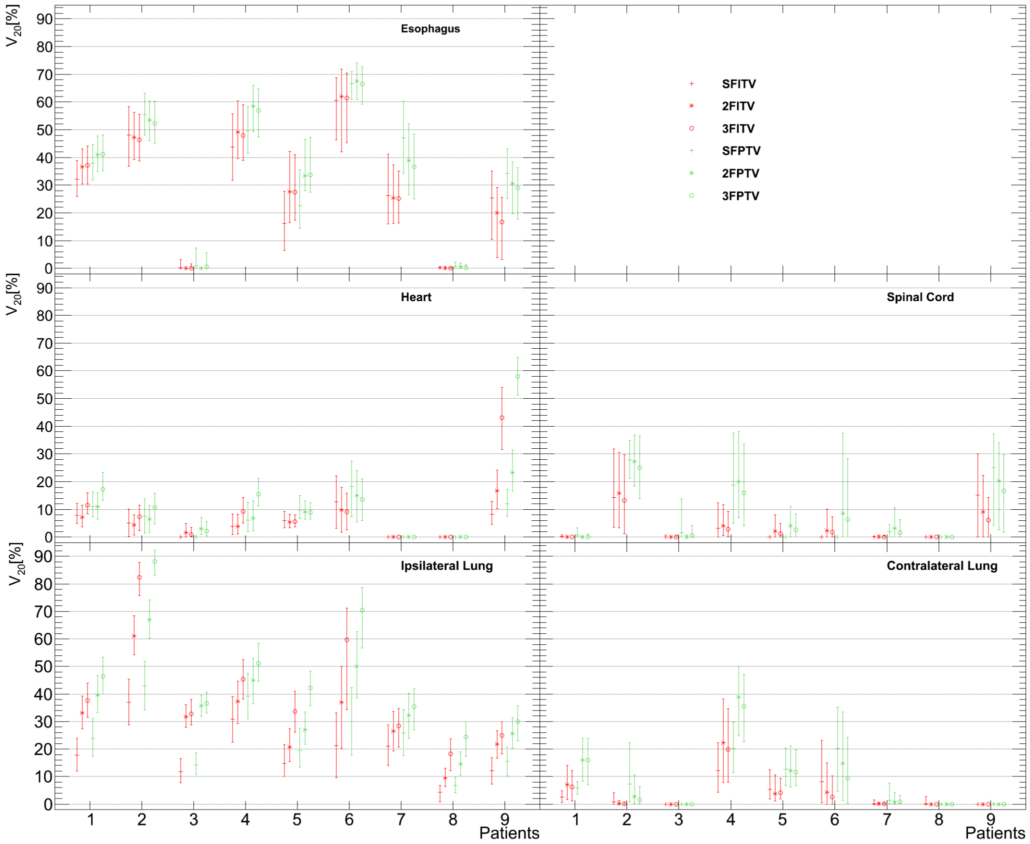

Figure E.17.: Detailed results of the impact of different numbers of fields and margins on the 20% dose volume V_{20} in the organs at risk (OARs).

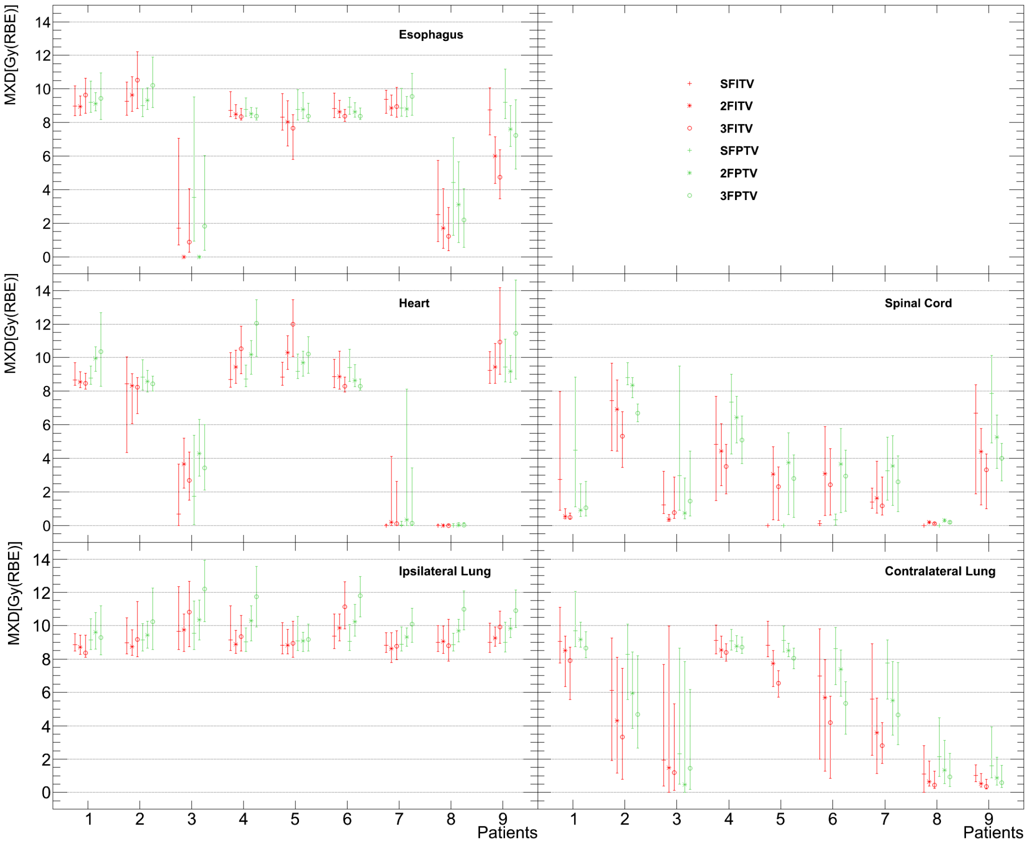

Figure E.18.: Detailed results of the impact of different numbers of fields and margins on the maximal dose point (MXD) in the organs at risk (OARs).

E.2 Comparison of different mitigation techniques

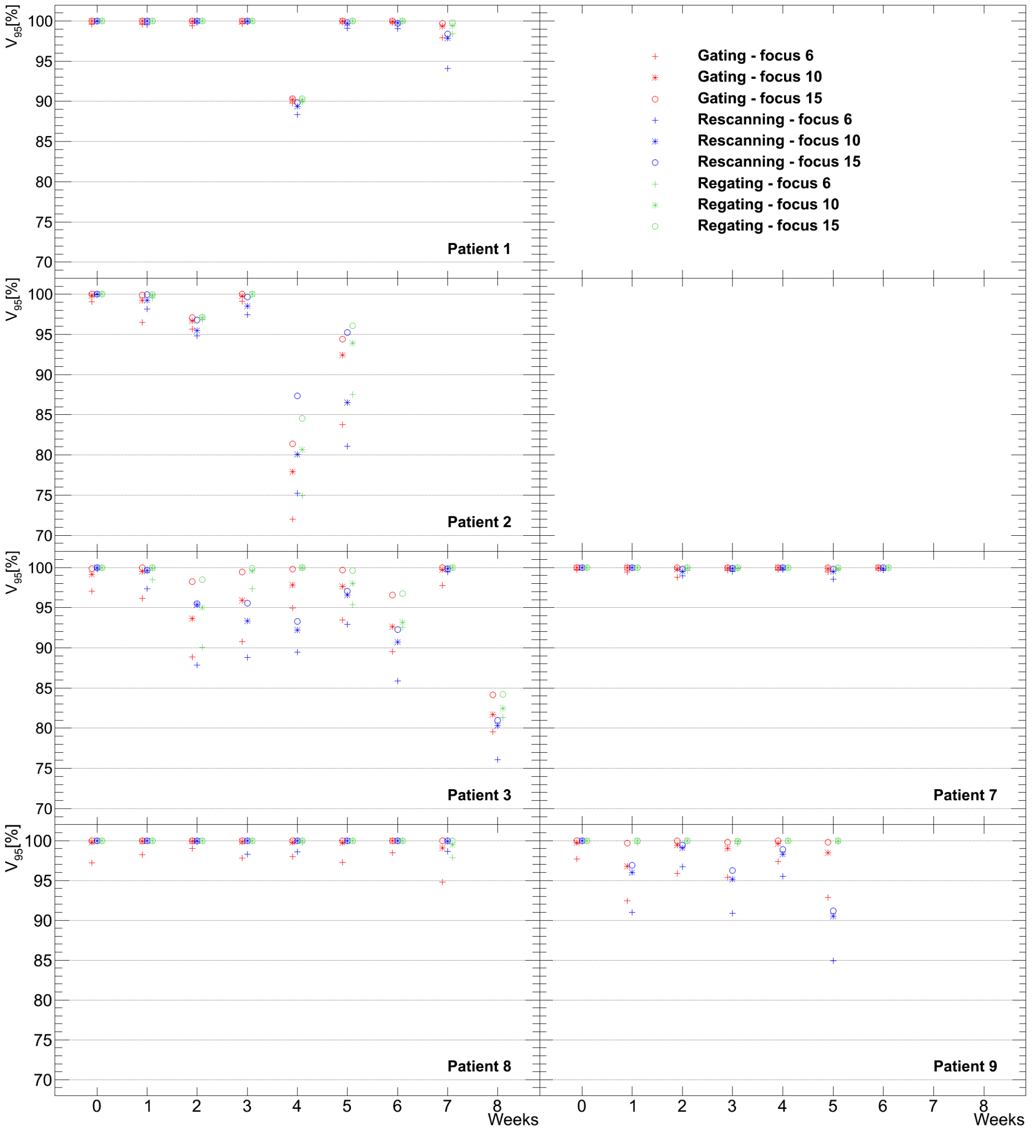

Figure E.19.: Detailed results yielded by gating, perfect rescanning (PRSC) and perfect regating (PRGT) regarding target coverage V_{95}.

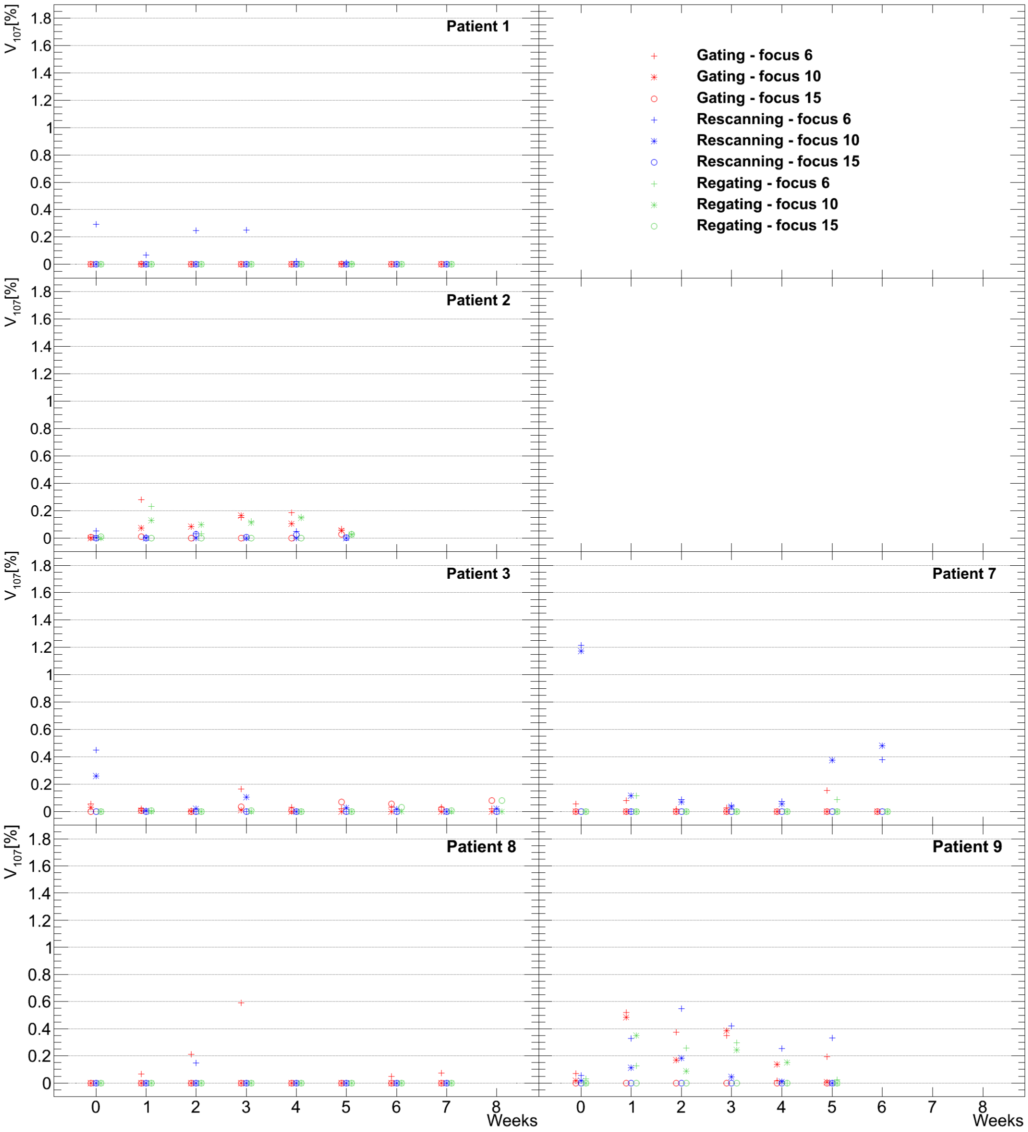

Figure E.20.: Detailed results yielded by gating, perfect rescanning (PRSC) and perfect regating (PRGT) regarding overdose V_{107}.

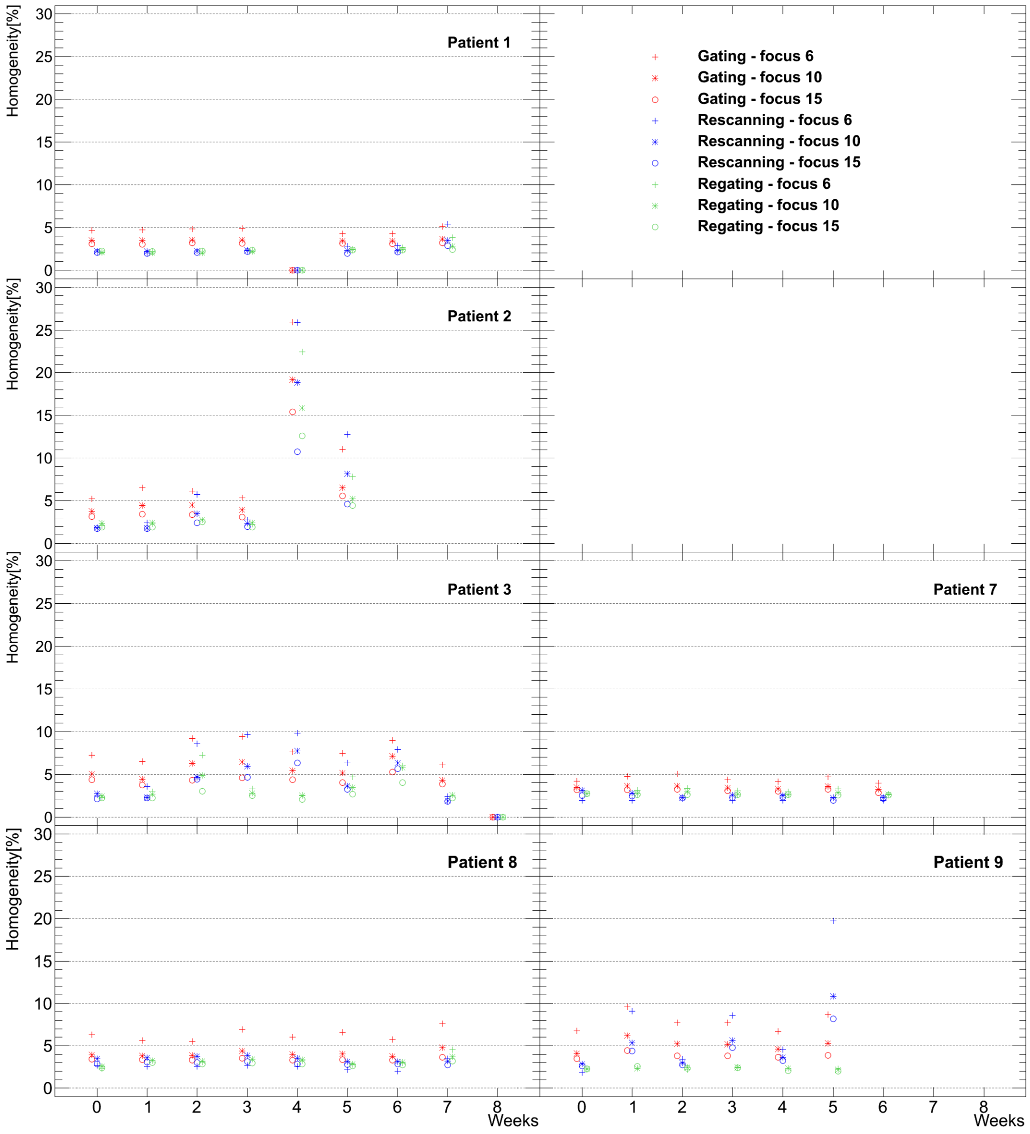

Figure E.21.: Detailed results yielded by gating, perfect rescanning (PRSC) and perfect regating (PRGT) regarding homogeneity.

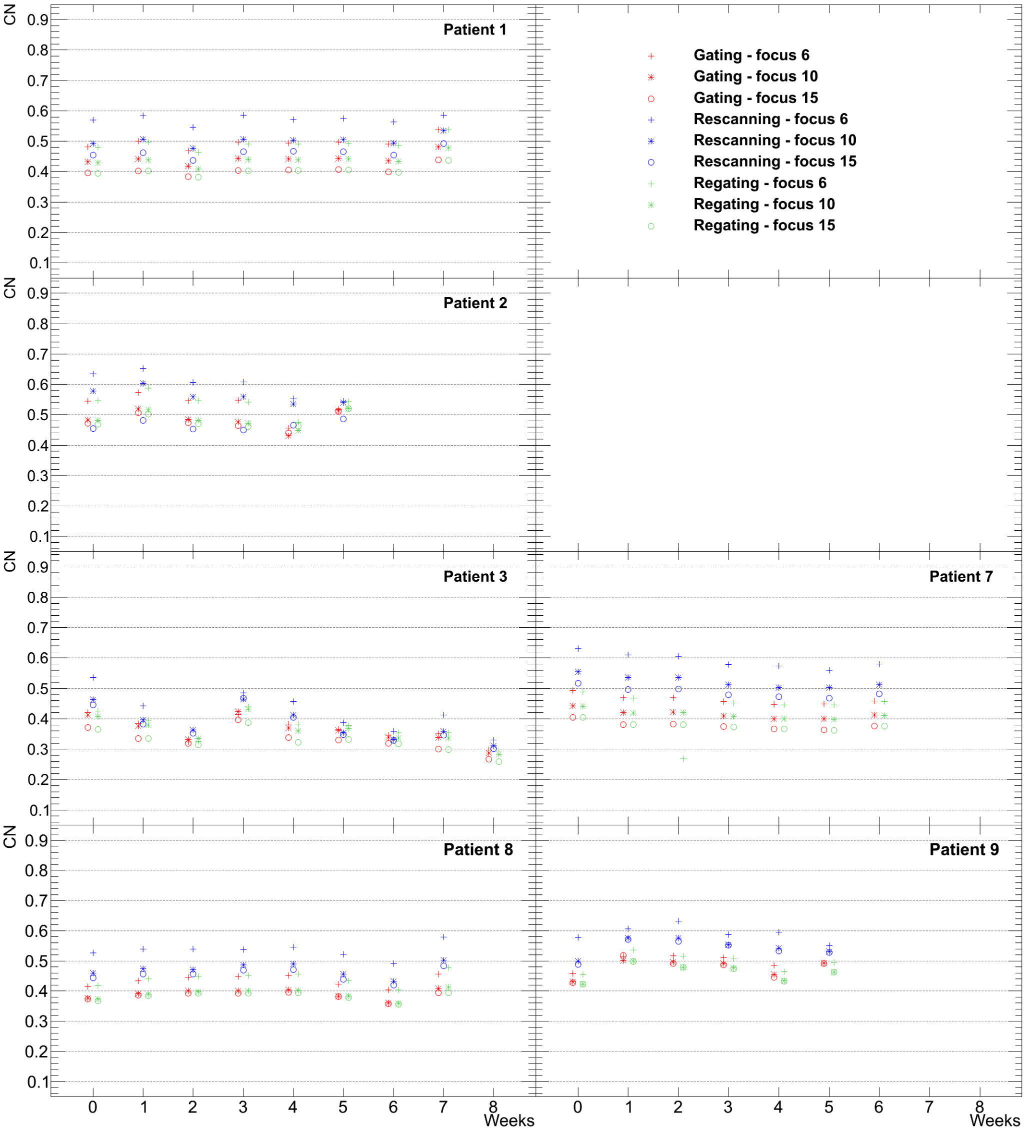

Figure E.22.: Detailed results yielded by gating, perfect rescanning (PRSC) and perfect regating (PRGT) regarding the conformity number (CN).

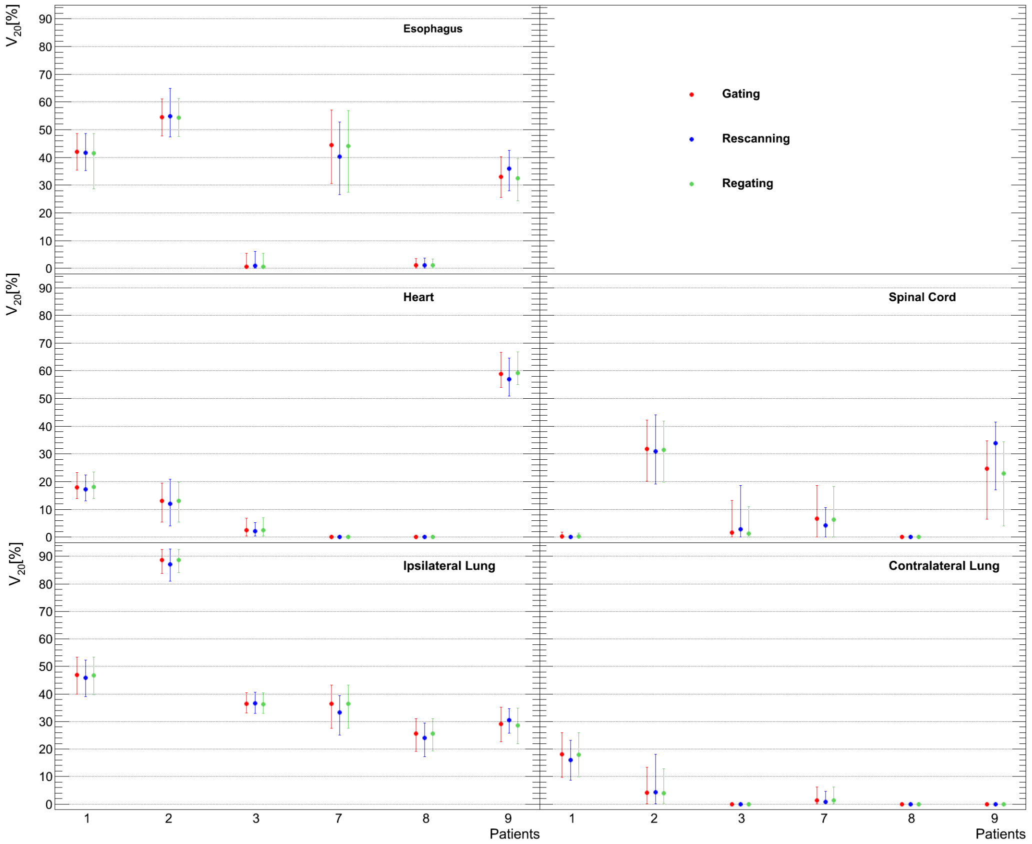

Figure E.23.: Detailed results yielded by gating, perfect rescanning (PRSC) and perfect regating (PRGT) regarding the 20% dose volume V_{20} in the organs at risk (OARs).

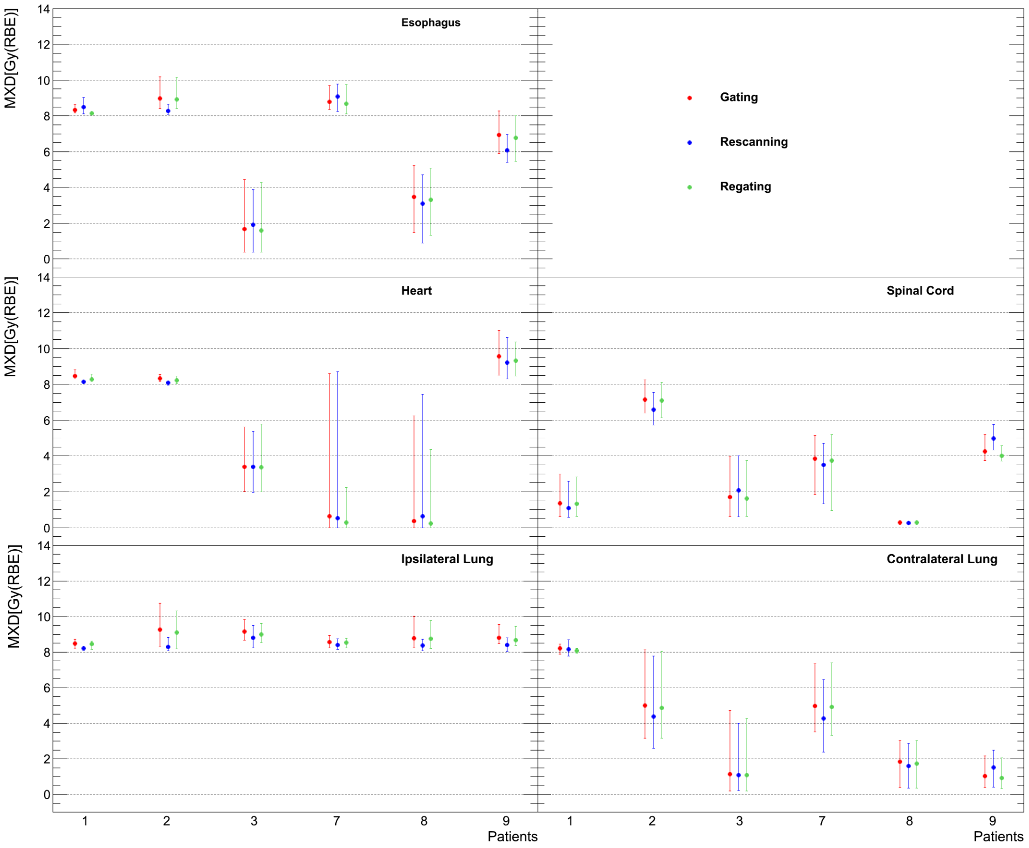

Figure E.24.: Detailed results yielded by gating, perfect rescanning (PRSC) and perfect regating (PRGT) regarding the maximal dose point (MXD) in the organs at risk (OARs).

E.3 Simulation of a clinical study

E.3.1 Investigation of robust field angles

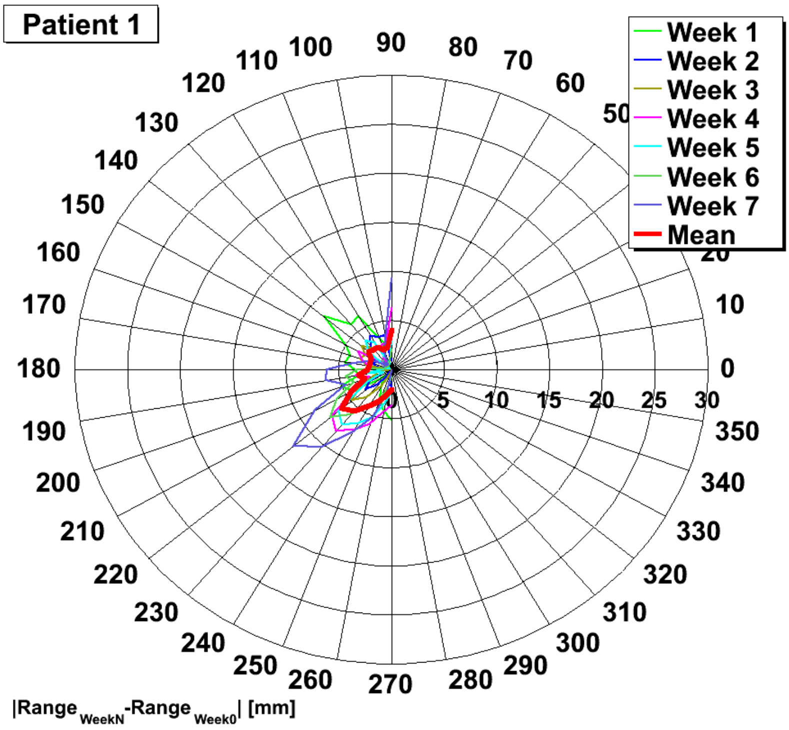

Figure E.25.: Weekly water-equivalent tumor median range differences for patient 1.

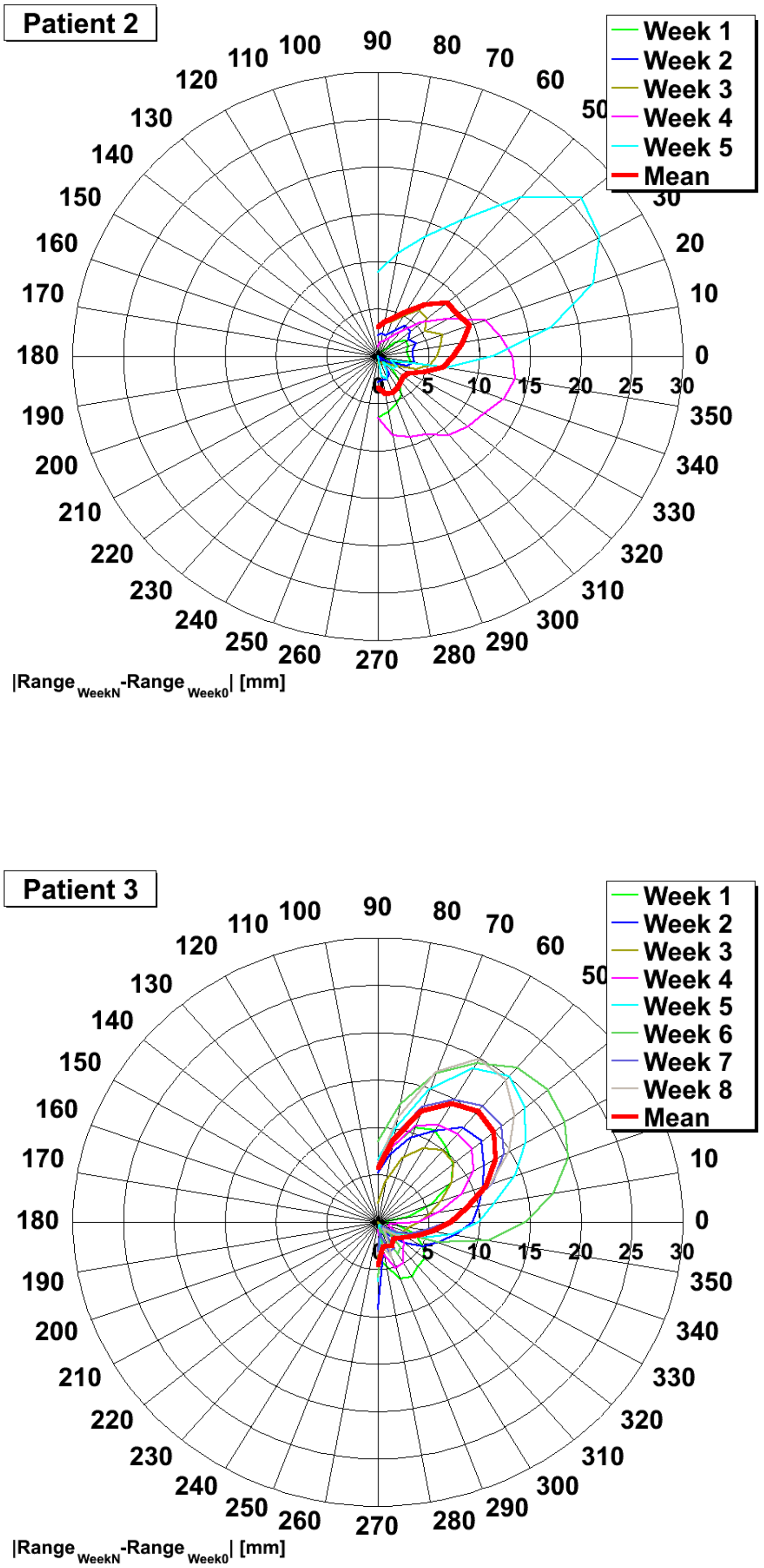

Figure E.26.: Weekly water-equivalent tumor median range differences for patients 2 and 3.

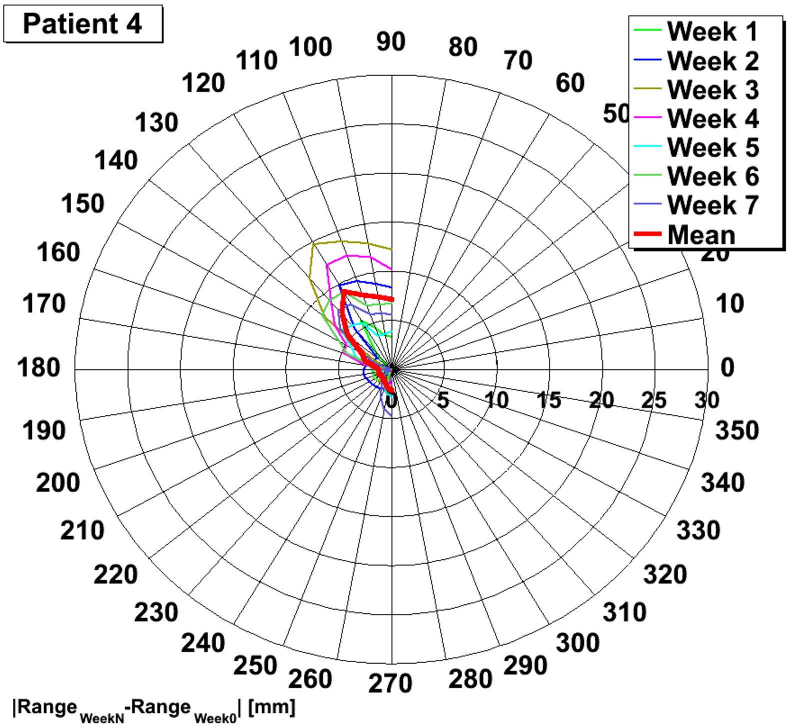

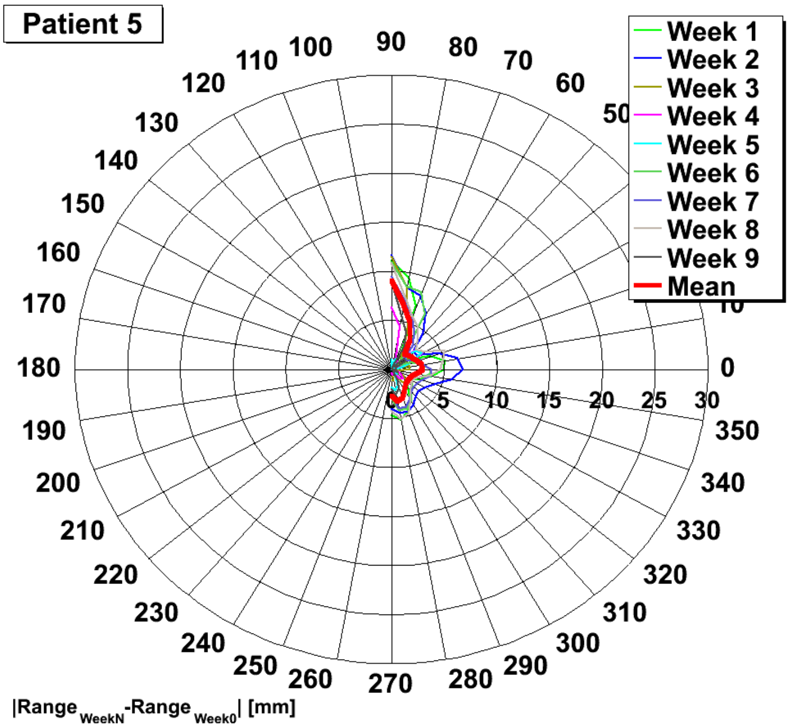

Figure E.27.: Weekly water-equivalent tumor median range differences for patients 4 and 5.

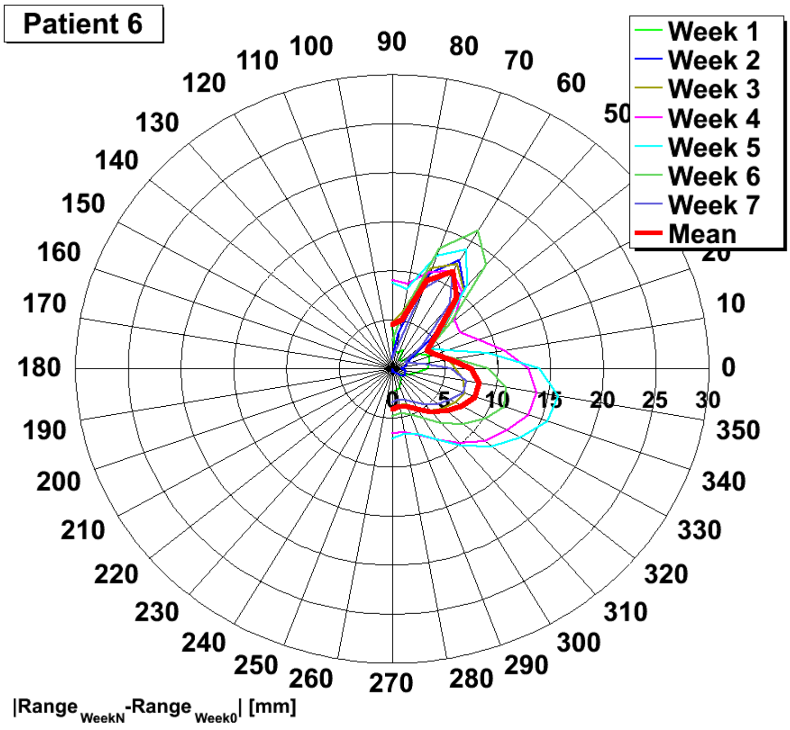

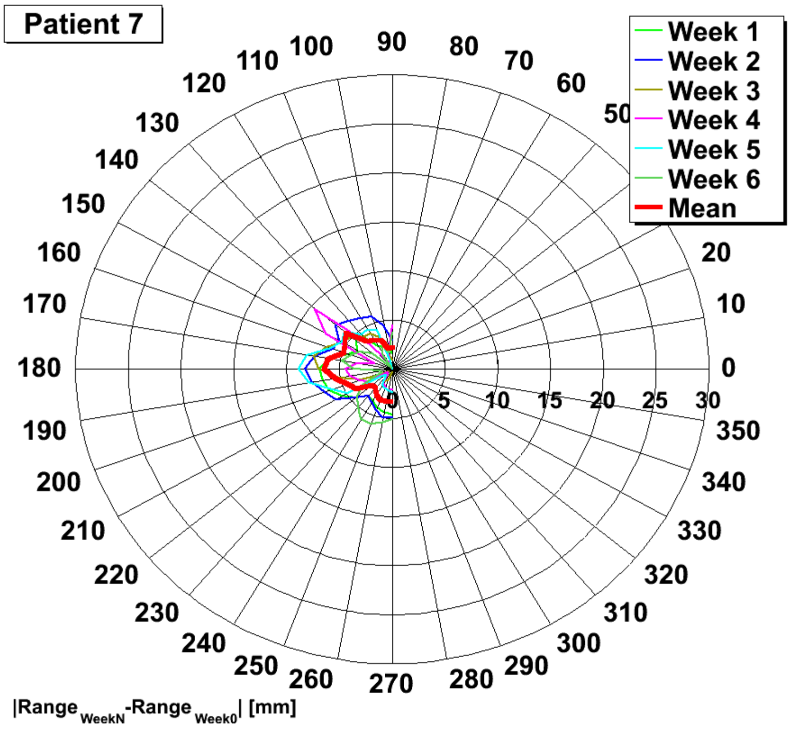

Figure E.28.: Weekly water-equivalent tumor median range differences for patients 6 and 7.

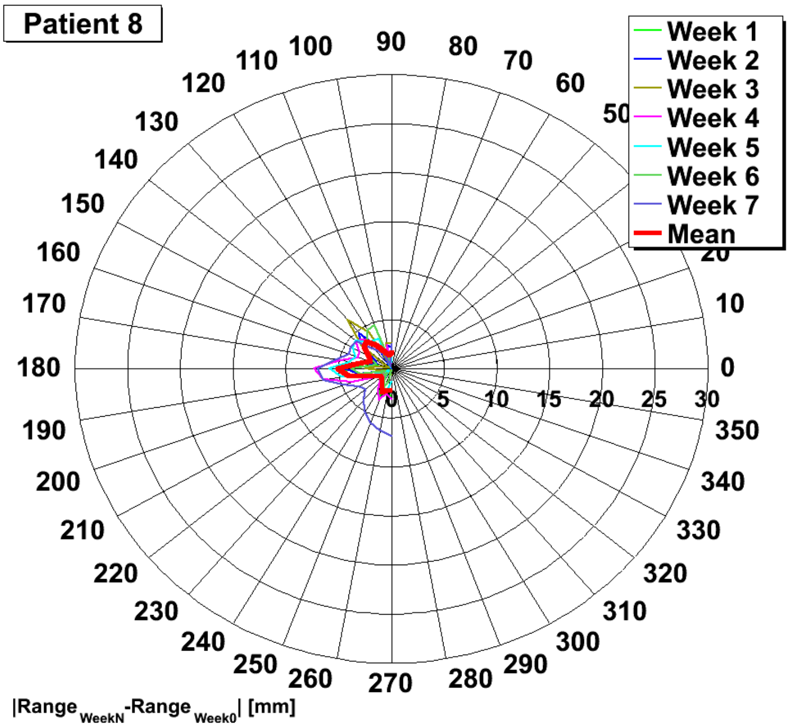

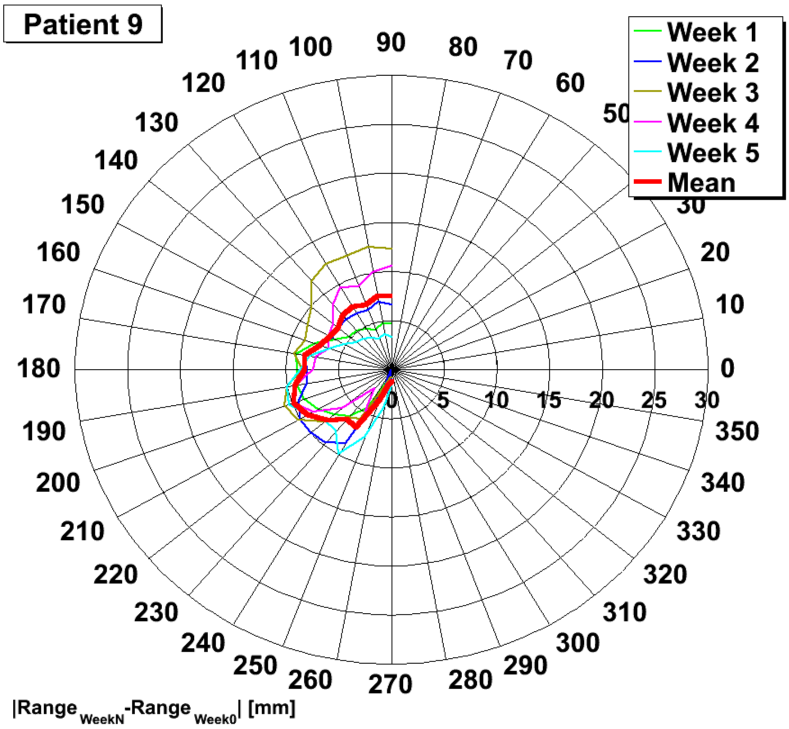

Figure E.29.: Weekly water-equivalent tumor median range differences for patients 8 and 9.

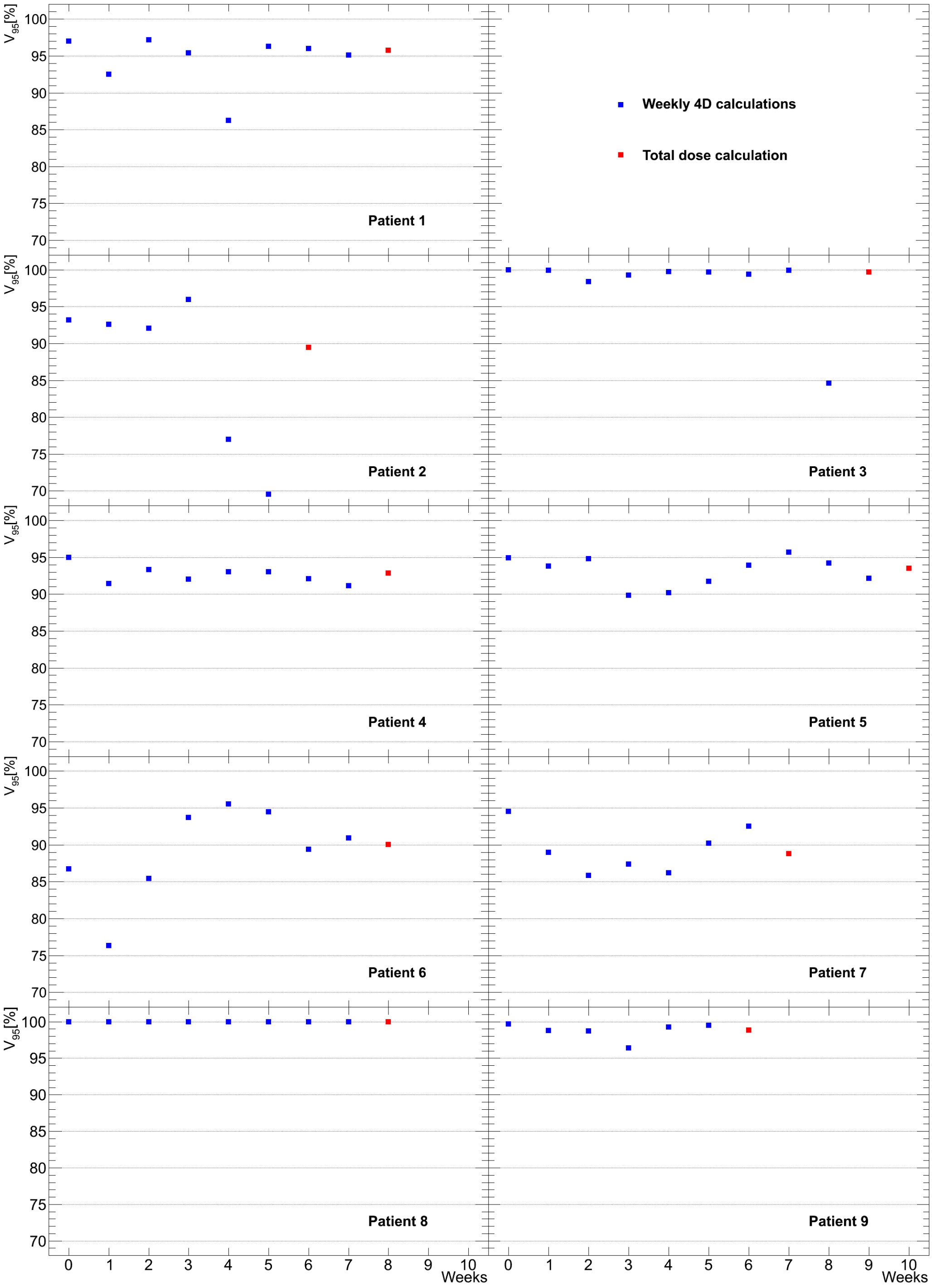

Figure E.30.: Detailed results yielded by gating, perfect rescanning (PRSC) and perfect regating (PRGT) regarding target coverage V_{95}.

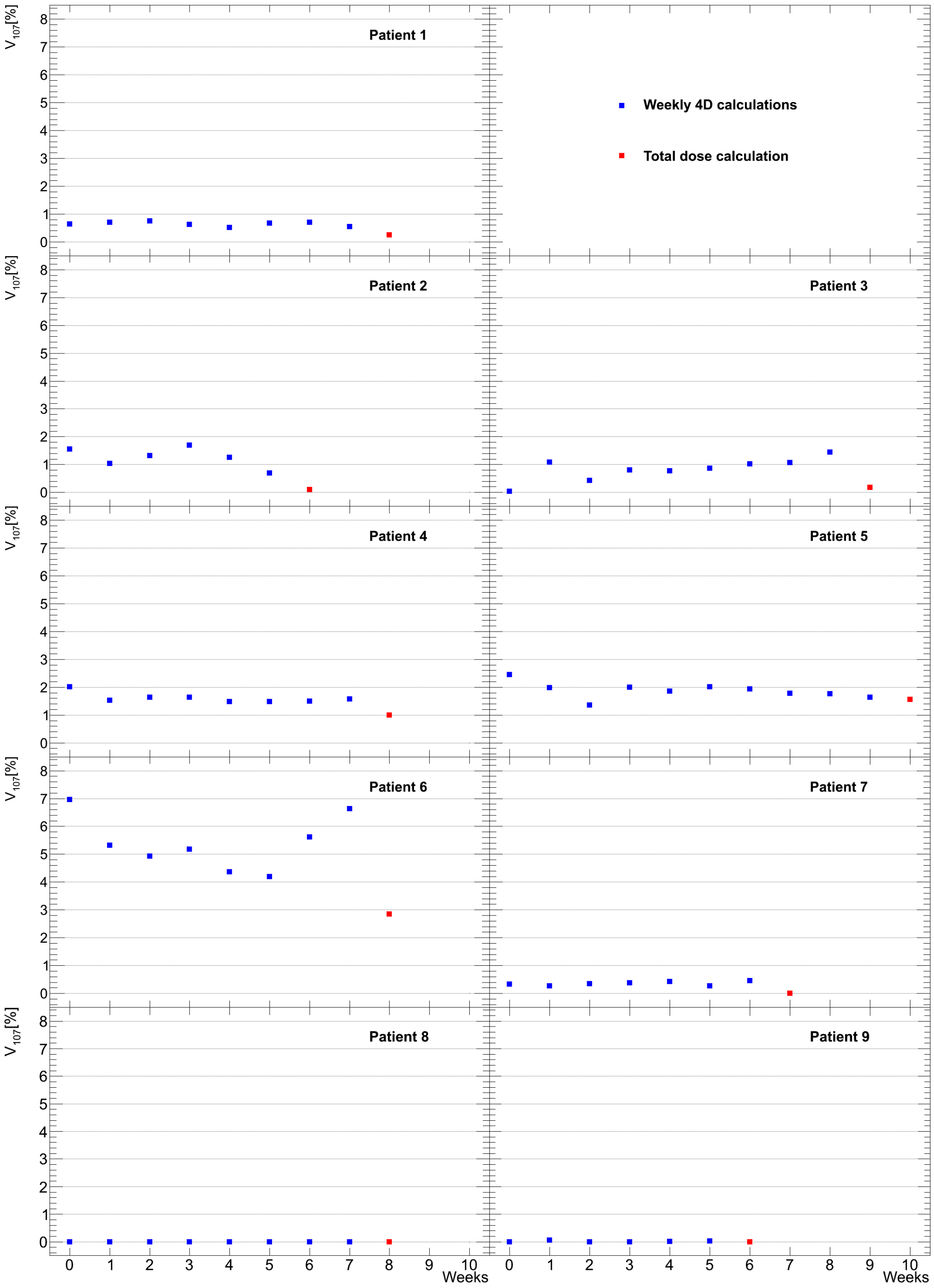

Figure E.31.: Detailed results yielded by gating, perfect rescanning (PRSC) and perfect regating (PRGT) regarding overdose V_{107}.

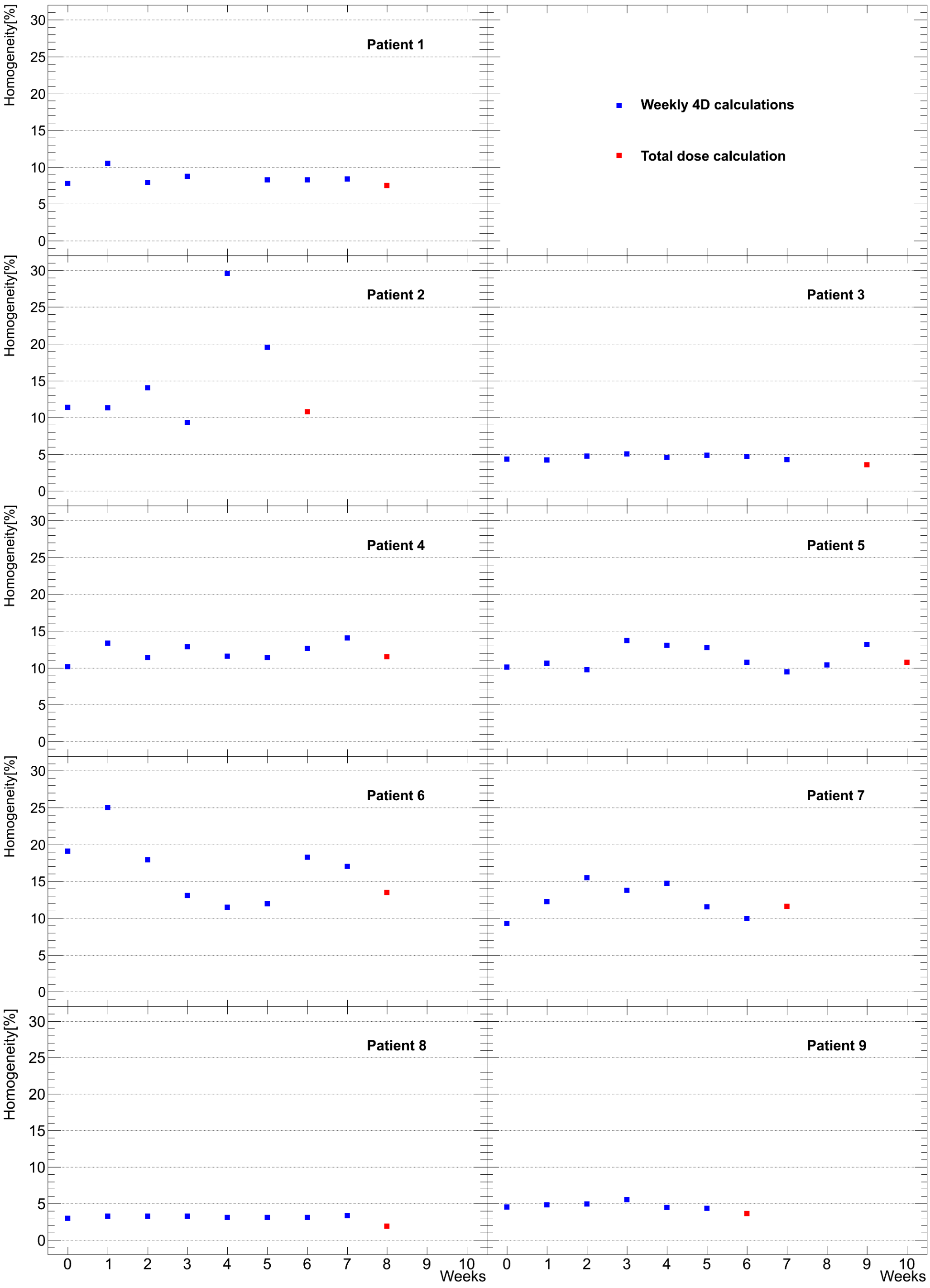

Figure E.32.: Detailed results yielded by gating, perfect rescanning (PRSC) and perfect regating (PRGT) regarding homogeneity.

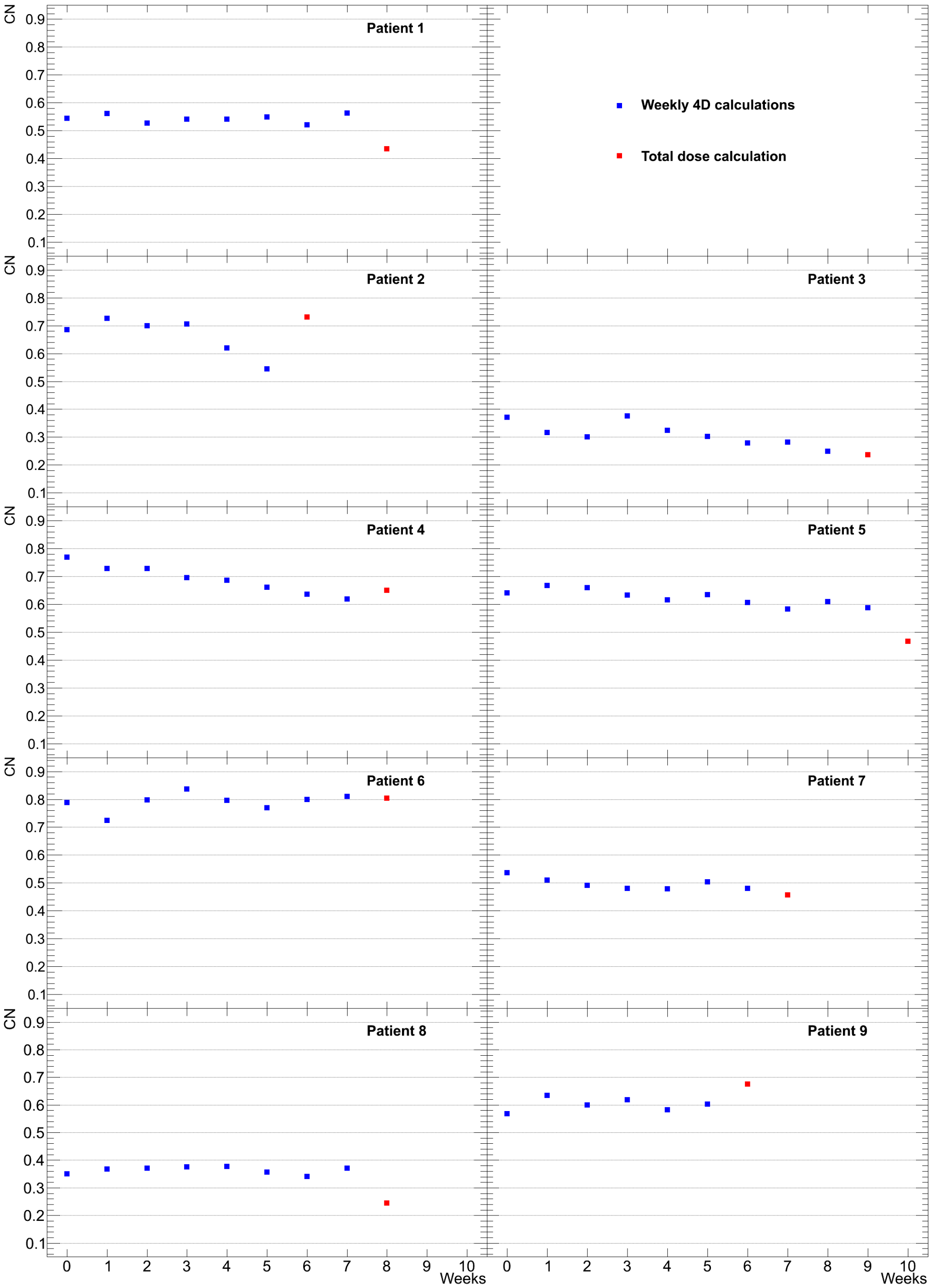

Figure E.33.: Detailed results yielded by gating, perfect rescanning (PRSC) and perfect regating (PRGT) regarding the conformity number (CN).

Bibliography

ACS (2011). Global Cancer, Facts & Figures, 2nd Edition, American Cancer Society (Atlanta).

Ahlen, S. P. (1980). Theoretical and experimental aspects of the enery loss of relativistic heavily ionizing particles. *Rev. Mod. Phys.*, 52(1):121.

Albertini, F., Hug, E. B., and Lomax, A. J. (2010). The influence of the optimzation starting conditions on the robustness of intensity-modulated proton therapy plans. *Phys. Med. Biol.*, 55(10):2863–2878.

Albertini, F., Hug, E. B., and Lomax, A. J. (2011). Is it necessazy to plan with safety margins for actively scanned proton therapy? *Phys. Med. Biol.*, 56(14):4399–4416.

Amaldi, H. and Kraft, G. (2005). Recent applications of synchrotrons in cancer therapy with carbon ions. *europhysics news*, 36(4):114–118.

Ando, K., Koike, S., Nojima, K., Chen, Y. J., Ohira, C., Ando, A., Kobayashi, N., ohbuchi, T., Shimizu, W., and Kanai, T. (1998). Mouse skin reactions following fractionated irradiation with carbon ions. *Int. J. Radiat. Biol.*, 74(1):129–138.

Astrahan, M. (2008). Some implications of linear-quadraticlinear radiation dose-response with regard to hypofractionation. *Med. Phys.*, 35(9):4161–4172.

Balter, J. M., Lam, K. L., McGinn, C. J., Lawrence, T. S., and Haken, R. K. T. (1998). Improvement of ct-based treatment-planning models of abdominal targets using static exhale imaging. *Int. J. Radiat. Oncol. Biol. Phys.*, 41(4):939–943.

Barkas, H. W. (1963). *Nuclear Research Emulsions*, volume I. Academic Press New York and London.

Belli, M., Cera, F., Cherubini, R., Dalla, V. M., Haque, A. M., Ianzini, F., Moschini, G., Sapora, O., Simone, G., Tabocchini, M. A., and Tiveron, P. (1998). Rbe-let relationships for cell inactivation and mutation induced by low energy protons in v79 cells: Further results at the lnl facility. *Int. J. Radiat. Biol.*, 74(4):501–509.

Benedict, S. H., Yenice, K. M., Followill, D., Galvin, J. M., Hinson, W., Kavanagh, B., Keall, P., Lovelock, M., Meeks, S., Papiez, L., Purdie, T., Schell, R. S. M. C., Salter, B., Schlesinger, D. J., Shiu, A. S., Solberg, T., Song, D. Y., Stieber, V., Timmerman, R., Tome, W. A., Verellen, D., Wang, L., and Yin, F. F. (2010). Stereotactic body radiation therapy: the report of aapm task group 101. *Med. Phys.*, 37(8):501–509.

Berbeco, R. I., Jiang, S. B., Sharp, G. C., Chen, G. T. Y., Mostafavi, H., and Shirato, H. (2004). Integrated radiotherapy imaging system (IRIS): design considerations of tumour tracking with linac gantry-mounted diagnostic x-ray systems with flat-panel detectors. *Phys. Med. Biol.*, 49(2):243–255.

Berbeco, R. I., Mostafavi, H., Sharp, G. C., and Jiang, S. B. (2005a). Towards fluoroscopic respiratory gating for lung tumours without radiopaque markers. *Phys. Med. Biol.*, 50(19):4481–4490.

Berbeco, R. I., Neicu, T., Rietzel, E., Chen, G. T., and Jiang, S. B. (2005b). A technique for respiratory-gated radiotherapy treatment verification with an epid in cine mode. *Phys. Med. Biol.*, 50(16):3669–3679.

Bert, C. and Durante, M. (2011). Motion in radiotherapy: particle therapy. *Phys. Med. Biol.*, 56(16):R113–R144.

Bert, C., Gemmel, A., Saito, N., Chaudhri, N., Schardt, D., Durante, M., Kraft, G., and Rietzel, E. (2010). Dosimetric precision of an ion beam tracking system. *Radiot. Oncol.*, 5(1):61.

Bert, C., Gemmel, A., Saito, N., and Rietzel, E. (2009). Gated irradiation with scanned particle beams. *Int. J. Radiat. Oncol. Biol. Phys.*, 73(4):1270–1275.

Bert, C., Grözinger, S. O., and Rietzel, E. (2008). Quantification of interplay effects of scanned particle beams and moving targets. *Phys. Med. Biol.*, 34(9):2253–2265.

Bert, C. and Rietzel, E. (2007). 4d treatment planning for scanned ion beams. *Radiat. Oncol.*, 2:24.

Bert, C., Saito, N., Schmidt, A., Chaudhri, N., Schardt, D., and Rietzel, E. (2007). Target motion tracking with a scanned particle beam. *Med. Phys.*, 34(12):4768–4771.

Bethe, H. (1930). Zur Theorie des Durchgangs schneller Korpuskularstrahlung durch Materie. *Annalen der Physik*, 5(5):325–400.

Bloch, F. (1933a). Bremsvermögen von Atomen mit mehreren Elektronen. *Zeitschrift für Physik*, 81(5):363–376.

Bloch, F. (1933b). Zur Bremsung rasch bewegter Teilchen beim Durchgang durch Materie. *Annalen der Physik*, 5(16):285–321.

Bohr, N. (1940). Scattering and stopping of fission fragments. *Phys. Rev.*, 58(7):654–655.

Bortfeld, T., Jiang, S. B., and Rietzel, E. (2004). Effects of motion on the total dose distribution. *Semin. Radiat. Oncol.*, 14(1):41–51.

Britton, K. R., Starkschall, G., Tucker, S. L., Pan, T., Nelson, C., Chang, J. Y., Cox, J. D., Mohan, R., and Komaki, R. (2007). Assessment of gross tumor volume regression and motion changes during radiotherapy for non-small-cell lung cancer as measured by four-dimensional computed tomography. *Int. J. Radiat. Oncol. Biol. Phys.*, 68(4):1036–1046.

Brock, K. K. (2010). Results of a multi-institution deformable registration accuracy study (midras). *Int. J. Radiat. Oncol. Biol. Phys.*, 76(2):583–596.

Brock, K. K., Dawson, L. A., Sharpe, M. B., Moseley, D. J., and Jaffray, D. A. (2006). Feasibility of a novel deformable image registration technique to facilitate classification, targeting, and monitoring of tumor and normal tissue. *Int. J. Radiat. Oncol. Biol. Phys.*, 64(4):1245–1254.

Brown, W. T., Wu, X., Fayad, F., Fowler, J. F., Amendola, B. E., Garcia, S., Han, H., de la, Z. A., Bossart, E., Huang, Z., and Schwade, J. G. (2007). Cyberknife radiosurgery for stage I lung cancer: results at 36 months. *Clin. Lung Cancer.*, 8(8):488–492.

Chatterjee, A. and Schaefer, H. J. (1976). Microdosimetric structure of heavy ion tracks in tissue. *Radiat. Environ. Biophys.*, 13:215–227.

Chiba, T., Tokuuye, K., Matsuzaki, Y., Sugahara, S., Chuganji, Y., Kagei, K., Shoda, J., Hata, M., Abei, M., Tanaka, H. I. N., and Akine, Y. (2005). Proton beam therapy for hepatocellular carcinoma: a retrospective review of 162 patients. *Clin. Cancer Res.*, 11(10):3799–3805.

Chu, W. T., Ludewigt, B. A., and Renner, T. R. (1993). Instrumentation for treatment of cancer using proton and light-ion beams. *Rev. Sci. Instrum.*, 64(8):2055–2122.

Cox, J. D., Stetz, J., and Pajak, T. F. (1995). Toxicty criteria of the radiation therapy oncology group (rtog) and the european organization for research and treatment of cancer (eortc). *Int. J. Radiat. Oncol. Biol. Phys.*, 31(5):1341–1346.

Cui, Y., Dy, J. G., Alexander, B., and Jiang, S. B. (2008). Fluoroscopic gating without implanted fiducial markers for lung cancer radiotherapy based on support vector machines. *Phys. Med. Biol.*, 53(16):N315–N327.

Cui, Y., Dy, J. G., Sharp, G. C., Alexander, B., and Jiang, S. B. (2007a). Multiple template-based fluoroscopic tracking of lung tumor mass without implanted fiducial markers. *Phys. Med. Biol.*, 52(20):6229–6242.

Cui, Y., Dy, J. G., Sharp, G. C., Alexander, B., and Jiang, S. B. (2007b). Robust fluoroscopic respiratory gating for lung cancer radiotherapy without implanted fiducial markers. *Phys. Med. Biol.*, 52(3):741–755.

Durante, M. and Loeffler, J. S. (2010). Charged particles in radiation oncology. *Nat. Rev. Clin. Oncol.*, 7(1):37–43.

Elsaesser, T. and Scholz, M. (2007). Cluster effects within the local effect model. *Radiat. Res.*, 167(3):319–329.

Engelsman, M., Rietzel, E., and Kooy, H. M. (2006). Four-dimensional proton treatment planning for lung tumors. *Int. J. Radiat. Oncol. Biol. Phys.*, 64(5):1589–1595.

Fano, U. (1963). Penetration of protons, alpha particles, and mesons. *Ann. Rev. Nucl. Sci.*, 13(1):1–66.

Fassi, A., Schaerer, J., Fernandes, M., Riboldi, M., Sarrut, D., and Baroni, G. (2014). Tumor tracking method based on a deformable 4d ct breathing motion model driven by an external surface surrogate. *Int. j. Radiat. Oncol. Biol. Phys.*, 88(1):182–188.

Ford, E. C., Mageras, G. S., Yorke, E., and Ling, C. C. (2003). Respiration-correlated spiral CT: A method of measuring respiratory-induced anatomic motion for radiation treatment planning. *Med. Phys.*, 30(1):88–97.

Fowler, J. F. (2003). The linear-quadratic formula and progress in fractionated radiotherapy. *Br. J. Radiol.*, 62(740):679–694.

Furukawa, T., Inaniwa, T., Sato, S., Shirai, T., Mori, S., Takeshita, E., Mizushima, K., Himukai, T., and Noda, K. (2010). Moving target irradiation with fast rescanning and gating in particle therapy. *Med. Phys.*, 37(9):4874–4879.

Furukawa, T., Inaniwa, T., Sato, S., Tomitani, T., Minohara, S., Noda, K., and Kanai, T. (2007). Design study of a raster scanning system for moving target irradiation in heavy-ion radiotherapy. *Med. Phys.*, 34(3):1085–1097.

Furusawa, Y., Fukutsu, K., Aoki, M., Itsukaichi, H., Eguchi-Kasai, K., Ohara, H., Yatagai, F., Kanai, T., and Ando, K. (2000). Inactivation of aerobic and hypoxic cells from three different cell lines by accelerated (3)he-, (12)c- and (20)ne-ion beams. *Radiat. Res.*, 154:485–496.

Gemmel, A., Rietzel, E., Kraft, G., Durante, M., and Bert, C. (2011). Calculation and experimental verification of the rbe-weighted dose for scanned ion beams in the presence of target motion. *Phys. Med. Biol.*, 56(23):7337–7351.

Goldhaber, A. S. and Heckman, H. H. (1978). High energy interactions of nuclei. *Ann. Rev. Nucl. Part. Sci.*, 28(1):161–205.

Gottschalk, B., Koehler, A. M., Schneider, R. J., Sisterson, J. M., and Wagner, M. S. (1993). Multiple coulomb scattering of 160 MeV protons. *Nucl. Instrum. Meth. B*, 74(4):467–490.

Gottschalk, B. and Wagner, M. S. (1989). Contoured scatterer for proton dose flattening. *Harvard Cyclotron Laboratory Technical Note*.

Graeff, C., Durante, M., and Bert, C. (2012). Motion mitigation in intensity modulated particle therapy by internal target volumes covering range changes. *Med. Phys.*, 39(10):6004–6013.

Grimm, J., LaCouture, T., Croce, R., Inhwan, Y., Zhu, Y., and Xue, J. (2011). Dose tolerance limits and dose volum histogram evaluation for stereostatic body radiotherapy. *J. Appl. Clin. Med. Phys.*, 12(2):267–292.

Groezinger, S. O., Bert, C., Haberer, T., Kraft, G., and Rietzel, E. (2008). Motion compensation with a scanned ion beam: a technical feasibility study. *Radiat. Oncol.*, 3(34).

Groezinger, S. O., Li, Q., Rietzel, E., Haberer, T., and Kraft, G. (2004). 3D online compensation of target motion with scanned particle beam. *Radiother. Oncol.*, 73 Suppl 2:S77–S79.

Groezinger, S. O., Rietzel, E., Li, Q., Bert, C., Haberer, T., and Kraft, G. (2006). Simulations to design an online motion compensation system for scanned particle beams. *Phys. Med. Biol.*, 51(14):3517–3531.

Guerrero, M. and Li, X. A. (2004). Extending the linear-quadratic model for large fraction doses pertinent to stereotactic radiotherapy. *Phys. Med. Biol.*, 49(20):4825–4835.

Haberer, T., Becher, W., Schardt, D., and Kraft, G. (1993). Magnetic scanning system for heavy ion therapy. *Nucl. Instrum. Meth. A*, 330:296–305.

Hall, E. J. and Garcia, A. J. (2011). *Radiobiology for the Radiologist*. Lippincott Williams & Wilkins, 7. edition.

Hüfner, J. (1985). Heavy fragments produced in proton-nucleus and nucleus-nucleus collisions at relativistic energies. *Phys. Rep.*, 125(4):129–185.

Hui, Z., Zhang, X., Starkschall, G., Li, Y., Mohan, R., Komaki, R., Cox, J. D., and Chang, J. Y. (2008). Effects of interfractional motion and anatomic changes on proton therapy dose distribution in lung cancer. *Int. J. Radiat. Oncol. Biol. Phys.*, 72(5):1385–1395.

IAEA (2008). Technical reports series no. 461, relative biological effectiveness in ion beam therapy. *Technical reports of the IAEA*.

ICRU (1993). ICRU report 50: Prescribing, recording and reporting proton-beam therapy. *Journal of the ICRU*.

ICRU (1999). ICRU report 62: Prescribing, recording and reporting proton-beam therapy (supplement to ICRU report 50). *Journal of the ICRU*.

ICRU (2007). ICRU report 78: Prescribing, recording and reporting proton-beam therapy. *Journal of the ICRU*.

Iwata, H., Murakami, M., Demizu, Y., Miyawaki, D., Terashima, K., Niwa, Y., Mima, M., Akagi, T., Hishikawa, Y., and Shibamoto, Y. (2010). High-dose proton therapy and carbon-ion therapy for stage I nonsmall cell lung cancer. *Cancer*, 116(10):2476–2485.

Jäkel, O., Karger, C. P., and Debus, J. (2008). The future of heavy ion therapy. *Med. Phys.*, 35(12):5653–5663.

Janssens, G., de Xivry, J. O., Fekkes, S., Dekker, A., Macq, B., Lambin, P., and can Elmpt, W. (2009). Effects of interfractional motoin and anatomic changes on proton therapy dose distribution in lung cancer. *Med. Phys.*, 36(9):4268–4276.

Jermann, M. (2014). Particle therapy statistics in 2013. *Int. J. Particle Ther.*, 1(1):40–43.

Kagawa, K., Murakami, M., Hishikawa, Y., Abe, M., Akagi, T., Yanou, T., Kagiya, G., Furusawa, Y., Ando, K., Nojima, K., Aoki, M., and Kanai, T. (2002). Preclinical biological assessment of proton and carbon ion beams at hyogo ion beam medical center. *Int. J. Radiat. Oncol. Biol. Phys.*, 54(3):928–938.

Kanai, T., Endo, M., Minohara, S., Miyahara, N., Koyama-ito, H., Tomura, H., Matsufuji, N., Futami, Y., Fukumura, A., and e. a. Takeshi, H. (1999). Biophysical characteristics of HIMAC clinical irradiation system for heavy-ion radiation therapy. *Int. J. Radiat. Oncol. Biol. Phys.*, 44(1):201–210.

Kanai, T., Furusawa, Y., Fukutsu, K., Itsukaichi, H., Eguchi-Kasai, K., and Ohara, H. (1997). Irradiation of mixed beam and design of spread-out bragg peak for heavy-ion radiotherapy. *Radiat. Res.*, 147(1):78–85.

Kanai, T., Kanematsu, N., Minohara, S., Komori, M., Torikoshi, M., Asakura, H., Ikeda, N., Uno, T., and Takei, Y. (2006). Commissioning of a conformal irradiation system for heavy-ion radiotherapy using a layer-stacking method. *Med. Phys.*, 33(8):2989–2997.

Kanai, T., Kawachi, K., Matsuzawa, H., and Inada, T. (1983). Three-dimensional beam scanning for proton therapy. *Nucl. Instrum. Methods Phys. Res.*, 214(2-3):491–496.

Kase, Y., Kanai, T., Matsufuji, N., Furusawa, Y., Elsasser, T., and Scholz, M. (2008). Biophysical calculation of cell survival probabilities using amorphous track structure models for heavy-ion irradiation. *Phys. Med. Biol.*, 53(1):37–59.

Katz, R. and Cucinotta, F. A. (1999). Tracks to therapy. *Radiat. Meas.*, 31:379–388.

Keall, P. J. (2004). 4-dimensional computed tomography imaging and treatment planning. *Semin. Radiat. Oncol.*, 14(1):81–90.

Keall, P. J., Kini, V. R., Vedam, S. S., and Mohan, R. (2001). Motion adaptive x-ray therapy: a feasibility study. *Phys. Med. Biol.*, 46(1):1–10.

Kilby, W., Dooley, J. R., Kuduvalli, G., Sayeh, S., and C. R. Maurer, J. (2010). The cyberknife robotic radiosurgery system in 2010. *Technol. Cancer Res. Treat.*, 9(5):433–452.

Knopf, A., Hug, E., and Lomax, A. (2010). Scanned proton radiotherapy for mobile targets - which plan characteristics require rescanning, which maybe not? In *Proc. 16th Int. Conf. on the Use of Computers in Radiation Therapy (Amsterdam)*.

Knopf, A. C., Boye, D., Lomax, A., and Mori, S. (2013). Adequate margin definition for scanned particle therapy in the incidence of intrafractional motion. *Phys. Med. Biol.*, 58(17):6079–6094.

Knopf, A. C., Hong, T. S., and Lomax, A. (2011). Scanned proton radiotherapy for mobile targets - the effectiveness of re-scanning in the context of different treatment planning approaches and for different motion characteristics. *Phys. Med. Biol.*, 56(22):7257–7271.

Koehler, A. M., Schneider, R. J., and Sisterson, J. M. (1975). Range modulators for protons and heavy ions. *Nuclear Instruments and Methods*, 131(3):437–440.

Koehler, A. M., Schneider, R. J., and Sisterson, J. M. (1977). Flattening of proton dose distributions for large-field radiotherapy. *Medical Physics*, 4(4):297–301.

Korreman, S. S. (2012). Motion in radiotherapy: photon therapy. *Phys. Med. Biol.*, 57(23):R161–R191.

Koto, M., Miyamoto, T., Yamamoto, N., Nishimura, H., Yamada, S., and Tsujii, H. (2004). Local control and recurrence of stage I non-small cell lung cancer after carbon ion radiotherapy. *Radiother. Oncol.*, 71(2):147–156.

Kraft, G. (2000). Tumor therapy with heavy charged particles. *Prog. Part. Nucl. Phys.*, 45(s2):s473–s544.

Kraft, G. (2007). Tumor therapy with heavy ions. GSI document.

Kraft, G. and Kraft, S. D. (2009). Research needed for improving heavy ion-therapy. *New Journal of Physics*, 11(2):025001.

Krämer, M. (1995). Calculations of heavy-ion track structure. *Nucl. Instrum. Methods Phys. Res.*, 105(1-4):14–20.

Krämer, M., Jäkel, O., Haberer, T., Kraft, G., Schardt, D., and Weber, U. (2000). Treatment planning for heavy-ion radiotherapy: physical beam model and dose optimization. *Phys. Med. Biol.*, 45(11):3299–3317.

Krämer, M. and Scholz, M. (2000). Treatment planning for heavy-ion radiotherapy: calculation and optimization of biologically effective dose. *Phys. Med. Biol.*, 45(11):3319–3330.

Lambert, J., Suchowerska, N., McKenzie, D. R., and Jackson, M. (2005). Intrafractional motion during proton beam scanning. *Phys. Med. Biol.*, 50(20):4853–4862.

Langen, K. M. and Jones, D. T. L. (2001). Organ motion and its management. *Int. J. Radiat. Oncol. Biol. Phys.*, 50(1):265–278.

Leith, J. T., McDonald, M., Powers-Risius, P., and anf J. Howard, S. F. B. (1982). Response of rat spinal cord to single and fractionated doses of accelerated heavy ions. *Radiat. Res.*, 89:176–193.

Liu, H. H., Balter, P., Tutt, T., Choi, B., Zhang, J., Wang, C., Chi, M., Luo, D., Pan, T., Hunjan, S., Starkschall, G., Rosen, I., Prado, K., Liao, Z., Chang, J., Komaki, R., Cox, J. D., Mohan, R., and Dong, L. (2007). Assessing respiration-induced tumor motion and internal target volume using four-dimensional computed tomography for radiotherapy of lung cancer. *Int. J. Radiat. Oncol. Biol. Phys.*, 68(2):531–540.

Lomax, A. J. (2008a). Intensity modulated proton therapy and its sensitivity to treatment uncertainties 1: the potential effects of calculational uncertainties. *Phys. Med. Biol.*, 53(4):1027–1042.

Lomax, A. J. (2008b). Intensity modulated proton therapy and its sensitivity to treatment uncertainties 2: the potential effects of inter-fraction and inter-field motions. *Phys. Med. Biol.*, 53(4):1043–1056.

Lu, H. M., Brett, R., Sharp, G., Safai, S., Jiang, S., Flanz, J., and Kooy, H. (2007). A respiratory-gated treatment system for proton therapy. *Med. Phys.*, 34(8):3273–3278.

Lujan, A. E., Larsen, E. W., Balter, J. M., and Haken, R. K. T. (1999). A method for incorporating organ motion due to breathing into 3D dose calculations. *Med. Phys.*, 26(5):715–720.

Lynch, W. G. (1987). Nuclear fragmentation in proton- and heavy-ion-induced reactions. *Ann. Rev. Nucl. Part. Sci.*, 37(1):493–535.

Mampuya, W. A., Nakamura, M., Matsuo, Y., Ueki, N., , Iizuka, Y., Fujimoto, T., Yano, S., Monzen, H., Mizowaki, T., and Hiraoka, M. (2013). Interfraction variation in lung tumor position with abdominal compression during stereotactic body radiotherapy. *Med. Phys.*, 40(9):091718.

McClelland, J. R., Hughes, S., Modat, M., Qureshi, A., Ahmad, S., Landau, D. B., Ourselin, S., and Hawkes, D. J. (2011). Inter-fraction variations in respiratory motion models. *Phys. Med. Biol.*, 56(1):251–272.

Men, C., Gu, X., Choi, D., Majumdar, A., Zheng, Z., Mueller, K., and Jiang, S. B. (2009). Gpu-based ultrafast imrt plan optimization. *Phys. Med. Biol.*, 54(21):6565–6573.

Minohara, S., Kanai, T., Endo, M., and Kawachi, K. (1993). Effects of object size on a function to convert x-ray CT numbers into the water equivalent path length of charged particle beam. pages 14–15.

Minohara, S., Kanai, T., Endo, M., Noda, K., and Kanazawa, M. (2000). Respiratory gated irradiation system for heavy-ion radiotherapy. *Int. J. Radiat. Oncol. Biol. Phys.*, 47(4):1097–1103.

Miyamoto, T., Baba, M., Yamamoto, N., Koto, M., Sugawara, T., Yashiro, T., Kadono, K., Ezawa, H., Tsuji, H., Mizoe, J. E., Yoshikawa, K., Kandatsu, S., and Fujisawa, T. (2007). Curative treatment of stage i non-small-cell lung cancer with carbon ion beams using a hypofractionated regimen. *Int. J. Radiat. Oncol. Biol. Phys.*, 67(3):750–758.

Miyamoto, T., Yamamoto, N., Nishimura, H., Koto, M., Tsuji, H., Mizoe, J. E., Kamada, T., Kato, H., Yamada, S., Morita, S., Yoshikawa, K., Kandatsu, S., and Fujisawa, T. (2003). Carbon ion radiotherapy for stage i non-small cell lung cancer. *Radiother. Oncol.*, 66(2):127–140.

Molière, G. (1948). Theorie der Streuung schneller geladener Teilchen II, Mehrfach- und Vielfachstreuung. *Zeitschrift für Naturforschung*, 3a:78–97.

Mori, S., Chen, G. T. Y., and Endo, M. (2007). Effects of intrafractional motion on water equivalent pathlength in respiratory-gated heavy charged particle beam radiotherapy. *Int. J. Radiat. Oncol. Biol. Phys.*, 69(1):308–317.

Mori, S., Furukawa, T., Inaniwa, T., Zenklusen, S., Nakao, M., Shirai, T., and Noda, K. (2013a). Systematic evaluation of four-dimensional hybrid depth scanning for carbon-ion lung therapy. *Med. Phys.*, 40(3):031720.

Mori, S., Inaniwa, T., Furukawa, T., Zenklusen, S., Shirai, T., and Noda, K. (2013b). Effects of a difference in respiratory cycle between treatment planning and irradiation for phase-controlled rescanning and carbon pencil beam scanning. *Br. J. Radiol.*, 86(1028):20130163.

Mori, S., Lu, H., Wolfgang, J. A., Choi, N. C., and Chen, G. T. Y. (2009). Effects of interfractional anatomical changes on water-equivalent pathlength in charged-particle radiotherapy of lung cancer. *J. Radiat. Res.*, 50(6):513–519.

Mori, S., Wolfgang, J., Lu, H. M., Schneider, R., Choi, N. C., and Chen, G. T. Y. (2008). Quantative assessment of range fluctuations in charged particle lung irradiation. *Int. J. Radiat. Oncol. Biol. Phys.*, 70(1):253–261.

Nihei, K., Ogino, T., Ishikura, S., and Nishimura, H. (2006). High-dose proton beam therapy for stage i non-small-cell lung cancer. *Int. J. Radiat. Oncol. Biol. Phys.*, 65(1):107–111.

Nikjoo, H., O'Neill, P., Terrissol, M., and Goodhead, D. T. (1999). Quantitative modelling of dna damage using monte carlo track structure method. *Radiat. Environ. Biophys.*, 38(1):31–38.

Nøttrup, T. J., Korreman, S. S., Pederson, A. N., Lasse, R. A., Nyström, H., and Specht, M. O. L. (2007). Intra- and interfraction breathing variations during curative radiotherapy for lung cancer. *Radiother. Oncol.*, 84(1):40–48.

Ohara, K., Okumura, T., Akisada, M., Inada, T., Mori, T., Yokota, H., and Caraguas, M. J. B. (1989). Irradiation synchronized with the respiration gate. *Int. J. Radiat. Oncol. Biol. Phys.*, 17:853–857.

Paganetti, H., Niemierko, A., Ancukiewicz, M., Gerweck, L. E., Goitein, M., Loeffler, J. S., and Suit, H. D. (2002). Relative biological effectiveness (RBE) values for proton beam therapy. *Int. J. Radiat. Oncol. Biol. Phys.*, 53(2):407–421.

Paretzke, H. G. (1986). Physical events of heavy ion interactions with matter. *Adv. Space Res.*, 6(11):67–73.

Park, C., Papiez, L., Zhang, S., Story, M., and Timmerman, R. D. (2008). Universal survival curve and single fraction equivalent dose: Useful tools in understanding potency of ablative radiotherapy. *Int. J. Radiat. Oncol. Biol. Phys.*, 70(3):847–852.

PDG (2010). Particle Physics Booklet.

Pedroni, E., Bacher, R., Blattmann, H., Bohringer, T., Coray, A., Lomax, A., Lin, S., Munkel, G., Scheib, S., Schneider, U., and Tourovsky, A. (1995). The 200-MeV proton therapy project at the Paul Scherrer Institute: Conceptual design and practical realization. *Med. Phys.*, 22(1):37–53.

Phillips, M. H., Pedroni, E., Blattmann, H., Boehringer, T., Coray, A., and Scheib, S. (1992). Effects of respiratory motion on dose uniformity with a charged particle scanning method. *Phys. Med. Biol.*, 37(1):223–233.

PTCOG. http://www.ptcog.ch/.

Richter, D. (2012). *Treatment planning for tumors with residual motion in scanned ion beam therapy*. PhD thesis, TU Darmstadt.

Richter, D., Schwarzkopf, A., Trautmann, J., Krämer, M., Durante, M., Jäkel, O., and Bert, C. (2013). Upgrade and benchmarking of a 4d treatment planning system for scanned ion beam therapy. *Med. Phys.*, 40(5):051722.

Rietzel, E. and Bert, C. (2010). Respiratory motion management in particle therapy. *Med. Phys.*, 37(2):449–460.

Rietzel, E. and Chen, G. T. Y. (2006). Deformable registration of 4D computed tomography data. *Med. Phys.*, 33(11):4423–4430.

Rietzel, E., Chen, G. T. Y., Choi, N. C., and Willet, C. G. (2005). Four-dimensional image-based treatment planning: Target volume segmentation and dose calculation in the presence of respiratory motion. *Int. J. Radiat. Oncol. Biol. Phys.*, 61(5):1535–1550.

Rietzel, E., Schardt, D., and Haberer, T. (2007). Range accuracy in carbon ion treatment planning based on CT-calibration with real tissue samples. *Radiat. Oncol.*, 2:14.

Ritchie, C. J., Hsieh, J., Gard, M. F., Godwin, J. D., Kim, Y., and Crawford, C. R. (1994). Predictive respiratory gating: a new method to reduce motion artifacts on CT scans. *Radiology*, 190(3):847–852.

RTOG (2014). Seamless phase i/ii study of stereotactic lung radiotherapy (sbrt) for early stage, centrally located, non-small cell lung cancer (nsclc) in medically inoperable patients. *RTOG 0813 Protocol Information*.

Saito, N., Bert, C., Chaudhri, N., Durante, M., Gemmel, A., Lüchtenborg, R., Schardt, D., and Rietzel, E. (2009). Technical status of the real-time beam tracking system. Report.

Sawakuchi, G. O., Titt, U., Mirkovic, D., and Mohan, R. (2008). Density heterogeneities and the influence of multiple coulomb and nuclear scatterings on the bragg peak distal edge of proton therapy beams. *Phys. Med. Biol.*, 53(17):4605–4619.

Schardt, D., Elsässer, T., and Schulz-Ertner, D. (2010). Heavy-ion tumor therapy: Physical and radiobiological benefits. *Rev. Mod. Phys.*, 82(1):383.

Scholz, M. (2003). Radiation effects on polymers for biological use. In *Effects of ion radiation on cells and tissues*, pages 95–155. Springer.

Scholz, M., Kellerer, A. M., Kraft-Weyrather, W., and Kraft, G. (1997). Computation of cell survival in heavy ion beams for therapy. the model and its approximation. *Radiat. Environ. Biophys.*, 36(1):59–66.

Scholz, M. and Kraft, G. (1994). Calculation of heavy ion inactivation probabilities based on track structure, x ray sensitivity and target size. *Radiat. Prot. Dosim.*, 52(1-4):29–33.

Scholz, M. and Kraft, G. (1996). Track structure and the calculation of biological effects of heavy charged particles. *Adv. Space. Res.*, 18(1-2):5–14.

Schulz-Ertner, D., Karger, C. P., Feuerhake, A., Nikoghosyan, A., Combs, S. E., Jäkel, O., Edler, L., Scholz, M., and Debus, J. (2007). Effectiveness of carbon ion radiotherapy in the treatment of skull-base chordomas. *Int. J. Radiat. Oncol. Biol. Phys.*, 68(2):449–457.

Seco, J., Robertson, D., Trofimov, A., and Paganetti, H. (2009). Breathing interplay effects during proton beam scanning: simulation and statistical analysis. *Phys. Med. Biol.*, 54(14):N283–N294.

Seppenwoolde, Y., Shirato, H., Kitamura, K., Shimizu, S., Lebesque, J. V., and Miyasaka, K. (2002). Precise and real-time measurement of 3D tumor motion in lung due to breathing and heartbeat, measured during radiotherapy. *Int. J. Radiat. Oncol. Biol. Phys.*, 53(4):822–834.

Shackleford, J. A., Kandasamy, N., and Sharp, G. C. (2010). On developing b-spline registration algorithms for multi-core processors. *Phys. Med. Biol.*, 55(21):6329–6351.

Shirato, H., Seppenwoolde, Y., Kitamura, K., Onimura, R., and Shimizu, S. (2004). Intrafractional tumor motion: Lung and liver. *Semin. Radiat. Oncol.*, 14(1):10–18.

Shirato, H., Shimizu, S., Kunieda, T., Kitamura, K., Kagei, K., Nishioka, T., Hashimoto, S., Fujita, K., and Aoyama, H. (2000). Physical aspects of a real-time tumor-tracking system for gated radiotherapy. *Int. J. Radiat. Oncol. Biol. Phys.*, 48(4):1187–1195.

Siegel, R., Ma, J., Zou, Z., and Jemal, A. (2014). Effectiveness of carbon ion radiotherapy in the treatment of skull-base chordomas. *CA Cancer J. Clin.*, 64(1):9–29.

Sonke, J. J., Lebesque, J., and van Herk, M. (2008). Variability of four-dimensional computed tomography patient models. *Int. J. Radiat. Oncol. Biol. Phys.*, 70(2):590–598.

Sonke, J. J., Zijp, L., Remeijer, P., and van Herk, M. (2005). Respiratory correlated cone beam CT. *Med. Phys.*, 32(4):1176–1186.

Steidl, P. (2011). *Gating for scanned ion beam therapy*. PhD thesis, TU Darmstadt.

Tai, A., Christensen, J. D., Gore, E., Khamene, A., Boettger, T., and Li, X. A. (2010). Gated treatment delivery verification with on-line megavoltage fluoroscopy. *Int. J. Radiat. Oncol. Biol. Phys.*, 76(5):1592–1598.

Tsujii, H. and Kamada, T. (2012). A review of update clinical results of carbon ion radiotherapy. *Jpn. J. Clin. Oncol.*, 42(8):670–685.

Tsujii, H., Kamada, T., Baba, M., Tsuji, H., Kato, H., Kato, S., Yamada, S., Yasuda, S., Yanagi, T., Kato, H., Hara, R., Yamamoto, N., and Mizoe, J. (2008). Clinical advantages of carbon-ion radiotherapy. *New J. Phys.*, 10(7):075009.

Tsujii, H., Mizoe, J., Kamada, T., Baba, M., Kato, S., Kato, H., Tsuji, H., Yamada, S., Yasuda, S., and Ohno, T. (2004). Overview of clinical experiences on carbon ion radiotherapy at NIRS. *Radiother. Oncol.*, 73(S2):41.

Tsujii, H., Mizoe, J., Kamada, T., Baba, M., Tsuji, H., Kato, H., Kato, S., Yamada, S., Yasuda, S., Ohno, T., Yanagi, T., Imai, R., Kagei, K., Kato, H., Hara, R., Hasegawa, A., Nakajima, M., Sugane, N., Tamaki, N., Takagi, R., Kandatsu, S., Yoshikawa, K., Kishimoto, R., and Miyamoto, T. (2007). Clinical results of carbon ion radiotherapy at NIRS. *J. Radiat. Res. (Tokyo).*, 48 Suppl A:A1–A13.

van't Riet, A., Mak, C. A., Moerland, M. A., Elders, L. H., and van der See, W. (1997). A conformation number to quantify the degree of conformity in brachytherapy and external beam irradiation: application to the prostate. *Int. J. Radiat. Oncol. Biol. Phys.*, 37(3):731–736.

Varma, M. N., Baum, J. W., and Kuehner, A. V. (1977). Radial dose, LET, and W for 160 ions in N2 and tissue-equivalent gases. *Radiat. Res.*, 70(3):511–518.

Weber, U. (1996). *Volumenkonforme Bestrahlung mit Kohlenstoff-Ionen zur Vorbereitung einer Strahlentherapie*. PhD thesis, TU Darmstadt.

Weber, U., Becher, W., and Kraft, G. (2000). Depth scanning for a conformal ion beam treatment of deep seated tumours. *Phys. Med. Biol.*, 45(12):3627–3641.

Weber, U. and Kraft, G. (1999). Design and construction of a ripple filter for a smoothed depth dose distribution in conformal particle therapy. *Phys. Med. Biol.*, 44(11):2765–2775.

Weyrather, W. K., Ritter, S., Scholz, M., and Kraft, G. (1999). RBE for carbon track-segment irradiation in cell lines of differing repair capacity. *Int. J. Radiat. Biol.*, 75(11):1357–1364.

Wikipedia. http://en.wikipedia.org/wiki/bronchopulmonary_segment.

Wilson, R. R. (1946). Radiological use of fast protons. *Radiology*, 47:487–491.

Zacharias, T., Dorr, W., Enghardt, W., Haberer, T., Krämer, M., Kumpf, R., Rothig, H., Scholz, M., Weber, U., Kraft, G., and Herrmann, T. (1997). Acute response of pig skin to irradiation with 12C-ions or 200 kV x-rays. *Acta Oncol.*, 36(6):637–642.

Zenklusen, S. M., Pedroni, E., and Meer, D. (2010). A study on repainting strategies for treating moderately moving targets with proton pencil beam scanning at the new gantry 2 at PSI. *Phys. Med. Biol.*, 55(17):5103–5121.

Ziegler, J. F. (1999). Stopping of energetic light ions in elemental matter. *J. Appl. Phys.*, 85:1249–1272.

Acknowledgements

In this antipenultimate section, I would like to thank the people who were involved in this work or who supported it. My first thanks go to the persons behind the ENTERVISION project, which funded this study, who managed to build a very supportive and motivating framework. I thank Manjit Dosanjh, Manuella Cirilli and Helen Dixon-Altaber in particular who have done everything to support all the researchers involved in this european project which turned out to be an unforgettable experience.

Then I would particularly like to thank Prof. Dr. Marco Durante who accepted me in the biophysics department of GSI as a PhD student to carry out an interesting study and to be part of the ENTERVISION project. I also thank Prof. Dr. Christoph Bert who helped me with my application to the ENTERVISION project and who provided helpful feedback about my results and suggestions for potential improvements during the last three years. Dr. Christian Graeff, as the new "moving targets" group leader, was always present to answer questions, to discuss about my results and to make TRiP work when some error message popped up. Also, his advice concerning statistics was also very useful. I thank him for his continuous follow-up.

Among the members of the "moving targets" group, I would like to thank Daniel Richter first, who took time to answer many questions regarding TRiP4D or radiotherapy in general. His point of view and his suggestions were always helpful and our discussions were always constructive. Results displayed in this study could not have been as exhaustive as they are without his help. I also thank all the members of the group I have discussed with and who helped me during the last three years, especially Nami Saito for performing image registration of all the 4DCTs used in this dissertation and leaving detailed documentation about her scripts, Sebastian Hild for providing the very useful dose visualization tool and Anna Constantinescu for sharing helpful literature regarding organ dose limits and, also with Anna Eichhorn, helping me with the thesis submission process.

From the other groups of the GSI biophysics department, I would like to thank Michaël Krämer for providing solutions regarding TRiP (and for providing TRiP itself) and the AIX system. I thanks Thomas Friedrich as well who also answered many of my questions about RBE and α/β ratios. This allowed me to have a better understanding of the biological aspects of radiotherapy. John Eley also helped me with the lung contour extraction algorithm by introducing the eroding/dilating method, which allowed me achieving this task faster and I thank him for that.

Of course, I thank my whole family who supported me during the last three years and during my entire education in general. Thanks to my parents, learning has always been a pleasure and I am pleased to have the opportunity to offer them such a reward for their constant dedication

and their continuous attention.

Finally, I would like to thank one teacher of mine who once quoted these wise words that I have since then not forgotten:

> *“Patience et longueur de temps*
> *Font plus que force ni que rage”*
> - Jean de la Fontaine

Those were particularly helpful during the numerous times I had to face an unexpected “segmentation fault” or a “not enough space” TRiP error message.

Curriculum vitae

Personal data

Name	Romain Brevet
Birth	13.10.1988 in Saint Brieuc, France

Education

Since 11.2011	ENTERVISION fellow (Marie Curie actions) & PhD study at GSI supervised by Prof. Marco Durante, TU Darmstadt & GSI (Darmstadt, Germany)
09.2010–06.2011	Master's degree ("Subatomical physics and astroparticules"), Université de Strasbourg (Strasbourg, France)
09.2008–09.2011	Engineering Diploma, Télécom Physique Strasbourg (Strasbourg, France)
09.2006–06.2008	CPGE MPSI/PSI (preparing for the competitive entrance exam to a "grande école"), Lycée François Rabelais (Saint Brieuc, France)
09.2003–06.2006	Lycée François Rabelais (Saint Brieuc, France)
09.1999–06.2003	Collège Léonard de Vinci (Saint Brieuc, France)
09.1991–06.1999	Ecole Louis Pasteur (Trégueux, France)

Erklärung zur Dissertation

Hiermit versichere ich, die vorliegende Dissertation ohne Hilfe Dritter nur mit den angegebenen Quellen und Hilfsmitteln angefertigt zu haben. Alle Stellen, die aus Quellen entnommen wurden, sind als solche kenntlich gemacht. Diese Arbeit hat in gleicher oder ähnlicher Form noch keiner Prüfungsbehörde vorgelegen.

Darmstadt, den February 16, 2015

(Romain Brevet)